Copyright

by

Nathaniel Lloyd Bill

2013

The Dissertation Committee for Nathaniel Lloyd Bill Certifies that this is the approved version of the following dissertation:

Extension of Tetrathiafulvalene Conjugation Through Pyrrollic-Based Dyes: ExTTF Porphyrin and ExTTF BODIPY

Committee:

Jonathan L. Sessler, Supervisor

Eric V. Anslyn

Christopher W. Bielawski

Alan H. Cowley

Donald R. Paul

Extension of Tetrathiafulvalene Conjugation Through Pyrrollic-Based Dyes: ExTTF Porphyrin and ExTTF BODIPY

by

Nathaniel Lloyd Bill, B.A.

Dissertation

Presented to the Faculty of the Graduate School of

The University of Texas at Austin

in Partial Fulfillment

of the Requirements

for the Degree of

Doctor of Philosophy

The University of Texas at Austin

December 2013

Dedication

"Never let your schooling interfere with your education."

–Mark Twain–

This dissertation is dedicated to my family, both old and new, without whom this would never have been possible. I am particularly indebted to my loving parents, Karen and Lloyd, whom worked tirelessly to foster a joyous and creative, albeit somewhat competitive, familial environment where all of their children felt loved, appreciated, and encouraged.

A special thanks goes to my grandparents, whom have been key supporters of my education, incredible role models, and have inspired wanderlust in each and every one of their six grandchildren.

Further thanks goes to my siblings—Stessie, Audrey, Tillie and Calvin. I feel blessed to have grown up in the same household with four of my best friends and closest allies.

Finally I would like to thank my beautiful wife, Jessica. During this arduous process, her unwavering support, patience, love, and friendship continually refilled my sails, after the wind had seemed to vanish.

I would like to extend an additional dedication to the memory of one of my few true friends—Brett Anderson. I had the fortune to share many years, experiences and memories with Brett. He will always hold a special place in my heart.

Acknowledgements

First and foremost I would like to acknowledge my “chemical grandfather” and graduate advisor, Professor Jonathan Sessler. Thank you Professor Sessler for your advice, encouragement, insight, patience and confidence during my time in your research lab. His light-hearted view of life and science, even in times of great trials and tribulations, will continue to be a great inspiration to me for years to come. Additionally, thank you for your rigorous efforts to improve both my scientific method as well as my scientific communication skills. I will forever be indebted to the support he provided during my work on this dissertation.

I would like to thank my coworkers in the Sessler group, whom have been my “brothers and sisters in arms” during this journey. Specifically, I would like to thank:

Dr. Dustin Gross—for taking me under his tutelage when I first joined the group.

Dr. Vladimir Roznyatovskiy—for being my close friend, labmate and mentor during our several years sharing a lab. He continues to patiently discuss my crazy ideas with me and has selflessly helped to stimulate my work without retribution.

Eric Silver and Dr. Christopher Bejger—for their immense friendship and fantastic conversations we shared in the “American Office.” I will always look back on the time we shared, discussing anything from chemistry to girlfriends, politics, pop culture, sports, teaching, etc. with the fondest of memories.

Dr. Vince Lynch—for patiently collecting the data and solving the structures of a seemingly endless number of single crystals.

Dr. Steffan Bähring, Christina Davis, and Zhan Zhang—for help with collaborating with me during my chemical endeavors.

Thank you to Netz Arroyo of the Prof. Alan Bard group for assisting in the ultramicroelectrode experiments.

I would like to thank the several other collaborators I had the pleasure of working with during my graduate studies. First, I would like to extend my gratitude to Prof. Phil Gale, Prof. Jason Love, and Dr. Bruce Moyer for the collaborations we shared during the early part of my career in the Sessler group. I would also like to graciously thank to thank Prof. Shunichi Fukuzumi and Prof. Dongho Kim, along with their groups, for performing the photophysical studies on several of my compounds. A special thanks goes to Prof. Masatoshi Ishida for all of his hard work concerning several of the compounds reported in this dissertation. This work would not have been as developed without his wisdom, guidance, and efforts.

Finally, I would like to thank all of the wonderful science instructors that have educated me over the years. In your own ways, you all inspired me to continue pursuing scientific endeavors. This list includes but is not limited to: Mrs. Brady (3rd grade), Mr. Petralia (5th grade), Ms. Stewart (7th grade), Mrs. Larsson (8th grade), Mr. Jose (HS, Chemistry and Physics), Prof. Zaffiro (undergraduate, Gen. Chem., P-Chem.), Prof. Haustein (undergraduate, Anal. Chem.), Prof. Benedict (undergraduate, Diversity of Life), Prof. "Viktor" Martisovits (undergraduate, Physics), Prof. Anslyn (graduate, Phys. Org.), Prof. Magnus (graduate, Org. Synthesis), Prof. Paul (graduate, Polymer Science) and Prof. Cowley, (graduate, Adv. Inorg.).

I am particularly indebted to my "chemical father," Prof. James Shriver. He not only taught me Organic Chemistry as an undergraduate at Central College, hired me as a teaching assistant for his labs and lectures, and gave me my first research experience, but also was a faithful advisor and close friend. Without him, I never would have matriculated to the University of Texas.

Extension of Tetrathiafulvalene Conjugation Through Pyrrollic-Based Dyes: ExTTF Porphyrin and ExTTF BODIPY

Publication No. _____

Nathaniel Lloyd Bill, Ph.D.
The University of Texas at Austin, 2013

Supervisor: Jonathan L. Sessler

The research and development of organic electron donors is essential in the discovery of photodynamic therapy photosensitizers and catalysts, as well as in the fabrication of organic-based electronic devices. Recently, π-extended tetrathiafulvalenes (exTTFs) have emerged as important organic donors due to their superb electronic properties. However, in general, exTTFs lack significant absorption in the visible and near-infrared portions of the electromagnetic spectrum, thereby limiting their utility. This doctoral dissertation depicts the author's efforts to address this inherent drawback of exTTFs by extending the electronic conjugation of tetrathiafulvalene moieties through pyrrole-based chromophores. The reported findings describe the design, synthesis, properties and potential applications of exTTFs with greatly enhanced absorption profiles.

The first Chapter provides a brief historical overview on the history and development of π-extended tetrathiafulvalenes. The various conjugated linkers

utilized in exTTF systems are reviewed. In the latter part of the Chapter, emphasis is given to the applications in which exTTFs find use.

Chapter 2, as the major focus of the dissertation, details the synthesis and characteristics of a quinoidal porphyrin-bridged exTTF, termed **MTTFP**. Several metalated complexes, including the Zn, Co, Cu, and Ni derivatives of **MTTFP** are reported. Additionally, the electrochemical, photophysical, and structural properties of **MTTFP**s are discussed. We also detail our efforts to synthesize and characterize both the one- and two-electron oxidized forms of **MTTFP**s. Finally, we discuss our efforts to reversibly switch thermodynamic electron transfer from **ZnTTFP** to Li@C_{60} through coordination of axial ligands.

Chapter 3 describes the formation of a 2:1 supramolecular ionic porphyrin complex between the two-electron oxidized form of **ZnTTFP** and a tetranionic sulfonated porphyrin. The association constants and the X-ray crystal structure of the complex are reported. A brief discussion outlining the photophysical characteristics (performed in Prof. Shunichi Fukuzumi and Prof. Dongho Kim's group) of the porphyrin donor-acceptor complexes are included.

Chapter 4 details the synthesis, photophysical properties, and spectroelectrochemistry of a difluoroboradiazaindacene (BODIPY) bridged exTTF. This compound is referred to as **ex-BODIPY**. A singlet oxygen generation study provides initial evidence that **ex-BODIPY** could potentially serve as a photosensitizer.

All of the experimental procedures, characterization data, and X-ray crystallographic data tables are reported in Chapter 5.

Table of Contents

List of Tables

List of Figures

List of Schemes

Chapter 1

Historical Development and Introduction into the Chemistry of π-Extended Tetrathiafulvalenes

1.1 Introduction

As the world population continues to grow and nations become more technologically developed, constant pressure is put on the scientific community to develop chemical systems of increased functionality, higher quality, and with specific mechanical properties—all at a lower cost and minimal environmental impact. To this end, organic-based electronic devices (OBEDs), which are potentially cheaper, lighter, and easier to process than their inorganic counterparts, are receiving increased attention.

As generally construed, OBEDs include solar cells, conductors, superconductors, molecular wires, transitors, and other advanced materials. The development and optimization of organic electron donors is of the utmost importance in the generation of such devices. Recently, organic donors have also received increased attention for their role in promoting and catalyzing new reactions. Subsequently, an extensive variety of molecules have been utilized as organic donors including tetrathiafulvalenes, porphyrins, ferrocenes, phthalocyanines, polythiophenes, aryl amines and etc., with the optimal donor properties depending solely on the desired

application. Thus, these classes of molecules have been and continue to be the subjects of extensive research.

A subset of tetrathiafulvalenes, π-extended tetrathiafulvalenes, has received decidedly less attention despite its beneficial attributes (e.g. charge stabilization and non-planar shape). To begin, this chapter aims to provide an historical overview of the developments in the area (starting with pristine tetrathiafulvalenes), as well as a basic understanding of the chemistry of π-extended tetrathiafulvalenes. Additionally, key findings made using this class of organic donor will be highlighted. Particular attention is given toward emerging applications and the barriers that need to be overcome before devices based on these materials can become commercially viable.

1.2 Tetrathiafulvalenes

In 1970, first Wudl[1.1] and others quickly thereafter,[1.2] reported on what would become an expansive class of electron donors, known as tetrathiafulvalenes (TTFs). In this system, two 1,3-dithiolidine rings are covalently linked with an alkenyl bridge,[1.3] a fortuitous combination that allows novel and exciting electrochemical properties to be realized. For instance, TTF was shown to undergo two reversible one-electron oxidations at mild potentials, first yielding a stable radical cation, and then upon further oxidation a dication (Figure 1.1).

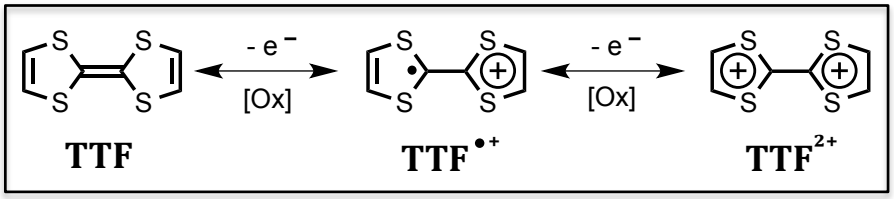

Figure 1.1 Stepwise one-electron oxidations of TTF.

The unique stability and accessibility of the intermediate radical cation of TTF was rationalized to result from a pair of orthogonal phenomenon: Aromaticity and columbic repulsion. TTF, which is a planar 14 π-electron system is not considered to be Hückel aromatic due to a lack of conjugation around the ring. However, after donation of an electron (forming $TTF^{\bullet+}$), one of the dithiole rings of TTF gains 4n +2 π-electron aromaticity by utilizing the remaining double bond, two lone pairs from the sulfur atoms and the vacant π orbital from the center bearing the positive charge. An increase in aromaticity accounts for the relative stability (compared to other radicals) of the organic radical species generated upon oxidation. Further oxidation to TTF^{2+}, leads to columbic repulsion from the generated positive charges, destabilizing the HOMO of $TTF^{\bullet+}$ and requiring a larger potential to achieve oxidation. Together, these properties account for the "splitting" of the first (+0.32 V vs. SCE) and second (+0.71 V vs. SCE) oxidation potentials of TTF and thus the stability of $TTF^{\bullet+}$ over a substantial voltage range.[1,4]

Shortly after the discovery of the electron donating ability of TTF, the first solid state "organic metal" was synthesized by combining TTF with an electron acceptor *p*-tetracyanoquinodimethane (TCNQ).[1,5] By combining TTF and TCNQ in acetonitrile, crystalline stacks of partially oxidized TTF adjacent to partially reduced TCNQ were isolated. These stacks displayed unidirectional metallic conductivity over a wide temperature range and down to 59 K. After this seminal discovery, a countless number of papers have been published that report improvements

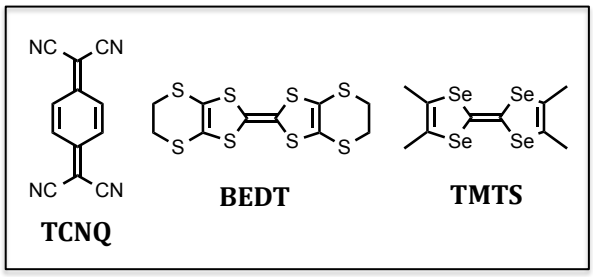

TCNQ **BEDT** **TMTS**

upon, or additions to, this pioneering work. One of the most important later findings was that derivatives of TTF, such as tetramethyltetraselenafulvalene (TMTS) and bis(ethylenedithio)-tetrathiafulvalene (BEDT), are capable of forming organic superconductors. For many years, the organic superconductor with the highest critical temperature (T_c) was a salt made from BEDT (T_c = 12.3 K),[1.6] and although derivatives with higher critical temperatures based on C_{60} or picene exist, they are very unstable.[1.7]

The favorable electronic and conductive properties of TTF sparked intense interest in the field. In fact, TTFs have been used in a wide variety of applications[1.8] (Figure 1.2) and have been featured in a staggering number of papers (>30,000). There have been several books[1.9] and reviews[1.10] summarizing the important developments of this chemistry and further discussion about basic TTFs is outside of the scope of this dissertation.

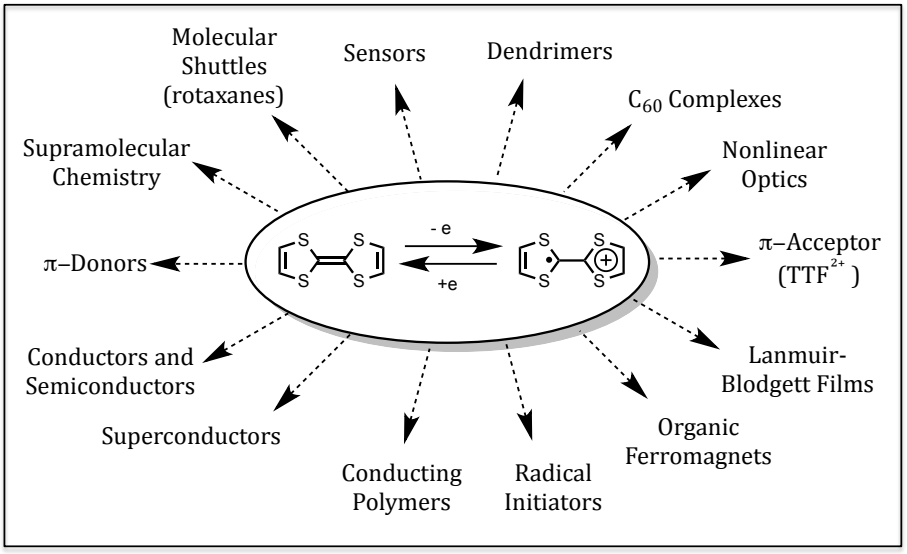

Figure 1.2. Several known applications of TTFs.

1.3 π-Extended Tetrathiafulvalenes

The crystal and packing structures, as well as the electronic properties of TTFs, can be significantly altered by insertion of a π-conjugated linker between the ditholidine rings. The advantages of incorporating a conjugated linker are two-fold. First, by increasing the distance between the dithiolidine rings, and subsequently the distance between the positive charges formed upon oxidation, columbic repulsions are minimized. A decrease in columbic repulsion removes a large barrier to electron transfer and can lead to higher conductivities and better-stacked crystalline materials. Second, the identity of the conjugated linker can be changed nearly at will. Thus, in principle, and in turn the physical, electronic and material properties of the system can be altered or tuned. Of particular interest is the ability to alter the electron donating power of TTFs since this may provide a way to optimize interactions with various acceptors, something that is important for practical applications.

Arguably, the two most important tunable traits of π-extended TTFs (exTTFs, taken ostensibly to refer to any system with dithiolidine rings connected through a conjugated linker), namely the degree of columbic repulsion and the electron donating ability, can easily by estimated from analysis of cyclic voltammagrams (CVs). The electron donating ability is simply estimated from the first oxidation wave of the CV. With this is mind, a shift to lower oxidation potentials is inherently tied to an increase in electron donating ability of a compound or system. Second, as mentioned previously in the discussion of simple TTFs, the first (E_1) and second (E_2) oxidation waves are split due to columbic interactions. Therefore, a reduction in the

separation of the half-wave potentials (E_2 - E_1) is indicative of a reduction in the columbic repulsions between the dithiolidine rings.

1.3.1 π-Expanded Tetrathiafulvalenes with Alkene and Alkyne Spacers

The simplest exTTF, in which a vinyl group is inserted between the dithiolidine rings (**1.1**), was reported by Yoshida in 1983.[1.11] The electronic behavior of this compound helped establish the trends that describe the effects of further extension of the π-system of TTFs. Namely, the CV of **1.1** shows a first oxidation wave at 0.20 V. This value is 0.15 V lower than that of corresponding TTF derivatives. The increase in electron donating ability is attributed to the larger π-system being able to delocalize more efficiently the charge of the radical cation generated by oxidation. Also, the difference between the first and second oxidation waves (E_2-E_1) was only 0.16 V, compared to a value of 0.44 V recorded for TTF itself under identical conditions. This drastic decrease in the splitting of the redox waves was rationalized in terms of the large decrease in columbic repulsion resulting from the physical separation of the oxidatively induced positive charges.

Modification of the basic vinylogous system of **1.1**, has been accomplished by altering the attached functional groups. For example, derivatives in which groups are appended to the 3 and 4 positions of the ditholidine rings are known. These systems display little to no change in the splitting of the oxidation potentials, compared to **1.1**. Further, the substitution of vinylogous exTTFs at the 3 and 4 positions alters the compounds electron donating ability. The magnitude of the redox shifts closely mirror those observed for substituted, but non-extended, TTFs.[1.9]

Substitution of the vinyl-hydrogens present in **1.1** is also possible. Such modifications are intrinsically impossible with TTF. Exchange at this position by bulky groups leads to non-planar molecules that are generally unsuited for studies of crystalline conductivity due to a lack of π-π interactions.[1.12] Alternatively, incorporation of phenyl groups at the vinyl positions (**1.2a-e**) allows for a planar geometry only in circumstances where the phenyl rings are twisted out of the plane, flattening the vinyl skeleton.

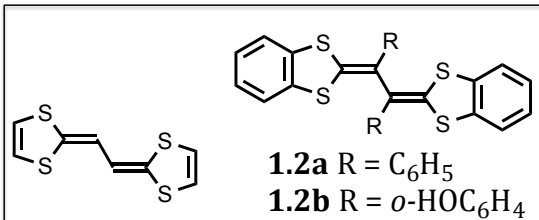

1.1

1.2a R = C_6H_5
1.2b R = *o*-HOC_6H_4
1.2c R = 2,6-$F_2C_6H_3$
1.2d R = *o*-ClC_6H_5
1.2e R = *p*-ClC_6H_5

Compound	E_1/V	E_2/V	E_2-E_1/V
1.1	0.20	0.36	0.16
1.2a	0.61 (2e)		—
1.2b	0.44	0.64	0.20
1.2c	0.66	0.85	0.19
1.2d	0.53	0.75	0.22
1.2e	0.67 (2e)		—

Figure 1.3. Selected examples of vinyl bridged tetrathiafulvalenes and their oxidation potentials.

The redox behavior of phenyl substituted compounds is greatly affected by the identity of the attached phenyl ring (Figure 1.3).[1.13] Although all are good donors, incorporation of electron donating groups (e.g. –OH, **1.2b**) increases the donor ability whereas withdrawing groups (e.g. –F, **1.2c**) dampens the donating strength, as expected. The position of phenyl ring substitution also has a drastic effect on the redox character of these species. Compounds with *para*-substitution (e.g **1.2d**) or unsubstituted phenyl rings (**1.2a**) undergo a single two-electron oxidation. On the other hand, compounds with *ortho*-substitutuents (e.g. **1.2e**) exhibit two one-electron peaks. Detailed studies have demonstrated that this differing redox behavior is attributed to a large change in conformation between the alternate

substitution patterns.[1.14] Specifically, the *para* and unsubstituted derivatives exist in an "X"-conformation in the neutral form. Upon oxidation (2 e^-) the compounds become planar with respect to the dithiolidine rings and the phenyl groups are twisted from the plane. In contrast, the *ortho*-substituted phenyl rings twist in the neutral form due to steric crowding. This permits the dithiolidine rings to be planar, similar to **1.1**, and stabilizes the one-electron oxidized radical cation by charge delocalization. Thus, two one-electron oxidation peaks are seen in the CV.

Further extension of the conjugation can be achieved by increasing the number of vinyl-groups in the linker bridging together the dithiolidine rings.[1.15] When the number of alkenyl bonds separating the ditholidine rings is two (**1.3**) or more, the splitting in the oxidation potentials seen in the smaller systems, is no longer observed. The increase in the dithioliding ring separation distance of the larger systems effectively eliminates columbic repulsion, causing a single oxidation wave, cooresponding to a two-electron process, to be observed in the CV. Increasing the π-conjugation further, by adding additional bridging double bonds, caused a slight reduction in the oxidation potential for every vinyl group added along with a 16-20 nm bathochromic shift in the lowest energy absorption maximum.[1.16]

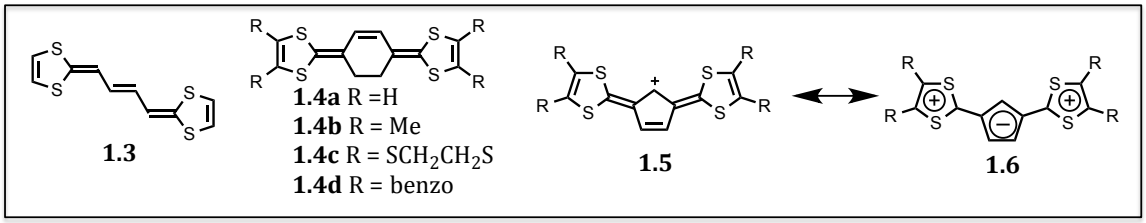

The effect of *cis* vs. *trans* double bonds was also investigated by utilizing cyclic olefins that are fixed in the *cis* conformation via covalent bonds. Simple cyclohexene bridged compounds were prepared with a variety of substituents at the 3 and 4

positions of the dithiolidine rings. Similar to its *trans* isomer, compound **1.4a** displayed no splitting between its oxidation peaks.[1.17] However, in a departure from their *trans* congeners, upon substitution of the dithiolidine rings (**1.4b-d**), a small splitting in the oxidation peaks was observed (from 0.11 to 0.06 V).[1.18] Cylcopentene derivatives have also been prepared. These display irreversible redox behavior. This is rationalized in terms of the formation of a stable cationic intermediate that is produced by an oxidative deprotonation reaction leading to compound **1.5**, a species that is stabilized by resonance structure **1.6**. Interestingly, these compounds are intensely colored, with tunable absorption and fluorescence profiles.[1.19]

Acetylene spacers have also been incorporated into exTTFs. These compounds show rather unremarkable characteristics. They show poorly reversible oxidation waves except in cases where additional acetylene units (not part of the conjugation pathway) are also present. In both cases, these compounds show little promise as conducting materials. Thus, studies concerning acetylene-linked exTTFs have been relatively limited.[1.20]

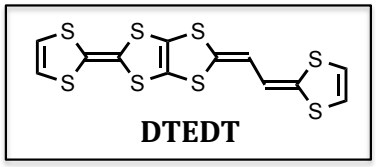

DTEDT

Of particular interest is a vinyl-extended TTF fused through the dithiolidene ring with a normal TTF subunit. This molecule, referred to as DTEDT, displays superconductivity at temperatures below 4 K as its $Au(CN)_2$ salt. Metallic salts of other metals were also stable down to liquid helium temperatures. These observations lend credence to the idea that manipulation of the electronic features of TTF derivatives through π-extension can lead to novel materials with interesting applications.

1.3.2 π-Expanded Tetrathiafulvalenes with Aromatic Spacers

In general exTTFs with aromatic groups as spacers have higher oxidation potentials (i.e., are weaker donors) than simple TTFs. Stabilization of the neutral state by an aromatic linker is the explanation for this finding. Upon oxidation, aromaticity is broken, and thus molecules of this nature resist initial oxidation. Benzene-linked derivatives have been prepared with *ortho-, meta-,* and *para*-substitution, displaying markedly different properties. The 1,4-substituted *para* compound unsurprisingly shows two irreversible oxidation peaks at higher potentials than TTF.[1.21] The 1,2-*ortho* derivative behaves electrochemically in a similar manner. However, it rearranges in the presence of acid or bromine due to the proximity of the reactive groups.[1.22] The *meta*-derivative undergoes oligomerization instead of the expected step-wise oxidation.[1.23] This is attributed to the rings not being in conjugation with one another, causing a reactive radical species to form upon initial oxidation. Napthalene derivatives exhibit relatively similar behavior.

Five-membered heterocyclic aromatic rings have also been probed for their utility in extending TTF conjugation (Figure 1.4). Undoubtedly driven by the availability of the requisite diformyl precursors, pyrrole (**1.12**), furan (**1.13**), and thiophene (**1.14**) rings have been incorporated into exTTF systems.[1.24] All three derivatives show two one-electron oxidations at varying potentials. These findings are consistent with the

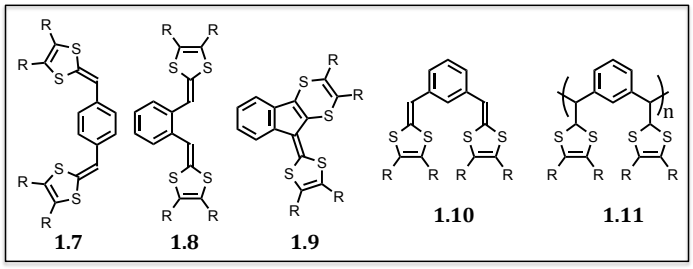

idea that the heteroatom contributes to the electronic structure of these systems. Was that not the case, only one oxidation wave would be expected, in analogy to the vinyl-conjugated systems discussed previously.

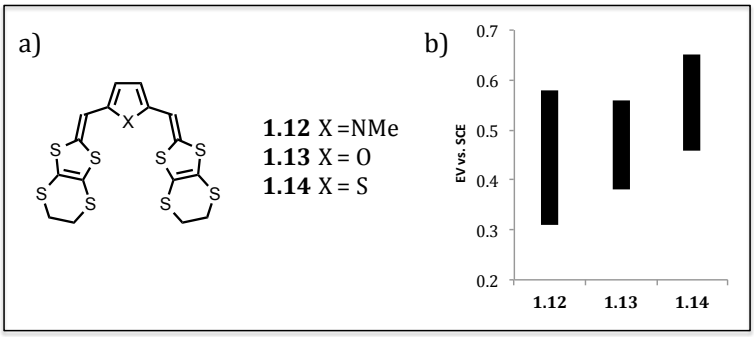

Figure 1.4. (a) Heterocycle-bridged exTTFs and (b) The black bars depict the range of potentials over which the radical cation is stable. Thus, the lower limit is the value of E_1 and the upper limit is the value of E_2.

Oxidation of heteroaromatic-linked exTTFs breaks the aromaticity of the linker in a similar manner to what was discussed for carboaromatic systems. Thus, one would expect the potential required to initiate electron transfer to be directly proportional to the strength of heterocyclic aromaticity. In the case of five membered rings, the degree of aromaticity has been well established and follows the trend furan << pyrrole < thiophene. When comparing heteroaromatic exTTFs with similar 3,4-dithiolidine substitutions, the order in which the second redox process (E_2) of the compounds occurs (**1.13** ≤ **1.12** < **1.14**) closely mimics the trend in the aromatic strength of the heteroaromatic linkers. In opposition, the first oxidation potential, E_1, follows the trend **1.12** < **1.13** < **1.14**. The order of E_1 more closely resembles the relative rates of electrophilic aromatic substitution for the heterocycles and gives evidence to the fact that the heteroatom plays a vital role in stabilizing the positive charge in present the radical cation state. Taken together,

these various findings demonstrate that the pyrrole-containing exTTFs are characterized by a larger peak separation, ΔE (E_2 - E_1), than its thiophene or furan counterparts. As a consequence, the pyrrole-exTTFs display a more stable radical cation state.

ExTTFs with olgiothiophene spacers have also been reported. Compounds with bi- (**1.15a**) and terthiophene (**1.15b**) spacers display convoluted electrochemical properties at relatively high potentials (0.17 V higher than the related mono-thiophene compound). Specifically, in the bi-thiophene analogues, E_1 and E_2 coalesce. However, in the terthiophene system the oxidation potentials split further.[1.25] This is counterintuitive to what would be expected based on other results. However, these observations are rationalized by considering the lack of planarity in **1.15b** due to rotation about the single bond between the thiophene rings. Rigidification of this bond through covalent attachment leads to a substantial lowering of E_1 as well a lowering of the HOMO-LUMO energy gap.[1.26]

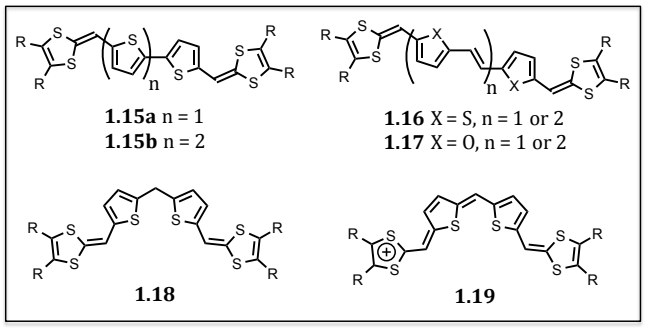

The use of polyvinyl-thiophene (**1.16**)[27] and furan (**1.17**)[1.28] spacers gives rise to species with absorption bands that are red-shifted compared to polythiophenes. Presumably, this reflects an increase in planarity and decreased aromatization. Both **1.16** and **1.17** exhibit two-electron oxidation processes. The recorded electron donating strengths of the compounds are nearly independent of the length of the bridging oligiomeric chain. For this reason the oxidation process is assigned to

occur at the dithiolidine ring moeities. Further oxidation gives rise to one-electron processes attributed to oxidation of the furan or thiophene rings. This assignment is based on the redox values being rather insensitive to changes in the substitution on the dithiolidine rings.

Finally, *bis*(thiophenyl)methane (**1.18**)[1.29] derivatives have been prepared. Although irreversible oxidation waves are recorded, upon reversal of the scan new reduction peaks arise in the CV. The new features are attributed to the formation of a stable cationic species (**1.19**). Oxidative deprotonation of the methylene protons, leads to a conjugated cationic product, which can be isolated with various counteranions. In contrast to the neutral species, which is severely twisted about the *meso* carbon, the salt produced upon oxidation is planar. This leads to intense near-IR absorption in the case of the salt.

1.3.3 π-Expanded Tetrathiafulvalenes with Quinoidal Spacers

Quinoidal-linked exTTFs are the best-studied group of linked dithiolidines. The breadth of work highlighting this class of compound stems from its superior electronic properties, ease of synthesis, and the fact that synthetic handles can easily be incorporated into this type of molecule. In general, quinoidal exTTFs are better electron donors than their smaller TTF cousins and other classes of exTTFs of similar size, containing analogous functional groups and degree of conjugation. This increased donor capability is the result of aromaticity being formed within the linker upon oxidation, which provides further driving force for electron transfer.

The pro-anthracene derivative **1.20**, was synthesized by Akiba[1.30] in 1978 utilizing, for the first time, the Horner-Wadsworth-Emmons (HWE) reaction with a

phophonate ester dithiolidine ring. This compound shows a two-electron oxidation at low potentials. Further, this reaction would prove to be a key step in the production of future homologues. In 1989, in seminal work carried out by Yamashita *et al.*, several derivatives of **1.20**, as well its pro-benzene (**1.21**), and pro-napthalene (**1.22**) analogues were reported.[1.31] The latter two were not readily attainable from their constituent quinones. To circumvent this problem the appropriate synthons were protected *via* a Diels-Alder reaction with cyclopentadiene, followed by a HWE reaction. A subsequent retro Diels-Alder reaction afforded the desired products.

Scheme 1.1. Synthesis of pro-benzene exTTF **1.21**, and structures of pro-napthalene **1.22** and pro-anthracene **1.20** exTTF.

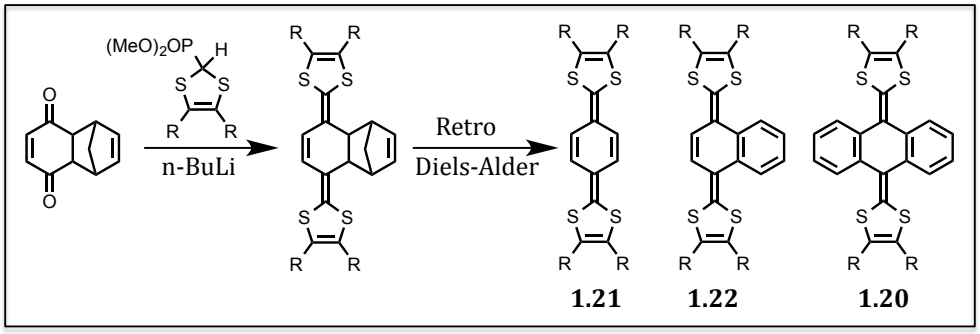

Both **1.21** and **1.22** are better donors than their pro-anthracene counterparts. In fact, **1.21** is one of the strongest TTF donors known (-0.11 V vs. SCE), and is unstable in solution. The final prepatory step of this compound must be performed in the solid state to avoid decomposition. A very small (0.07 V) peak separation is observed for **1.21.** The synthetic addition of a benzene ring to **1.21,** giving **1.22,** results in a slight increase in the oxidation potential (0.00 V vs. SCE), although the separation between E_1 and E_2 no longer exists resulting in a two-electron process. Appending additional benzene rings further raises the oxidation potential.

The separation of E_1 and E_2 in **1.21** and the lack of splitting between E_1 and E_2 seen for the larger derivatives led to the realization that Coloumbic repulsion was not the sole factor governing the separation of half-wave potentials. Examination of the oxidized and reduced crystal structures of **1.20** (R = Me) led to the realization that geometric factors are also important. In the neutral (reduced) state, **1.20** was found to have a butterfly shape, whereas the two-electron oxidized structure was planar with the dithiolidinium rings nearly orthogonal to the anthracene core (Figure 1.5).[1.32] A change in molecular structure at one or both electron transfer steps has been found to be a requisite for the occurrence of inverted potentials (when $E_2 < E_1$),[1.33] and thus a lack of planarity is expected in **1.20**. Designs seeking to stabilize the radical cation state should consequently be flat throughout the conjugation pathway as non-planar structures are thermodynamically unstable due to a lack of sufficient orbital overlap to sustain conjugation.

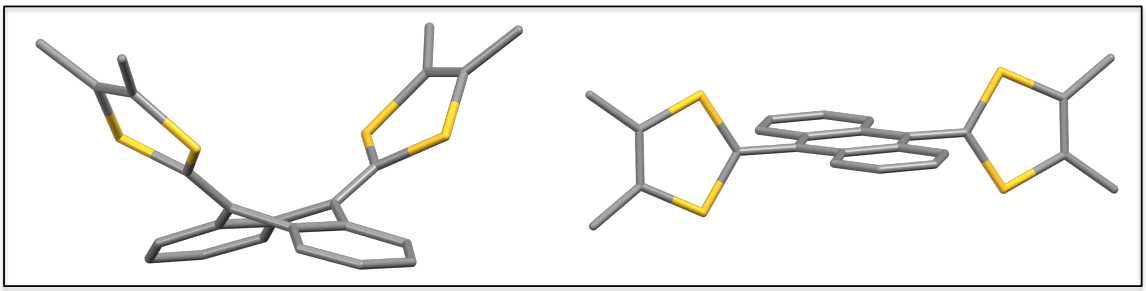

Figure 1.5. Butterfly shape of neutral **1.20** (left). Two-electron oxidized form **1.20**$^{2+}$ (right). Hydrogen atoms and counter anions of **1.20**$^{2+}$ are omitted for clarity.

Attempts to retain the quinoidal design but flatten the reduced state have focused on removing the so-called peri-hydrogens, which are hypothesized to stericly conflict with the sulfur atoms of the dithiolidine rings. This theory nicely explains why compound **1.21** has split potentials, although the split is minimal.

Moreover, derivatives with annulated benzene rings display only one two-electron oxidation process. Further credence to the theory that steric effects are important came with the synthesis of the 1,2,5-thiadiazole compound **1.23**.[1.34] This compound lacks peri-hydrogens and is planar. CV studies revealed split oxidation waves at potentials higher than other exTTFs but still lower than TTF. Annulation of a benzene ring onto compound **1.23** to give **1.24** results in reintroduction of the peri-hydrogen and deterioration of cathodic peak separation.[1.35]

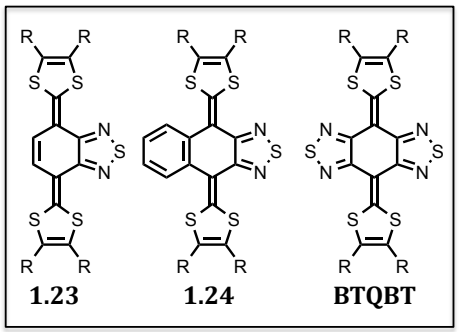

Bisthiadiazole compounds show extraordinary characteristics with respect to organic electronics. In particular, bis(1,2,5)thiadiazolo-*p*-quinobis(1,2-dithiole) (BTQBT) demonstrates remarkable single component semiconductor properties with a crystalline conductivity of 8.3 x 10^{-4} S/cm.[1.36] The crystal structure, Figure 1.6, shows a planar sheet like structure, with short S—S contacts that facilitate conductivity. Further, the anisotropy of conductivity is small and these compounds display the Hall effect. Thin films of these molecules show hole mobility and on/off ratios in line with those of pentacene films and recently patents detailing their utility for organic electronics have been filed.[1.37]

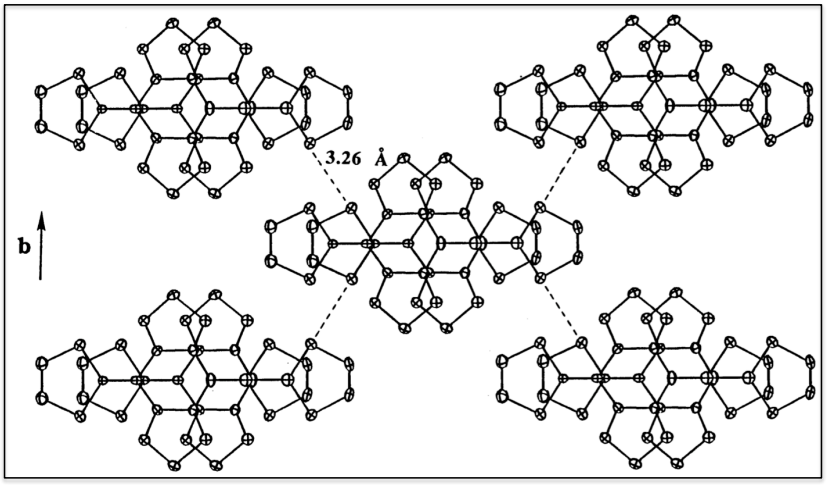

Figure 1.6. Crystal packing structure of BTQBT. Reproduced with permission from *J. Org. Chem.* **1992**, 57, 5517, Copyright 1992 American Chemical Society.

1.3.4 Applications of π-Expanded Tetrathiafulvalenes

Due to their unique electrical properties, exTTFs have found a variety of uses in organic electronics. Apart from their conductivity (discussed in the general overview of exTTFs, sect. 1.3.3), most studies of potential utility have centered around the pro-anthracene derivative **1.20**. The reasons for this choice are multi-fold, with the major emphasis depending solely on the desired application. Some of the beneficial properties of **1.20** include: Ease of synthesis and fully-developed synthetic protocols, tunability at the pro-anthracene position in addition to the 4,5-position of the dithiolidine, thermal and photochemical stability, butterfly shape (which reduces aggregation and provides a curved surface), and inverted potentials. For this reason **1.20** has been utilized in a wide-range of applications, including molecular wires, organic photovoltaics (OPV), hosts for carbon nanoforms, photosynthetic mimics, chemosenors, NLO devices, and supramolecular patterning motifs. Important findings and breakthroughs are discussed further below.

Most applications of exTTFs revolve around their interaction, in some manner, with fullerenes. C_{60} for instance, is known to be a superb electron acceptor that can accept up to six electrons. Simple dyads covalently linking exTTF with C_{60} have been synthesized. A variety of connections, varying in regio-connectivity and number of carbons between the donor and acceptor, have been investigated (**1.25** – **1.27**).[1.38] Regardless of the linkage, these systems display greatly enhanced stability of the charge separated (CS) excited states, with CS lifetimes up to 174 to 200 ns. Remarkably, this value is about two orders of magnitude longer than analogous systems utilizing TTF as a donor (2 ns).[1.39] Although these CS lifetimes are not long-lived enough to warrant incorporating these molecules as an active layer in solar cell devices (where CS lifetimes ≥ 1 ms are ideal[1.40]), this provides a good foundation for further work in this area.

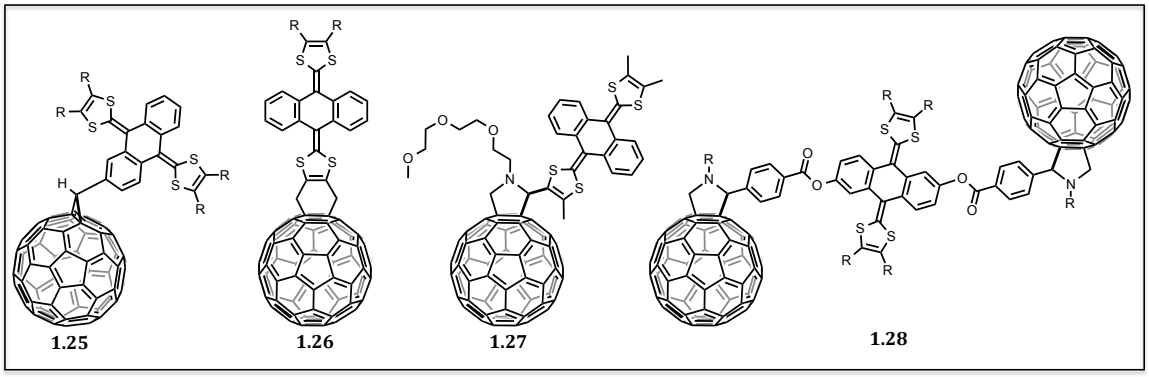

Dyads of **1.20** and C_{60} have also been used to investigate the proficiency of conjugated molecular wires. In these systems, the ability of the electronically isolated bridge to transport charge or energy is investigated by covalently linking the exTTF donor to C_{60} with the "wire" of interest. Irradiation of these systems leads to the exTTF donating an electron to the fullerene *via* the wire. The kinetics of

the process, including the charge separation (CS) and charge recombination (CR) dynamics, are driven by the electron transfer rate constant:

$$k_{\mathrm{ET}} = k_0 \mathrm{e}^{-\beta R_{\mathrm{DA}}}$$

where k_0 is the kinetic prefactor, β is the attenuation or dumping factor which is representative of the rate of decay of the CS state, and R_{DA} is the distance between the donor and acceptor. All other things equal, minimization of the dumping factor, *β,* leads to an increase in the conductivity of the bridge.

Molecular wires of oligio *p*-phenylenevinylenes have been prepared linking exTTF to a molecule of C_{60}.[1.41] Facile hole-electron injection into the wire takes place, with a very small attenuation factor of 0.01 $Å^{-1}$. The radical pair generated as a result, was found to be quite stable, with a CS lifetime of 4.35 μs in benzonitrile. Using the same basic setup (C_{60}-wire-exTTF) other linkers have been tested as molecular wires, such as alkynyl,[1.42] *meta*- and *para*-oligo(phenyleneethynylene),[1.43] and oligofluorenes.[1.44] The photophysical and wire-like behavior of these linkers was probed and attenuation factors between 0.2 $Å^{-1}$ (oligo(*p*-phenyleneethynylene)) to 0.09 $Å^{-1}$ for oligofluorenes were recorded. In short, a systematic comparison of the attenuation factors utilizing identical donors (exTTF), acceptors (C_{60}) and connectivity allows direct comparisons as to the performance of various molecular wires to be made.

Covalently linked triads have also succumbed to synthetic efforts and provide further insights into the utility of these fullerene-linked exTTFs. "Dumbbell" shaped systems in which an exTTF is covalently capped by C_{60} on either end, have been produced with a variety of substituents connected to the dithiolidine rings.[1.45]

Photophysical studies demonstrate that **1.28** has CS state lifetimes of up to 630 ns (in PhCN). Removal of one of the C_{60} "caps", leads to a reduction in the stability of the CS excited state (lifetime = 480 ns in PhCN). Thus, incorporation of two electron acceptors has a stabilizing effect on the radical CS state. However, the theoretical reasons for this trend have yet to be elucidated.

In contrast to the aforementioned dumbbell shaped triads, linear triads containing two exTTF subunits have been reported that participate in long-range electron transfer reactions. The efficiency of electron-transfer at longer distances is governed by a superexchange mechanism, which has, as its rate determining step, the electronic coupling of the donor and acceptor. At distances greater than 20 Å, relaxation of the excited state dominates over electronic coupling (which diminishes exponentially with increasing distance between the donor and acceptor). Thus, separation of the electroactive components over 20 Å leads to a reduction in electron transfer efficiency.

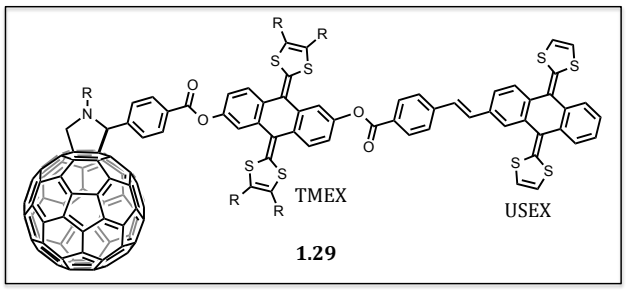

1.29

In an attempt to combat the intrinsic distance limitations to electron transfer, electronic cascades, such as **1.29** have been employed.[1.46] In this triad, C_{60} is tethered to two redox inequivalent exTTFs. Substitution of thio-methyl groups to the central bridging exTTF unit alters the redox properties of the moiety, shifting the oxidation potential to more positive potentials.[1.9] Thus, a redox gradient is established between the thio-methyl substituted exTTF (TMEX) and the unsubstituted exTTF (USEX). Upon

photoexcitation of the fullerene, efficient electron transfer occurs from TMEX to C_{60} generating the radical pair $C_{60}^{\bullet-}$-$TMEX^{\bullet+}$-USEX. Photophysical measurements demonstrate the lifetime of this excited state is 54 to 460 ns, depending on the solvent. After initial transport from TMEX to C_{60}, a second electron transfer process, driven by the electrochemical bias between the two exTTFs, takes place from USEX to $TMEX^{\bullet+}$, generating the long-range radical pair $C_{60}^{\bullet-}$-TMEX-$USEX^{\bullet+}$. A drastic increase in the lifetime of the separated radical pair species is observed, up to 111 μs. The stability of this CS species was rationalized by the large distance (30 Å) between the oppositely charged radicals, diminishing the electronic coupling between the oxidized USEX and reduced $C_{60,}$ and drastically inhibiting recombination. Instead, because direct recombination is blocked, a step-wise recombination mechanism must occur, accounting for the long lifetimes. Overall, compound **1.29** provides a mimic of the photosynthetic process, namely, well-defined redox cascades and long-lived CS states.

Carbon nanoforms other than fullerenes have been covalently linked to exTTFs. One such nanoform is carbon nanotubes (CNTs). A subset of CNTs, single-walled carbon nanotubes (SWNT), which can be produced in a variety of diameters, lengths, chiralities, conductivities, and mechanical and electrical properties, have been of increasing interest in molecular electronics and in the construction of donor/acceptor conjugates. Thus, SWNT with covalently appended exTTF units have been made. Nanosecond flash photolysis revealed the presence of the exTTF radical cation and reduced SWNTs, with a transient lifetime of 160 to 335 ns. Similar to the work with dyads of C_{60}, the exTTF appended SWNTs were longer lived

than their TTF appended counterparts.[1.47] Graphene linked exTTFs have also been reported.[1.48] However, to the best of the author's knowledge no photophysical studies of these latter compounds have been reported. Thus, comparisons with other carbon nanoforms cannot be made at the present time.

The demonstration of persistent radical CS excited states of covalent linked exTTF-carbon nanoform systems inspired efforts to incorporate these structures into bulk hetero junction (BHJ) OPV devices. The basic setup of a BHJ device involves an intimate blend of active layers (donor and acceptor) sandwiched between two electrodes (Figure 1.7). The efficiency of a BHJ solar cell requires several complex factors, to be optimized simultaneously. Several of these factors relate directly to the active material, including: (1) Efficient harvesting of, ideally, the entire solar-spectrum and, upon absorption of light, production of a long-lived excited state or exiton. (2) The exiton must be formed or migrate to a nearby interface (< 10 nm) where electron transfer takes place. (3) The reduced and oxidized species must be separated and stable enough to travel several micrometers through the cell to opposite electrodes where the charge and energy can be collected. Manipulation of one factor, such as the electronics of a molecule, to maximize absorption and electron transfer often drastically changes the material properties, including the crystal packing, solubility, and intermolecular interactions. This in turn, alters the proficiency of charge separation, the nature of the interfaces, the degree of conductivity and overall device efficiency. Thus, a systematic study of solar cell parameters is difficult at best and usually impossible due to the intrinsic

inability to isolate a single independent variable. Consequently, extensive research in this field is ongoing despite decades of prior dedicated efforts in the area.

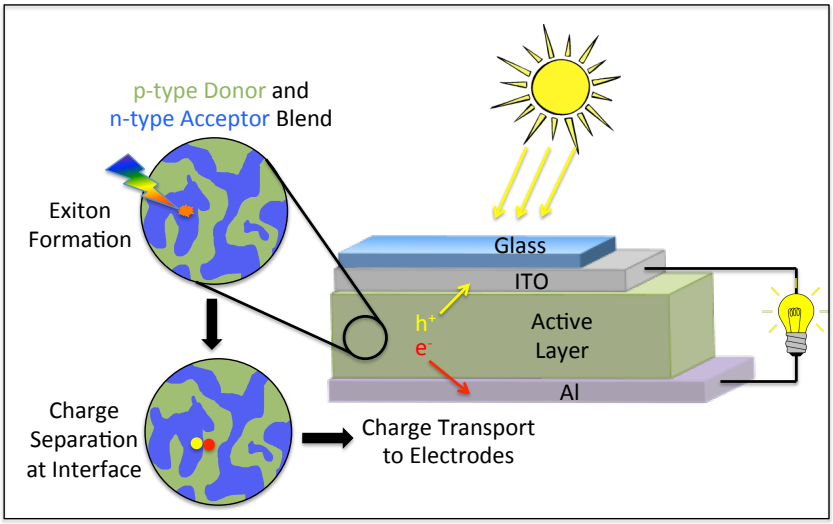

Figure 1.7. Schematic diagram of a bulk heterojunction (BHJ) solar cell.

Despite the fact that a truly viable system has yet to be reported, the potential benefits of highly efficient solar cells are innumerable. Accordingly, the search for active layers and dyes that improve on reported systems are of immense interest. Due to their long-lived CS state lifetimes, dyads **1.25-1.27** and dumbbell **1.28**, have been incorporated into (BHJ) devices. In addition to their promising photophysical properties, these compounds possess donors and acceptors that are covalently linked. This ensures that phase segregations, which are detrimental to device performance,[1.49] are minimized. Unfortunately, devices made from these materials initially have shown poor performances (<1% efficiency).[1.45, 1.50] The authors of the studies (Martín, Guldi, and Janssen et al.) attribute this failure to two factors. First, facile recombination is suspected, outpacing exiton formation and charge-separation within the thin films containing these substances. Although this contradicts what is seen in solution-state studies, interactions like those in BHJ cells

often vary drastically from those in homogeneous media. Second, weak light absorption by the exTTF-C_{60} conjugates limits the efficiency of such devices.[1.51] Currently, the use of these molecules as additives in polymer-fullerene BHJ solar cells is being investigated.

Dye sensitized solar cells (DSSCs) provide an alternative to BHJ cells. In DSSCs, also known as Grätzel cells, a monolayer of light absorbing dye is bonded to a semiconductor nanoparticle, such as TiO_2, which is sintered to an electrode (Figure 1.8). The monolayer ensures that, assuming appropriately matched energy levels, the dye is physically close enough to the semiconductor for electron transfer to be rapid, while simultaneously maximizing surface area and therefore light absorption. Completing the circuit to the counterelectrode is a redox electrolyte (usually I^-/I_3^-), which has to be chosen carefully so as to be effective in regenerating the ground state of the oxidized dye. A disadvantage of DSSCs is their reliance on liquids for diffusive charge transport. However, recent breakthroughs have addressed this problem *via* the creation of solid-state electrolytes.[1.52]

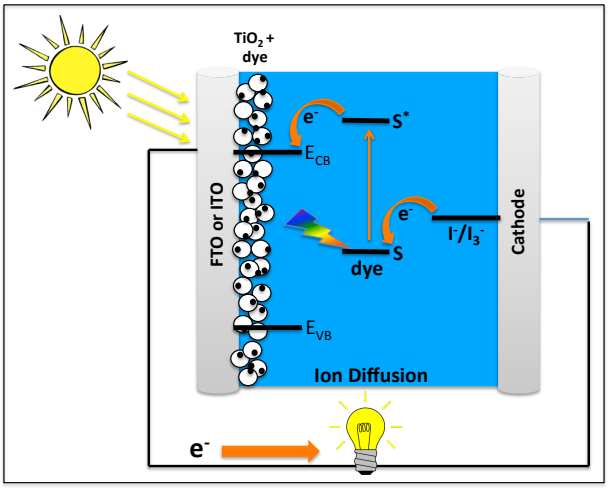

Figure 1.8. Schematic diagram of a dye-sensitized solar cell (DSSC).

ExTTF-based dyes have been synthesized and optimized for their incorporation in dye-sensitized solar cells (DSSCs). Among them are the donor-acceptor systems **1.30-1.32,** which were synthesized through Knoevenagel condensations to append the cyanoacrylic acid acceptors. Simple absorption studies showed an enhanced uptake of light compared to unfunctionalized exTTFs or those appended with carbon based nanoforms. Efficiencies from 2.9% for **1.30**, up to 3.8% for **1.32** were seen in DSSCs made from these molecules.[1.53] Aggregation of the dyes on the surface of the TiO_2 can be problematic to device performance. However, it is proposed that the saddle shape of neutral exTTF prevents aggregation.

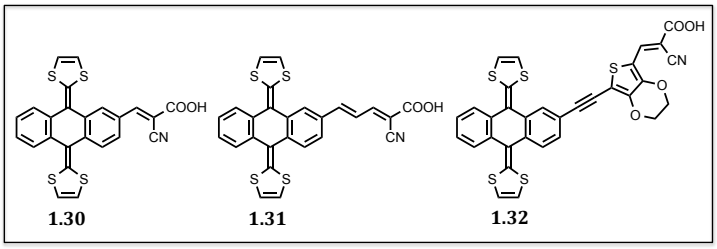

1.30 **1.31** **1.32**

Additionally, this study demonstrated the iodine-triiodide redox couple was able to efficiently regenerate the neutral state of the exTTF-based dyes. The regeneration of the ground state of the dyes was efficient despite merely 150 mV separating the redox potentials of the dyes from the redox potential of the iodine-triiodide couple. Typically a separation of 500 mv is required for efficient regeneration.[1.51] However, an increase in the driving force leads to a loss of photovolatage and cell efficiency. Therefore, this study provides a proof of concept that reduction in the driving force is feasible, possibly leading to more efficient cells. Additional improvements in the device efficiencies are expected as exTTF based materials that are better at absorbing light are discovered.[1.54]

ExTTF based systems have also found utility outside of the realm of organic electronics, particularly in supramolecular chemistry. Due to the concave/convex complementarity between exTTF and fulleres, as well as the well-known supramolecular interactions between electron donor and acceptors, exTTF was proposed to be a good host for C_{60}. In fact, theoretical calculations predicted binding energies of up to 7.00 kcal/mol for a single molecule of **1.20** with C_{60}.[1.55] However, experimental data providing evidence of a binding interaction is so far lacking.

Tweezer-like systems **1.33** and **1.34** on the other hand show significant UV/vis spectral changes upon addition of fullerene. Synthesized from the exTTF methyl alcohol and commercially available diacid chlorides, tweezer **1.33**, in aromatic solvents such as chlorobenzene, binds to C_{60} in a 1:1 manner.[1.56] Moderate association constants (log K_a = 3.5) were recorded in this solvent. Interestingly, alternative binding interactions were detailed in more polar solvents. In a mixture of chloroform and carbon disulfide, a sigmoidal curve was evident in the plot of ΔAbs vs. [C_{60}], a finding interpreted in terms of possible cooperativity. Indeed, this data fit nicely to the Hill equation, yielding a binding constant of K_a = 3.0 x 10^3 M^{-1} and a Hill coefficient of n_H = 2.7. Since the Hill coefficient is larger than 2.0 (predicting more than two binding sites), a pincher type complex can be ruled out in polar solvents. Nevertheless, a Job plot indicated a 1:1 stoichiometry. To account for both phenomenons, a supramolecular tetramer was proposed as the dominant species in polar solutions, although this was never confirmed in the solid state by crystallographic studies. Photophysical studies of the compounds bound to C_{60} in

aromatic solvents (pincher-like structure) show only very brief (<20 ps) CS lifetimes.[1.57]

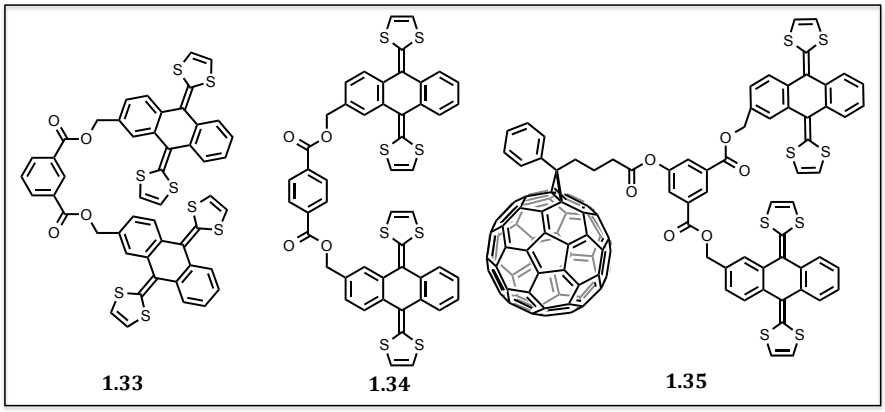

Covalent attachment of C_{60} to tweezer-like compound **1.33** gave compound **1.35**. At increasing concentrations, supramolecular polymers of **1.35** were observed by NMR spectroscopy. Variable temperature NMR spectroscopic studies, as well as MALDI-TOF-MS analyses, further provided support for the contention that supramolecular aggregates are formed. Additional evidence for the formation of oligiomers came from atomic force microscopy (AFM) analyses, whereby long necklace like strings of aggregates up to 300 nm in length (corresponding to > 100 mer) were observed. UV/vis and CV measurements confirmed the donor and acceptor fragments were in communication in the ground state. This research provides a novel approach to patterning donor-acceptor interfaces (of the utmost importance in device fabrication) through supramolecular interactions and warrants considerable further work.

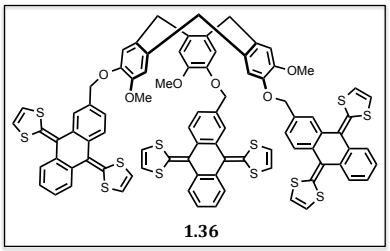

Including an additional exTTF moiety in the design of the host, affording tripodal structure **1.36**, results in a drastic increase in binding affinity from

pincher **1.33**.[1.58] A cyclotriveratrylene (CTV) core, which in itself forms "ball and socket" complexes with C60,[1.59] was appended to three exTTFs, resulting in a two order of magnitude enrichment of the binding strength of tripod **1.36** (log K_a = 5.3) over **1.33** with respect to C_{60} in chlorobenzene. Further, another order of magnitude increase was seen when C_{70} was employed as the guest (log K_a = 6.3). This was particularly noteworthy as no interaction was reported between C_{70} and compound **1.33**. The complexation of C_{70} by **1.36** provides a proof of concept to support the notion that receptors containing multiple exTTFs are beneficial in binding higher order fullerenes. Further, the CTV core is chiral, opening up the possibility that the D_2-isomers of higher fullerenes C_{76} and C_{84} could be recognized slectively.

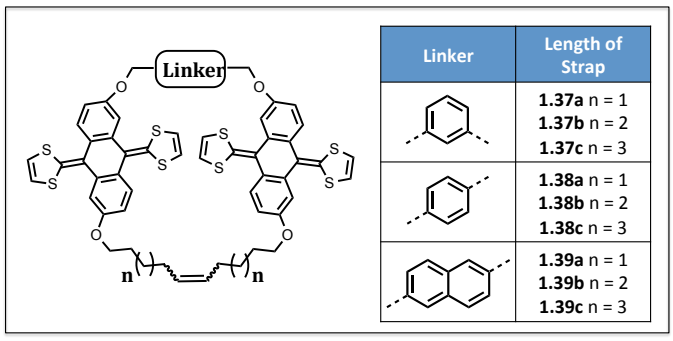

Linker	Length of Strap
	1.37a n = 1 **1.37b** n = 2 **1.37c** n = 3
	1.38a n = 1 **1.38b** n = 2 **1.38c** n = 3
	1.39a n = 1 **1.39b** n = 2 **1.39c** n = 3

A logical progression for the design of hosts with greater affinity for fullerenes than the flexible and therefore inherently disordered systems discussed above would include preorganization of the binding pocket. Reducing the flexibility of a host by physically locking it into a conformation of suitable size and shape to recognize the targeted guest is a well-established concept in supramolecular chemistry. It has been used frequently to increase the binding affinity and selectivity of hosts.[1.60] Thus, a reasonable evolution from **1.33** in the design of exTTF hosts for fullerenes would be toward a macrocyclic system, locked in the shape of a "binding pocket", so as to reduce unfavorable entropy loss upon binding. In this

vein, compounds **1.37-1.39** have been synthesized. In accord with design expectations, they displayed remarkable properties and tunability from small synthetic changes.[1.61]

Macrocycle **1.37b**, synthesized by a ring closing metathesis, displays markedly higher affinity for C_{60} than its open chain counterpart **1.33**. An increase in association constant of over three orders of magnitude was seen for **1.37b** (log K_a = 6.5), as inferred by UV/vis tirations in chlorobenzene. This provides an illustration of the effect of preorganization. The connectivity to the benzene ring (*meta* and *para*) as well as the length of the alkyl chains (from pentene to heptene) was varied. Simple synthetic changes led to vastly different properties. For instance, adding an additional carbon to **1.37b** on both sides of the alkyl strap, giving **1.37c** resulted in a three orders of magnitude reduction in the binding constant. Alternatively, removal of a carbon from the strap, affording **1.37a**, alters the binding stoichiometries. For **1.37a** and **1.38a** binding with C_{60} occurs in a 1:1 fashion. However with C_{70}, a 2:1 stoichiometry is observed. Increasing the size of the linker by replacing benzene with naphthalene (**1.39a**) results in a slight expansion of the binding pocket and in this case a 1:1 binding stoichiometry is seen for both C_{60} and C_{70}. These systems exhibit some of the strongest binding affinities for fullerenes recorded to date. These studies also serve to underscore how seemingly small structural changes can lead to large differences in binding affinity.

Although not spherical in shape like many of the fullerenes, SWNT also contain curved surfaces, and can be thought of as a sheet of graphene rolled up into a cylindrical shape. A single molecule of exTTF was not found to have a significant

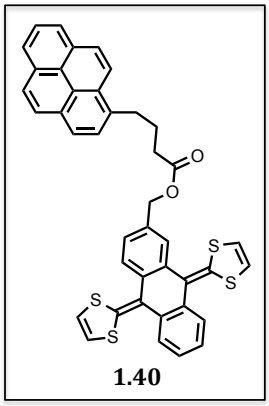

1.40

supramolecular interaction with SWNTs. However, a pyrene-functionalized exTTF, **1.40**, was found to anchor to the surface of SWNTs. This result was attributed to an enhancement in the π-π interactions permitted by the pyrene subunit.[1.62] The curved shape of the exTTF moiety, allowed for very close contacts based on computer modeling. Further, lack of change in the Raman intensities confirmed the interaction was supramolecular in nature. This was considered important since it allowed the unique electronic properties of the SWNTs to be preserved in the complex. CV analyses confirmed electronic coupling and π-π interactions as inferred from the significant shifts in redox potentials observed in the complex. Disappointingly, CS states were short lived (0.9 ps), resulting most likely from the intimate distance between the donor and acceptor. This finding has limited the use of complexes derived from **1.40** in organic electronics.

CNTs are poorly soluble in most common solvents (both aqueous and organic), which severely limits their processability and utility. Work to chemically modify (preferentially non-covalently) CNTs in order to exfoliate and disperse them in solution is an active area of research and has been met with some success in organic media.[1.63] Similar systems for aqueous media are still quite rare. To this end, pioneering work by the Martín group to modify synthetically tweezers like such as **1.33** so as to affix a second-generation dendrimer containing nine pendant carboxyl groups.[1.64] In basic aqueous

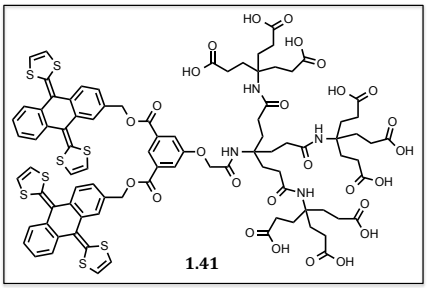

1.41

solutions, the resultant pincher **1.41** was fully soluble. Moreover, its exposure to SWNT or multi-wall carbon nanotubes (MWNT) resulted in stable CNT-**1.41** complexes. AFM and transmission electron microscopy (TEM) images gave clear evidence for the dispersal of SWNTs (complexes to **1.41**) in films made from aqueous solutions (Figure 1.9). Electronic coupling of **1.41** with SWNTs was confirmed by comparison of the UV/vis absorption peaks and Raman intensities of SWNT-**1.41** versus SWNT-SDBS (sodium dodecyl benzene sulfonate) solutions. In both cases, a bathochromic shift was observed for the CNTs solubilized by **1.41**, this was taken as an indicator of an electronic interaction between the donor **1.41** and receptor SWNTs. Transient absorption (TA) studies displayed CS lifetimes of 160 ps for **1.41**-SWNT and 380 ps for **1.41**-MWNT. This work thus provides support for the notion that exTTFs could emerge as useful tools for the processing and fabrication of organic electronics devices containing CNTs.

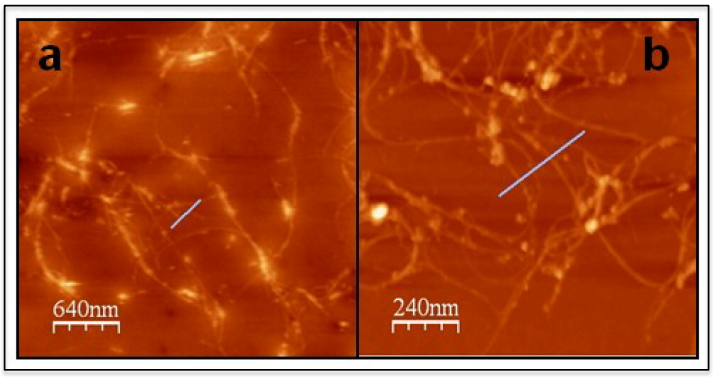

Figures 1.9. AFM images of (a) HiPco SWNT/**1.41** and (b) CoMoCAT SWNT/**1.41**. Reproduced with permission from *J. Am. Chem. Soc.* **2012**, 134, 9183-9192. Copyright 2008 American Chemical Society.

Supramolecular systems of exTTFs forming a wide variety of intricate nano-scale patterns and possessing unique properties have recently been reported (*vide infra*). Driven by a need to control the morphology of the active layer in solar cells, in

which the nano-orientation of the material dictates the optoelectronic properties and behavior of the semiconductors, intense interest has been given to the nano-patterning of donors and acceptors.[1.65] Supramolecular self-assembly is an ideal way to create these intricate patterns without relying on complicated synthetic and systematic processes. Well-organized materials with defined sizes should increase both exiton transport properties, as well as CS transport to the electrodes.

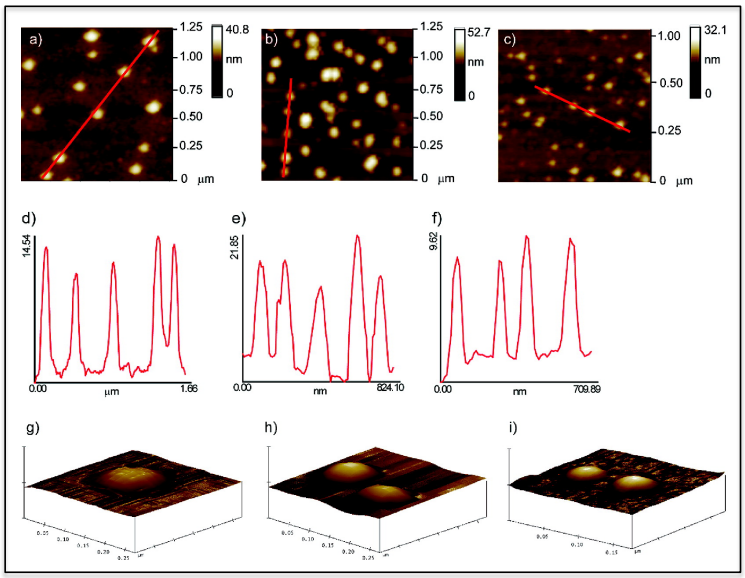

Figure 1.10. AFM images of (a) G2, (b) G3, and (c) G4 on mica. Height Profiles (d-f) along the red lines of the above corresponding AFM images. 3-D images illustrating the disk-like geometry of (g) G2, (h) G3, and (i) G4. Reproduced with permission from *J. Am. Chem. Soc.* **2008**, 130, 10674-10683. Copyright 2008 American Chemical Society.

Second (G2), third (G3) and fourth (G4) generation dendrimers made form 1,3,5-ester-substituted benzenes, containing 6, 12, and 24 capping exTTF capping groups, respectively, have been synthesized displaying marked aggregation effects.[1.66] In these systems, self-aggregation of the exTTF units was seen in both the gas and solution states. In the gas phase, MALDI-TOF MS analysis revealed a *m/z* corresponding to the dendritic "monomer" as well as higher ordered aggregates or

clusters. In solution, variable temperature NMR spectal studies revealed shifts in the peaks of the anthracene core and dithiolidene rings were indicative of aggregation. The aggregates were further studied with dynamic light scattering. These studies revealed a narrow distribution of hydrodynamic radii (30 nm for G2, 60 nm for G3, and 120 nm for G4). However, the UV/vis spectra of the dendrimers was found to be unchanged, leading the authors to conclude no well-defined electronic states were formed as a result of randomization of the orientation of exTTFs in the dendrimers. Solid-state studies by AFM and SEM showed disc-like pseudoglobular structures (Figure 1.10). The addition of C_{60} to these aggregates resulted in poorly defined complexes with a high degree of coopertivity, most likely resulting from the debundling of aggregates prior to binding. More work is needed to make these dendrimers suitable for incorporation in OPV devices.

Arguably one of the most unique applications of exTTFs is their propensity to form self-assembled superlattices on gold surfaces. Reconstructed Au (111) surfaces were exposed to sub monolayer coverage of exTTF **1.20** resulting in the formation of stripe islands of exTTFs at room temperature.[1.67] The intention of this work was to impose the $22 \times \sqrt{3}$ "herringbone" pattern of Au (111) surfaces onto films of exTTFs. In contrast to what was predicted, the stripe islands were found to modify the reconstruction instead of mimicking it, an effect ascribed to strong adsorbate-substrate interactions (Figure 1.11). Increasing the amount of exTTF to one monolayer resulted in the coalescence of the stripe islands into alternating stripes with different domain orientations. Further, up to three patterned monolayers can be grown. The second and third layers stripe islands align with the

first layers but lack the long-range order of the first monolayer. Energy minimization calculations led to the suggestion that the exTTFs align to the gold surface with only one of the dithiolidene rings interacting with the surface. In constrast, TTF interacts with both rings. This difference was attributed to the butterfly shape of the exTTF prohibiting favorable interactions between both rings with the gold surface and allowing intermolecular stacking to take place.[1.68]

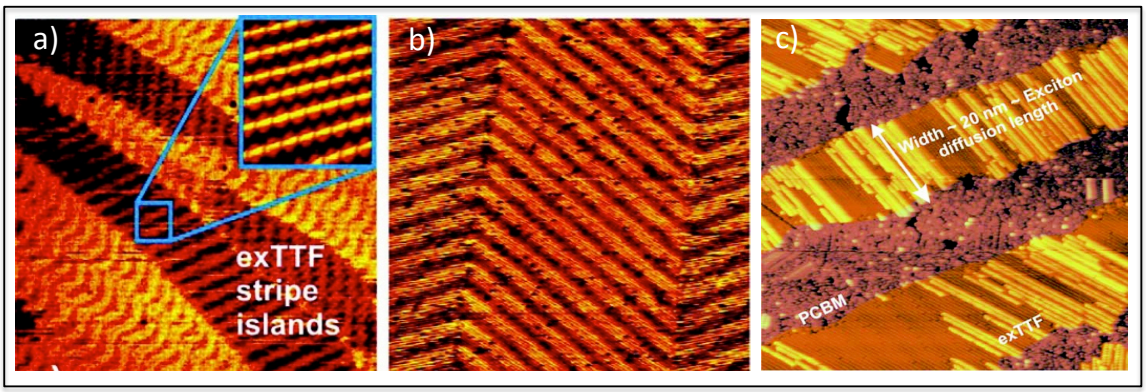

Figure 1.11. (a) STM image of a sub monolayer (0.3 ML) coverage of **1.20** on a reconstructed Au (111) surface at 300 K and (b) after completion of the first monlayer. (c) Organic donor/acceptor superlattice of **1.20**/PCBM grown on an Au(111) surface. The widths of the **1.20** stripes are about 20 nm, a value that is comparable to exiton diffusion lengths. Reproduced with permission from *Nano Lett.*, **2007**, 7, 2602-2607. Copyright 2007 American Chemical Society.

The width of the exTTF stripe islands was found to be between 10 – 20 nm. This is on the order of exiton diffusion lengths. The stripe islands are of an optimal width for the creation of a highly ordered active layer for OPVs. Absorption studies of the commonly used electron acceptor phenyl-C_{61}-butyric acid methyl ester (PCBM) on Au (111) surfaces were thus undertaken. At room temperature, PCBM was found to behave as a two-dimensional gas at sub monolayer concentrations. This was attributed to evidence of low affinity between PCBM and the gold surface, as well as minimal intermolecular attractions of PCBM.

ExTTF and PCBM were also combined on a single Au (111) surface resulting in a intricately patterned arrangement. To do this, a sub-monolayer coverage of PCBM was first applied to the gold (111) surface at room temperature. As mentioned previously (*vide supra*) PCBM behaves as a 2D gas under these conditions, and covers the gold (111) surface in a random manner. PCBM and exTTF have a low affinity for one another. Therefore, addition of exTTF to the fractionally PCBM-covered gold surface led to the formation of exTTF stripe islands in a manner analogous to those formed on substrate-less Au (111) surfaces. As the stripe islands are formed, the gas-like PCBM fills in the areas not covered by the exTTF. Upon addition of enough exTTF such that the combined quantities of the exTTF and PCBM serve to complete a monolayer, the PCBM becomes "locked" into place. As such it serves to fill the exTTF stripeless voids, resulting in alternating stripes of PCBM acceptor molecules and exTTF donor molecules (Figure 1.11). The 10 – 20 nm widths of the islands (corresponding nicely to the exiton diffusion lengths) are retained under these conditions.

Hydrogen bonding motifs attached to exTTF allow for supramolecular fiber formation. ExTTF was appended with a damino-triazine group (**1.42**), a subunit known to form strong hydrogen bonds with cyanuric acid derivatives, such as **1.43**.[1.69] A mixture of these two compounds in nonpolar methylcyclohexane (MCH) resulted in spectral features with peaks that were shifted relative to those seen in $CHCl_3$. This was true for both absorption and NMR spectra. This was taken as evidence of hydrogen bonding in MCH. Further, a new broad and weak absorption peak in MCH extending out to 700 nm was seen. It was attributed to aggregation. In

contrast, an analogous study in $CHCl_3$ displayed no such peak. Aging of the MCH solution for one week resulted in the disappearance of the characteristic exTTF peaks and the growth of the red-shifted peak ascribed to aggregation. Addition of $CHCl_3$ to the MCH solution led to regeneration of the original exTTF spectrum.

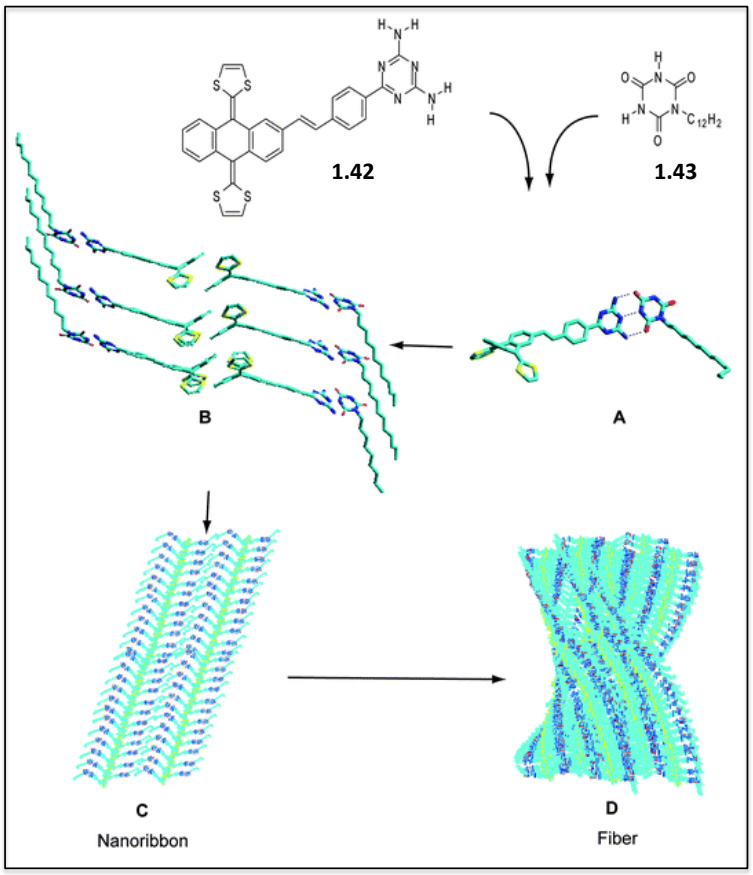

Figure 1.12. Models of the primary (A), secondary (B), tertiary (C), and quaternary (D) structures of the mixture of **1.42** and **1.43** in MCH. Reproduced with permission from *Angew. Chem. Int. Ed.,* 2010, **49**, 9876-9880. Copyright 2010, Wiley-VCH Verlag GmbH & Co. KGaA.

Microscopy of MCH solutions containing a mixture of **1.42** and **1.43** provided additional insight into the structures formed upon aging. At early stages "barrel-shaped" structures were observed by AFM imaging. These structures were of uniform height (20-35 nm) and planar in shape. Upon further aging, an orange precipitate was obtained. It was collected and subject to SEM analysis. The

resulting images demonstrated the presence of homogenous fibers twisted in a clockwise or counterclockwise direction. Closer examination revealed that these fibers were comprised of nano-ribbons, which themselves were composed of stripes of material separated by 3.2 nm. Fibers containing quaternary structuring were thus created as the result of hydrogen bonding-mediated self-assembly of the exTTFs. The primary structure in these ensembles is defined by the complementary hydrogen bonding pairs. The secondary structure results from π-π donor-acceptor interactions between the exTTFs; this results in linear columns. The tertiary structure is formed when the columns interdigitate, forming nano-ribbons which are unstable and thus intertwine by twisting, creating the quaternary fiber structure. This methodology once again provides a unique way to self-assemble electroactive molecules on a nanomolecular scale. This assembly, like others, could prove useful in the composition of organic electronics.

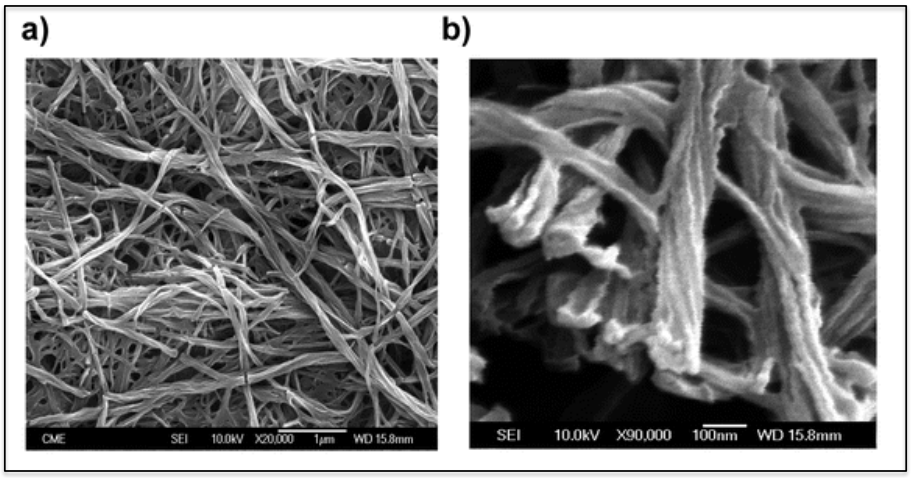

Figure 1.13. (a) SEM images of supramolecular fibers precipitated from a solution of **1.42** and **1.43**. (b) SEM image with 10x the magnification (from image a) where the twisted nanoribbons are discernable. Figure reproduced with permission from *Angew. Chem. Int. Ed.,* 2010, **49**, 9876-9880. Copyright 2010. Wiley-VCH Verlag GmbH & Co. KGaA.

Finally, a report detailing the use of exTTF as a chemosensor has been published by the Hudhomme group.[1.70] A dipyridoquinoxaline (dpq) moiety was appended to napthoquinone and subjected to Horner-Wadsworth-Emmons coupling conditions. This yielded **1.44**. Binding and recognition studies were carried out with a variety of metal cations (as perchlorate salts) including Fe^{2+}, Ni^{2+}, Ca^{2+}, Pb^{2+}, and Zn^{2+}. An obvious color shift from orange to dark red was noted upon addition of cations, regardless of the identity of the metal species. The titrations reached equilibrium at around 0.3 equivalents. Moreover, Job plot analysis provided support for the conclusion that the complexes were formed in a 3:1, **1.44** to metal ion stoichiometry for all metals studied. Further, as previously demonstrated with crown ether derivatives of exTTF,[1.71] anodic shifts in the oxidation potentials were observed in the CVs of metal complexes of **1.44**. Thus, a dual-mode signaling system (optical and electrochemical) was demonstrated. Unfortunately, the system lacked selectivity.

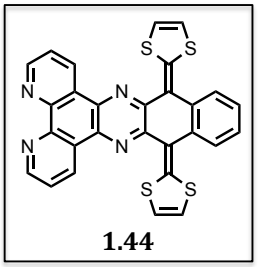

1.44

1.4 Summary and Outline

As detailed in this introductory chapter, exTTFs have been extensively studied. They are attractive for use in wide variety of intriguing applications. Most notably, their demonstrated properties may allow them to address several current challenges within the field of solar cell fabrication and optimization. Specifically, exTTFs are (1) excellent electron donors that are simple and cheap to make and can be tuned by straightforward techniques; (2) exTTFs form tightly bound complexes with carbon nanoforms which are suitable electron acceptors; (3) covalent and

supramolecular attachment to fullerenes and CNTs is facile. The resulting constructs display long lived CS states upon photoirridiation; and (4) well-defined nano-scale structures produced from exTTFs have been published of similar size to exiton diffusion lengths.

Based on their properties, exTTFs and their constructs seem poised to become excellent candidates for incorporation into commercially viable solar cell devices. In fact, initial studies demonstrate efficiencies in DSSCs of up to 3.8% for exTTF-based dyes. In contrast, more work is needed to improve the efficiencies in exTTF BHJ cells, where despite astounding properties, to date, few notable results have been reported.

One of the most apparent attributes limiting the capabilities of exTTF based OPVs are their inability to efficiently absorb light. The majority of pro-anthracene based exTTFs (e.g. **1.20**) absorb light below 500 nm. As a result, they are unable to take advantage of a large swath of the solar spectrum. Further, the absorption coefficients of exTTFs are low compared to other common dyes (e.g., porphyrins, phthalacyanines). Recent attempts to address this issue by synthesizing covalently attached electron donor/acceptor chimeras, envisaged to lower optical band gaps, have been met with only mild success. Thus, we realized there was an opportunity to contribute to this field by creating exTTF-based systems characterized by broad wavelength absorption and large molar absorptivity features. The pursuit of such systems was the original inspiration for our work in the area and is the subject of this dissertation:

Chapter 2 details the synthesis and metalation of a quinoidal exTTF porphyrin. Basic redox and photophysical properties are probed demonstrating the unique properties of this system. Of particular interest is the ability to tune the redox nature of this system through anion-metal coordination. The majority of this work was published as an article in the *Journal of the American Chemical Society* in a collaborative effort involving the groups of Profs. Dongho Kim and Shunichi Fukuzumi groups. The candidate is first author of this publication and was responsible for the synthetics, electrochemical, and supramolecular aspects of the work.

Chapter 3 describes the supramolecular interaction of two-electron oxidized exTTF porphyrins with tetrasulfonyltetraphenyl porphyrins. Excited state lifetimes of the supramolecular complexes are lengthened compared to what is seen for the monomers. This work was performed in collaboration with Profs. Shunichi Fukuzumi and Dongho Kim and their respective groups, including Drs. Masatoshi Ishida and Kei Ohkubo. The photophysical analyses of this system, which are outside the scope of this dissertation, have yet to be completed. Therefore, as yet, this work has not been submitted for publication.

Chapter 4 features our work with dithiolidine rings bridged by highly fluorescent BODIPY linkers. Basic properties and potential applications are discussed. A manuscript detailing this synthesis of BODIPY-based exTTFs is currently in preparation.

In Chapter 5, experimental procedures and characterization data all compounds are given. Additionally, data tables for the refinement of obtained crystal structures

are included. All structural refinements were performed by Dr. Vincent Lynch of the X-ray Diffraction Laboratory of the University of Texas Chemistry and Biochemistry.

1.5 Chapter 1 References

1. Wudl, F.; Smith, G.M.; Hufnagel, E.J.; *Chem. Commun.* **1970**, 1453.
2. (a) Coffen, D.L.; Chamber, J.Q.; Williams, D.R.; Garret, P.E.; Canfield, N.D. *J. Am. Chem. Soc.* **1971**, 109. (b) Hünig, S.; Kiesslich, G.; Scheutzow, D.; Zahradnik, R.; Carsky, P. *Int. J. Sulfur. Chem. Part C.* **1971**, 6, 109.
3. The first synthesis of TTF was reported in 1965 under the name bis-1,3-dithiolium. However, the electron donating ability of this molecule was not discovered until several years later. Prinzback, H,; Berger, H,; Luttringhaus, A. *Angew, Chem. Int. Ed. Engl.* **1965**, 4, 435.
4. Ashton, P.R.; Balzani, V.; Becher, J.; Credi, A.; Fyfe, M.C.T.; Mattersteig, G.; Menzer, S.; Venturi, M.; Williams, D.J. *J. Am. Chem. Soc.* **1999**, 121, 3951.
5. Ferraris, J.; Cowan, D. O.; Walatka, V. V.; Perlstein, J. H. *J. Am Chem. Soc.,* **1973**, 93, 948.
6. (a) Williams, J.M.; Schultz, A.J.; Geiser, U.; Carlson, K.D.; Kini, A.M.; Wang, H.H.; Kowk, W.K.; Whangbo, M.H. Schirber, J.E. *Science*, **1991**, 252, 1501. (b) Williams, J.M.; Ferraro, J.R.; Thorn, R.J.; Carlson, K.D.; Geiser, U.; Wang, H.H.; Kini, A.M.; Whangbo, M.H. *Organic Superconductors (Including Fullerenes) Synthesis, Structure, Properties, and Theory*, Prentice-Hall Inc., New Jersey, 1992.
7. Saito, G.; Yoshida, Y. *The Chemical Record*. **2011**, 11, 124.
8. Becher, J.; Li, Z.-T.; Blanchard, P.; Svenstrup, N.; Lau, J.; Nielsen, M. B.; Leriche, P. *Pure Appl. Chem.,* **1997**, 69,465.
9. *TTF Chemistry: Fundamentals and Applications of Tetrathiafulvalene.* Yamada, J.; Sugimoto, T. eds.; Springer, Berlin, 2004.
10. (a) Salle, M.; Canevet, D.; Balandier, J.-Y.; Lyskawa, J.; Trippe, G.; Goeb, S.; Le Derf, F. Phosphorous, Sulfur Silicon Relat. Elem. 2011, 186, 1153. (b) Canevet, D.; Salle, M.; Zhang, G.; Zhang, D.; Zhu, D. Chem Commun. 2009, 2245. (c) Lorcy, D.; Bellec, N.; Fourmigue, M.; Avarvari, N. Coord. Chem. Rev. 2009, 253, 1398. (d) Li, H.-Q.; Song, Y.-X.; Peng, X.-F. Huaxue Shijie, 2008, 49, 306. (e) Pauliukaite, R.; Malinauskas, A.; Zhylyak, G.; Spichiger-Keller, U.E. Electroanalysis, 2007, 19, 2491. (f) Li, H.-Q.; Song, Y.-K.; Yin, Q.-F.; Zhu, D.-B. Youiji Huaxue, 2007, 27, 1220. (g) Zhu, Y.-L.; Yang, Y.-J.; Yin, Q.-F.; Zhu, D.-B. Youiji Huaxue, 2005, 25, 1167. (h) Abd El-Wareth, A.O.S. Tetrahedron, 2005, 61, 3889. (i) Jeppesen, J.O.; Becher, J. Eur. J. Org. Chem. 2003, 3245. (j)Segura, J.L.; Martín, N. Angew. Chem. Int. Ed. 2001, 40, 1372. (k) Bryce, M.R.; J. Mater. Chem. 2000, 10, 589.
11. Yoshida, Z.; Kawase, T.; Awaji, H.; Sugimoto, I.; Sugimoto, T.; Yoneda, S. *Tetrahedron Lett.*, **1983**, 24, 3469.
12. Lorcy, D.; Carlier, R.; Robert, A.; Tallec, A.; Le Marguerés, P.; Quahab, L. *J. Org. Chem.*, **1995**, 60, 2443.
13. Yamashita, Y.; Tomura, M.; Zaman, M. B.; Imaeda, K.; *Chem. Commun.* **1998**, 1657.
14. (a) Bellec, N.; Boubekeur, K.; Carlier, R.; Hapiot, P.; Lorcy, D.; Tallec, A.; *J. Phys. Chem. A*, **2000**, 104, 9750. (b) Yamashita, Y.; Tomura, M.; Badruz Zaman, M.,

Chem. Commun. **1998**, 1657. (c) Lorcy, D. ; Carlier, R.; Robert, A.; Tallec, A.; Le Magueres, P.; Ouahab, L. *J. Org. Chem.* **1995,** *60*, 2443-2447
15. Yoshida, Z.; Kawase, T.; Awaji, H.; Yoneda, S. *Tetrahedron Lett.*, **1983**, 24, 3473
16. Märkl, G.; Pöll, A.; Aschenbrenner, N. G.; Schmaus, C.; Troll, T.; Kreitmeier, P.; Nöth, H.; Schmidt, M. *Helv. Chim. Acta*, **1996**, 79, 1497
17. Sugimoto, T.; Awaji, H.; Sugimoto, I.; Misaki, Y.; Kawase, T.; Yoneda, S.; Yoshida, Z. *Chem. Mater.*, **1989**, 1, 535
18. Yamashita, Y.; Tomura, M.; Uruichi, M.; Yakushi, K. *Mol. Cryst. Liq. Cryst.,* **2002**, 376, 19
19. Yamashita, Y.; Tanaka, S.; Tomura, M. *J. Chem. Soc. Chem. Commun.*, **1993**, 652
20. (a) Khanous, A.; Gorgues, A.; Texier, F. *Tetrahedron Lett.*, **1990**, 31. 7307. (b) Khanous, A.; Gorgues, A.; Jubault, M.; *Tetrahedron Lett.*, **1990**, 31, 7311. (c) Nielsen, M. B.; Moonen, N. N. P.; Boudon, C.; Giesselbrecht, J.-P.; Seiler, P.; Gross, M.; Diederich, F. *Chem Commun.* **2001**, 1848.
21. Salle, M.; Belyasmine, A.; Gorgues, A.; Jubault, M.; Soyer, N. *Tetrahedron Lett.*, **1991**, 32, 2897.
22. (a) Frére, P.; Gorgues, A.; Jubault, M.; Riou, A.; Gouriou, Y.; Roncali, J. *Tetrahedron Lett.*, **1994**, 35, 1991. (b) Lakshmikantham, M.V.; Cava, M.P.; Caroll, P.J. *J. Org. Chem.* **1984**, 49, 726.
23. Frére, P.; Benahamed-Gasumi, A.; Roncali, J.; Jubault, M.; Gorgues, A.; *J. Chim. Phys.*, **1995**, 92, 863.
24. (a) Hansen, T.K.; Lakshmikantham, M.V.; Cava, M.P.; Niziurski-Mann, R.E.; Jensen, F.; Becher, J. *J. Am. Chem. Soc.* **1992**, 114, 5035. (b) Takahashi, K.; Nihira, T.; Yoshifuji, M.; Tomitani, K. *Bull. Chem. Soc. Jpn.*, **1993**, 66, 2330.
25. (a) Roncali, J.; Rasumussen, L.; Thobie-Gautier, C.; Frére, P.; Brisset, H.; Sallé, M.; Becher, J.; Simonsen, O.; Hansen, T.K.; Benahmed-Gasumi, A.; Orduna, J.; Carin, J.; Jubault, J.; Gorgues, A. *Adv. Mater.*, **1994**, 6, 841. (b) Roncali, J.; M. Giffard, M.; Frére, P.; Jubault, M.; Gorgues, A.; *J. Chem. Soc. Chem. Commun.*, **1993**, 689.
26. Brisset, H.; Thobie-Gautier, C.; Jubault, M.; Gorgues, A.; Roncali, J. *J. Chem. Soc. Chem. Commun.* B1994B, 1765.
27. Elandaloussi, E.; Frére, P.; Roncali, J.; Richomme, P. Jubault, M. Gorgues, A. *Adv. Mater.* **1995**, 7. 390
28. Elandaloussi, E.; Frére, P.; Benahmed-Gasumi, A.; Riou, A.; Gorgues, A.; Roncali, J. *J. Mater. Chem.*, **1996**, 6, 1859.
29. (a) Ohta, A.; Yamashita, Y. *J. Chem. Soc. Chem. Commun.* **1995**, 557. (b) Ohta, A.; Yamashita, A. *Heterocycles*, **1997**, 44, 263.
30. Akiba, K.; Ishikawa, K.; Inamoto, N. *Bull. Chem. Soc. Jpn.*, **1978**, 51, 2674.
31. Yamashita, Y.; Kobayashi, Y.; Miyashi, T.; *Angew. Chem. Int. Ed. Engl.*, **1989**, 28, 1052.
32. Evans, D.H.; Hu, K. *J. Chem. Soc. Faraday Trans.* **1996**, 92, 3983.
33. Bryce, M.; Moore, A.; Hasan, M.; Ashwell, G.; Fraser, A.; Clegg, W.; Hursthouse, M.; Karaulov, A. *Angew. Chem. Int. Ed.,* **1990**, 29, 1450
34. Yamashita, Y.; Tanaka, S.; Imaeda, K.; Inokuchi, H.; Sano, M. *Chem. Lett.,* **1992**, 419

35. Yamashita, Y.; Ono, K.; Tanaka, S.; Imaeda, K.; Inokuchi, H. *Adv. Mater.*, **1994**, 6, 295.
36. (a) Yamashita, Y.; Tanaka, S.; Imaeda, K.; Inokuchi, H. *Chem. Lett.*, **1991**, 1213. (b) Yamashita, Y.; Tanaka, S.; Imaeda, K.; Inokuchi, H.; Sano, M. *J. Org. Chem.*, **1992**, 57, 5517.
37. (a) Takeda, M.; Graaf, H.; Yamashita, Y.; Tada, H.; *Jp. J. Appl. Phys.* 2002, 41, L4 (b) Forrest, S. Organic Heterojunction Bipolar Transistor. US Patent 2005275056, December 15th, 2005. (c) Forrest, S. Xue, J. Biopolar Organic Devices. US Patent 20050110005, May 26th, 2005. (d) Japan Broadcasting Corp. Organic Photoelectric Conversion Material, and Organic Photoelectric Conversion Element and Organic Thin-Film Solar Cell each Employing the Same. Japan Patent 2012064650, March 29th, 2012.
38. (a) Martín, N.; Sánchez, L.; Guldi, D.M. *Chem Commun.* **2000**, 113. (b) Diaz, M.C.; Herranz, M.A.; Illescas, B.M.; Martín, N; Godbert, N.; Bryce, M.R.; Luo, C.; Swartz, A.; Anderson, G.; Guldi, D.M. *J. Org. Chem.* **2003**, 68, 7711
39. (a) Prato, M.; Maggini, M.; Giacometti, C.; Scorrano, G.; Sandoni, G.; Farnia, G. *Tetrahedron*, **1996**, 52, 5221 (b) Martín, N.; Sánchez, L.; Seoane, C.; Andreu, R.; Garín, J.; Orduna, J. *Tetrahedron Lett.* **1996**, 37, 5979. (c) Martín, N.; Sánchez, L.; Herranz, M.A.; Guldi, D. M. *J. Phys. Chem. A* **2000**, 104, 4648
40. (a) Jiwan, J.L.H.; Soumillion, J.P. *J. Phys. Chem.* **1995**, 99, 14223. (b) Joliffe, K.A.; Langford, S.J.; Ranasinghe, M.G.; Shephard, M.J.; Paddon-Row, M.N. *J. Org. Chem.* **1999**, 64, 1238
41. Giacalone, F.; Segura, J.L.; Guldi, G.M.; Martín, N. *J. Am. Chem. Soc.* **2004**, 126, 5340.
42. Atienza, C.; Martín, N.; Wielopolski, M.; Hawarth, N.; Clark, T.; Guldi, D.M. *Chem. Commun.* **2006**, 3202
43. (a) Wielopolski, M.; Atienza, C.; Clark, T.; Guldi, D.M.; Martín, N. *Chem.-Eur. J.*, **2008**, 14, 6379. (b) Molina-Ontoria, A.; Fernandez, G.; Wielopolski, M.; Atienza, C.; Sanchez, L,; Gouloumis, A.; Clark, T.; Martín, N.; Guldi, D.M. *J. Am. Chem. Soc.* **2009**, 131, 12218.
44. Atienza-Castellanos, C.; Wielopolski, M.; Guldi, D.M.; van der Pol, C.; Bryce, M.R.; Filippone, S.; Martín, N. *Chem. Commun.* **2007**, 5164.
45. Sánchez, L.; Herranz, M.A.; Martín, N. *J. Mater. Chem.* **2005**, 15, 1409.
46. (a) Sánchez, L.; Pérez, I.; Martín, N.; Guldi, D.M. *Chem.-Eur. J.* **2003**, 9, 2457. (b) Illescas, B.M.; Santos, J.; Wielopolski, M.; Atienza, C.M.; Martín, N.; Guldi, D.M. *Chem. Commun.* **2009**, 5374.
47. Herranz, M.A.; Martín, N.; Campidelli, S.P.; Prato, M.; Brehm. G.; Guldi, G.M. *Angew. Chem. Int. Ed.*, **2006**, 45, 4478.
48. Economopoulos, S.P.; Rotas, G.; Miyata, Y.; Shinohara, H.; Tagmatarchis, N. *ACS Nano*, **2010**, 4, 7499.
49. Klok, H.A.; Lecommandoux, S.; *Adv. Mater.* **2001**, 13, 1217.
50. Sánchez, L.; Sierra, M.; Martín, N.; Guldi, D.M.; Wienk, M.W.; Janssen, R.A.J. *Org. Lett.* **2005**, 1691
51. Brunetti, F.G.; López, J.L.; Atienza, C.; Martín, N. *J. Mater. Chem.* **2012**, 4188.
52. Chung, I.; Lee, B.; He, J.; Chang, R.P.H. Kanatzidis, M.G. *Nature* **2012,** 485, 486.
53. Wenger, S.; Bouit, P-A.; Chen, Q.; Teuscher, J.; Censo, D.D.; Humphry-Baker, R.;

Moser, J.E.; Delgado, J.L.; Mártin, N.; Zakeeruddin, S.M.; Grätzel, M. *J. Am. Chem. Soc.* **2010**, 132, 5164.
54. Bouit, P-A.; Villegas, C.; Delgado, J.L.; Viruela, P.M.; Pou-Amérigo, R.; Orti, E.; Mártin, N. *Org. Lett.* **2011**, 13, 605.
55. Pérez, E.M.; Mártin, N. *Chem. Soc. Rev.* **2008**, 37, 1512.
56. Pérez, E.M.; Sänchez, L.; Fernandez, G.; Mártin, N. *J. Am. Chem. Soc.* **2006**, 128, 7172.
57. Gayathri, S.S.; Wielopolski, M.; Pérez, E.M.; Fernandez, G.; Sánchez, L.; Viruela, R.; Orti, E.; Guldi, D.M.; Mártin, N. *Angew. Chem., Int. Ed.* **2009**, 48, 815.
58. Huerta, E.; Isla, H.; Pérez, E.M.; Bo, C.; Mártin, N.; de Mendoza, J. *J. Am. Chem. Soc.* **2010,** 132, 5351.
59. Steed, J.W.; Junk, P.C.; Atwood, J.L.; Barnes, M.J.; Raston, C.L.; Burkhalter, R.S. *J. Am. Chem. Soc.* **1994**, 116, 10346.
60. Steed, J.W., Atwood, J.L., *Supramolecular Chemistry*, 2nd ed.; Jon Wiley & Sons, Ltd.: 2009.
61. (a) Isla, H.; Gallego, M; Pérez, E.M.; Viruela, R.; Ortí, E.; Martín, N.; *J. Am. Chem. Soc.* **2010**, 132, 1772. (b) Canevet, D.; Gallego, M.; Isla, H.; de Juan, A.; Pérez, E.M.; Martín, N. *J. Am. Chem. Soc.* **2011**, 133, 3184.
62. Herranz, M.A.; Ehli, C.; Campidelli, S.; Gutierez, M.; Hug, G.L.; Ohkubo, K.; Fukuzumi, S.; Prato, M.; Martín, N.; Guldi, D.M. *J. Am. Chem. Soc.* **2008**, 130, 66.
63. Bergin, S. D.; Nicolosi, V.; Streich, P. V.; Giordani, S.; Sun, Z.; Windle, A. H.; Ryan, P.; Niraj, N. P. P.; Wang, Z.-T. T.; Carpenter, L.; Blau, W. J.; Boland, J. J.; Hamilton, J. P.; Coleman, J. N. *Adv. Mater*. **2008**, 20, 1876.
64. Romero-Nieto, C.; García, R,; Herranz, M.A.; Ehli, C.; Ruppert, M.; Hirsch, A.; Guldi, D.M.; Martín, N. *J. Am. Chem. Soc.* **2012**, 134, 9183.
65. (a) De Luca, G.; Pisula, W.; Credgington, D.; Treossi, E.; Fenwick, O.; Lazzerini, G.M.; Dabirian. R.; Orgiu, E.; Liscio. A; Palermo, V.; Müllen, K.; Cacialli, F.; Samori. P. *Adv. Funct. Mater.* **2011**, 21, 1279. (b) Kim, F.S.; Ren, G.Q.; Jenekhe, S.A. *Chem. Mater.* **2011**, 23, 682. (c) Ozin, G.A.; Cademartiri, L. *Small*, **2009**, 5, 1240. (d) Whitesides, G.M. *Small*, **2005**, 1, 172. (e) Law, M.; Goldberger, J.; Yang, P.D. *Annu. Rev. Mater. Res.*, **2004**, 34, 83. (f) Yin, Y.; Alivisatos, A.P. *Nature,* **2005**, 437, 664.
66. Fernandez, S.; Sánchez, L.; Pérez, E.M.; Martín, N. *J. Am. Chem. Soc.* **2008**, 130, 10674.
67. Otero, R.; Ecija, D.; Fernandez, G.; Gallego, J.M.; Sánchez, L.; Martín, N.; Miranda, R. *Nano Lett.* **2007**, 7, 2602.
68. Urban, C.; Ecija, D.; Wang, Y.; Trelka, M.; Preda, I.; Vollmer, A.; Lorente, N.; Arnau, A.; Alcami, M.; Soriano, L.; Martín, N.; Martin, F.; Otero, R.; Gallego, J.M., Miranda, R. *J. Phys. Chem. C,* **2010**, 114, 6503.
69. López, J. L.; Atienza, C.; Seitz, W.; Guldi, D. M.; Martín, N. *Angew. Chem. Int. Ed.* **2010**, 49, 9876.
70. Hardouin-Lerouge, M.; Chesneau, B.; Allain, M.; Hudhomme, P. *J. Org. Chem.* **2012**, 2441.
71. Bryce, M. R.; Batsanov, A. S.; Finn, T.; Hansen, T. K.; Moore, A. J.; Howard, J. A. K.; Kamenjicki, M.; Lednev, I. K.; Asher, S. A. *Eur. J. Org. Chem*. **2001**, 933.

Chapter 2

ExTTF Porphyrin: Synthesis, Metalation, Photophysical Properties, and Redox Control through Metalation and Coordination of Anions

2.1 Introduction

With regards to organic solar cell applications, π-extended tetrathiafulvalenes (exTTFs) are suitable candidates for electron donors due to their beneficial electronic features (highlighted in Chapter 1.3). However, these systems lack an inherent ability to absorb light, particularly at wavelengths above 500 nm.

Porphyrins and other closely related tetra-pyrrolic porphyrinoids on the other hand, are prolific absorbers of light. They have been nicknamed the "pigments of life" due to their intense colors and fact that several key biological macromolecules are comprised of porphyrinoid rings (e.g. chlorophylls a and b, haem, cyctochrome c, and etc.).[2.1] Chlorophylls a and b, congeners of porphyrin, are responsible for 100 TW of energy conversion annually through photosynthesis,[2.2] an amount over six times the current world energy demand (15 TW),[2.3] despite being relatively inefficient (merely at the leaf level the efficiency has been estimated to be 5.4%).[2.4] Systematic improvements to synthetic porphyrins have produced solar cells with greatly improved productivities over their natural living counterparts. In fact, porphyrin-dye based systems with up to 12.3% efficiencies are among some of the highest ever reported.[2.5]

We, and others, realized a chimera of porphyrins and exTTFs could exhibit the beneficial properties of both systems. Of particular interest would be a system in which the electronic states are coupled to one another, allowing multiple redox states to be accessed. One method to construct said systems would be to covalently attach exTTFs to porphyrinoids. Previously, several systems have been reported with non-extended tetrathiafulvalenes (TTFs) appended to the porphyrin core (Chapter 2.2). In general, these systems display a dearth of electronic communication between the electroactive components.

In contrast to previous TTF-porphyrinoid systems, in this Chapter we present the synthesis and properties of a π-extended tetrathiafulvalenes porphyrin (**MTTFP**) with direct electronic communication between the dithiole rings and porphyrin core. The synthesis, photophysics, electrochemistry, metalation, crystal structure, and other properties of the molecule are reported. Properties of note for **MTTFP**s include the ability to access multiple redox states through judicial choice of solvent, the tuning of the redox potentials *via* metalation and axial ligand coordination, and the intense absorption of the complexes in the visible red/near infrared region of the electromagnetic spectrum.

The majority of this work was published as an article in *The Journal of the American Chemical Society*:

> **Bill, N. L.**; Ishida, M.; Bahring, S.; Lim, J. M.; Lee, S. S.; Davis, C.; Lynch, V.; Nielsen, K.A.; Jeppesen, J.O.; Ohkubo, K.; Fukusumi, S.; Kim D.; Sessler, J. L.; "'ExTTF-Porphyrin' A π-Extended Tetrathiafulvalene Analogue with Multiple Accessible Redox States" *J. Am. Chem. Soc.* **2013**, 135, 10852-10862

2.2 TTF-Porphyrin and TTF-Phthalocyanine Based Systems

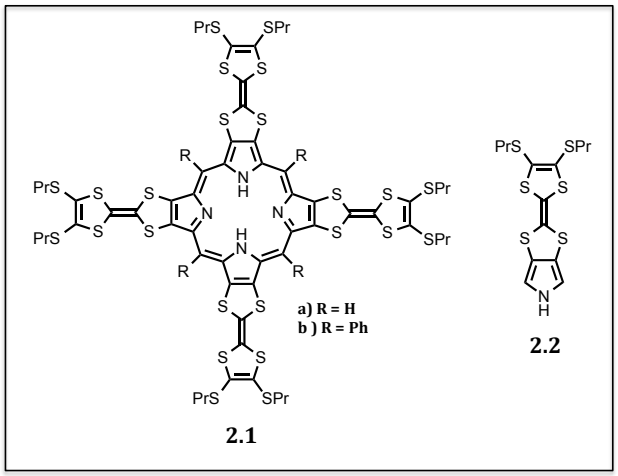

2.1

2.2

To date, a handful of examples detailing porphyrins covalently attached to TTFs have been reported. In 2001,[2.6] the Becher group first reported on TTF-annulated porphyrins (**2.1**) shortly after the discovery of the requisite pyrrolic precursor (**2.2**).[2.7] In this system, four TTF units were directly annulated to the so-called beta positions of the porphyrins pyrrolic rings in an end-to-end fashion. Initial studies and full characterization was limited due to the presence of c.a. 20% radical impurity, limiting meaningful nuclear magnetic resonance (NMR) and absorption spectroscopy studies. However, the proposed porphyrin structure was supported by mass spectroscopic (MS) analysis and X-ray diffraction analyses with the compounds contained in Langmuir films. The electron paramagnetic resonance (EPR) spectrum gave evidence for TTF centered radicals with g-values of 2.0084 and 2.0044 for **2.1a** and **2.1b** respectively, neither system showed hyperfine coupling features and the g-values were in accord with those reported previously for TTF radicals.[2.8] Cyclic voltammetry (CV) displayed unremarkable oxidation peaks with limited electronic communication (splitting or oxidative peaks) between the TTF moieties, leading to the suggestion that, although conjugated, the porphyrin core and TTF subunits are electronically independent of one another.

Shortly after the initial report of *tetrakis*-TTF-annulated porphyrins (**2.1**), a mono-TTF annulated *tetrakis*(p-cyanophenyl)porphyrin (**2.3**) was reported by the same researchers.[2.9] Fortunately, **2.3** was absent of the radical impurities that plagued its higher order forebearer, allowing more advanced analyses to be undertaken. Two one-electron reduction peaks (assigned to the porphyrin ring) and two one-electron oxidations (attributed to TTF) were evident for **2.3** as determined by CV analysis. In each case, the redox processes occurred at higher potentials than were observed in control compounds consisting of the individual subunits (tetra(p-cyanophenyl)porphyrin (TCPP) and **2.2** respectively). Absorption spectroscopy of **2.3** revealed features that were a linear combination of those for TCPP and **2.2**. This finding was taken as an indication that in the ground state there is a dearth of electronic communication between the porphyrin core and TTF periphery. However, in the excited state the opposite conclusion was reached as inferred from analyses of the fluorescent characteristics of the system. In the neutral state, **2.3** displayed an emission spectrum that was quenched by 98% compared to its TTF-free counterpart TCPP. Most likely, this quenching is a result of significant charge transfer that occurs from the TTF subunit to the porphyrin core upon excitation. Chemical oxidation of the TTF subunit to $TTF^{\bullet+}$ results in restoration of a significant portion of the emission of **2.3**, further supporting this claim.

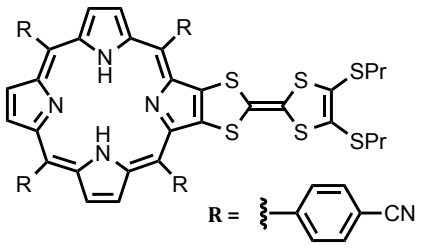

2.3

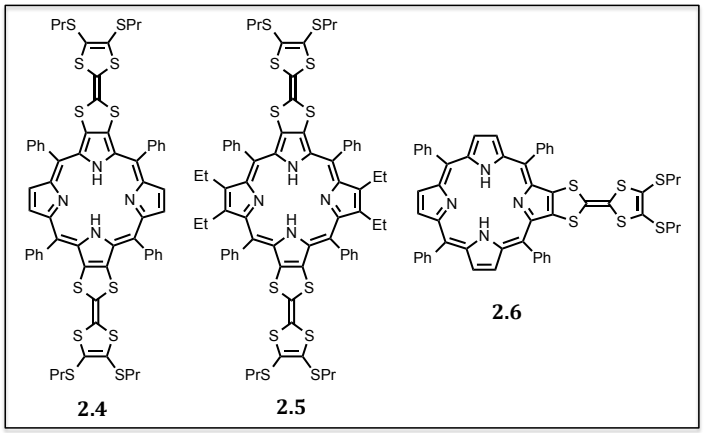

Several years later, in a collaborative effort with the Jeppesen group,[2.10] the Sessler group detailed the synthesis of radical-free **2.1** as well as the *bis*-TTF porphyrins **2.4** and **2.5** and the mono-TTF porphyrin **2.6**.[2.11] Suprisingly, CV studies revealed **2.6** to be more difficult to oxidize than its tetra-cyano derivative **2.3** despite the presence of the electron withdrawing cyano groups. Most likely this study reflects the fact that the annulated TTF is more fully incorporated into the 18-π porphyrin aromatic ring in the case of **2.6** than it is in **2.3**. Also of note were the differences in the CV spectra of **2.4** and **2.5**. Splitting of the first oxidation waves in **2.4** was apparent, whereas in compound **2.5** the first oxidation waves coalesce. Further, **2.4** is oxidized at substantially lower potentials than **2.5**. To account for these discrepancies, the difference in planarity between the molecules is suggested to have a drastic effect on the oxidation potentials. Compound **2.5**, for which a diffraction grade crystal and X-ray structure was obtained, is severely distorted from planarity due to the steric clashes between the sulfur atoms, *meso*-phenyl groups, and *β*-substituted ethyl groups. In contrast, porphyrin **2.4**, which lacks beta substitution, is expected to adopt a much more planar conformation allowing for electronic communication between the TTF moieties, splitting the oxidation waves and increasing the effective electron density, thereby lowering the oxidation potentials. Unlike what was previously found for compound **2.1**, in this report CV analysis showed at least five

oxidative processes. Unfortunately, peak separations were not significant enough to allow further analyses. A later report by the Sessler group generalized this finding of multiple (>2) redox waves to other arrangements of planar TTF-annulated porphyrins.[2.12] However, in all examples studied, upon zinc metalation a coalescence of the numerous redox waves was observed into only two well-defined processes. The current associated with these peaks was found to correspond to *n*-times the number of appended TTFs electrons per peak.

Alternation of the *meso*-substituents of porphyrins is a well-known way to introduce functionality into the basic macrocylic core. This approach has been employed to affix TTFs moieties to porphyrins. In the simplest case, dyad **2.7** was formed *via* the trimethylphosphite-promoted cross-coupling of porphyrin-thione **2.8** and ketone **2.9**.[2.13] Dyad **2.7** was found to lack electronic communication between its components in the ground state as inferred from absorption spectroscopic analyses. Most likely this lack of communication reflects the fact that the TTF moieties are orthogonal to the porphyrin core. In analogy to what was seen for the annulated porphyrins, efficient porphyrin fluorescence quenching was observed, which could be attenuated by chemical oxidation.

Scheme 2.1. Synthesis of dyad **2.7**

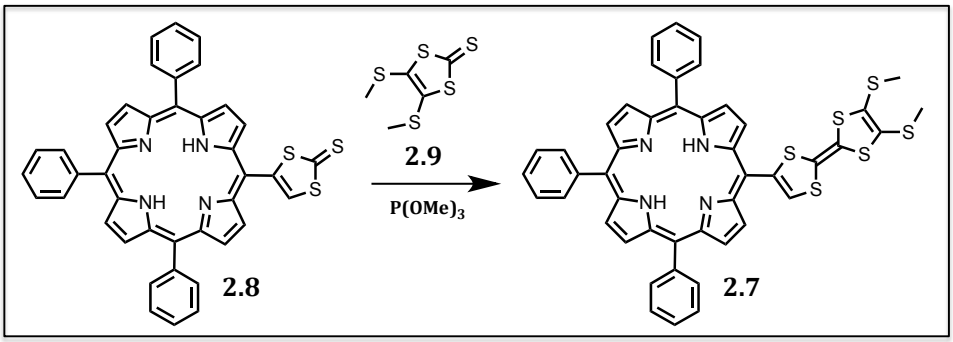

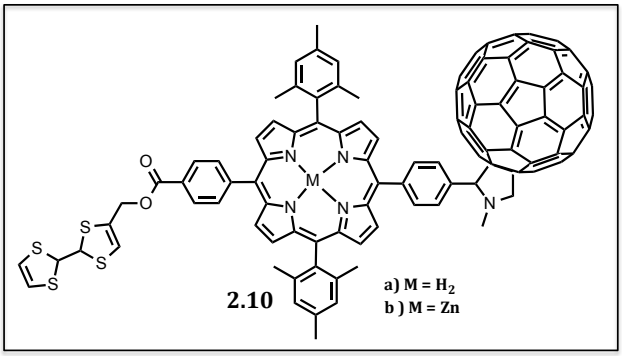

Examples of meso-substituted porphyrin systems, incorporating both electron donating TTF and the electron acceptor C_{60}, have been reported (**2.10**).[2.14] For free-base compound **2.10a**, photoexcitation of the porphyrin core at 590 nm leads to efficient electron transfer from the porphyrin excited state to the TTF subunit (time constant = 25 ps) in essentially quantitative yield. The C_{60}/porprhyin$^{\bullet+}$/TTF$^{\bullet-}$ radical pair generated in this way decays with a time constant of 230 ps to the final charge separated (CS) $C_{60}^{\bullet-}$/Porphryin/TTF$^{\bullet+}$ state, which is stable for hundreds of nanoseconds (660 ns time constant). Decay to the ground state from the C_{60}/porprhyin$^{\bullet-}$/TTF$^{\bullet+}$ state has a larger driving force (1.62 eV) than the charge shift process that forms the $C_{60}^{\bullet-}$/Porphryin/TTF$^{\bullet+}$ state (0.66 eV). However, the latter is produced in ca. 92% overall yield, a result ascribed to the recombination process falling in the inverted Marcus region. The zinc complex **2.10b** displays similar CS characteristics to **2.10a**. However, formation of the final long-range charge separated state ($C_{60}^{\bullet-}$/Porphryin/TTF$^{\bullet+}$) is less favored (16% yield), presumably due to increased competition from faster recombinatorial processes.

The CS state of compound **2.10** was determined to be singlet in nature and decay directly to the ground state despite examples of previous donor compounds decaying to the triplet state.[2.15] The absence of low-lying triplet states was proposed to account for this phenomenon. Time resolved electron paramagnetic resonance spectroscopy of **2.10a** supported the characterization of the CS state. [2.16] In frozen

glass, **2.10a** was found to display similar separation features as were seen under ambient conditions although a markedly longer CS lifetime of 8 μs was recorded. Unfortunately, attempts to order these compounds by suspending them in liquid crystals led to the generation of low-lying triplet states, which are undesirable for device formation.

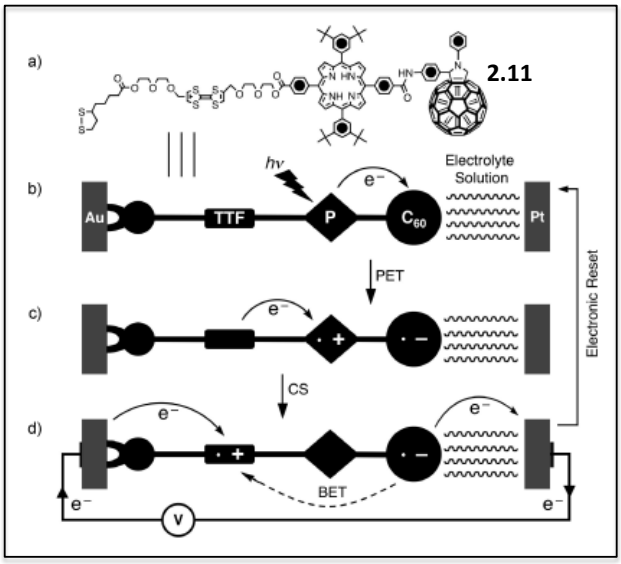

Figure 2.1. (a) The structural formula of the tetrathiafulvalene-porphyrin-fullerene molecular triad **2.11** bearing a disulfide anchoring group (b)–(d) Proposed vectorial electron transfer mechanism for the photo-response of a photoelectrochemical cell comprised of triad **2.11** on an Au electrode in contact with an electrolyte solution that contains a platinum (Pt) counter electrode (PET = photoinduced electron transfer; CS = charge shift; BET = back-electron transfer). Figure reproduced with permission from *Chem. Eur. J.* **2005**, 11, 6846. Copyright 2005. John Wiley and Sons.

The Stoddart group has further advanced the utility of *meso*-linked TTFs by incorporating them into complex and functional molecular architechtures. A TTF/porphyrin/C_{60} triad (**2.11**) covalently linked to a disulfide anchoring group provided a means to tether the photoactive triad to a gold surface.[2.17] A single self-assembled monolayer was found to coat the gold surface in an hexagonal close packed arrangement. A device incorporating the aforementioned triad was

fabricated by connecting the gold surface (electrode) with a conducting wire to a platinum electrode and employing a redox electrolyte to complete the circuit. Switchable photocurrent was observed upon light irradiation near the maximum absorption band of the porphyrin core (413 nm), driving photoinduced electron transfer from the porphyrin to the fullerene. The electron is then collected at the platinum electrode, while simultaneously, the hole is shuttled through the TTF linker to the gold electrode. The energy difference produced in this way is manifest as voltage difference across the electrodes and can be collected *via* the conducting wire (Figure 2.1). Further experiments demonstrated this system was capable of dethreading a rotaxane, specifically a cyclobis(paraquat-*p*-phenylene) ($CBPQT^{4+}$) and a 1,5-bis[(2-hydroxyethoxy)ethoxy] naphthalene thread, thus "powering" a molecular machine.

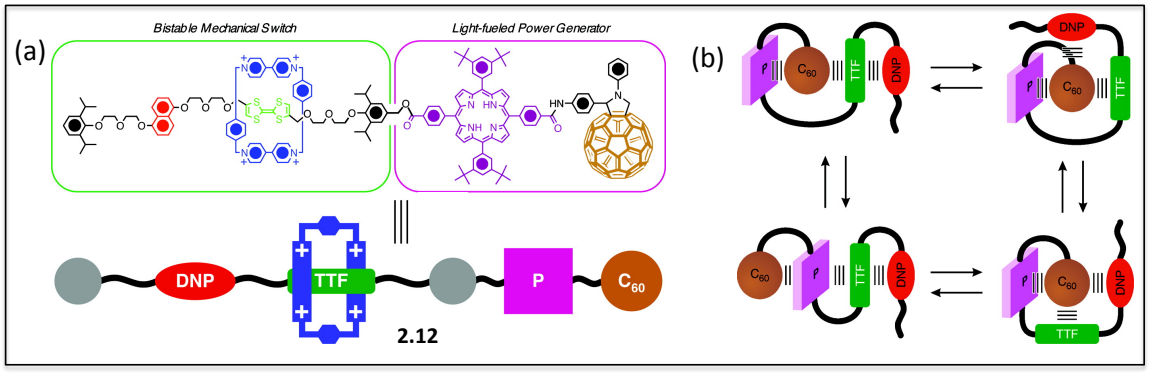

Figure 2.2. (a) Structure of **2.12** displaying left (green box), the bistable mechanical switch components and right (pink box) the light-fueled power generator. (b) Schematic representation of the four possible folded conformations of **2.12**, colors in the figure correspond to the color-code demonstrated in (a). Reproduced with permission from *J. Am Chem. Soc.* **2007**, 129, 12159. Copyright 2007 American Chemical Society.

In an extension of the above work, the rotaxane moiety was linked to a light-driven TTF/porphyrin/C_{60} "motor", to generate a proposed photoinduced molecular shuttle (**2.12**).[2.18] Although the structure of **2.12** was supported by full

characterization (NMR, UV-vis absorption, and MS), the shuttling of the $CBPQT^{4+}$ (blue box) from the favored TTF donor to the dioxynapthalene group was greatly hampered due to complex intramolecular folding (Figure 2.2). Examination of the redox properties of **2.12** by CV analysis demonstrated an anodic shift in the TTF oxidation peaks, something that was suggested to result from the folded confirmation of the tetrad blocking the TTF moiety from accessing the electrode.

There is also a report where a TTF subunit is bound to porphyrin through a coordination bond. The previously reported pyridine TTF derivative **2.13**[2.19] was found to coordinate to the zinc atom of zinc(tetraphenyl)porphyrin (ZnTPP) forming complex **2.14**.[2.20] Upon binding of **2.13** to the ZnTPP, a decrease in fluorescence intensity was observed. Chemical oxidation of TTF to $TTF^{\bullet+}$ also led to partial restoration of the fluorescence strength. The CV of **2.14** revealed six reversible one-electron redox waves, giving rise to a voltammogram with redox peaks that were more or less a superimposition of those for **2.13** and ZnTPP. Nevertheless, a fluorescent sensor could be produced by alternating the electrochemical oxidation and reduction of **2.14**, which had the effect of reinstating and diminishing fluorescence intensity, respectively.

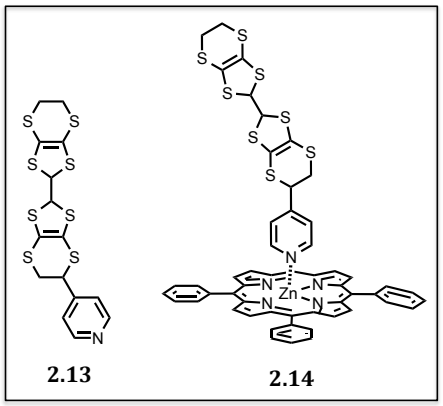

Phthalocyanines (Pc), which are structurally, photochemically, and electronically similar to porphyrins, also deserve mention as scaffolds that have been combined with TTFs. In fact, several years before the first report of TTF-porphyrin chimeras, Bryce reported a TTF appended phthalocyanine (**2.15**).[2.21] In the absorption profile

of **2.15**, split Pc Q-bands were recorded. These were taken as an indication that **2.15** was not aggregated under the experimental conditions of the study. Upon chemical or electrochemical oxidation of **2.15**, the absorption of the Q-bands were relatively unchanged, and pointed toward the absence of electronic coupling between the TTF and Pc core. Findings from CV studies were in line with the results of the absorption spectroscopic analysis in that a CV scan of **2.15** displayed a trace that was more or less a superimposition of its constituents. The sole exception was that the second oxidation wave ($E_2^{1/2}$) of TTF was slightly broadened and anodically shifted, presumably as a result of Coulombic interactions. In this initial report, no evidence of supramolecular ordering was put forth; however, this paper provided the precedent for future work with TTF-Pcs and established that TTF could survive harsh Pc forming reaction conditions.

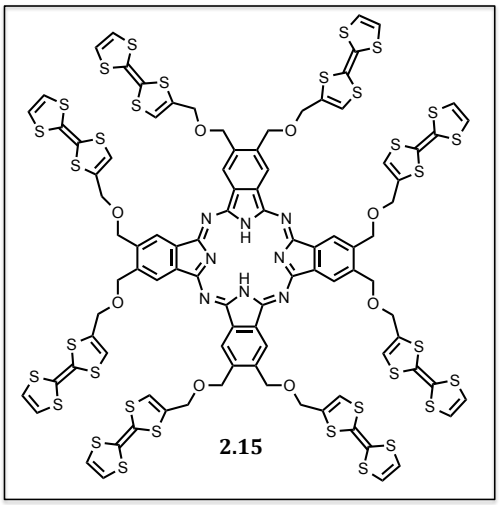
2.15

Around the same time, Pc-TTF composite (**2.16**) was incorporated into a liquid crystalline architecture. This was done by coupling previously known liquid crystalline Pc derivatives with TTF through a DCC promoted esterification.[2.22] Aggregated solutions of **2.16** were inferred based on absorption and NMR spectroscopic analyses. Aggregation was considered to result from TTF-TTF stacking instead of TTF-Pc

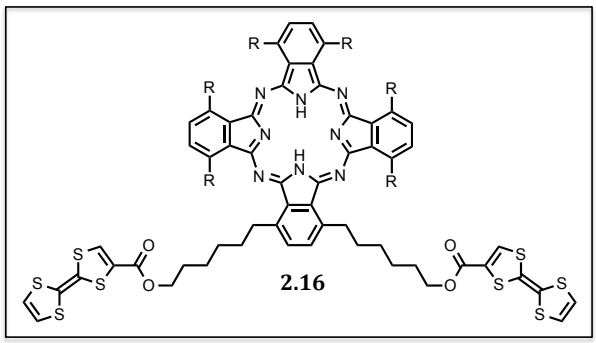
2.16

stacking. Upon heating **2.16** transitions to the mesophase, although the temperature range over which the mesophase is observed is much smaller (ca. 24 °C) than over a similar Pc compound that does not bear TTF subunits (ca. 90 °C). Thin films of **2.16** made by spin coating the compound on a rotating glass slide displayed reversible molecular packing modifications (based on UV/vis spectroscopy) when heating and cooling the compound into and out of the mesophase range.

TTFs directly annulated to Pc rings have also been reported. The simplest example, where all four isoindole fragments are appended with TTF units (**2.17**), was synthesized shortly after the discovery of the requisite dicyanobenzene-dithiole precursor.[2.23] Analysis of the solution-state absorption profile demonstrated a lack of electronic communication between the TTF and Pc core, along with aggregation effects that were highly dependent on the identity of the solvent, increasing upon exchanging THF for pyridine.

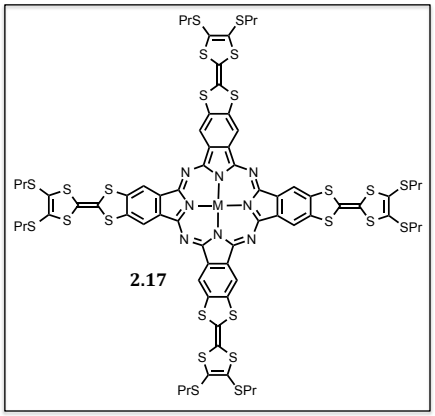

CV measurements of **2.17** revealed two four-electron oxidation waves. Although the second oxidation wave is sharp and fully reversible, the first is split, broad, and convoluted, most likely the result of aggregation effects allowing for the stabilization of a mixed valence TTF species between two adjacent Pc rings. No detectable fluorescence was observed upon excitation of neutral **2.17**. However, in analogy to TTF-annulated porphyrins, upon chemical oxidation of **2.17** fluorescence was restored. Further, the aggregation of **2.17** was greatly diminished upon oxidation,

as evidenced by a characteristic sharpening of diagnostic Q-bands[2.24] in the absorption spectrum. Appending longer alkyl chains to the thioethers lining the periphery of **2.17** was achieved, but unfortunately in all cases no discotic mesophase was achieved.[2.25] Mono-, bis-, and tri-substituted TTF-annulated Pc derivatives have also been reported, although their properties do not differ substantially from **2.17**. [2.26]

TTF-crown ether-Pc conglomerate **2.18** was synthesized in an effort to impart interesting electronic properties to previously known self-assembling crown ether-Pc architectures.[2.27] Compound **2.18** was discovered to aggregate upon addition of

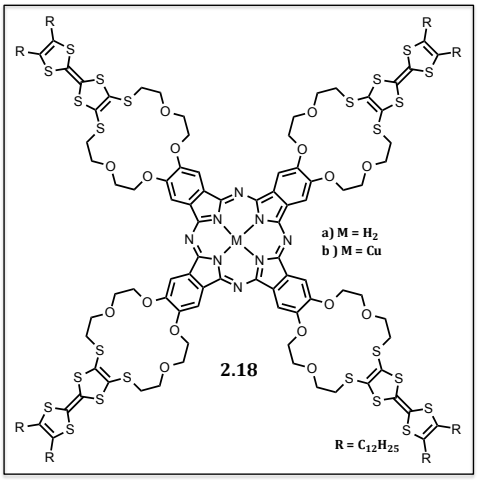

polar solvents (MeOH, dioxane) to $CHCl_3$ solutions. TEM images of the resulting aggregates displayed two types of macrostructures, tapes and fibers. The tape-like structues were up to 20 nm in width, four times the calculated width of a single molecule of **2.18**. More interestingly, the fibrous assemblies were helical in nature, with a racemic mixture of handedness. While TTF-free Pcs with appended crown-ether moieties had previously been shown to form columnar fibers,[2.28] the fibers produced with compound **2.18** are of too great a width (15-20 nm) to be columnar in nature. Previous examples of TTF-Pc interactions have been reported,[2.29] and this interaction (as opposed to Pc-Pc interactions which would lead to columnar structures) is proposed to lead to the formation of tapes and the twisting of these tapes into helical fibers. Initial

conductivity experiments demonstrated a new charge-transfer absorption band upon addition of TCNQ to **2.18**, although no quantitative measurements were reported.

Similar to porphyrin-based system **2.14**, coordination bonds to macrocylic bound metals have been utilized to bring TTF moieties in close proximity to a Pc core.[2.30]

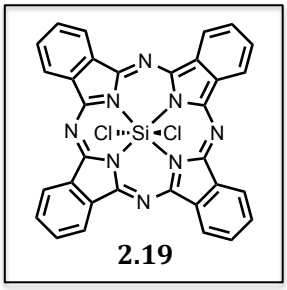

2.19

Specifically, the SiPc system **2.19** has been studied. In this case, between two and six TTF units were coordinated to the silicon center *via* a carboxyl linker. The emission of the Pc subunit was reduced based on quenching from the TTF moieties. Further, like **2.14**, electrochemical switching allowed a fluorescent redox sensor to be realized.

Subphthalocyanines (SubPcs) are an emerging class of 14 π-electron donors that are attracting interest for their unique C_3–symmetry, sharp Q-band absorption, strong fluorescence, and bowl-shaped structure. Similar to their tetrapyrrolic cousins, SubPcs have recently been combined with TTF systems. Directly annulated systems with 1-3 appended TTF units have been reported (**2.20**).[2.31] These systems display increased solubility (compared to TTF-Pc or TTF-Porphyrin scaffolds) as a result of their non-planar structures promoting increased solvation and reduced aggregation.

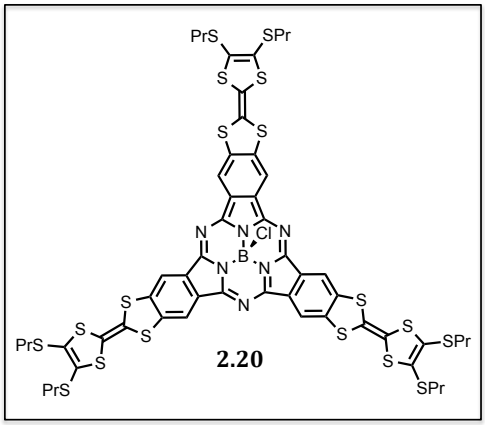

2.20

The fluorescence intensity of the SubPc core is diminished upon successive addition of TTF units, eventually resulting in complete quenching. CV and absorption studies

demonstrated that the oxidation processes were TTF centered that there was limited interaction with the SubPc core, as was true for the similar to TTF-appended tetrapyrrolic systems discussed above.

The central boron atom of SubPcs has also been used as a means of linking an exTTF subunit to the macrocycle (**2.21**).[2.32] To our knowledge, at the writing of this dissertation this was the lone example of an exTTF based system being combined with a pyrrole-based dye. The fluorescence emission of the SubPc was quenched by the exTTF, suggesting that in the excited state there was electronic communication between the TTF moiety and the macrocycle. Further, the rate of excited state decay was found to be dependent on the length of the alkyl linker. Specifically, adding a single additional carbon into the linker was found to move decay process from the normal to inverted Marcus region, shortening the excited state liftetime. Further, this work demonstrated the favorable features that result from using SubPcs as electron acceptors and provides an alternative method to enhance the light harvesting properties of organic electronics.

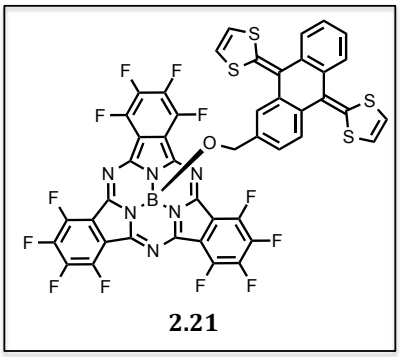

2.21

In all of the known examples of systems in which TTFs (or exTTFs) have been combined with porphyrins or phthalocyanines, a lack of electronic communication in the ground state between the photoactive core and electroactive appendages is seen. Further, oxidation of combined systems results in TTF-centered processes (as opposed to porphyrin- or phthalocyanine-centered) that are affected little by the identity of the attached dye. These two characteristics of combined TTF-dye

systems reported to date limit their functionality and tunability. We aimed to address this shortcoming by extending the conjugation of the TTF system through a quinoidal porphyrin core. Our rationale was this would enforce electronic communication between the two components.

In concert with the aforementioned benefits of creating dye affixed π-extended TTFs, the exceptional optoelectronic and redox properties of porphyrins have driven efforts to prepare derivatives with more than one accessible and well-defined electronic state (e.g., aromatic, nonaromatic, and antiaromatic). In recent years, this challenge has been met in a number of instances via the use of so-called expanded porphyrins, analogues of porphyrins containing larger conjugated peripheries or a greater number of pyrrolic subunits than present in porphyrins.[2.33] For example, we recently reported that a sterically restricted "rosarin", a hexapyrrolic expanded porphyrin, is capable of transitioning between its antiaromatic and reduced aromatic electronic forms via a stable one-electron oxidized radical state.[2.34] However, there remains a need for smaller, electronically switchable materials that more closely resemble porphyrins.

In this chapter, we report a new exTTF derivative, namely the bis(1,3-dithiol-2-ylidene) quinoidal porphyrin (**H_2TTFP**) and its Cu(II), Ni(II), Zn(II), and Co(II) derivatives (**MTTFP**; M = Cu^{II}, Ni^{II}, Zn^{II}, and Co^{II}). Unlike previous work, wherein the TTF subunits were directly annulated to the porphyrin core, **MTTFPs** differ from these earlier systems in that it is a direct "extended" (or "ex") analogue of TTF. As such, it was expected to combine the desirable optical features of the known, but not extensively studied, quinoidal porphyrins[2.35] with the redox features of the so-called

"exTTF" class of compounds (e.g., 9,10-bis(1,3-dithiol-2-ylidene)-9,10-dihydro-anthracene). As detailed below, this combination permits access to three stable oxidation states, as well as to the rich metalation chemistry of porphyrins. This latter attribute allows the electronic and redox properties of **MTTFP** to be tuned without additional synthetic modification. Additionally, complexation of either a chloride or bromide anion to a bound metal center permits fine-tuning of the redox properties of the **MTTFP**. This, in turn, enables control of electron transfer reactions, including specifically thermal processes involving transfer of an electron from **ZnTTFP** to Li^+–encapsulated C_{60} ($Li^+@C_{60}$) in benzonitrile (PhCN). This combination of chemical features, as well as the separate metal- and anion-based control of the redox properties is not possible with the previously reported ex-TTF systems. Nor, is it attainable with simple porphyrin derivatives. A further notable feature of the present system is that, in contrast to unmodified and dithiole-free quinoidal porphyrins, the **MTTFPs** display relatively large two-photon absorption (TPA) cross-section values.

2.3 Synthesis and Characterization of H_2TTFP and MTTFP

Traditionally, non-symmetric TTFs are synthesized through a triethylphosphite promoted cross-coupling reaction of a ketone and thioketone dithiolidene ring. Thus, initial attempts to synthesize **H_2TTFP** revolved around utilization of dipyrroloketone **2.22** and dipyrrolothioketone **2.23** as a "dipyrromethane-like" synthetic handle that could be subjected to acid catalyzed cyclization conditions to afford **H_2TTFP** (Scheme 2.2). Compound **2.22** is readily produced from an addition-elimination reaction involving thiophosgene and pyrrole in good yield. It is

transformed into ketone **2.23** upon exposure to potassium hydroxide and hydrogen peroxide.[2.36] Subjecting **2.22** or **2.23** to standard triethylphosphite promoted TTF coupling conditions (neat $P(OEt)_3$ or solvated in toluene and heat) and thione **2.24** resulted in the isolation of no desired product. Instead, in the case of **2.23** a phosphorylated byproduct (as inferred from ^{31}P NMR spectral analyses) was isolated as a red oil. This species was not fully characterized, but desymmetrization of the pyrrole peaks was evident by ^{1}H NMR spectral analysis. Interestingly, when **2.22** was subjected to the same reaction conditions, 2,2'-bipyrrole was isolated. Although not considered beneficial transformations in the context of preparing **H_2TTFP**, further work is planned to investigate the scope and utility of this serendipitous finding.

Scheme 2.2. Attempted synthesis of **H_2TTFP**, *via* the "dipyrromethane-like" precursors **2.22** and **2.23**.

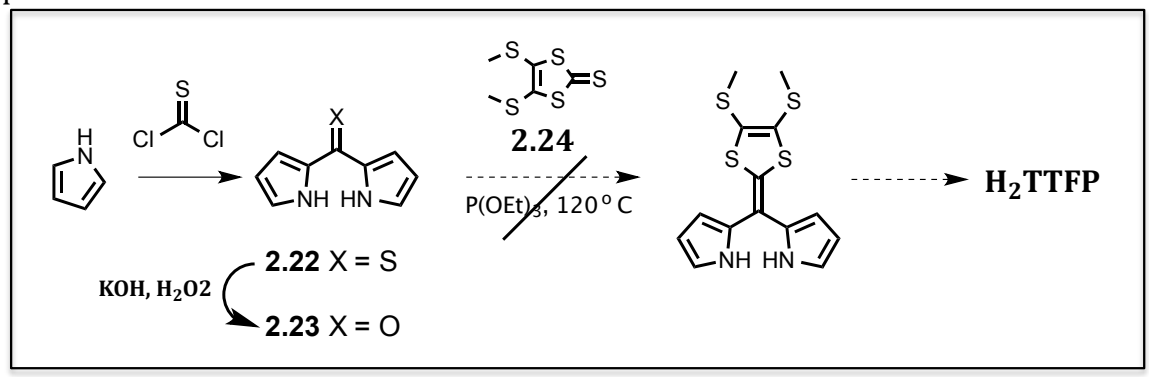

After our failure to couple successfully dipyrrolochalcogenones **2.22** and **2.23**, we turned our attention to preforming the porphyrin ring (Scheme 2.3). The Lindsey group had previously reported the preparation of diketone porphyrinoid **2.26**, a species obtained through the thallium promoted oxidation of 5,15-diphenylporphine **2.25**.[2.37] Although moderate yields were reported, in our hands

yields were consistently low over the two requisite steps. Fortunately, we then found that compound **2.26** can be conveniently prepared (1 step, 56% yield) by treating **2.25** with PbO_2 in accord with a decades old procedure for the synthesis of xanthoporphyrinogen.[2.38] Coupling of **2.26** and **2.24** the provided the desired product **H_2TTFP** as an intensely colored dark green solid in 27% yield.

Scheme 2.3. Syntheses of **H_2TTFP** and **MTTFP**s.

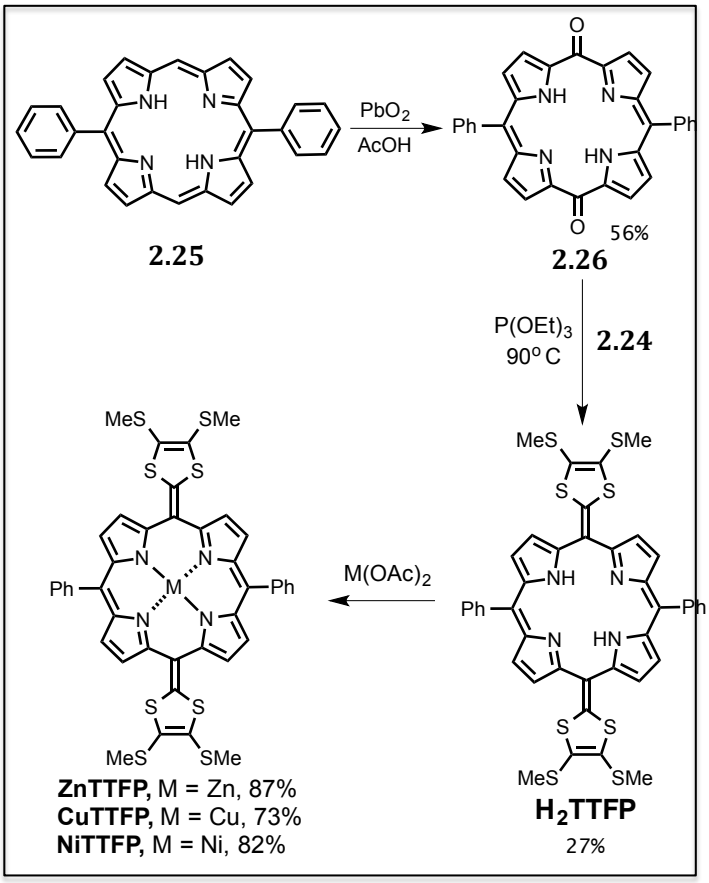

Although *tautomerization* of the exocyclic double bonds would result in a fully conjugated core, a quinoidal structure was assigned to **H_2TTFP** after examination of the ^{1}H NMR spectrum (Figure 2.3). This is consistent with what has been observed in the case of recently reported alkylidene porphyrins.[2.35] This conclusion is also specifically supported by the fact that the interior N-H protons within the

porphyrinoid core resonate at 12.5 ppm (aromatic porphyrins N-Hs resonate at c.a. -2 to -4 ppm). In addition, the outer β-C-Hs of the pyrrolic rings give rise to signals at 6.5 and 6.9 ppm (aromatic porphyrins β-C-Hs are downfield shifted). Consequently, the ^{1}H NMR spectrum is consistent with the lack of a diatropic ring current, and a corresponding lack of aromaticity in **H_2TTFP**. A non-aromatic quinoidal core is thus taken to be the dominant species in solution.

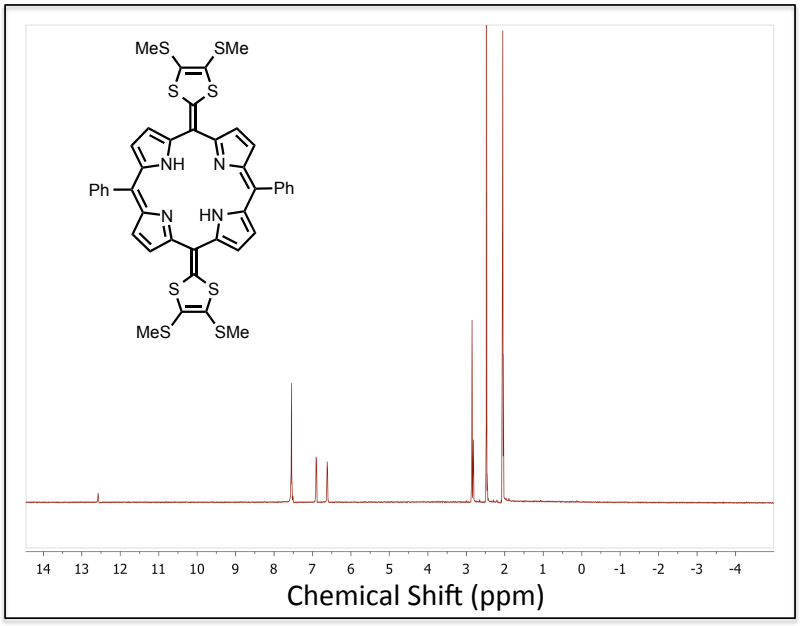

Figure 2.3. ^{1}H NMR spectrum of **H_2TTFP** recorded in acetone-d_6 at 298 K.

Metalation of the free-base porphyrinoid was straightforward with Cu(II), Ni(II), and Zn(II) cations, yielding **CuTTFP**, **NiTTFP**, and **ZnTTFP** respectively *via* the standard acetate protocol.[2.66] Several milligrams of these metal species can be made in one batch. The synthesis of the Co(II) complex, **CoTTFP**, proved more challenging. However, with the help of Dr. Zhan Zhang, this target recently succumbed to synthesis through air-free conditions in the glove box.

Evidence for metal complexation came from high-resolution mass spectrometry (HR-MS), where mass peaks corresponding to the singly charged metal compounds were observed. Further characterization of the diamagnetic metal species (Ni and Zn) was carried out using ^{1}H NMR analyses, revealing spectral patterns and chemical shifts similar to those for the corresponding *β*-pyrrolic and *meso*-phenyl proton signals of **H_2TTFP**. A lack of N-H proton resonances is consistent with metal coordination within the macrocyclic core present in **H_2TTFP.** On the basis of these spectroscopic analyses, the resulting complexes, **ZnTTFP** and **NiTTFP** were also assigned a quinoidal structure analogous to **H_2TTFP**.

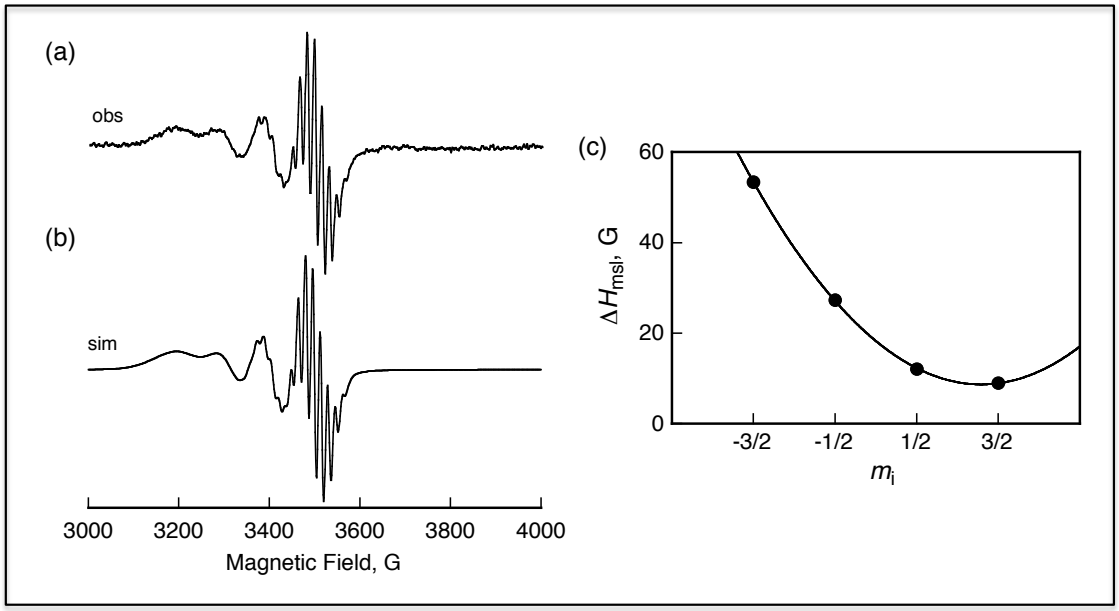

Figure 2.4. (a) ESR spectrum of **CuTTFP** recorded in CH_2Cl_2 at 298 K. Experiment performed with the help of Christina Davis. (b) The computer simulated spectrum; a(Cu) = 91 G, a(4N) = 16 G, ΔH_{msl} = 53, 27, 12, and 9.0 G at m_i = -3/2, -1/2, 1/2 and 3/2, respectively, and (c) plot of ΔH_{msl} vs m_i. Simulated spectra were created by Dr. Kei Ohkubo of the Fukuzumi group at Osaka University.

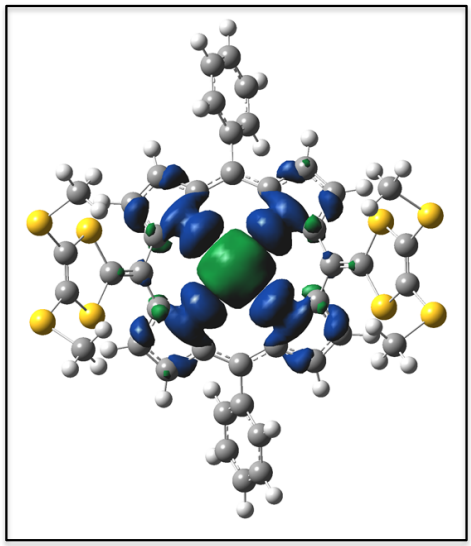

Figure 2.5. Spin density map of **CuTTFP** obtained from UB3LYP/LanL2DZ calculations.

For the paramagnetic complex **CuTTFP**, electron paramagnetic resonance (EPR) analyses were carried out. These analyses were performed at the University of Texas with the assistance of Christina Davis. The EPR spectrum of **CuTTFP** recorded in CH_2Cl_2 at 298 K is typical of what is expected for a square planar Cu(II) complex with hyperfine interactions between the d^9 configured copper ion and the four magnetically equivalent ^{14}N atoms of the ligand (Figure 2.4). A simulated EPR spectrum of the **CuTTFP** complex was created by Dr. Kei Ohkubo of the Fukuzumi group at Osaka University. A near-perfect agreement between the observed and simulated spectra was obtained using an isotropic *g*-value of g = 2.090, super-hyperfine splitting of a(Cu) = 91 G, a(N) = 16 G, and by changing the linewidth (DH_{msl}) depending on the m_I values of Cu (Figures 2.4b and 2.4c). The observed a(Cu) value is smaller than those of typical Cu(II) porphyrin complexes.[2.39] This difference is ascribed to the fact that the unpaired electron density in **CuTTFP** is largely centered on the macrocycle and the associated orbital has d_{x2-y2} character.

This acts to delocalize ca. 50% of the spin density away from the copper center, as inferred from the theoretical spin density map obtained from UB3LYP/LanL2DZ calculations (Figure 2.5). Dr. Masatoshi Ishida carried out these calculations at Yonsei University.

Crystals of **H_2TTFP** suitable for X-ray diffraction analysis were grown from a 1:1 mixture of MeCN and CH_2Cl_2 as dark violet prisms. A severe saddle-shape distortion was clearly evident in the resulting structure (solved by Dr. Vince Lynch of this department), with the dithiole rings pointing back toward one another (Figure 2.6). A distinct lack of planarity is evident, providing further support for the conclusion drawn from the spectroscopic analysis, namely that **H_2TTFP** is non-aromatic.

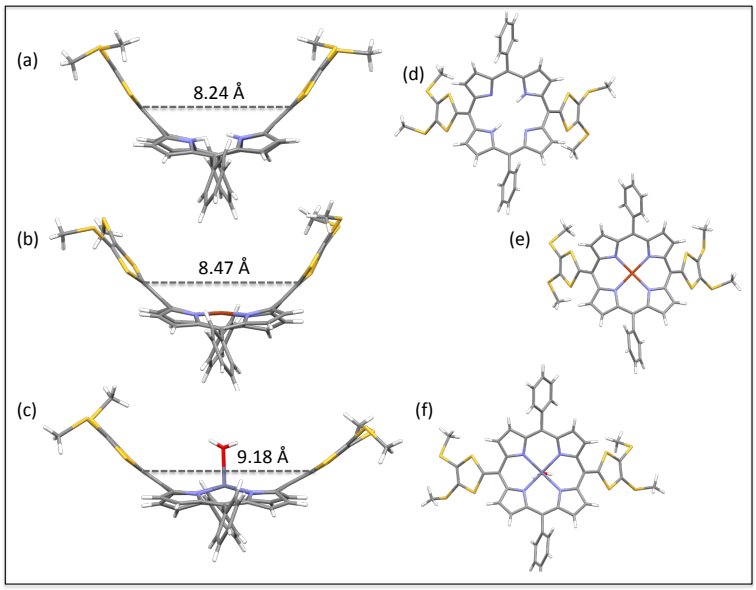

Figure 2.6. X-ray crystal structures of **MTTFP**s. On the left, side views of (a) **H_2TTFP**, (b) **CuTTFP**, and (c) **ZnTTFP**. The indicated distance corresponds to the length between the sulfur-sandwiched alkenyl carbon atoms of the dithiole rings. The right side of the figure shows the top views of the adjacent (d) **H_2TTFP**, (e) **CuTTFP**, and (f) **ZnTTFP**. Dr. Vince Lynch solved all X-ray structures shown.

Single crystals of X-ray quality were also obtained for some of the metallated compounds. **CuTTFP** crystals grew as long violet needles by slow-evaporation of

CH_2Cl_2 and **ZnTTFP** crystals were obtained as violet prisms from slow-evaporation of a 1:1 mixture of tetrahydrofuran and acetone.[2.40] For both metal complexes, a saddle-shape distortion, similar to what was observed for **H_2TTFP**, was found in the solid-state structure (Figure 2.6). The distance between the dithiole rings was greatly affected by the identity of the metal bound to the porphyrinoid core with the trend in the distance between the rings following the order **H_2TTFP** < **CuTTFP** < **ZnTTFP**. The distance between the alkenyl carbons directly between the sulfur atoms of the dithiole rings is 8.24 Å **H_2TTFP**, 8.47 Å for **CuTTFP**, and 9.18 Å for **ZnTTFP**. For the latter complex, water, as an axial ligand was bound to the zinc center between the dithiole rings. This ligation is through to force the rings to adopt a more obtuse conformation. It is unclear whether the X-ray structures are representative of the compounds in the solution state, limiting the conclusions that can be drawn from these metal-induced structural changes.

2.4 Photophysical Studies of MTTFP

The UV-visible spectrum of **H_2TTFP** recorded in CH_2Cl_2 at 298 K supports the assignment of the system as being non-aromatic. For instance, broad absorption bands are seen at λ_{max} = 650 nm (ε = 58000 M^{-1}), 429 nm (ε = 53700 M^{-1}), and 317 nm (ε = 38700 M^{-1}) (Figure 2.7). These spectral features resemble those of the various reported quinoidal porphyrins.[2.41] The molecular orbitals (MOs), obtained from B3LYP/6-31G(d) calculations, provide support for the conclusion that the highest occupied MO (HOMO) is mainly localized on the dithiole subunits. In contrast, the lowest unoccupied MO (LUMO) is primarily centered within the macrocycle. This is taken as evidence that the observed optical transition includes a

contribution involving an intramolecular charge transfer from the dithiole subunits to the central macrocyclic core (cf. Figure 2.8) and thus is good indication of ground state electronic communication between the porphyrinoid core and dithiole rings.[2.42]

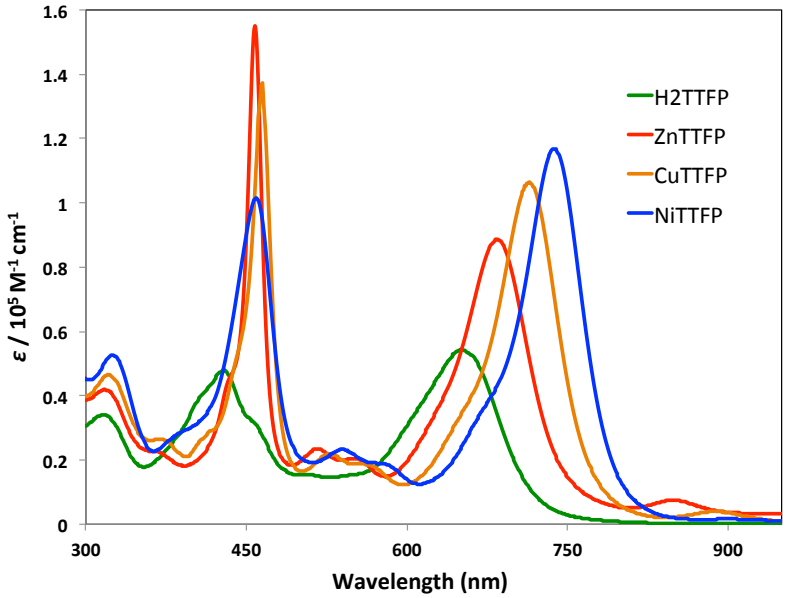

Figure 2.7. UV/Vis absorption profiles of the metal derivatives of H_2TTFP recorded in CH_2Cl_2 including ZnTTFP (red), CuTTFP (orange), and NiTTFP (blue).

Upon metalation, similar low energy broad absorption bands are seen (Figure 2.7) above 650 nm. The order of the red-shift in these energy transitions is as follows: **ZnTTFP** < **CuTTFP** < **NiTTFP**. In the case of **ZnTTFP**, a small intense band around 850 nm is typically seen in the UV-vis spectrum. This band is thought to reflect the presence of a radical cation impurity formed in small amounts under ambient aerobic conditions. The redox properties and dedicated formation of this and other oxidized forms of **MTTFP** are discussed later on in the dissertation.

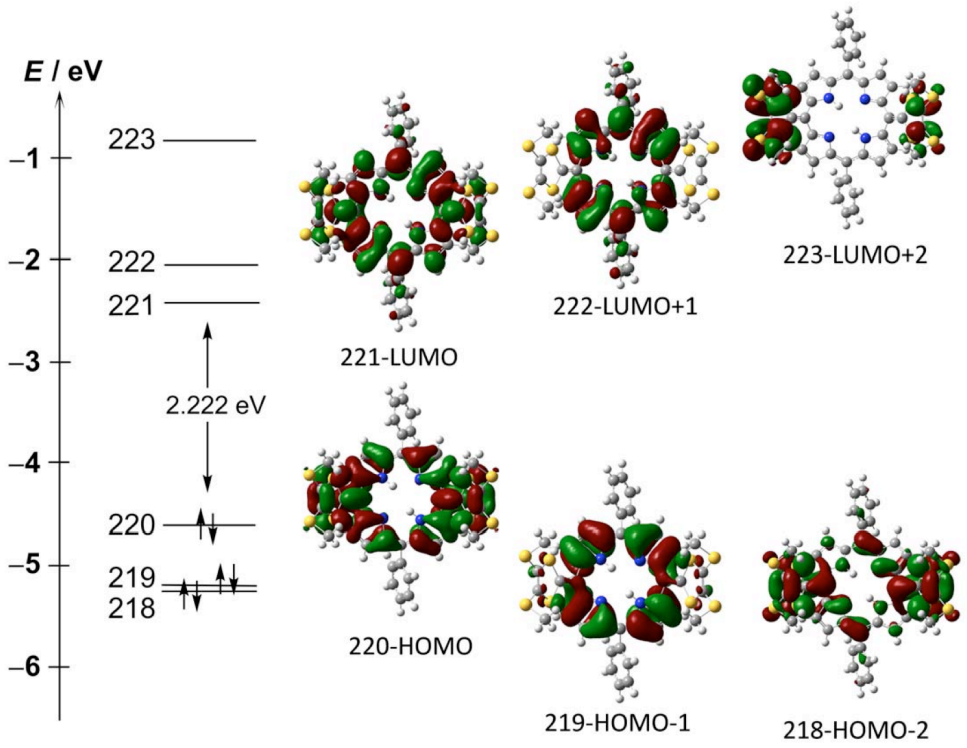

Figure 2.8. Selected MOs of **H_2TTFP** as determined from calculations carried out at the B3LYP/6-31G(d) level. Calculations performed by Dr. Masatoshi Ishida at Yonsei University.

Under ambient conditions, no detectable fluorescence emission was observed for the quinoidal porphyrins **MTTFP**. However, the excited state dynamics of **H_2TTFP** were further explored by femtosecond (fs) transient absorption (TA) spectroscopy in toluene. This work was performed by Dr. Jongmin Lim of the Dr. Dongho Kim group at Yonsei University. The transient species produced from **H_2TTFP** by fs laser irradiation at 650 nm exhibited both broad excited state absorption (ESA) and ground state bleaching (GSB) features across the entire spectral region as shown in Figure 2.9. The temporal profile of the prominent GSB signal at 660 nm was fitted to a biexponential function. This fitting revealed a short time constant of ≈ 77 ps, as well as a longer time constant (> 500 ps) ascribed to a subsequent transition to the

triplet manifold. Presumably, this latter intersystem crossing reflects the heavy atom effect of the sulfur atoms.

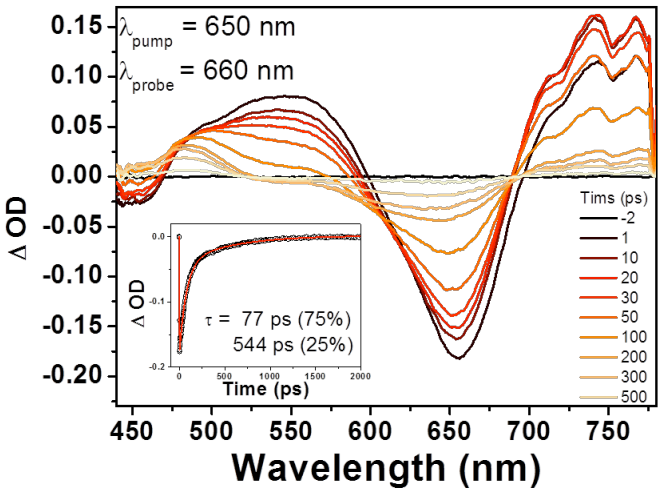

Figure 2.9. Femtosecond transient absorption spectra and decay profiles of free base **H_2TTFP** recorded in toluene at 298 K. This experiment was performed by Dr. Jongmin Lim at Yonsei University.

The TPA spectrum of **H_2TTFP** was also recorded in CH_2Cl_2 using the open aperture z-scan method (Figure 2.10). This work was performed by Sangsu Lee of the Dr. Dongho Kim group at Yonsei University. This analysis revealed spectral features coincident with the lowest one-photon absorption band. The maximum TPA cross-section value, $\sigma^{(2)}$ = 1700 GM, was attained upon excitation at 1400 nm. This value is notably larger than those for analogous (but dithiole-free) quinoidal porphyrins ($\sigma^{(2)}$ = ca. 500 GM at 1200 nm).[2.41] On this basis, it was proposed that the unusual π-donor-π-acceptor-π-donor structure of **H_2TTFP** gives rise to the relatively enhanced nonlinear optical response. The TPA properties of the metal complexes, **MTTFP**s (M = Zn, Ni, Cu) were also examined (Figure 2.10). The **ZnTTFP** ($\sigma^{(2)}$ = 1100 GM at 1300 nm), **NiTTFP** ($\sigma^{(2)}$ = 510 GM at 1300 nm) and **CuTTFP** ($\sigma^{(2)}$ = 450 GM at 1300 nm) complexes gave values that were reduced compared to

H_2TTFP, but still relatively large with respect to the corresponding metallated porphryins.[2.43]

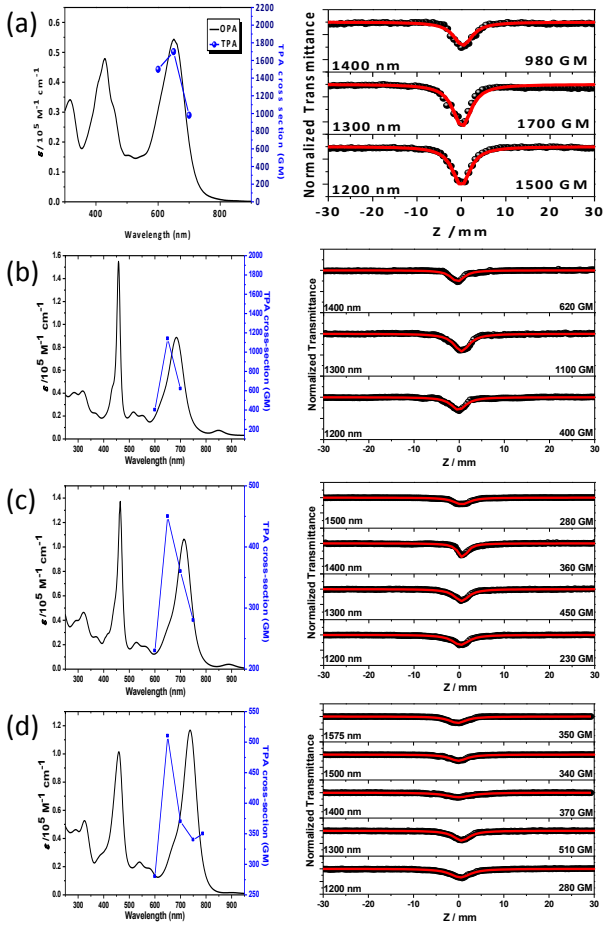

Figure 2.10. The left hand side shows the one-photon absorption (OPA, black trace) and TPA (blue trace) spectra of (a) **H_2TTFP** (b) **ZnTTFP** (c) **CuTTFP**, and (d) **NiTTFP** taken in CH_2Cl_2 at 298 K. On the right hand side are the Z-scan traces cooresponding to the adjacent absorption spectra. The maximum TPA cross-section values ($\sigma^{(2)}$) are estimated to be 1700, 1100, 450, and 510 GM for **H_2TTFP**, **ZnTTFP**, **CuTTFP**, and **NiTTFP**, respectively. This work was performed by Sangsu Lee at Yonsei.

2.5 Electrochemical and Chemical Oxidation of MTTFPs

The electrochemical properties of **H_2TTFP** and its metallated counterparts were analyzed by CV (Figure 2.11). In the case of the free base, **H_2TTFP**, only one redox wave at -0.01 V (vs Fc/Fc^+) was seen, a value ca. 0.07 V lower than pro-anthracene

exTTFs with analogous dithiolidene ring substitution. Broad peaks and a cathodic/anodic peak separation of 215 mV were also noted for the metal-free compound **H_2TTFP**, indicating the system was only quasi-reversible. This was taken as initial evidence that a large conformational change occurs during oxidation of **H_2TTFP** and, in analogy to what is true for exTTFs, the potentials are most likely inverted ($E_2 < E_1$).

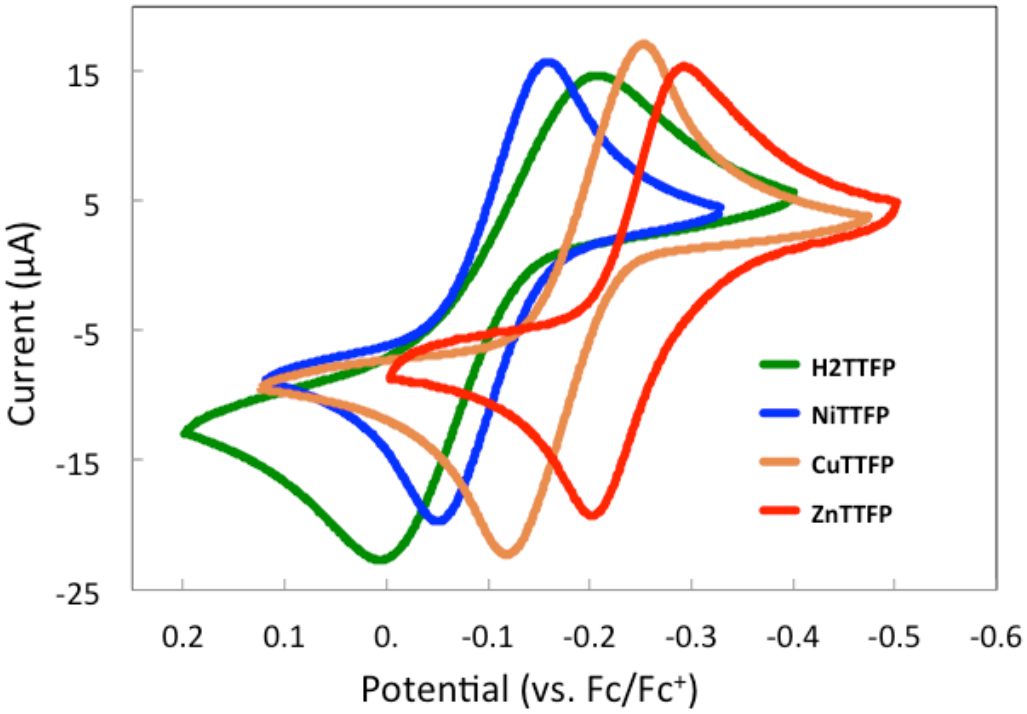

Figure 2.11. Cyclic voltammetry of **MTTFP**s. All spectra recorded in CH_2Cl_2 solutions at 0.001 M concentration with 0.100 M $TBAPF_6$ as the supporting electrolyte. Working electrode was a glassy carbon disc, reference electrode was Ag/AgCl, and Pt wire was the auxiliary electrode. All compounds were referenced to ferrocene *in situ*.

Upon metalation, shifts in the oxidation potentials and a sharpening of the redox waves were seen. **NiTTFP** displayed a nominal shift of -0.01 V, making it only slightly easier to oxidize than the parent compound, **H_2TTFP**. However, the complexes, **CuTTFP** and **ZnTTFP** displayed marked anodic shifts to -0.19 V and

-0.25 V, respectively. These findings provide support for the notion that the oxidation potential of the bis-dithiole quinoidal porphyrin **H_2TTPF** can be tuned by simple metal cation complexation. To our knowledge, this is a property unique to **MTTFP**s that sets them apart from other exTTF and TTF-porphyrin systems. Further, metalation enhances the electron donating ability of **H_2TTFP** and **MTTFP**s appear to be significantly better donors than either simple TTFs or the pro-anthracene exTTFs.

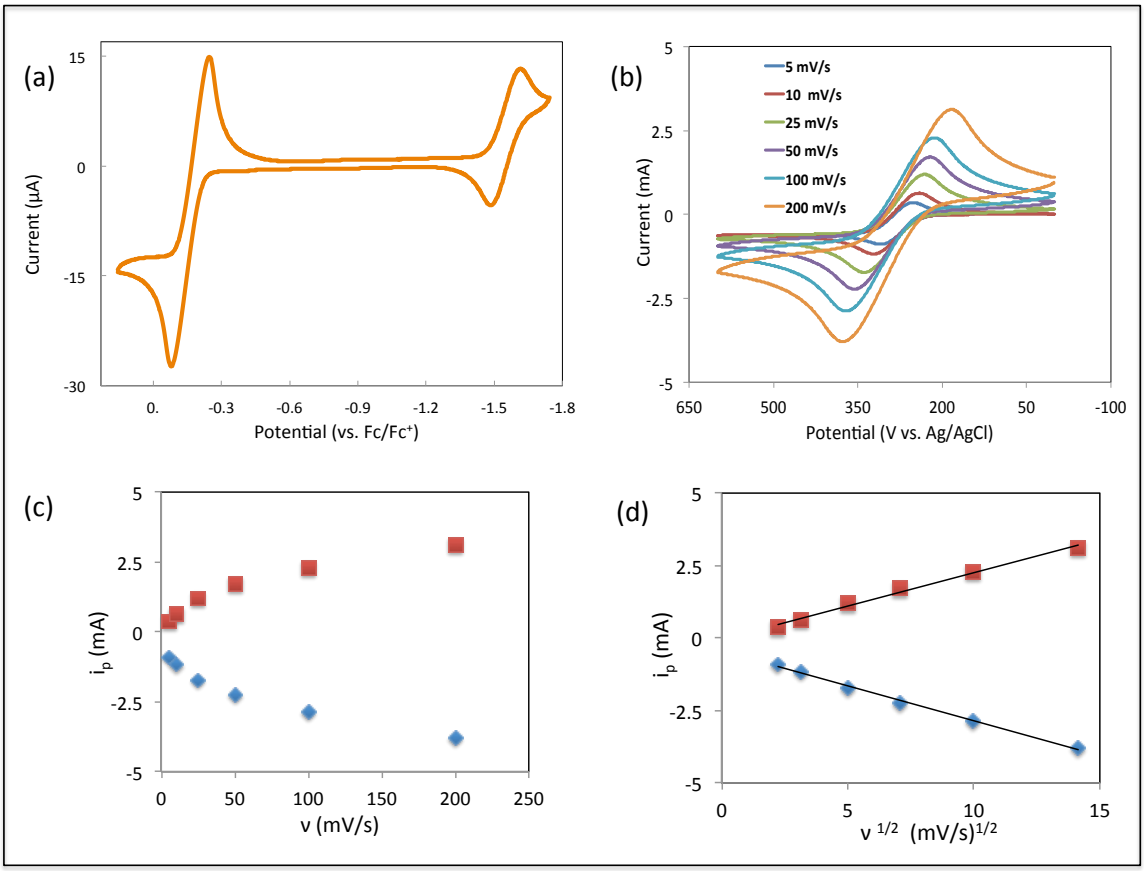

Figure 2.12. (a) CV scan of **CuTTFP**, showing the first (two-electron) oxidation and (one-electron) reduction waves. (b) CV scans of the first oxidation wave of **CuTTFP** at various scan rates ranging from 5 mv/s to 200 mv/s. (C) The scan rate of trials in graph (b) plotted against the intensity of the peak currents. (d) The scan rate of trials in graph (b) plotted against the square root of the intensity of the peak currents yielded linear lines. This provides support for the conclustion that the measurements are under diffusion control.

Insight into the number of electrons being transferred during the oxidation of **MTTFP**s was inferred from the full CV of **CuTTFP** recorded in CH_2Cl_2 (Figure 2.12a). A reversible one-electron feature ascribed to the reduction of **CuTTFP** is observed at -1.580 V whose size is approximately half that of the TTFP oxidation peaks; on this basis we propose that twice as many electrons are being transferred (2 e^-) in the TTFP oxidation than in the Cu reduction (1 e^-). This conclusion is based on the assumption that the system is under diffusion control, which was confirmed by varying the scan rate and plotting the square root of the scan rate versus the intensity of the redox peak yielding a linear plot (Figure 2.12b-d).

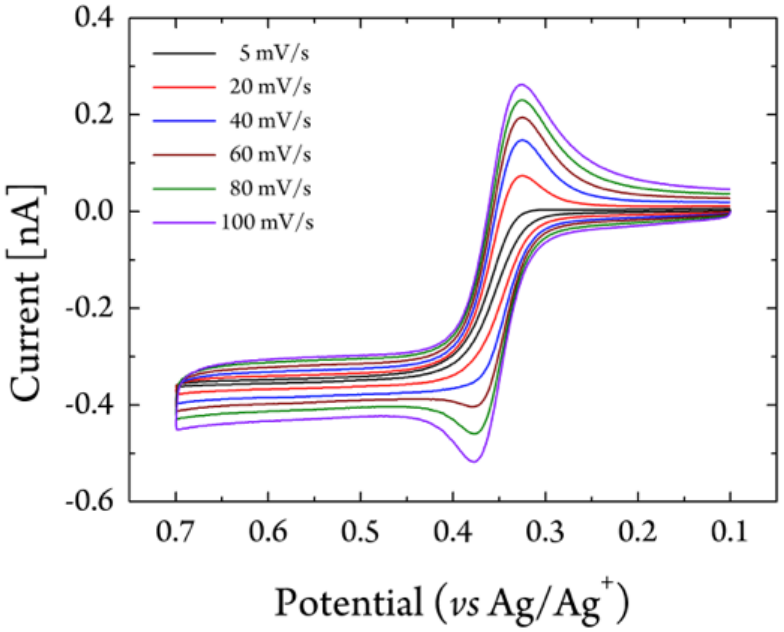

Figure 2.13. CV scans at multiple scan rates of **H_2TTFP**, using a glassy carbon UME as the working electrode. Experiments performed with the assistance of Netz Arroyo of the Dr. Alan Bard group at the University of Texas.

Initially we attempted to quantify the number of electrons transferred through ultramicroelectrode (UME) experiments in collaboration with Netz Arroyo of the Bard group (Figure 2.13). Use of an UME allows for the system to be observed under steady-state dynamics and for the diffusion coefficient to be measured by

variation of the scan rate.[2.44] However, at even very slow scan rates (10 mv/s), a diffusion-controlled process was evident, most likely a result from a chemical process or conformation change coupled to the redox event, followed by a second redox process. Although theoretical simulations could allow for the determination of a diffusion coefficient despite the presence of a surface process, we felt the information we would obtain from these later analyses were not worth the requisite time and effort and thus focused our efforts elsewhere.

Scheme 2.4. Oxidation pathways of **H_2TTFP** to the radical cation and dication forms.

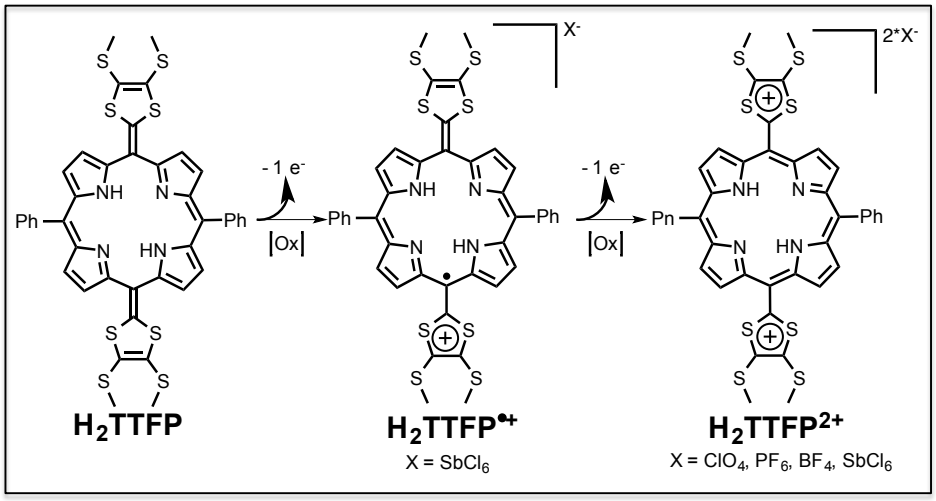

The doubly oxidized form of **H_2TTFP** was also prepared by chemical means (Scheme 2.4). Specifically, it was found that by dissolving **H_2TTFP** in CH_2Cl_2 and adding an excess of crystalline nitrosyl hexafluorophosphate, the oxidized product could be precipitated from solution in quantitative yield in the form of its PF_6 salt (**H_2TTFP•2PF_6**). In a similar fashion, complexes with other counteranions were easily obtained by altering the identity of the oxidant used. The conversion of **H_2TTFP** to **H_2TTFP**$^{2+}$ gave rise to distinctive spectral changes. In the ^{1}H NMR spectrum (Figure 2.14) of the dication, **H_2TTFP•2PF_6**, the N-H protons are shifted

upfield to –2.8 ppm, while the signals for the *β*-hydrogens on the porphyrin core are shifted downfield. These changes are thought to reflect the macrocyclic diamagnetic ring current of the central tetrapyrrolic unit. Further, the appearance of well-resolved peaks allows us to eliminate the possibility that the precipitated species is the paramagnetic radical cation $\mathbf{H_2TTFP^{\bullet+}}$.

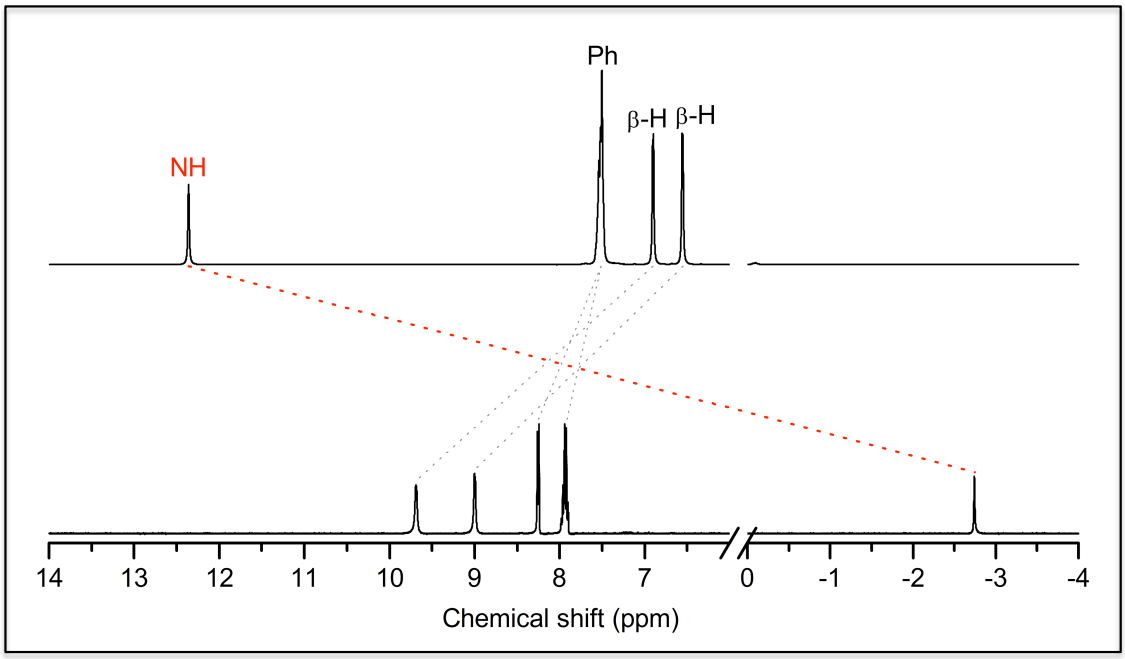

Figure 2.14. Partial NMR spectra of $\mathbf{H_2TTFP}$ (top) and $\mathbf{H_2TTFP{\bullet}2PF_6}$ (bottom) demonstrating the shifts upon oxidation of selected peaks.

The nucleus independent chemical shifts (NICS) were determined from DFT calculations (performed by Masatoshi Ishida at Yonsei University). NICS values calculate the absolute magnetic shielding computed at ring centers.[2.45] To correspond to NMR-shift convention, the signs are reversed, thus, a compound with a NICS value that is significantly negative is considered aromatic whereas a positive value denotes antiaromaticity. Values near zero are considered to be non-aromatic. The NICS values for $\mathbf{H_2TTFP}$, $\mathbf{H_2TTFP^{\bullet+}}$, and $\mathbf{H_2TTFP^{2+}}$ were determined and are displayed in the table within Figure 2.15. For the dication, the "A" ring at the center

of the macrocyclic core has a calculated value of −12.1 ppm; this provides further support for the assignment of **H_2TTFP**$^{2+}$ as being aromatic. Values of 1.29 and -2.53 for this same ring are found for **H_2TTFP** and **H_2TTFP**$^{\bullet+}$, respectively, indicating the ring is non-aromatic in both of these species.

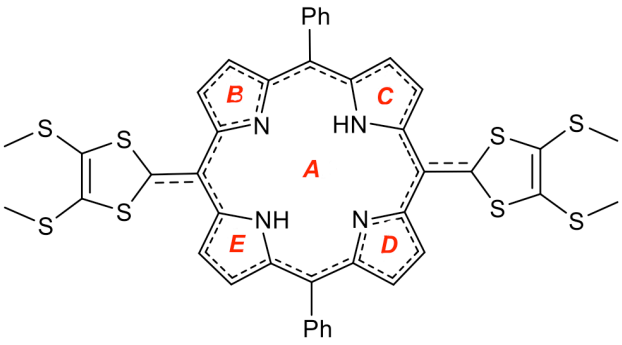

Positions	H_2TTFP	H_2TTFP$^{\bullet+}$	H_2TTFP^{2+}
A	+1.29	-2.53	**-12.12**
B	-4.75	-3.45	-3.32
C	-10.57	-11.37	-12.18
D	-4.76	-4.63	-3.26
E	-10.82	-11.49	-12.03

Figure 2.15. NICS(0) values of **H_2TTFP, H_2TTFP**$^{\bullet+}$ and **H_2TTFP**$^{2+}$ determined from calculations carried out at the (U)B3LYP/6-31G(d) level. These calculations were performed by Masatoshi Ishida at Yonsei University.

Final support for inducing aromaticity through chemical oxidation came from a single crystal X-ray diffraction structure of the doubly oxidized dication species derived from **CuTTFP** (i.e., **CuTTFP•2OTf**). This structure revealed a highly planar geometry, demonstrating a *bona fide* central porphyrin core (Figures 2.16). The bond lengths between the dithiole rings and the *meso*-carbon atom of the porphyrin also increased upon oxidation, as would be expected for the conversion of a C(sp^2)=C(sp^2) double bond (average length = 1.364 Å in the case of **CuTTFP**) to a

single bond (length = 1.48 Å from **CuTTFP•2OTf**). Moreover, some bond length equalization was observed around the porphyrin core. These structural features are thus consistent with the proposed aromatic formulation.

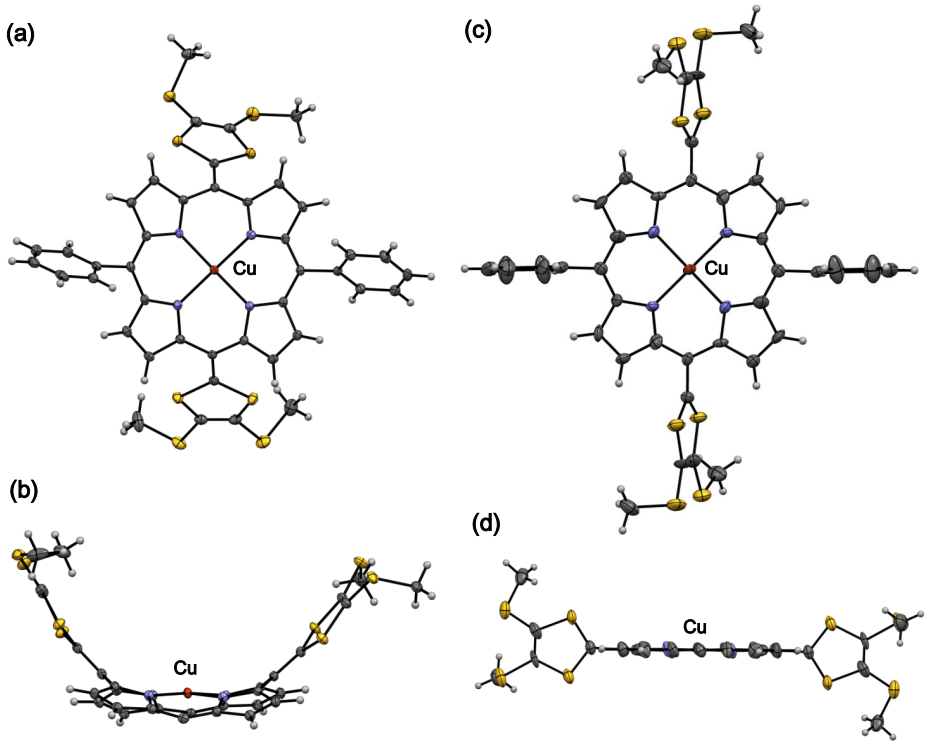

Figure 2.16. Crystal structure of **CuTTFP** (a) front and (b) side views. Crystal structures of **CuTTFP•2OTf** (c) front and (d) side views. The thermal ellipsoids represent 50% probability. The triflate counteranions and the *meso*-phenyl groups (in the side view) of **CuTTFP•2OTf** are omitted for clarity. The data for these structures was collected and solved by Dr. Vince Lynch.

The steady-state UV-vis absorption spectrum of $\mathbf{H_2TTFP•2PF_6}$, recorded in acetonitrile at 298 K, revealed features characteristic of a porphyrin (e.g., tetraphenylporphyrin). For instance, well resolved Q-like bands and an intense Soret band at 410 nm (e = 121000 M^{-1}) were seen (Figure 17a). The porphyrin-like MO density distributions of $\mathbf{H_2TTFP^{2+}}$ is in good agreement with the experimental spectrum (Figure 2.17d and 2.18).[2.46] However, differences from normal porphyrins were revealed in the fs TA spectra of the dication as recorded in acetonitrile. In

particular, an ultrashort singlet excited state lifetime of 26 ps (with a component with a prolonged decay profile ascribed to population of the triplet state) was seen in Figure 2.17c. This short lifetime[2.47] is consistent with the non-fluorescent nature of the dication and is thought to reflect electronic coupling with the dithiole moieties.

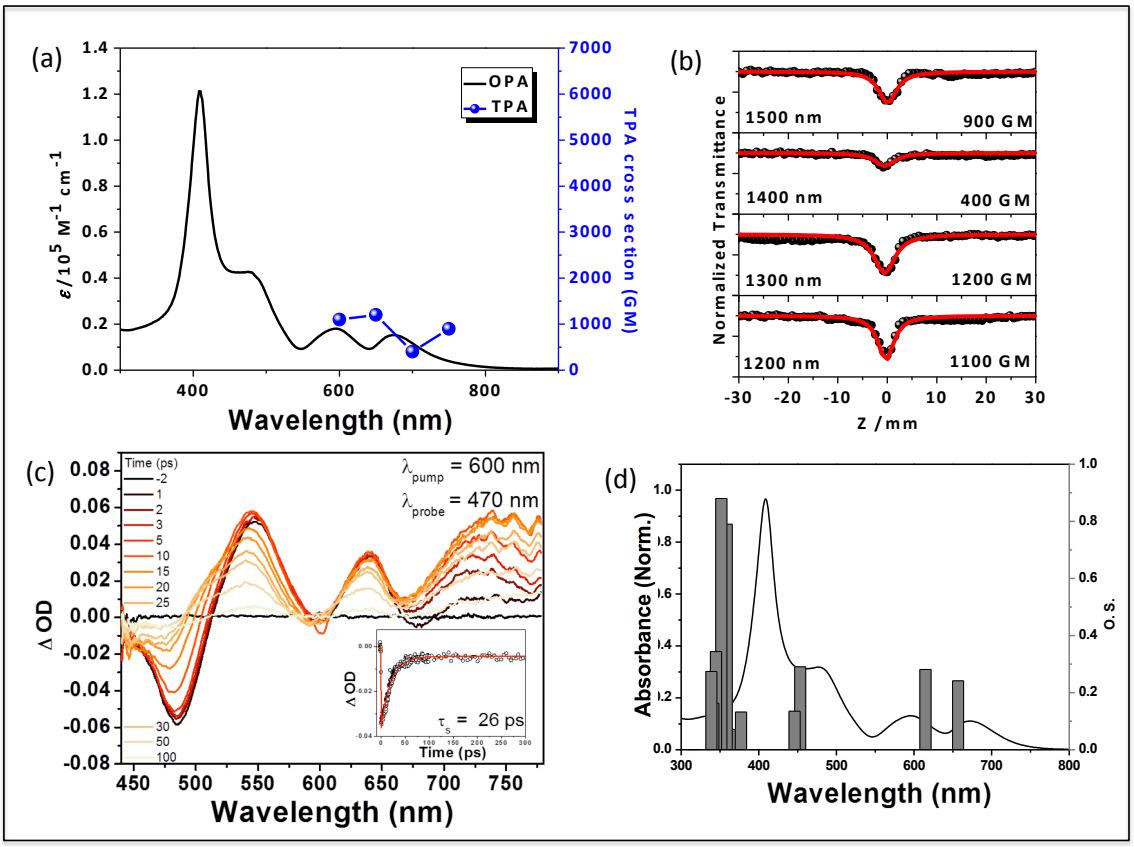

Figure 2.17. (a) OPA and TPA of $\mathbf{H_2TTFP^{2+}}$ taken in MeCN at 298 K. (b) Z-scan traces of TPA of $\mathbf{H_2TTFP^{2+}}$**.** (c) Femtosecond transient absorption spectra and decay profiles of $\mathbf{H_2TTFP^{2+}}$ taken in MeCN at 298 K. (d) Superposition of the steady-state absorption spectra (black line) and theoretical vertical excitation energies (grey bars) obtained from TD-DFT calculations carried out at the (U)B3LYP/LanL2DZ level. These studies were carried out by members of the Kim group at Yonsei University.

Further underscoring the differences relative to porphyrins (taken as ostensibly analogous control aromatic systems) is the relatively large TPA cross-section value of $\mathbf{H_2TTFP^{2+}}$. Specifically, a TPA value of 1200 GM was recorded upon excitation at

1300 nm (Figures 2.17a and b). These values are considerably higher than those typically seen for porphyrins for which TPA values of <100 GM are found.[2.43] These differences are ascribed to the charged dithiole sites that serve to perturb the intrinsic electronic structure of the central porphyrin core present in **H_2TTFP^{2+}**.[2.48]

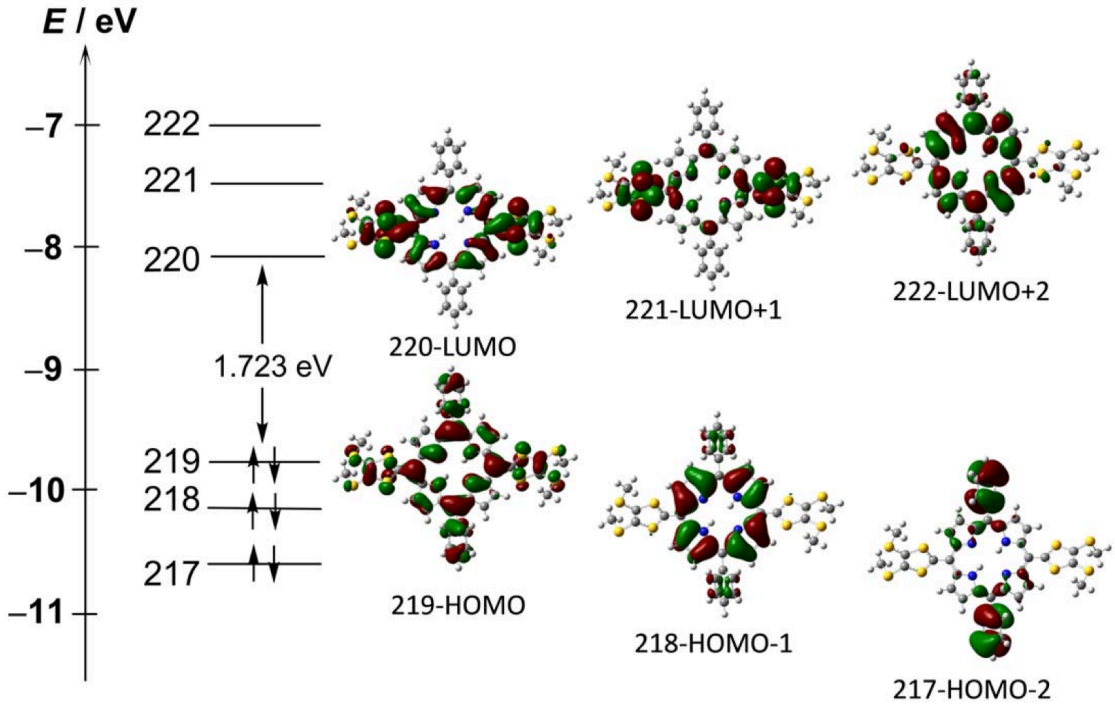

Figure 2.18. Selected MOs of **H_2TTFP^{2+}** as determined from calculations carried out at the B3LYP/6-31G(d) level. Calculations performed by Masatoshi Ishida at Yonsei University.

The singly oxidized radical cation form, **H_2TTFP$^{\bullet+}$**, could be prepared *in situ* by the careful addition of tris(4-bromophenyl)aminium hexachloroantimonate (so-called "magic blue") in CH_2Cl_2.[2.49] The formation of a species with an intense absorption band at 930 nm was seen, with a maximal intensity being observed upon the addition of one equivalent of oxidant (Figure 2.19a).[2.50] Further, broad absorption bands in the near-IR (NIR) region, with a maximal intensity at c.a. 1225 nm were also observed. Taken together, these bands are suggested to be indicative

of the presence of a radical speicies (**H_2TTFP$^{\bullet+}$**) in solution. Upon addition of another molar equivalent of oxidant, the absorption bands at 930 and 1225 nm decayed (which is predicted for our classification of this transient species as **H_2TTFP$^{\bullet+}$**) and the intensity of the Soret band reached saturation. At this point, the spectrum is identical to that produced from the two-electron chemical oxidation with nitrosyl oxidants. The species in question is thus considered to be **H_2TTFP^{2+}**.

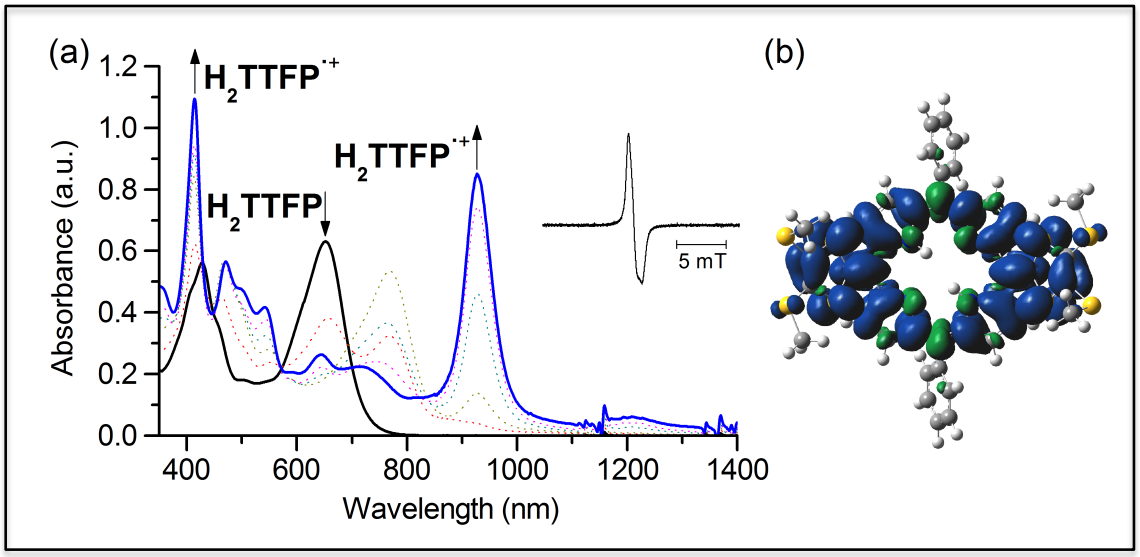

Figure 2.19. (a) UV/vis/NIR absorption spectra of **H_2TTFP** recorded in CH_2Cl_2 at 298 K in the presence of increasing quantities (up to one molar equivalent) of magic blue. Inset shows the EPR spectrum of **H_2TTFP$^{\bullet+}$** (as the $SbCl_6^-$ salt) prepared via the addition of 1 equivalent of magic blue. (b) Spin density map of **H_2TTFP$^{\bullet+}$** obtained at the UB3LYP/6-31G(d) level.

Complicating the spectral assignment of the oxidative states is the existence of a transient species detected prior to the addition of one molar equivalent of magic blue, with an absorption maximum (λ_{max}) at 760 nm. Several possible explanations for the appearance of this species were proposed including dimerization to a mixed-valence (MV) species, oxidation induced aggregation, and simple protonation. Formation of a mixed valence species is predicted to be unlikely due to steric

hindrance. Likewise, the saddle-shape (Figure 2.6, 2.8, and 2.19c) of the quinoidal **H_2TTFP** and **H_2TTFP$^{\bullet+}$** is expected to preclude significant aggregation. Consequently, we focused on acid/base effects in an effort to elucidate the origin of this peak.

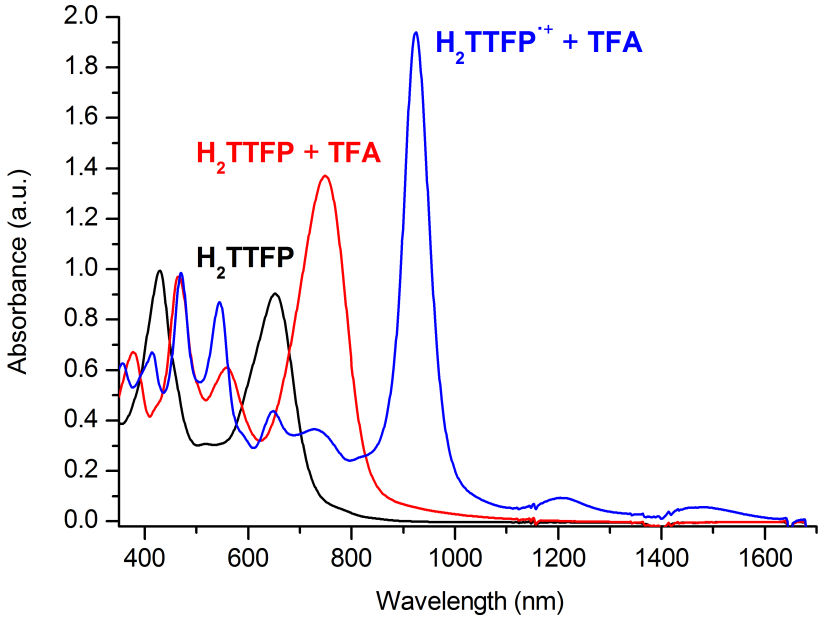

Figure 2.20. UV/vis/NIR absorption spectra of **H_2TTFP** (black), **H_2TTFP** + excess TFA (red), and **H_2TTFP** + excess TFA + 1 equiv of magic blue (blue) recorded in CH_2Cl_2 at 298 K.

After several control experiments, we determined with confidence that the transient species in the oxidation of **H_2TTFP** absorbing at 760 nm reflects protonation of **H_2TTFP** (for which enhanced acidity is expected due to the saddle-type distortion of the porphyrinoid core[2.50]) by residual acid present in the oxidant.[2.51] Support for this suggestion comes from the observation that adding trifluoroacetic acid to the free-base species **H_2TTFP** in the absence of magic blue likewise gives rise to an analogous 760 nm spectral feature while leading to a decrease of the original absorption peak at 650 nm (Figure 2.20). As an additional control experiment, we studied the chemical oxidation of **ZnTTFP** (which lacks the

basic pyrrolic sites present in **H_2TTFP)** by UV/vis absorption spectroscopy. Under identical conditions, oxidation of **ZnTTFP** with magic blue fails to produce a transient species similar to the one observed (at $\lambda_{max} \approx 760$ nm) for **H_2TTFP** (Figure 2.21).

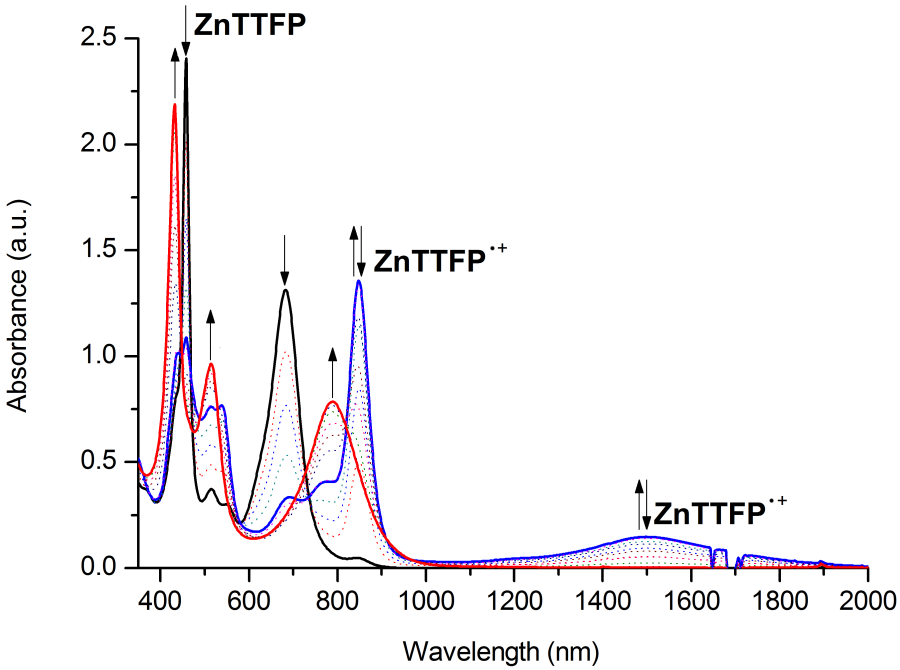

Figure 2.21. UV/vis/NIR absorption spectra of **ZnTTFP** recorded in CH_2Cl_2 at 298 K with increasing amounts of magic blue oxidant. The original spectra of **ZnTTFP** is shown in black, which transitions to the blue spectra **ZnTTFP$^{\bullet+}$** upon addition of one equiv of magic blue. After the two or more molar equiv of magic blue have been added, spectral features corresponding to **ZnTTFP^{2+}** is observed, highlighted in red.

An electron paramagnetic resonance spectrum was taken of the free base species absorbing at $\lambda_{max} \approx 930$ nm (assigned to **H_2TTFP$^{\bullet+}$**) by pre-forming the compound in a CH_2Cl_2 solution followed by spectral analysis at 77 K. This technique revealed features at $g_{\perp} = 2.001$ and $g_{//} = 2.006$ at 77 K,[2.26] thus supporting assignment of this oxidized species as the radical cation. Such readily accessible 4n + 1 π-electron radical cation species are not attainable with either simple quinoidal porphyrins or the pro-anthracene derived exTTF species discussed earlier. The behavior of

MTTFP also stands in contrast to what is seen for the previously reported TTF porphyrins, where TTF-centered, but not porphyrinoid 4n+1 π-electron, radicals may be observed (Chapter 2.1).

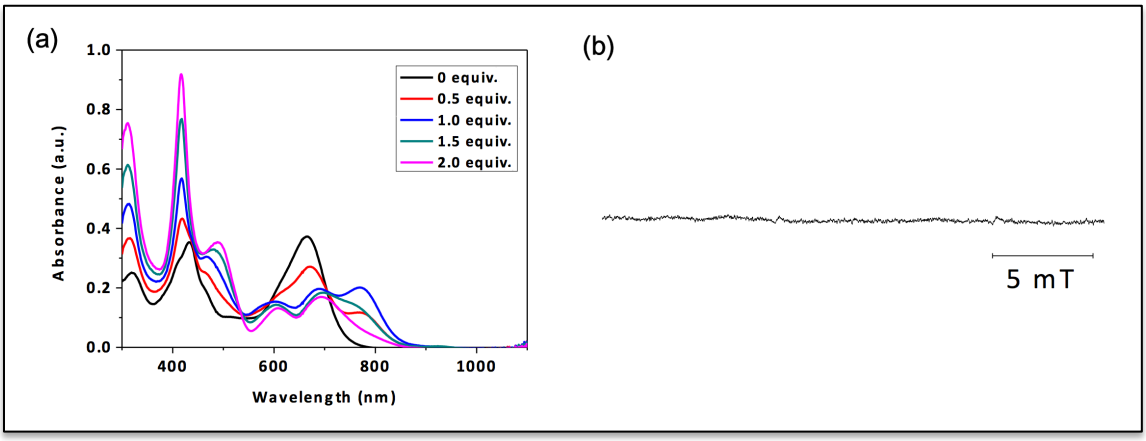

Figure 2.22. (a) UV/vis/NIR absorption spectral changes of **H_2TTFP** seen upon the addition of up to two equiv of magic blue in C_6H_5CN. (b) EPR spectrum of **H_2TTFP** recorded in the presence of one equiv of magic blue in C_6H_5CN. Note the absence of signal in this solvent. EPR done by Masatoshi Ishida at Osaka University.

The stability of **H_2TTFP$^{\bullet+}$** proved to be highly dependent on the choice of solvent. In contrast to what was seen in pure CH_2Cl_2, in polar solvents, such as acetonitrile, benzonitrile (PhCN) or mixtures of these solvents in CH_2Cl_2, the spectral features corresponding to **H_2TTFP$^{\bullet+}$** were not observed (Figure 2.22a). This is ascribed to the disproportionation of the radical cation **H_2TTFP$^{+\bullet}$**. Disproportionation leads to formation of the closed shell neutral (**H_2TTFP**) and dication (**H_2TTFP^{2+}**) species in analogy to what was found in the exTTFs.[2.53] An alternative explanation, involving dimerization to form a closed shell, EPR silent dimer (e.g., [(**H_2TTFP**)$_2$] $^{2+}$), is ruled out on steric grounds; the large *meso*-phenyl groups and saddle-shape are expected to prohibit the necessary intermolecular contact. The lack of paramagnetic radical species was supported by EPR analysis, which failed to reveal any signal upon addition of one equivalent of magic blue in a PhCN solution (Figure 2.22b).

2.6 Fine Redox Control by Axial Ligand Coordination

As discussed in the previous section, metal coordination was found to affect the oxidation potential of **MTTFP**s. Although this phenomenon is commonplace in porphyrin literature, it is inherently absent from exTTF-based systems, which lack a metal complexation site. Another manner in which the redox potential of porphyrins can be manipulated is by axial ligand coordination to the central metal.[2.54] We thus decided to investigate the effect of axial metal coordination on the redox features of **MTTFP**s. Particular emphasis was placed on **ZnTTFP**, which should bind one (and only one) axial ligand. An added benefit of this choice is that **ZnTTFP** is diamagnetic, simplifying characterization.

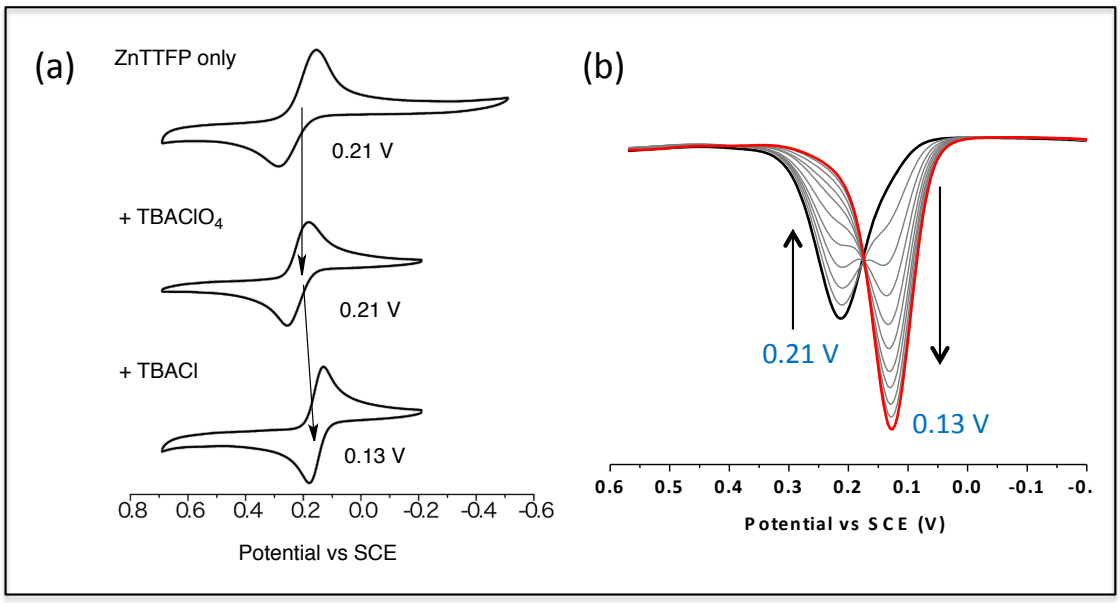

Figure 2.23. (a) Cyclic voltammograms of a 0.2 mM solution of **ZnTTFP** in PhCN: (top) recorded in the presence of $TBAPF_6$ (100 mM) as a supporting electrolyte, (middle) after the addition of $TBAClO_4$ (20 mM) as a non-coordinating control, and (bottom) after the addition of TBACl (20 mM). (b) Differential pulse voltammogram (DPV) for the titration of TBACl into a 0.2 mM PhCN solution of **ZnTTFP**. The original spectrum of pristine **ZnTTFP** is highlighted in black. The final spectrum (where the concentration of TBACl was 0.2 mM) is highlighted in red.

We found that in PhCN, the strong electron donating ability of **ZnTTFP** can be further enhanced by the axial coordination of anions, specifically chloride and bromide. In CV measurements, a shift in the two-electron oxidation potential (E_{ox}) of **ZnTTFP** was induced by binding to Cl^- (Figure 2.23). In the absence of a coordinating ligand, the E_{ox} value of **ZnTTFP** in PhCN was determined to be 0.21 V vs. SCE. The E_{ox} value remained the same after the addition of the non-coordinating anion tetra-*n*-butylammonium perchlorate ($TBAClO_4$). However, upon addition of tetra-*n*-butylammonium chloride (TBACl) a cathodic shift of the E_{ox} value to (0.13 V vs SCE) was apparent. We believe that by coordinating to the metal center, chloride serves as an external electron donor, and in concert stabilizes the oxidized state through charge stabilization. The binding of Cl^- to **ZnTTFP** was confirmed *via* single crystal X-ray diffraction analysis. The resulting structure, shown in Figure 2.24, reveals that the Cl^- anion is coordinated to the Zn^{2+} center of **ZnTTFP**.

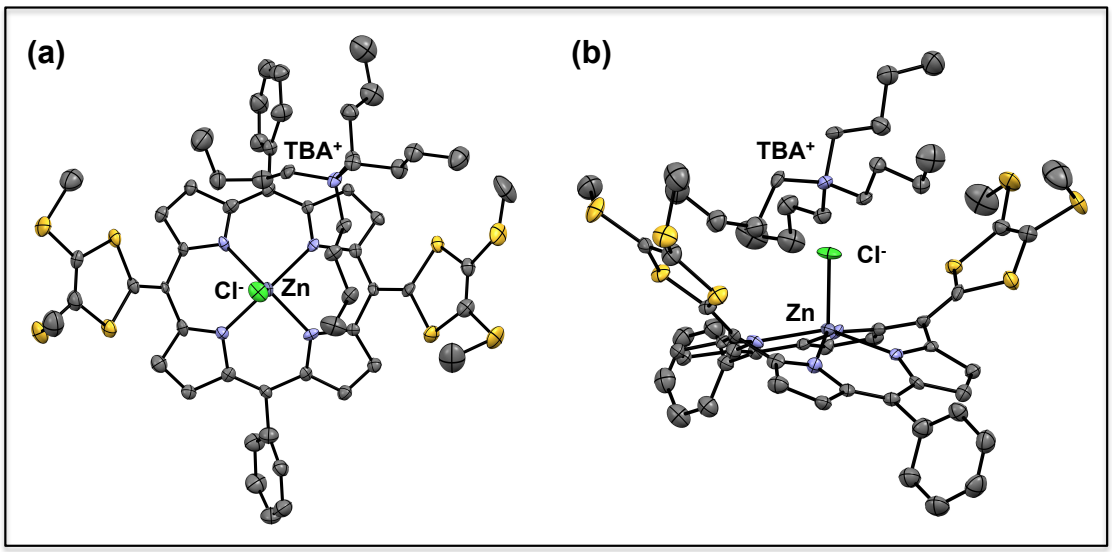

Figure 2.24. Two views of the single crystal X-ray diffraction structure of **ZnTTFP•TBACl** shown at the 50% thermal ellipsoids probability level. The solvent of crystallization and the hydrogen atoms are omitted for clarity. Data collection and refinement was done by Dr. Vince Lynch.

The observation of anion induced shifts in E_{ox} inspired us to examine the applicability of incoporating **ZnTTFP-**anion constructs into thermodynamically induced electron transfer schemes. To this end, Li^+–encapsulated C_{60} ($Li^+@C_{60}$) was chosen as an electron acceptor, because $Li^+@C_{60}$ has been reported to undergo a one-electron reduction at 0.13 V (vs SCE), which corresponds nicely to the oxidation potential of **ZnTTFP-Cl** (cf. Figure 2.25).[2.55] A CV of the mixture of **ZnTTFP** and $Li^+@C_{60}$ in PhCN clearly displayed two redox processes between 0.00 V and 0.30 V. The calculated half-wave potentials of the peaks in this convoluted region are identical to the previously reported values for the oxidation of **ZnTTFP** and the first reduction of $Li^+@C_{60}$, and the spectra appeared to be little more than a superimposition of expected spectra for the individual components. Addition of $TBAClO_4$ resulted in no observable changes in the CV. However, upon addition of TBACl, a coalescence of the peaks in the 0.00-0.30 V region is seen, resulting in a single peak with a half-wave potential of 0.14V.[2.56] We took this as initial evidence of the feasibility of anion-induced thermodynamic electron transfer within this system.

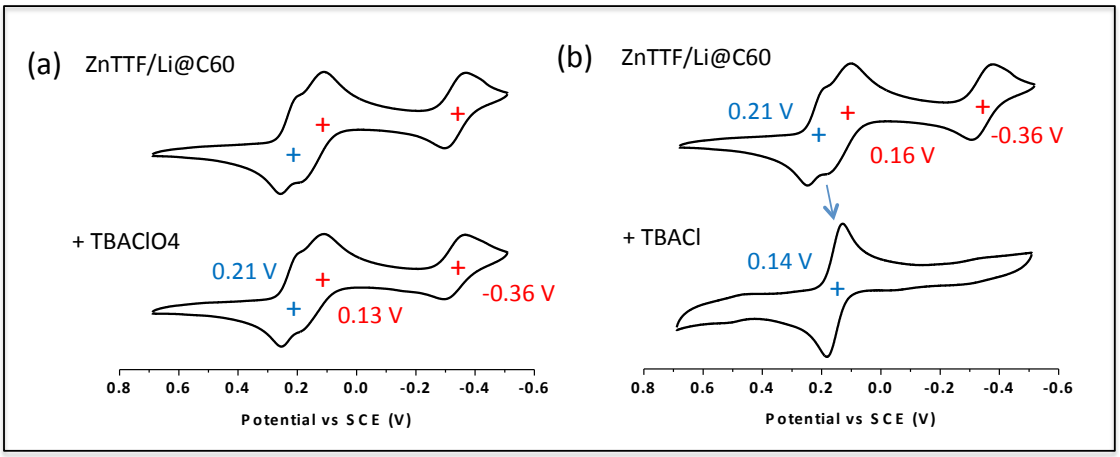

Figure 2.25. The top CVs in both cases show a 1:1 mixture of **ZnTTFP** and $Li^+@C_{60}$, and the bottom shows the same solution after addition of 100 equiv of salt: (a) $TBAClO_4$ and (b) TBACl.

Supporting evidence for anion-induced electron transfer was obtained by absorption spectroscopy. Upon mixing equimolar amounts of **ZnTTFP** and $Li^+@C_{60}$ in PhCN no significant absorption changes were noted. Furthermore, addition of non-coordinating ligand ($TBAClO_4$ or $TBAPF_6$) resulted in no significant change of the optical features of the **ZnTTFP**/$Li^+@C_{60}$ solution (Figure 2.26a). However, the addition of chloride, as TBACl, to the PhCN solution containing **ZnTTFP** and $Li^+@C_{60}$ resulted in a new spectral species, attributed to thermal electron transfer from **ZnTTFP** to $Li^+@C_{60}$. A control experiment in which TBACl was added to **ZnTTFP** without $Li^+@C_{60}$ resulted in no spectral changes (Figure 2.26d), indicating all three species are required for transformation of the absorption spectrum of **ZnTTFP**.

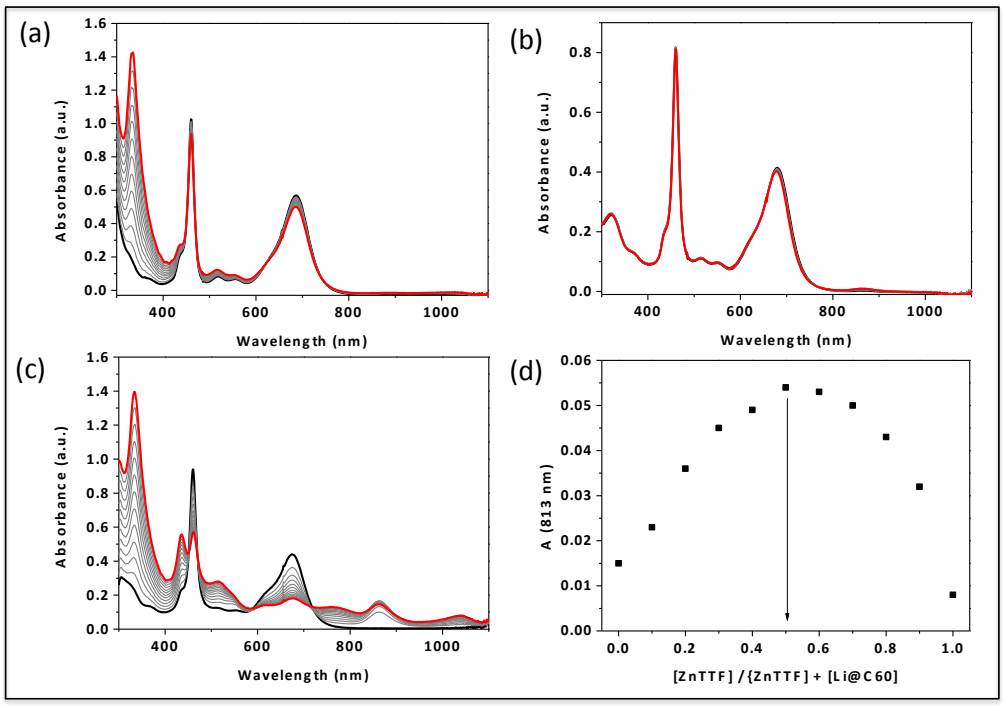

Figure 2.26. (a) Titration of $Li^+@C_{60}$ (up to 15 μM) into a premixed PhCN solution of **ZnTTFP** (5 μM) and $TBAClO_4$ (0.5 mM). (b) Stacked spectra of a 5 μM solution of **ZnTTFP** (black) and after the addition of 100 equiv of TBACl (red) (c) Titration of $Li^+@C_{60}$ (up to 30 μM) into a premixed PhCN solution of **ZnTTFP** (10 μM) and TBACl (1 mM). (d) A Job's plot of the absorbance at 813 nm (a transition ascribed to **ZnTTFP**$^{\bullet+}$) vs. the mole fraction of **ZnTTFP**.

A titration of $Li^+@C_{60}$ into a premixed solution of **ZnTTFP** and TBACl resulted in the generation of spectral features ascribable to **ZnTTFP**$^{\bullet+}$ (λ_{max} = 865 nm) and $Li^+@C_{60}^{\bullet-}$ (λ_{max} = 1035 nm) (Figure 2.26c).[2.55] A 1:1 stoichiometry for the electron transfer between **ZnTTFP** and $Li^+@C_{60}$ in the presence of TBACl was predicted by Job plot analysis (Figure 2.26d). The yield of the electron-transfer products increased with increasing concentration of $Li^+@C_{60}$. The electron-transfer equilibrium constant (K_{et}), determined from the titration shown in Figure 2.26c, is 0.53. Similar spectral changes were seen when Br^- (as TBABr) was used as the coordinating anion. Iodide on the other hand, resulted in direct reduction of $Li^+@C_{60}$ without assistance from **ZnTTFP**.

The thermodynamically driven formation of **ZnTTFP**$^{\bullet+}$ and $Li^+@C_{60}^{\bullet-}$ was further confirmed by EPR spectral analyses. In this study, a premixed solution of **ZnTTFP** (5 μM), $Li^+@C_{60}$ (15 μM), and TBACl (5 mM) was prepared in PhCN. EPR analysis presented a spectrum in which two radical signals were observed in the region typical of organic radicals, superimposed on one another (Figure 2.27). On the basis of independent analyses, the broad signal at g = 2.0036 is assigned to **ZnTTFP**$^{\bullet+}$, while the center sharp signal at g = 2.0022 is ascribed to $Li^+@C_{60}^{\bullet-}$. We thus conclude from CV, absorption spectroscopy and EPR analyses, that electron transfer from **ZnTTFP** to $Li^+@C_{60}$ becomes thermodynamically feasible as the result of the complexation of the Cl^- anion to **ZnTTFP**.

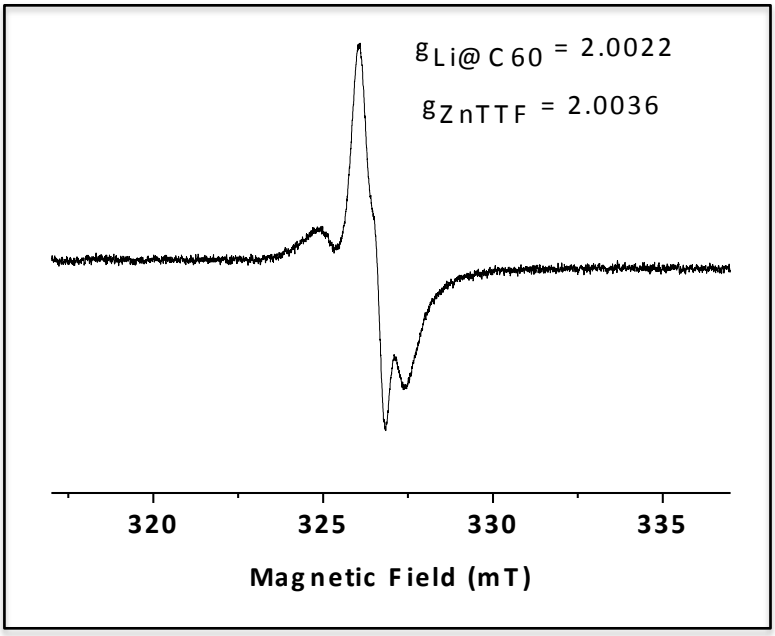

Figure 2.27. EPR spectrum of a PhCN solution of **ZnTTFP** (5 uM) and $Li^+@C_{60}$ (15 uM) recorded in the presence of TBACl (0.5 mM) at 77 K.

The charge separated species induced by the presence of chloride can be reverted to the neutral form via the addition of excess pyridine; presumably this reflects competitive binding to the zinc center and displacement of the Cl^- ligand (Figure 2.28). In this "molecular switch", the thermal electron transfer from **ZnTTFP** to $Li^+@C_{60}$ is "turned on" via the addition of chloride and is "turned off" upon treatment with excess pyridine (Scheme 2.5). This provides an additional level of control over a process that is not reflected in the chemistry of either exTTFs or quinoidal porphyrins.

Scheme 2.5. Reversible thermodynamic electron transfer between **ZnTTFP** and $Li^+@C_{60}$ controlled by axial coordination.

$$\mathbf{ZnTTFP} + Li^+@C_{60} \underset{\mathbf{Pyridine}}{\overset{\mathbf{Cl^-}}{\rightleftharpoons}} [\mathbf{Zn(Cl)TTFP}]^{+\bullet} + [Li@C_{60}]^{\bullet}$$

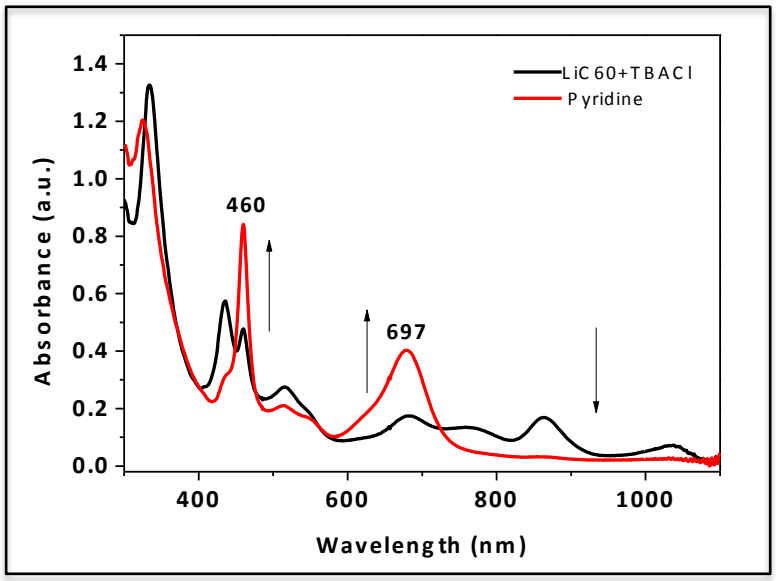

Figure 2.28. Changes in the UV-vis absorption spectrum corresponding to the back electron transfer from $Li^{+}@C_{60}^{\bullet-}$ to **ZnTTFP**$^{\bullet+}$ induced by the addition of pyridine (0.10 mM) to a PhCN solution of **ZnTTFP** (5 mM) and $Li^{+}@C_{60}$ (15 mM) as recorded in the presence of 0.5 mM TBACl at 298 K (the black and red spectra correspond to those obtained before and after the addition of pyridine).

2.7 Interaction of MTTFPs with Fullerenes

Inspired by previous work in which both exTTF based systems (Chapter 1.3)[2.57] and metalated-porphyrins[2.58] have been shown to form tightly bound complexes with fullerenes, we explored the possibilities of similar interactions existing between fullerenes and **MTTFP**s. We surmised that the curved nature of the saddle-shape structure of **MTTFP**s would provide additional faces for π-π stacking interactions with spherical fullerenes. Further, as discussed briefly in section 2.5 of this Chapter, coordination to the metal center by axial ligands is straightforward, as reflected in the interaction of **ZnTTFP** with Lewis bases. This could provide an additional handle for creating discreet complexes with fullerenes.

Fortunately, we were able to grow a crystal of a complex formed between C_{60} and **ZnTTFP** from slow diffusion of hexanes into benzene. The crystals grew as dark

colored plates after being left for several weeks undisturbed at 298 K. X-ray diffraction analysis produced a structure with a 2:1 stoichiometry of C_{60} to **ZnTTFP** (Figure 2.29). Variation in the stoichiometry of the cyrstalization solution anywhere from a 0.5:1 to 4:1, C_{60}:**ZnTTFP** composition yielded, in all cases, crystals of the 2:1 complex. Solving the crystal structure revealed an arrangement wherein sheets of alternating dimers of **ZnTTFP** molecules are interlaced with four C_{60} molecules. Unlike what is seen when various exTTFs are allowed to interact with fullerenes, wherein carbocycle-fullerene interactions dominate, the dithiolidene rings in **ZnTTFP** seem to extend around and thus "hug" the fullerene. This latter arrangement is similar to what is seen with TTF-calix[4]pyrroles. This is most likely the result of the expanded distance between the dithiolidene rings in **ZnTTFP**, which permits the fullerene to sit between the electron-rich thiolidene rings. The molecule of C_{60} that sits within the porphyrinoid is disordered whereas the one outside of the cavity is well ordered. This structure provides initial evidence of a supramolecular interaction between **ZnTTFP** and C_{60}, albeit only in the solid-state.

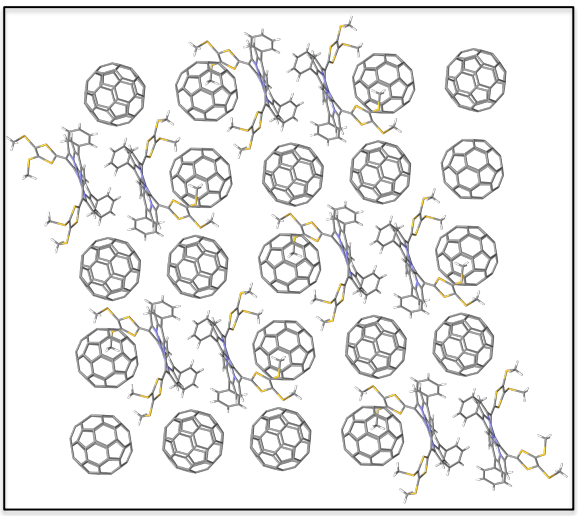

Figure 2.29. View of the packing structure of **ZnTTFP**•$(C_{60})_2$ as determined by X-ray diffraction analysis.

Spectroscopic studies attempting to elucidate the solution-state binding strength and properties were inconclusive. In UV/vis/NIR absorption spectroscopic studies, it was found that the addition of either C_{60} or C_{70} to a solution of **H_2TTFP** or **ZnTTFP** failed to produce appreciable spectral changes over all observed wavelengths. Further, similar titrations monitored by NMR spectroscopy were limited by solubility considerations and a lack of substantial changes in the peaks of the ^{1}H NMR analyses at low concentrations.

In an attempt to increase the amount of π-faces available for interacting with the fullerene and to expand the π-conjugation of the porphyrinoid, we synthesized the dibenzo analouge (**2.27**) of **ZnTTFP**. It was prepared using methodology identical to that outlined for **ZnTTFP**. Disappointingly, in titrations with fullerenes, the optical changes observed with **2.27** were not significantly improved over those seen in similar titrations with **ZnTTFP**. Fitable titration data, albeit far from satisfactory, was only obtained observed in one case: The titration of **2.27** with C_{70} in CH_2Cl_2. In this titration, like before, minimal changes were observed in the Soret bands. The large Q-band diminished slightly in intensity; however, this process was determined to be dynamic, producing a linear plot (absorbance at 666 nm vs. equivalents of C_{70} added), even after the addition of several molar equivalents of C_{70}. Plotting the small band at 816 nm vs. the concentration of C_{70}, gave a parabolic curve that could be fit to a 1:1 binding equation giving a strong association constant (Figure 2.30).

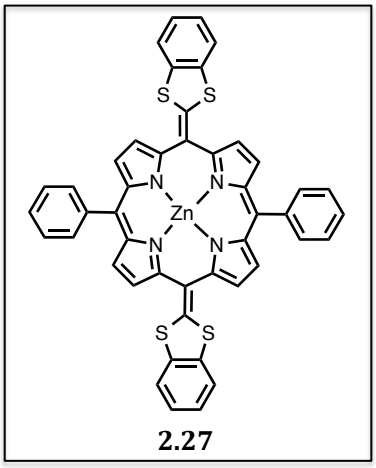

2.27

Unfortunately, no satisfactory Job plots could be constructed by monitoring the spectral changes at this wavelength. Thus, the stoichiometry is in doubt. Moreover, the 816 nm band is assigned to the radical cation of **2.27**, based on a separate absorption spectroscopy titration with magic blue. Thus, analysis at this wavelength would more closely model the interaction of **2.27**$^{\bullet+}$ with C_{70} than neutral **2.27**. Further, if addition of C_{70} facilitates electron transfer, a static 1:1 binding model is inappropriate. Rather, a K_{et} should be calculated. In addtion, the absorption data was found to vary on the purity of the solvent, time elapsed after preparation of the solutions, and from batch to batch of **2.27**. Therefore, this data should be taken with a "grain of salt", and more in depth studies are needed for substantial conclusions to be drawn about the supramolecular interaction in the solution state between **MTTFP**s and pristine fullerenes.

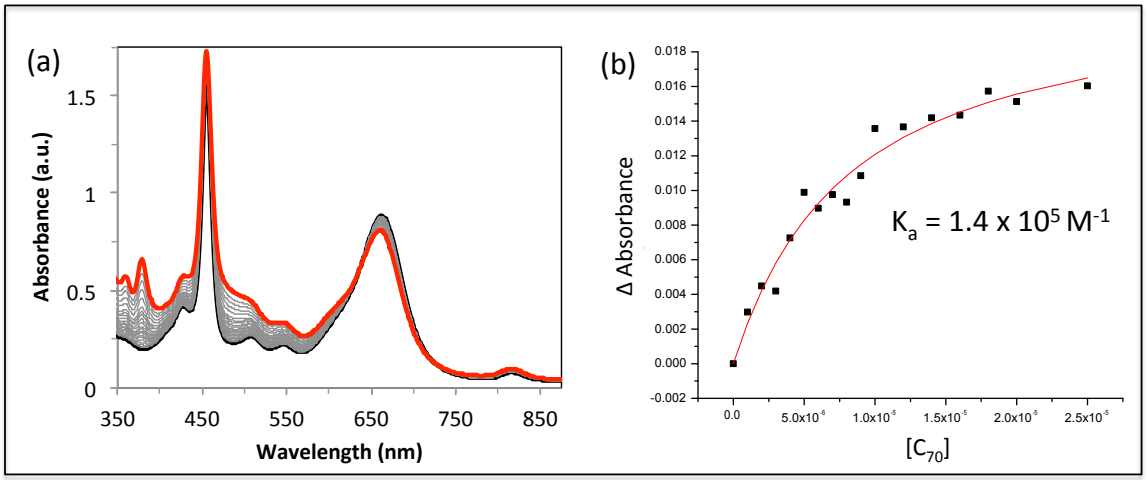

Figure 2.30. (a) Spectral changes associated with the titration of C_{70} into **2.27** (10 uM) in CH_2Cl_2 at 298 K. The original spectrum is traced in black whereas the final (5 equiv C_{70}) is in red. (b) Binding isotherm from the data in (a). The shortcomings of this binding model are discussed in the text.

After failing to obtain significant evidence for binding based on π-π interactions we decided to explore utilizing the coordination ability of the central metal to create

well-defined fullerene/**MTTFP** constructs. From our thermodynamically driven electron transfer studies (Chapter 2.5), we surmised that pyridine forms a strong coordination bond with **ZnTTFP**, displacing chloride to drive back electron transfer. A titration of pyridine into a 10 μM solution of **ZnTTFP** in CH_2Cl_2, resulted in a shift in the λ_{max} of the most intense Q-band (Figure 2.31). Fitting of this data to a 1:1 binding isotherm gave a binding constant of 1.0 x 10^5 M^{-1}. This value is almost two-orders of magnitude stronger than typical of porphyrin binding to pyridine (K_a = 4.17 x 10^3 M^{-1} for 5,10,15,20-tetraphenylporphyrin and pyridine),[2.54] and is in line with the values reported for dioxoporphryins (K_a = 5.2 x 10^5 M^{-1} for a 5,15-dioxo-10,20-bisarylporphyrin (DOBAP) and pyridine) in matching solvents.[2.59] Although

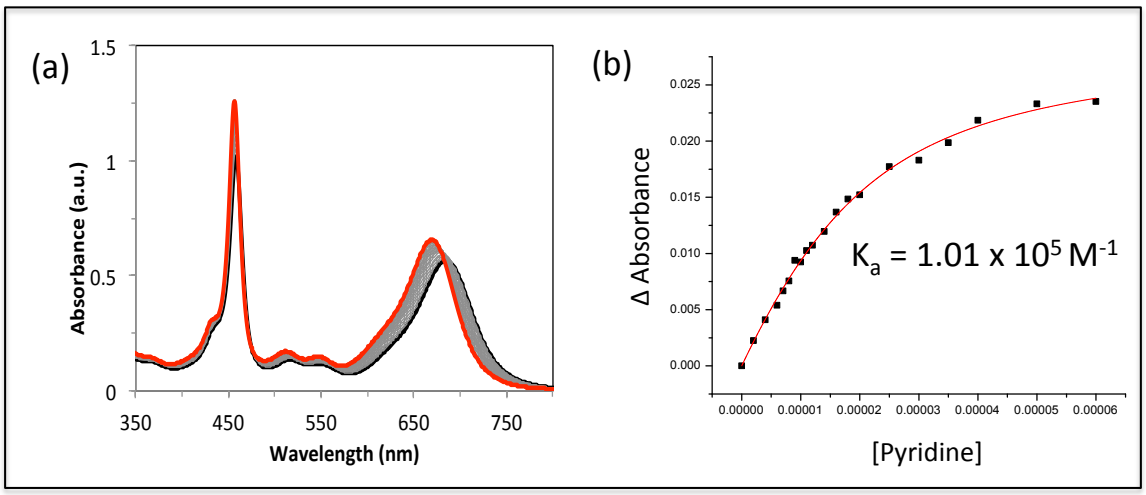

Figure 2.31. (a) Spectral changes associated with the titration of pyridine into a 10 μM solution of **ZnTTFP** in CH_2Cl_2. (b) Fitted binding isotherm obtained from the change in absorption at 649 nm for the data shown in (a).

ZnTTFP is saddle-shaped whereas DOBAPs have been reported as planar, a substantial degradation in axial binding was not seen. This data leads us to suggest that pyridyl compounds should form tightly bound complexes with **ZnTTFP**. Further, the synthetic chemistry of porphyrins is well developed with a variety of

functionalized pyridyl species known, including fullerene-substituted pyridines. We thus predicted that a fullerene-substituted pyridine would serve as a good synthetic handle to bring an electron acceptor into close contact with **ZnTTFP** donors.

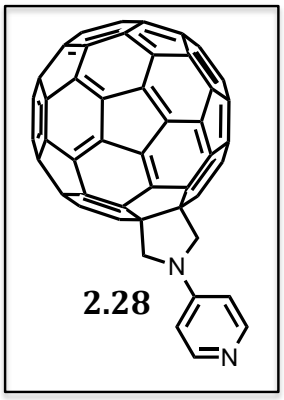

In collaboration with the Tomas Torres group we obtained a sample of pyridine-substituted C_{60} **2.28**. Titration of **2.28** into a 12 μM toluene solution of **ZnTTFP** resulted in significant changes in the intense Q-band (λ_{max} = 684 nm) of **ZnTTFP** (Figure 2.32). Upon saturation, a blue-shift in this band resulted in the λ_{max} of absorption moving to 666 nm. Non-linear least-squares linear regression analysis at 668 nm produced a binding isotherm with a K_a = 1.58 x 10^6 M^{-1}. We take this data as evidence of the solution-state formation of a tightly bound complex between **ZnTTFP** and **2.28**.

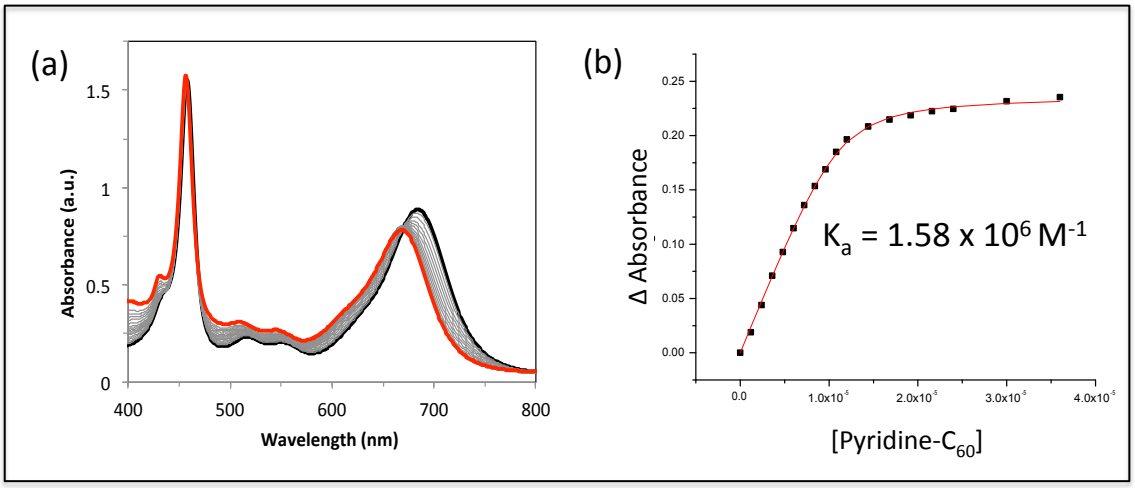

Figure 2.32. (a) Spectral changes observed during the titration of **2.28** into a 12 μM solution of **ZnTTFP** in CH_2Cl_2. (b) Fitted binding isotherm from the change in absorption at 649 nm for the data shown in (a).

As discussed briefly in Chapter 1, the intricate ordering of donors and acceptors is a crucial factor associated with the optimization of OPV devices. While further studies are needed, we have demonstrated that the metal-coordination site in

ZnTTFP provides a handle for bringing complementary electroactive components in close proximity to the electron donor. Needless to say, such coordination chemistry-based ordering is not possible for the ostensibly related exTTF compounds. Currently, advanced photophysical studies, examining the CS state lifetimes of the **ZnTTFP**-**2.28** complex are underway at Yonsei University.

2.8 Summary and Outlook

We have presented a viable synthetic pathway and demonstrated the unique properties of quidoidal π-expanded tetrathiafulvalenes (**MTTFP**s). THis preparative work provides a foundation for in-depth studies of this novel class of molecules. Some analyses have already been carried out. For instance, these compounds are characterized by intense absorption bands throughout the visible region that extend into the NIR region. They also behave (as evidenced by redox and electron transfer studies) as strong electron donors. In this manner, **MTTFP**s integrate the noteworthy properties of exTTFs (excellent two-electron donors) with porphyrins (excellent absorbers of light). They are thus attractive candidates for incorporation into sophisticated organic electronics, such as OPVs.

Through metalation of **H_2TTFP**, we have demonstrated that the absorption characteristics and redox behavior of our system can be easily altered. In principle, this allows both features to be tailored to fit the application of interest. Moreover, there is a plethora of synthetic modifications and substitutions that have been reported for porphyrins that could potentially be applied to **MTTFP**s, hypothetically increasing their diversity multi-fold. Among the more attractive suggestions along these latter lines entail the functionalization with electron withdrawing or donating

groups, adding aqueous or organic solubilizing groups, and modifying the steric bulk of the system.

Additionally, although we have reported the formation of several metal complexes, we have merely scratched the surface of the metals known to coordinate with porphyrins. An obvious extension of this work would include expansion of the **MTTFP** library to include additional metal complexes. Of particular interest is metal-porphyrin species known to exhibit photocatalytic activity (e.g. Co,[2.60] Fe,[2.61] Mn,[2.62] Pd,[2.63] Ru,[2.64] and etc.).[2.65] We have recently achieved the synthesis of **CoTTFP** although to date our studies have been limited. The complex may emerge as a useful water-oxidation catalyst as has previously been reported for Co^{III} porphyrins, although differences in the electronic character of the system exist. An added benefit of **CoTTFP**, is it could potentially remove the need for a Ru-based oxidant as an intermediate in the catalytic cycle, instead the dithiole rings could serve this purpose, assuming they could be regenerated by a sacrificial reductant.

One of the hallmarks of this work is the existence of a post-synthetic control mechanism, namely the ability to fine-tune the redox potential though axial ligand coordination—driving thermodynamic electron transfer between **ZnTTFP-Cl** and $Li^+@C_{60}$. We also found the process can be reversed by administering pyridine to the system and forcing back-electron transfer through competitive binding. The storage of energy in **MTTFP**s through chemical manipulations could allow this compound to find use in the fabrication of organic-based batteries.

An orthogonal area that may warrant exploration involves the use of the anion-induced redox fluctuations that are an inherent feature of **ZnTTFP** to design

synthetic muscle mimics. Human muscles are contracted by the release of calcium ions into the cytoplasm which bind to troponin-tropomyosin molecules. This frees up sites on actin that can cross-link with myosin and contract the muscle. Removal of calcium, by calcium specific pumps, reverses the process and relaxes the muscle. We envision the possibility of similar ion-controlled muscle (albeit anion-controlled), fabricated from polymeric fibers of **ZnTTFP** (Figure 2.33). From the crystals structures of **MTTFP**s, we have found that in the neutral state a saddle-shaped structure is predominant, and conversely upon oxidation the core planarizes. As a result of the core transformation, the dithiole rings are forced apart, elongating the distance between their end groups. By linking **ZnTTFP** through the dithiole moieties, a polymeric material could be realized that, in principle, should elongate upon two-electron oxidation. In theory, the oxidized material would then mimic a "relaxed" muscle and upon reduction to the neutral state, the muscle would "contract". From here, it is only a small reach to consider, at specific potentials (e.g., 0.17 V vs. SCE) a state could be engineered in which the presence of chloride would cause the muscle to adopt a "relaxed" state and upon removal of chloride the muscle would "contract".

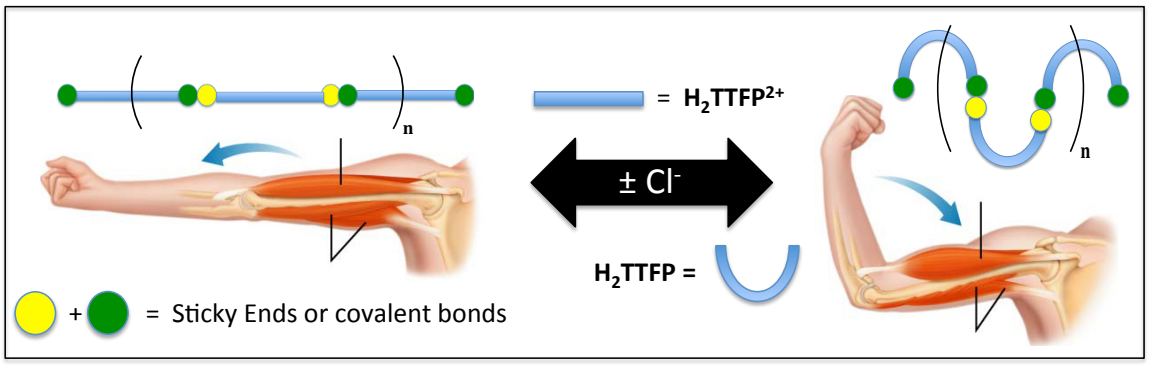

Figure 2.33. Proposed mechanism for a putative artificial muscle composed of fibers made from **H_2TTFP**.

Another intriguing property of **MTTFP**s (and in particular **H_2TTFP** and **H_2TTFP^{2+}**) is their high two-photon absorption coefficients. **H_2TTFP** and **H_2TTFP^{2+}** outperform previously reported quinoidal and normal unexpanded porphyrin samples by factors of 3:1 and >10:1, respectively. Further, improvement in the TPA absorption parameters could see these materials used as optical limiters or second harmonic generators. One method to enhance the non-linear optical properties of compounds is to create species with a high degree of polarization. Thus, replacement of the *meso*-phenyl groups by electron donating or withdrawing fragments, such as in targets **2.29** or **2.30**, would create enhanced polarization, and possibly lead to improved TPA cross-sections. Similarly, substitution of the *β*-positions of the pyrrole rings with electron withdrawing halogens (**2.31**) could have a constructive effect. We have begun work to prepare both **2.29** and **2.30**, and currently the requisite porphyrins precursors are in hand.

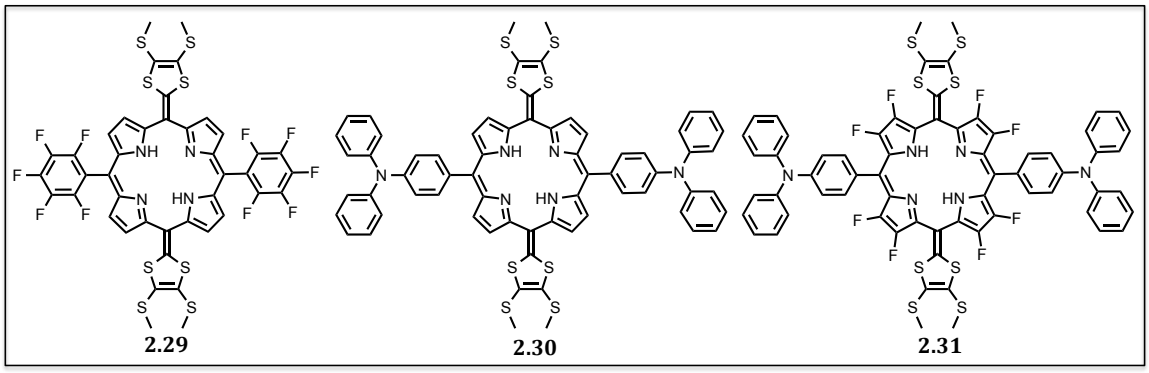

Finally, it is suggested that further effort be devoted to studying the interaction of **MTTFP**s with electron acceptors, especially fullerenes. Although a crystal structure was obtained for the 2:1 co-crystallized product of **ZnTTFP** and C_{60} (*vide supra*), solution based studies involving this mixture proved inconclusive. Among anthracene-based exTTFs, tweezer-like systems (e.g., **1.33 – 1.35**) and macrocycles

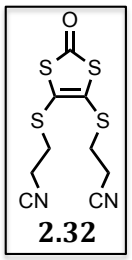

2.32

made of the quinoidal compounds were found to greatly enhance the binding with fullerenes (Chapter 1.4). To date, we have been able to couple bis(cyanoethyl) protected thiones (**2.32**) with diketone **2.26** (although they require relatively high temperatures to couple), and plan to make pinchers and/or macrocycles from this compound though simple S_N2 reactions of the deprotected thiolates. In this manner, it should be possible to study the chelate effect (pinchers) and how preorganization of the binding pocket (macrocycles) serves to modulate the affinity for fullerenes.

We were able to unambiguously characterize the binding interactions between pyridyl-C_{60} and **ZnTTFP** *via* a coordinative bond. Based on UV/vis/NIR spectroscopy, the association in toluene strong, with calculated constants exceeding 10^6 M^{-1}. Current photophysical work with this latter complex is underway, and if favorable CS lifetimes are observed further efforts devoted to device fabrication would be warranted.

In summary, **MTTFP**s have been synthesized. It is hoped these hybrid macrocycles will emerge as an exhilarating new class of electron donors with exceptional optical properties. Further dedicated work in the area may serve to elevate this compound to a status in line with its exTTF and porphyrin forebearers in terms of interest and utility. Several potential courses for the near-term future studies of this class of compound have been laid out and discussed, although this is not to be taken as an exhaustive list. Many more intriguing possibilities are available, such as using **MTTFP**s as redox switchable G-tetrad intercalators (cationic porphyrins have been shown to form strong complexes with G-tetrads), building

metal-organic frameworks with fluctuating pore sizes, and utilizing the strong coordinating ability of the metal center to create complex molecular architectures in analogy to what has been done by Harry Anderson and others. However, dedicated effort beyond what has been described here will be needed to test these various possibilities.

2.9 Chapter 2 References

1. Battersby, A.R. *Nat. Prod. Rep.*, **2000**, 17, 507.
2. Barber, J. *Phil. Trans. R. Soc. A.* **2007**, 365, 1007
3. Makarieva, A.M.; Gorshkov, V.G.; Li, B.-L.. *Ecological Complexity*, **2008**, 281
4. Hall, D.O.; Rao, K.K. *Photosynthesis*. Cambridge University Press, Cambridge, 1999.
5. Yella, A.; Lee, H.-W.; Tsao, H.N.; Yi, C.; Chandiran, A.K.; Nazeerudding, M.K.; Diau, E.W.; Yeh, C.-Y.; Zakeeruddin, S.M.; Grätzel, M. *Science*, **2011**, 334, 629.
6. Becher, J.; Brimert, T.; Jeppesen, J.O.; Pedersen, J.Z.; Zubarev, R.; Bjùrnholm, T.; Reitzel, N.; Jensen, T.R.; Kjaer, K,; Levillain, E. *Angew. Chem. Int. Ed.* **2001**, 40, 2497
7. (a) Jeppesen, J.O.; Takimiya, K.; Jensen, F.; Becher, J. *Org. Lett.* **1999**, 1, 1291 (b) Jeppesen, J.O.; Takimiya, K.; Jensen, F.; Brimert, T.; Nielsen, K.; Thorup, N.; Becher, J. *J. Org. Chem.* **2000**, 65, 5784.
8. Wudl, F.; Smith, G. M.; Hufnagel, E. J. *J. Chem. Soc. Chem. Commun.* **1970**, 1453.
9. Li, H.; Jeppesen, J.O.; Levillain, E.; Becher, J. *Chem Commun.* **2003**, 846
10. Nielsen, K. A.; Levillain, E.; Lynch, V. M.; Sessler, J. L.; Jeppesen, J. O. *Chem. Eur. J.,* **2009**, 15, 506.
11. Replacement of the acid catalyst (from TsOH to TFA) was found to be essential to eliminating contamination by radicals, allowing **2.X** to be studied in further detail along with the other novel compounds
12. Jana, A.; Ishida, M.; Kwak, K.; Sung, Y. M.; Kim, D. S.; Lynch, V. M.; Lee, D.; Kim. D; Sessler, J. L. *Chem. Eur. J.* **2013**, 19, 338
13. Sadaike, S.; Takimiya, K.; Aso, Y.; Otsubo, T. *Tetrahedron Lett.* **2003**, 44, 161
14. Liddell, P. A.; Kodis, G.; de la Garza, L.; Bahr, J. L.; Moore, A. L.; Moore, T. A.; Gust, D. *Helv. Chim. Acta.* **2001**, 84, 2765
15. (a)Bahr, J. L.; Kuciauskas, D.; Liddell, P.A.; Moore, A. L.; Moore, T. A.; Gust, D. *J. Photochem. Photobiol.* **2000**, 72, 598. (b) Carbonera, D.; Valentin, M. D.; Corvaja, C.; Agostini, G.; Giacometti, G.; Liddell, P.A.; Kuciauskas, D.; Moore, A.L.; Moore, T.A.; Gust, D. *J. Am. Chem. Soc.* **1998**, 120, 4398. (c) Kuciauskas, D.; Liddell, P.A.; Moore, T.A.; Moore, A.L.; Gust, D. *Recent Advances in the Chemistry and Physics of Fullerenes and Related Materials*. Ed. Kadish, K. M.; Ruoff, R.S., The Electrochemical Society, Pennington, NJ, 1998, Vol. 6 (d) Kuciauskcas, D.; Liddell, P.A.; Lin, S.; Stone, S.; Moore, A.L.; Moore, T.A.; Gust, D. *J. Am. Chem. Soc.* **1998**, 120, 10880.
16. Di Valentin, M.; Bisol, A.; Agostini, G.; Liddell, P.A.; Kodis, G.; Moore, A.L.; Moore, T.A.; Gust, D.; Carbonera, D. *J. Phys. Chem. B* **2005**, 109, 14401.
17. Saha, S.; Johansson, E.; Flood, A.H.; Tseng, H.-R.; Zink, J.I.; Stoddart, J.F. *Chem. Eur. J.* **2005**, 6846.
18. Saha, S.; Flood, A.H.; Stoddart, J.F.; Impellizzeri, S.; Silvi, S.; Venturi, M.; Credi. A. *J. Am. Chem. Soc.* **2007**, 129, 12159.
19. Arnold, D.P.; Blok, J. *Coord. Chem. Rev.* **2004**, 248, 3-4, 299.
20. Xiao, X.; Xu, W.; Zhang, D.; Xu, H.; Lu, H.; Zhu, D. *J. Mater. Chem.* **2005**, 15, 2557
21. Blower, M.A.; Bryce, M.R.; Devonport, W. *Adv. Mater.* **1996**, 8, 1, 63

22. Cook, M.J.; Cooke, G.; Jafari-Fini, A. *Chem. Commun.*, **1996**, 1925
23. Loosli, C.; Jia, C.; Liu, S.-X.; Haas, M.; Dias. M.; Levillain, E.; Neels, A.; Labat, G.; Hauser, A.; Decurtins, S. *J. Org. Chem.* **2005**, 70, 4988.
24. Farren, C.; Fitzgerald, S.; Beeby, A.; Bryce, M. R. *Chem. Commun*. **2002**, 572.
25. Donders, C.A.; Liu, S.-X.; Loosli, C.; Sanguinet, L.; Neels, A.; Decurtins, S. *Tetrahedron*, **2006**, 62, 3543
26. Kimura, T.; Watanabe, D.; Namauo, T. *Heteroat. Chem.* **2011**, 22, 605
27. Sly, J.; Kasák, P.; Gomar-Nadal, E.; Rovira, C.; Górriz, L.; Thordarson, P.; Amabilino, D. B.; Rowan, A. E.; Nolte, R. J. M. *Chem Commun*. **2005**, 1255.
28. (a) Van Nostrum, C.F.; Picken, S.J.; Schouten, A.-J.; Nolte, R.J.M. *J. Am. Chem. Soc.* **1995**, 117, 9957. (b) Van Nostrum, C.F. *Adv. Mater.* **1996**, 8, 1027. (c) Samori, P.; Engelkamp, H.; de Witte, P.; Rowan, A.E.; Nolte, R.J.M.; Rabe, J.P. *Angew. Chem. Int. Ed.* **2001**, 2348. (d) Engelkamp, H.; Middelbeek, S.; Nolte, R.J.M. *Science,* **1999**, 284, 785.
29. Wang, C.; Bryce, M.R.; Batsanov, A.S.; Stanley, C.F.; Beeby, A.; Howard, J.A.K. *J. Chem. Soc., Perkin Trans. 2,* **1997**, 1671
30. Farren, C.; Christensen, C.A.; Fitzgerald, S.; Bryce, M.R.; Beeby, A. *J. Org. Chem.*, **2002**, 67, 26, 9131
31. Shimizu, S.; Yamazaki, Y.; Kobayashi, N. *Chem. Eur. J.* **2013**, DOI: 10.1002/chem.201300709
32. Romero-Nieto, C.; Medina, A.; Molina-Ontoria, A.; Claessens, C.G.; Echegoyen, L.; Martín, N.; Torren, T.; Guldi, D.M. *Chem. Commun.*, **2012**, 48, 4953
33. (a) Saito, S.; Osuka, A. *Angew. Chem. Int. Ed.* **2011**, 50, 4342-4373. (b) Osuka, A.; Saito, S. *Chem. Commun.* **2011**, 47, 4330-4339. (c) Roznyatovskiy, V.V.; Lee, C.-H.; Sessler, J. L. *Chem. Soc. Rev.* **2013**, 42, 1921-1933.
34. Ishida, M.; Kim, S.-J.; Preihs, C.; Ohkubo, K.; Lim, J. M.; Lee, B. S.; Park, J. S.; Lynch, V. M.; Roznyatovskiy, V. V.; Sarma, T.; Panda, P. K.; Lee, C.-H.; Fukuzumi, S.; Kim, D.; Sessler, J. L. *Nat. Chem*. **2013**, *5*, 15-20.
35. (a) Lee, C.-H.; Roznyatovskiy, V. V.; Hong, S.-L.; Sessler, J. L. in *Handbook of Porphyin Science,* Kadish, K.M.; Smith, K. M.; Guilard, R. Eds.; World Scientific, Singapore, 2011, pp 197-252. (b)
36. Plater, J.M.; Aiken, S.; Bourhill, G. *Tetrahedron,* **2002**, 2405.
37. Lahaye, D.; Muthukumaran, K.; Hung, C-H.; Gryko, D; Reboucas, J. S.; Spasojevic, I.; Batinic-Haberle, I.; Lindsey, J. S. *Bioorg. Med. Chem.* **2007**, *15*, 7066-6086.
38. (a) Fischer, H.; Treibs, A. *Annalen* **1927**, *457*, 209-248. (b) Inhoffen, H. H.; Fuhrhop, J. R.; von der Haar, F. *Justus Liebigs Ann. Chem.* **1966**, *700*, 92-105.
39. Cunningham, K. L.; McNett, K. M.; Pierce, R. A.; Davis, K. A.; Harris, H. H.; Falck, D. M.; McMillin, D. R. *Inorg. Chem*. **1997**, *36*, 608-613.
40. Although crystals were obtained for **NiTTFP** as dark brown cubes from diffusion of diethylether into CH_2Cl_2, they did not defract well enough to produce a useful data set.
41. Zeng, W.; Lee, B. S.; Sung, Y. M.; Huang, K.-W.; Li, Y.; Kim, D.; Wu, J. *Chem. Commun*., **2012**, 48, 7684-7686.

42. Similar conclusions were drawn in the case of simple exTTF derivatives: e.g. Diaz, M. C.; Illescas, B. M.; Martin, N.; Viruela, R.; Viruela, P. M.; Orti, E.; Brede, O.; Zilbermann, I.; Guldi, D. M. *Chem.–Eur. J.* **2004**, 10, 2067-2077.
43. TPA cross-section values referenced for metalated tetraphenylporphyrins (TPP) have been reported as follows: For ZnTPP: (a) Drobizhev, M.; Karotki, A.; Kruk, M.; Rebane, A. *Chem. Phys. Lett.* **2002**, *355*, 175-182; for NiTPP: (b) Yoon, M.-C.; Noh, S.-B.; Tsuda, A.; Nakamura, Y.; Osuka, A.; Kim, D. *J. Am. Chem. Soc.* **2007**, 129, 10080-10081; for CuTPP: (c) Morone, M.; Beverina, L.; Abbotto, A.; Silvestri, F.; Collini, E.; Ferrante, C.; Bozio, R.; Pagani, G.A. *Org. Lett.* **2006**, 8, 2719-2722.
44. Denuault, G.; Mirkin, M. V.; Bard, A. J. *J. Electroanal. Chem.* **1991**, 308, 27.
45. Schleyer, P.vR.; Maerker, C.; Dransfeld, A.; Jiao, H.; Eikema Hommes, N.J.R. *J. Am. Chem. Soc.* **1996**, 118, 6317
46. Goutermann, M. in *The Porphyrins*, Dolphin, D., Ed.; Academic: New York, 1978.
47. Typical metal-free porphyrin lifetimes are on the order of nano seconds.
48. The choice of the counter anions (OTf^-, BF_4^- or ClO_4^-) does not appear to affect significantly the properties of dication $\mathbf{H_2TTFP^{2+}}$.
49. The radical cation form of "exTTF" quickly disproportionates in the same solvent: Guldi, G. M.; Sanchez, L.; Martin, N. *J. Phys. Chem. B* **2001**, 105, 7139-7144.
50. (a) Shen, Y.; Ryde, U. *Chem. Eur. J.* **2005**, *11*, 1549. (b) Bain-Ackerman, M. J.; Lavallee, D. K. *Inorg. Chem.* **1979**, 18, 3358.
51. Todres, Z. V. *Ion-Radical Organic Chemistry: Principles and Applications,* 2nd ed*.;* CRC Press: Boca Raton, 2009.
52. Calculations reveal that the spin density on the nitrogen atoms of $\mathbf{H_2TTFP^{\bullet+}}$ is relatively delocalized. This is consistent with the absence of appreciable hyperfine coupling seen in the EPR spectrum.
53. Frere, P.; Allain, M.; Elandaloussi, E. H.; Levillain, E.; Sauvage, F.-X.; Riou, A.; Roncali, J. *Chem.–Eur. J.* **2002**, *8*, 784-792.
54. (a) Kadish, K.M.; Shiue, L.R.; Rhodes, R.K.; Bottomley, L.A. *Inorg. Chem.* **1981**, 20, 1274. (b) Kadish, K.M.; Shiue, L.R. *Inorg. Chem.* **1982**, 21, 3623
55. (a) Kawashima, Y.; Ohkubo, K.; Fukuzumi, S. *J. Phys. Chem. A* **2012**, *116*, 8942−8948. (b) Fukuzumi, S.; Ohkubo, K.; Kawashima, Y.; Kim, D. S.; Park, J. S.; Jana, A.; Lynch, V. M.; Kim, D.; Sessler, J. L. *J. Am. Chem. Soc*. **2011**, *133*, 15938–15941.
56. A significant change in the second redox peak of $Li@C_{60}$ was also noted. However, a DPV analysis of this region revealed a redox process centered around 0.35 V.
57. Pérez, E.; Martín, N. *Chem. Soc. Rev.* **2008**, 37, 1512
58. Canevet, D.; Pérez, E.; Martín, N. *Ang. Chem. Int. Ed.* **2011**, 50, 9248
59. Clyde-Watson, Z.; Bampos, N.; Sander, J.K.M. *New J. Chem.* **1998**, 1135
60. Nakazono, T.; Parent, A.R.; Sakai, K. *Chem. Commun.* **2013**, 49, 6325
61. (a) Fujiwara, K,; Kurahashi, T.; Matsubara, S. *J. Am. Chem. Soc.* **2012**, 134, 5512 (b) Singh, A.; Agarwala, A.; Kamaraj, K.; Bandyopadhay, D. *Inorg. Chim. Acta.* **2011**, 372, 295

62. Srour, H.; Le Maux, P.; Simonneaus, G.; *Inorg. Chem.* **2012**, 51, 5850
63. Kostas, I.D.; Coutsolelos, A.G.; Charalambidis, G.; Skondra, A. *Tetrahedron Lett.* **2007**, 48, 6688
64. Cenini, S.; Gallo, E.; Caselli, A.; Ragaini, F.; Fantauzzi, S.; Piangiolino, C. *Coord. Chem. Rev.* **2006**, 250, 1234.
65. *Handbook of Porphyrin Science*. *With Applications to Chemistry, Physics, Materials Science, Engineering, Biology and Medicine — Volume 21: Catalysis*. Ed. Kadish, K.M.; Smith, K.M.; Guilard, R. 2012 World Scientific. Hackensack, NJ.

Chapter 3

Supramolecular Interactions of $ZnTTFP^{2+}$ with Sulfonated Porphyrins

3.1 Introduction

The supramolecular ordering and nanopatterning of organic electron donors and acceptors has received increasing attention in the last decade. The growing interest in the field reflects the need for nanopatterned structures in a variety of important application areas, including catalysis, solar cells, sensors, organic electronics, etc.[3.1] Of particular interest are self-assembled systems, which reduce the cost and time required to prepare the requisite patterned materials.

Nanostructures of organic donors and acceptors that also absorb light efficiently, offer additional opportunities. These include being able to synthetically mimic photosynthetic pathways and/or produce electrical energy in organic based solar cells. As a class, porphyrin dyes are well-suited for incorporation into functional nanocomposites due to their excellent photophysical properties, diversity of known structures, number of metal complexes reported, ability to support supramolecular interactions, as well as the generally planar conformations.[3.2] Nature utilizes porphyrinoids, in intricately patterned arrangements, to efficiently harness energy from the sun and transform it into chemical energy. In fact, nanorods of bacteriochloropyll are among the most prevalent of the known harvesters of light.[3.3] Thus, producing self-assembled porphyrin-based structures with efficient light-

harvesting ability and long-lived charge separated (CS) lifetimes is of primary interest. Achieving this goal efficiently is expected to lead to improved materials for organic photovoltaic devices.

This Chapter details the ionic self-assembly of an all-porphyrin donor-acceptor complex. Specifically, it will be shown that the cationic, two-electron oxidized form of **ZnTTFP** interacts with the anionic sulfonated tetraphenylporphyrin **MTPPS^{4-}** (M = H_2 and Zn) in a 2:1 stoichiometry, respectively. Binding studies based on absorption spectroscopy, emission spectroscopy, and isothermal titration calorimetry provide evidence for moderate association constants between the porphyrins. Additionally, an X-ray crystal structure (solved by Dr. Vince Lynch) is reported. This structure confirms the association and provides insights into the structure of the ionic self-assembled complex.

The groups of Prof. Dongho Kim and Prof. Shunichi Fukuzumi examined the advanced photophysical properties of the complex. Specifically, the lifetimes of the charge separated (CS) states were examined by transient absorption spectroscopy. Initial experiments gave evidence of a long-lived (on the order of ms) CS lifetime in the Fukuzumi group. However, the Kim group was not able to duplicate these findings. Currently, efforts to resolve the discrepancies in the recorded lifetimes are ongoing.

3.2 Porphyrin-Porphyrin Ionic Complexes

The exceptional photophysical properties of porphyrins have prompted a wide-body of literature to be devoted to them. In the last quarter century, the fabrication of porphyrin-donor/acceptor conjugates has attracted considerable research

efforts. Although some porphyrins have been reported to act as electron acceptors (e.g., Sn-porphyrins and pheophytin), generally, porphyrins are used as electron donors due to their suitable HOMO energy levels. A variety of electron acceptors (e.g., fullerenes,[3.4] perylenediamides,[3.5] quinoines,[3.6] etc.[3.7]) have been used to create porphyrin-electron acceptor systems. As varied as the components making up the donor-acceptor ensembles, are the methods employed to bring the electroactive pieces together (e.g. hydrogen bonding,[3.8] axial metal coordination,[3.9] π-π stacking,[3.10] covalent bonding,[3.11] etc.). Most of these approaches have been reviewed (see references 3.4 – 3.11) and are considered outside of the scope of this Chapter. However, approaches based on electrostatic interactions are directly relevant to the strategy being pursued by the author. A brief overview is thus appropriate here.

Recently, electrostatic interactions have reemerged as a viable supramolecular "handle" for creating functional scaffolds.[3.12] Electrostatic interactions have several advantageous characteristics. For instance, they are relatively strong (but not too strong), easy to incorporate into a system, lead to reliable bonding, and can be used in concert with other supramolecular interactions. Electrostatic interactions have been used to bring oppositely charged porphyrin complexes in close contact with one another. This phenomenon was first reported by the Linschitz group in 1985.[3.13] Binding between anionic and cationic porphyrins occurs in a variety of solvents, including aqueous systems. The association constants have been estimated to be on the order of 10^7 M^{-1} for tetraanionic porphyrin **MTPPS**$^{4-}$ mixed with tetracationic porphyrin **M3.3** (drawn below).[3.14] Since the initial report, ionic

porphyrin complexes have been used in a variety of applications, including: photosynthetic mimics, photocatalyis,[3.15] electrocatalysis,[3.16] photo-induced electron transfer at interfaces,[3.17] photoactive polymers,[3.18] and supramolecular porphyrin-dye arrays,[3.19] among others. Further, in the last decade this method has been utilized to create donor-acceptor complexes based exclusively on porphyrins. Several of these systems display interesting physical and chemical properties and are discussed below.

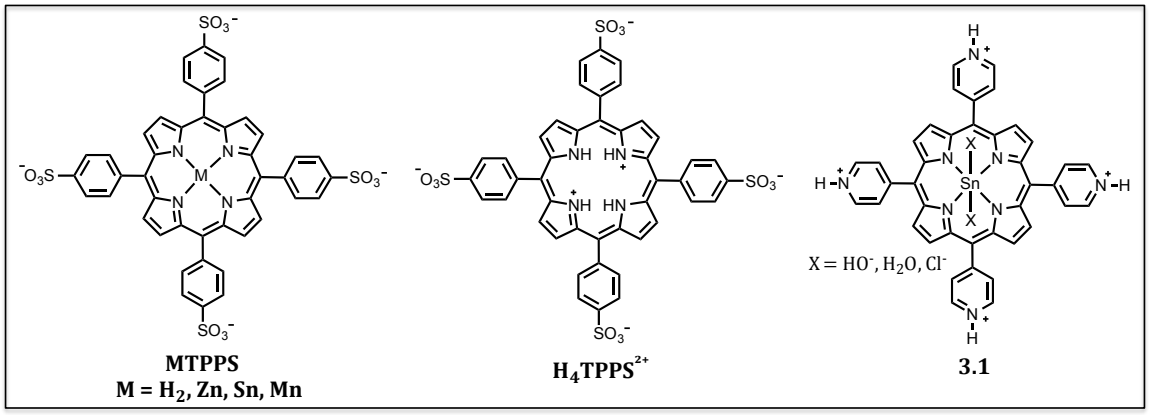

In 2004, the first example of an ionic porphyrin donor-porphyrin acceptor supramolecular complex was detailed by the Shelnutt group.[3.20] In this seminal work, the anionic sulfonated tetraphenylporphyrin **H_2TPPS**$^{4-}$ and a cationic 4-pyridyl tin porphyrin **3.1** were the building blocks (tectons) studied. The porphyrins were combined in aqueous solutions at pH 2.0. At this pH, the most prominent protonation states of the porphyrins are **H_4TPPS**$^{2-}$ and **3.1**$^{4.5+}$ (the "1/2" charge in 3.5^{4+} is reflective of a 1:1 mixture of 3.1^{4+} and 3.1^{5+} based on the protonation state of the axial ligand, X = OH or H_2O). After the aqueous solutions of these two components were allowed to stand for 72 h in the dark, around 90% of the material had formed nanotubes. Transmission emission microscope (TEM)

images revealed the nanotubes were micrometers in length and had an average diameter of 60 nm (Figure 3.1). Tubes imaged in a vertical orientation were found to have walls approximately 20 nm thick, and hollow centers (inset, Figure 3.1). These images confirmed the tube-like (as opposed to rod-like) structure of the complexes.

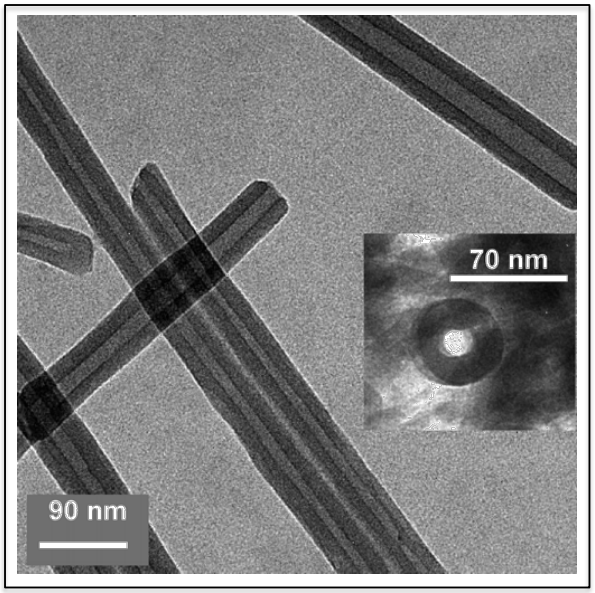

Figure 3.1. A TEM image of self-assembled porphyrin nanotubes produced by mixing aqueous solutions of $\mathbf{H_4TPPS}^{2-}$ and $\mathbf{3.1}^{4.5+}$ at pH 2.0. Tubes formed upon standing for 72 h. The inset shows a tube in the vertical orientation, allowing the hollow center to be clearly seen. Figure reproduced with permission from *J. Am. Chem. Soc.* **2004**, 15954. Copyright 2004 American Chemical Society.

On the basis of ultraviolet visible (UV/vis) absorption spectroscopic studies, the ratio of $\mathbf{H_4TPPS}^{2-}$ to $\mathbf{3.1}^{4.5+}$ was found to vary from 2-2.5 to 1 within the nanotubes. The ratio of the porphyrins in the nanotubes is thought to reflect the need to balance opposite charges and form overall neutral structures. Therefore, the overall charges of the tectons, at a specific pH, are predicted to dictate the resultant complex stoichiometry. This hypothesis was supported by two sets of observations. First, altering the pH of the solution (to pH =1 or 3), and subsequently the protonation

state of the porphyrins, resulted in no nanotube formation. Second, altering the stoichiometric equivalents of the initial porphyrin solutions resulted in nanotubes with identical ratios of $\mathbf{H_4TPPS}^{2-}$ to $\mathbf{3.1}^{4.5+}$. These findings are taken as additional evidence that nanoscale self-assembly is occurring in this system.

Several other intriguing properties of the nanotubes were revealed in this work. For example, changing from 4-pyridyl to 3-pyridyl tin porphyrins resulted in the formation of nanotubes of smaller diameters (35 nm compared to 60 nm). The change in the pyridyl positioning is thought to alter the alignment and angle of the electrostatic bonds, influencing the overall structure of the complex. When a 2-pyridyl porphyrin was used, no nanotube formation was seen. Altering the identity of the metal coordinated porphyrin also had an affect on the formation of nanotubes. Specifically, it was found that axial ligation was key to the self-assembly of the tube structures. Upon replacement of the Sn(IV) metal with other six-coordinate metals (e.g. Fe^{3+}, Co^{3+}, VO^{2+}) tubes were obtained in a similar manner. However, the exchange of Sn(IV) with metals unable to accommodate axial ligands (e.g., Cu) resulted in no nanotube formation.

Finally, exposing the original nanotubes (made from $\mathbf{H_4TPPS}^{2-}$ and $\mathbf{3.1}^{4.5+}$) to light was found to collapse the tubes into rod-like structures. More interestingly, the removal of light led to self-healing, restoring the tubular structure of the initial complex. This effect is thought to reflect the disturbance of the charge balance through either photo-induced charge transfer, or nonradiative heating of the complex. This results in a reduction of the rigidity of the structure and a collapse of the tubes.

In a later report,[3.21] the photocatalytic activity of the above nanotubes was reported. In aqueous solutions, nanotubes made from **H$_4$TPPS**$^{2-}$ and **3.1**$^{4.5+}$ were combined with non-porphyrin Au(I) or Pt(II) metal complexes in the presence of ascorbic acid (as the terminal electron donor). Upon exposure to light, the photocatalytic reduction of gold and platinum metals was observed. Further, the metal was deposited onto the nanotubes (Figure 3.2). When gold was reduced, the resulting metal was found to fill the inner cavity of the porphyrin nanotube, forming a long and continuous nanowire. Large spheres of gold formed at the ends of the tubes, extending beyond the diameter of the tubes. The tube could be dissolved away by adding NaOH, leaving just the gold nanowire. On the other hand, platinum reduction led to dendritic globules of platinum nanoparticles deposited on the sides of the tubes. After deposition, the platinum dendrite-nanotube complex was found to reduce water photocatalyticly, producing hydrogen gas.

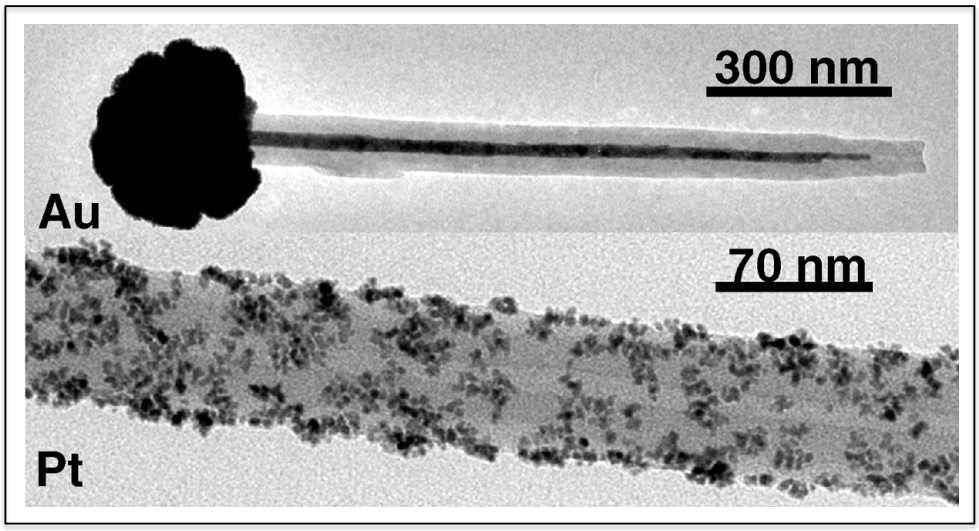

Figure 3.2. TEM images of the deposition of gold (top) and platinum (bottom) onto porphyrin nanotubes made from **H$_4$TPPS**$^{2-}$ and **3.1**$^{4.5+}$. The deposition proceeds by photocatalytic reduction of the metal cations by the nanotubes. This Figure was reproduced with permission from *J. Am. Chem. Soc.* **2004**, 16720. Copyright 2004 American Chemical Society.

In 2010, the Shelnutt group reported on the facile self-assembly of **MTPPS**$^{4-}$ with hydroxyethyl-substituted pyridyl porphyrins **3.2**$^{4+}$.[3.22] The nanostructures formed had a clover shape with four distinct "leafs" (Figure 3.3) and are considered to be biomorphs (mimics of living structures). The formation of the "clovers" was found to be very rapid. Mature clovers were observed by scanning electron microscope (SEM), with the images being recorded within five minutes of mixing the component porphyrins in an aqueous solution. Unlike the previously discussed nanorods, the clover structures were found to be a 1:1 mixture of cation **3.2**$^{4+}$ and anion **MTPPS**$^{4-}$ for all metal combinations studied.

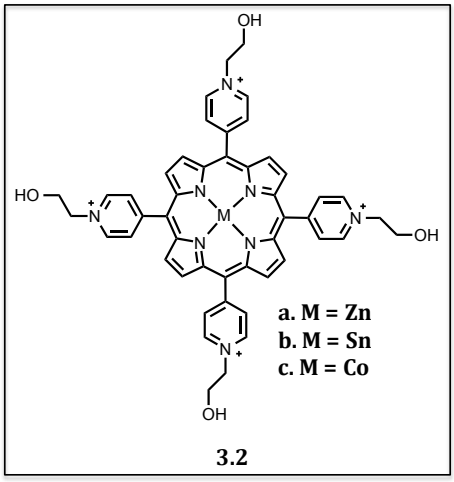

3.2

The scope of porphyrin-metal complexes suitable for clover formation was explored. Zinc(II) and tin(IV) metal complexes of **3.2**$^{4+}$ and **MTPPS**$^{4-}$ led to clover formation in all possible combinations of these metals (i.e. Zn-Zn, Zn-Sn, Sn-Zn, Sn-Sn). Additionally, **SnTPPS-3.2c** and **Mn(III)TPPS-3.2a** porphyrins also produced clover structures. However, metals that do not accept an axial ligand (e.g. Cu(II), Ni(II)) did not produce clover structures. Powder X-ray diffraction (p-XRD) analyses led to similar spectra for all clover structures. This is taken as evidence that the clover nanoforms have similar crystal structures, regardless of the identity of the coordinated metals.

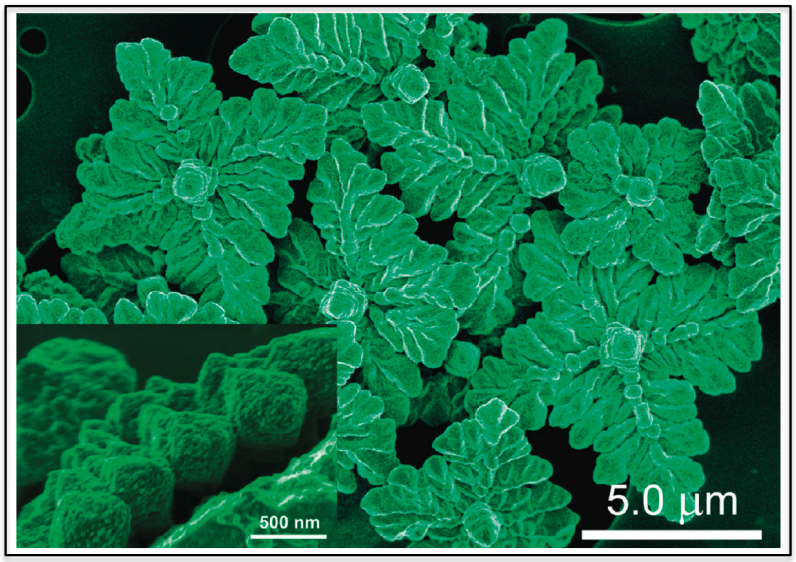

Figure 3.3. SEM images of porphyrin clover structures. These structures were formed from a 1:1 mixture of **SnTPPS**$^{4-}$ and **3.2a**$^{4+}$. The inset shows the side-view of the clovers. This Figure was reproduced with permission from *J. Am. Chem. Soc.* **2010**, 8194. Copyright 2010 American Chemical Society.

The ionic strength of the solution was found to have an effect on the formation of porphyrin clovers. Specifically, an increase in the salt concentration (NaCl) resulted in the smoothing of the "leaves" surfaces. At the highest concentration (20 mM), a smooth four-pointed star was observed. Addition of salts is thought to alter the diffusion-controlled growth rate of the clovers by shielding the ionic groups from binding interactions. This in turn changes the morphology of the nanostructure.

The temperature at which the porphyrins were mixed had an even more drastic effect on the morphology of clover growth (Figure 3.4). Upon increasing the temperature of the solution the clovers retain their four-fold symmetry but they lose features at the nanoscale level. At 80 °C the complexes have a smooth pod-like structure. Analogous to what was observed upon increasing the ionic strength, raising the temperature was also thought to alter the diffusion-limited growth rate and thus, the morphology.

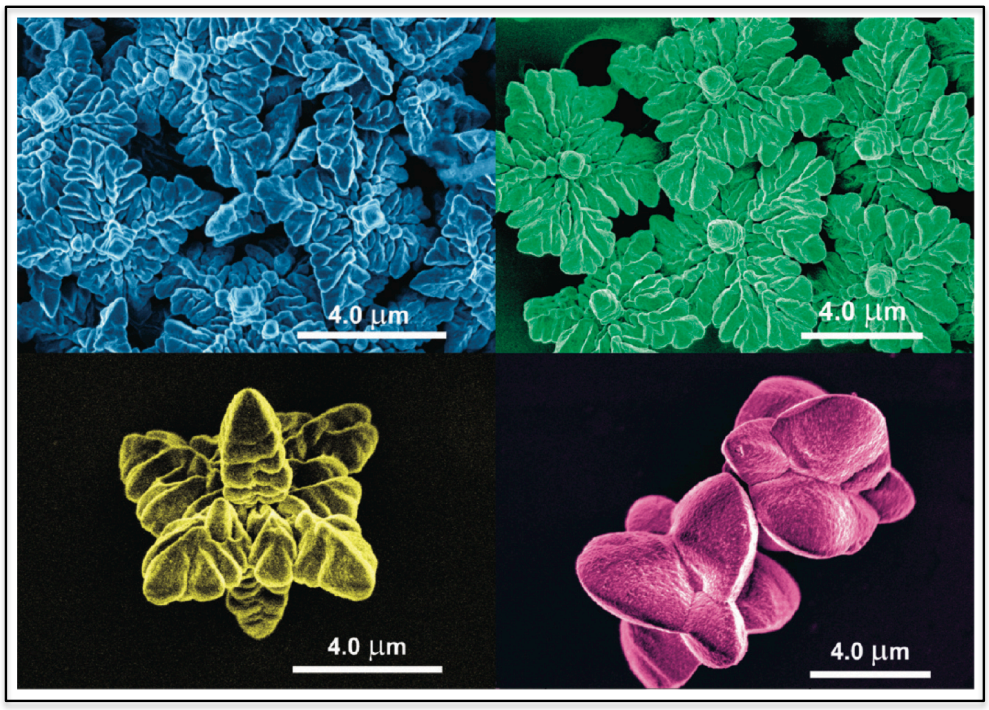

Figure 3.4. SEM images of clovers of **SnTPPS**$^{4-}$ and **Zn3.2**$^{2+}$ formed at variable temperatures. The temperatures shown include 10 (blue), 23 (green), 60 (yellow), and 80 °C (pink). This Figured was reproduced with permission from *J. Am. Chem. Soc.* **2010**, 8194. Copyright 2010 American Chemical Society.

The conductivity of the clover structures was determined by conductive AFM experiments. For these studies **ZnTPPS**$^{4-}$ and **3.2b** were chosen as the donor and acceptor, respectively, based on redox energy level considerations. In the dark, little conductivity was measured by tunneling currents through the porphyrin clover. However, upon illumination by visible light, a 5-fold increase in the conductivity was observed. When the coordinated metals within the porphyrins are exchanged (clovers made from **SnTPPS**$^{4-}$ and **3.2a**), photoconductivity is not observed despite the complexes **SnTPPS-3.2a** and **ZnTPPS-3.2b** having similar crystal structures (based on p-XRD measurements). This finding is thought to reflect the mismatched energy levels between **ZnTPPS** and **3.2b**. Explicitly, the pyridinium groups are significant electron withdrawing groups. Thus, when **3.2** acts as an *acceptor*

(complexed with Sn(IV)), the pyridinium groups enhance the electron accepting ability of the porphyrin (shifting the reduction potential anodically). However, when **3.2** is the *donor* (complexed with Zn(II)), the electron withdrawing pyridinium groups have a detrimental effect (shifting the oxidation potential anodically). This destroys the photoconductivity.

Like the porphyrin nanotubes discussed above, zinc and tin porphyrin nanoclovers were platinized by photocatalytic methods.[3.23] Exposure of the clovers to a platinum(II) complex, in the presence of light and ascorbic acid, led to platinum deposition on the clover surface. Following platinization, the clovers were found to reduce water photocatalytically (in the presence of methyl viologen as an electron relay and triethanolamine as a sacrificial electron donor) to evolve hydrogen. No dark catalytic activity was observed. The clovers continued to evolve hydrogen for up to two weeks under continuous irradiation. Further, the platinized clovers were found to be more efficient (at hydrogen generation) and durable than individual porphyrins.

More complex nano-architectures can be produced from the clover structures.[3.24] The crystal structures of ionic porphyrin nanoclovers are similar (based on p-XRD) regardless of the identities of the central metals. Therefore, one combination of porphyrins known to form clovers can nucleate and grow upon a preformed clover of another combination of metals. Specifically, clovers made from **SnTPPS-3.2a** were exposed to solutions of **SnTPPS^{4-}** and **3.2c**. The Sn-Co complex were found to "grow" onto the Sn-Zn clovers producing nanoparticles on the surface. Although no catalytic activity was reported for these complexes, this study was considered to

represent a proof of concept demonstrating that ionic bonding has the potential to produce complex porphyrin architectures.

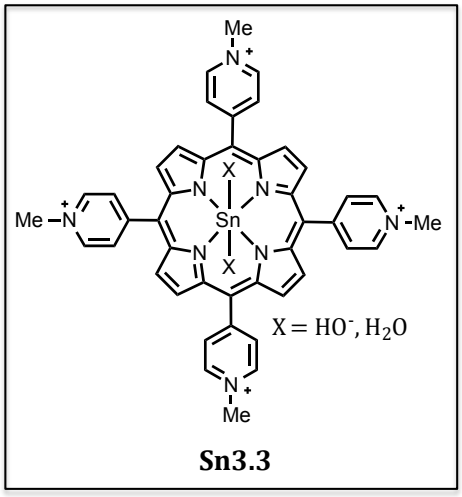

Sn3.3

In other work, the methylated pyridinium porphyrin **Sn3.3^{4+}** was found to form nanosheets upon mixing with **ZnTPPS^{4-}** at pH 7.0.[3.25] The crystal structure of the resulting nanosheets confirmed the formation of an overall neutral complex, with no external counterions. This particular nanocomposite was found to be an insulator, both in the dark and under conditions of photoillumination. The lack of conductivity is thought to reflect the absence of J-aggregates within the crystal structure. Platinization and subsequent water reduction studies revealed that the nanosheets of **ZnTPPS-Sn3.3** were less catalytically active than their clover analogues.

The morphology of the **ZnTPPS-Sn3.3** nanostructures was found to be highly dependent on the pH of the solution, and subsequently, the balance of charge between the porphyrins.[3.26] Lowering the pH of the solution (to pH < 6.0) led to a change in the stoichiometric equivalents of **ZnTPPS-Sn3.3** from 1:1 to 1.25:1. The change in stoichiometry is thought to result from the protonation of an axial hydroxide ligand of **Sn3.3^{4+}** resulting in formation of **Sn3.3^{5+}**. Thus, to balance the charge additional equivalents of **ZnTPPS^{4-}** are needed. The morphology, in turn, is drastically altered. This study supports the theory that the shape, size, and

morphology of ionic porphyrin complexes are determined primarily by the charges of the cationic and anionic constituents.

In summary, the basic properties of ionic porphyrin-porphyrin complexes have been established. In general, charge balance dictates the binding interactions of these systems. The Shelnutt group demonstrated that donor-acceptor porphyrin complexes have photocatalytic activity and intricate nanostructures. However, in the systems reported to date, only tin-based complexes have been used as the electron acceptors. This limits the tunability and morphologies of the resultant nanostrucutres. Also, tin compounds are non-ideal due to their toxicity. Fortunately, a limited number of charge combinations and porphyrin building blocks have been explored—leaving room for additional investigations. In this chapter we report efforts to expand the repertoire of useful ionic porphyrin complexes to include **ZnTTFP^{2+}** as an electron acceptor. Specifically, we detail the structure, binding affinity and photophysical properties of **ZnTTFP-MTPPS** complexes.

3.3 Binding Studies of ZnTTFP^{2+} and MTPPS^{4-}

The synthesis of **ZnTTFP** is reported in Chapter 2.3. To obtain the dication of **ZnTTFP**, a procedure similar to the protocol used to oxidize **CuTTFP** to **CuTTFP•**2OTf was followed. Specifically, **ZnTTFP** was dissolved in dichloromethane while, separately, $Cu(ClO_4)_2$ was dissolved in a minimal amount of methanol. Mixing the solutions led to the precipitation of **ZnTTFP•**$2ClO_4$, which was filtered, washed, dried, and used without further purification (Scheme 3.1).

Scheme 3.1. The synthesis of **ZnTTFP•**$2ClO_4$ from **ZnTTFP**.

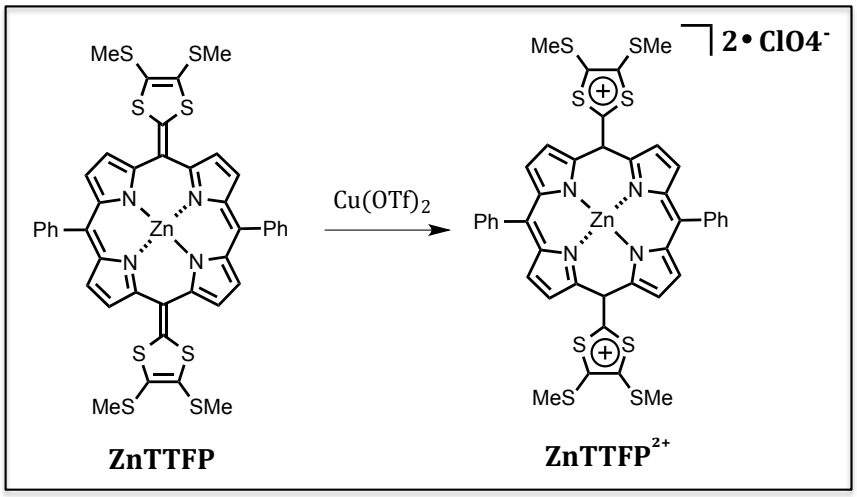

The syntheses of **H_2TPPS** and **ZnTPPS** have previously been reported.[3.27] Porphyrin tetrasulfonic acid was obtained from TCI America. The compound was then dissolved in water and exposed to tetrabutylammonium (TBA) hydroxide. The aqueous solution was extracted with dichloromethane, under these conditions the TBA salt acts as a phase transfer agent, allowing the porphyrin to be carried into the organic phase. Evaporation of the dichloromethane layer then provided 4TBA**•H_2TPPS** in acceptable purity. Metalation with zinc was then effected by exposing a dichloromethane solution of 4TBA**•H_2TPPS** to a concentrated methanolic solution of Zn(OAc); this yielded 4TBA**•ZnTPPS** in almost quantitative yield.

With the aforementioned compounds in hand, the supramolecular association between the ionic species was investigated using a variety of methods. For example, in dry, freshly distilled benzonitrile (PhCN) 4TBA**•MTPPS**s (**H_2** and **Zn**) were titrated into **ZnTTFP•**$2ClO_4$ and monitored by ultraviolet/visible spectroscopy (Figure 3.5). In both cases, a bathochromic shift in the longest wavelength Q-band

of **ZnTTFP•**$2ClO_4$ was observed. Specifically, the λ_{max} of the longest Q-band in **ZnTTFP•**$2ClO_4$ shifts from 690 nm in the original spectrum, to 732 nm at the saturation point (after addition of more than 0.5 equiv of 4TBA•**MTPPS**). In these experiments, the metalation state of **MTPPS** seems to have little effect on the degree of Q-band red-shifting. Unfortunately, no significant information could be gleaned from the Soret band of **ZnTTFP•**$2ClO_4$ due to band overlap with the Soret band of **MTPPS**. Clear isobestic points are observed in both titrations.

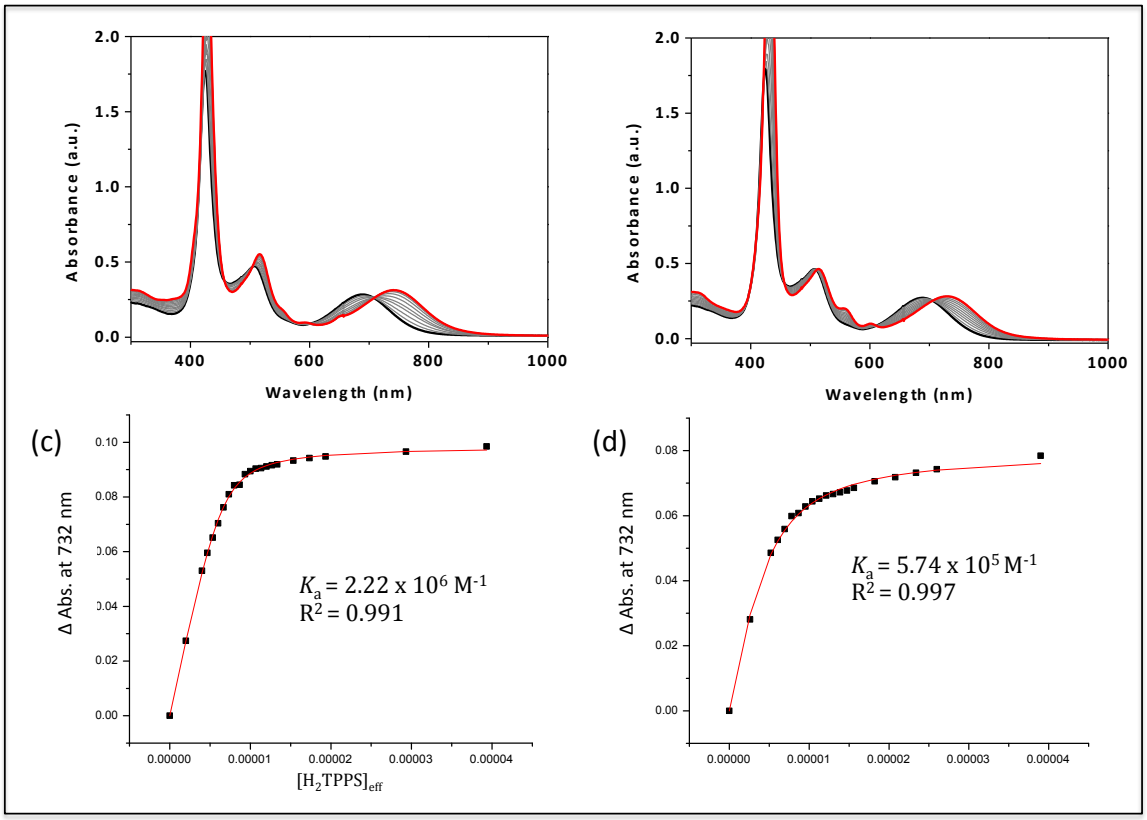

Figure 3.5. (a) Absorption spectra recorded upon the titration 4TBA•**H_2TPPS** into **ZnTTFP•**$2ClO_4$. (b) Absorption spectra for the titration of a 4TBA•**ZnTPPS** into **ZnTTFP•**$2ClO_4$. (c) Absorption data at 732 nm fitted to a 1:1 binding isotherm for the titration data in segment (a). (d) Absorption data at 732 nm fitted to a 1:1 binding isotherm for the titration data in segment (b). All titrations were performed with solutions made from freshly distilled PhCN and at 298 K.

Using the method of continuous variation, a Job plot was constructed for the interaction of **ZnTTFP•**$2ClO_4$ with 4TBA•**ZnTPPS**. Based on this plot, a 2:1

stoichiometry for the interaction of **ZnTTFP**$^{2+}$ with **ZnTPPS**$^{4-}$ was inferred (Figure 3.6). This inference is supported by the observation that the maximum absorption at 732 nm occurs at the point where the mole fraction of **ZnTTFP**$^{2+}$ is ca. 0.66. A Hill plot was constructed to gain insight into the degree of cooperativity between the first and second binding event (Figure 3.6). For the titration of **ZnTTFP**•$2ClO_4$ with 4TBA•**ZnTPPS** the slope of the Hill plot was 1.035. This value indicates non-cooperative binding. In contrast, the Hill plot of **H_2TTFP**•$2ClO_4$ with 4TBA•**ZnTPPS** gave a value of 1.637, indicative of cooperative binding interactions.

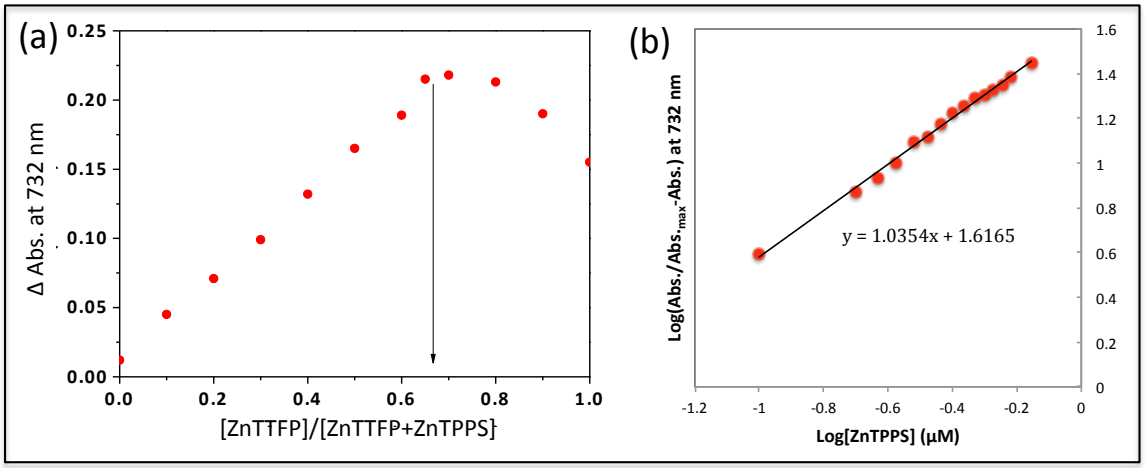

Figure 3.6. (a) Job plot providing support for the proposed 2:1 binding interaction between **ZnTTFP**•$2ClO_4$ and 4TBA•**ZnTPPS**. (b) A Hill-plot for the binding binding interaction of **ZnTTFP**•$2ClO_4$ with 4TBA•**ZnTPPS**.

To obtain a binding constant for the absorption titration data, the absorbance at 732 nm was plotted versus the concentration of 4TBA•**MTPPS** for both titrations (Figure 3.5). Analysis of the data provided support for the conclusion that, in both cases, the system reaches saturation shortly after 0.5 molar equiv of 4TBA•**MTPPS** is added. We attempted to fit the data to a 2:1 binding equation using non-linear regression software. However, the binding constants obtained by these methods were unreliable. Namely, unreasonable values for both the change in the absorption

coefficient and the binding constant were obtained. The difficulty in fitting the data to a 2:1 binding equation arises from the parabolic nature of the binding isotherm at 732 nm. The 2:1 binding equation has four independent variables, thus without complex curve features in the plot of absorption vs. concentration, an infinite number of solutions to the 2:1 binding equation are possible.

The absorption vs. concentration data was also fit to a 1:1 binding equation. As a general rule, if $K_1 >> K_2$ or $K_2 >> K_1$ then the weaker equilibrium reflected in the smaller binding constant does not make a significant contribution to the overall binding expression. Thus, equilibria may be approximated using the 1:1 binding expression. To fit the data to a 1:1 equation the value used in the calculations for the concentration of 4TBA•**MTPPS** was doubled relative to the actual concentration to reflect the concentration of "available" binding sites. Using this approach, an association constant of 2.22 x 10^6 M^{-1} was obtained for the titration of 4TBA•**ZnTPPS** into **ZnTTFP**•$2ClO_4$. A weaker association (K_a = 5.75 x 10^5 M^{-2} was obtained when 4TBA•**ZnTPPS** was titrated into **ZnTTFP**•$2ClO_4$ (Figure 3.5). These values are though to represent the overall binding constant of their respective systems.

The observation of fluorescence bleaching upon the addition of **ZnTTFP**•$2ClO_4$ to 4TBA•**ZnTPPS** was also taken as an indication of a binding interaction between the porphyrin species. Specifically, the change in the fluorescence intensity at 609 nm was monitored during the titration of aliquots of **ZnTTFP**•$2ClO_4$ into a PhCN solution of 4TBA•**ZnTPPS** (Figure 3.7). A clear attenuation of the fluorescence peak was observed upon the addition of **ZnTTFP**•$2ClO_4$. The intensity of the **ZnTPPS**$^{4-}$

emission peak continued to decrease up until the point when two molar equivalents of **ZnTTFP^{2+}** had been added. At this point, the emission of 4TBA•**ZnTPPS** was nearly fully quenched, being merely 5.5% of its original intensity. A similar titration was carried out using 4TBA•**H_2TPPS** and **ZnTTFP**•$2ClO_4$. This latter titration yielded analogous results. In this experiment the fluorescence signal at 654 nm was followed. After the addition of two molar equivalents of **ZnTTFP**•$2ClO_4$, only 3.6% of the original emission intensity of **H_2TPPS^{4-}** remained. In analogy to what proved true for the absorption titration data, a lack of complex curve shape prohibited reasonable fitting of the data to a 1:2 binding equation. However, the strong fluorescence quenching was taken as additional evidence of the formation of a supramolecular complex.

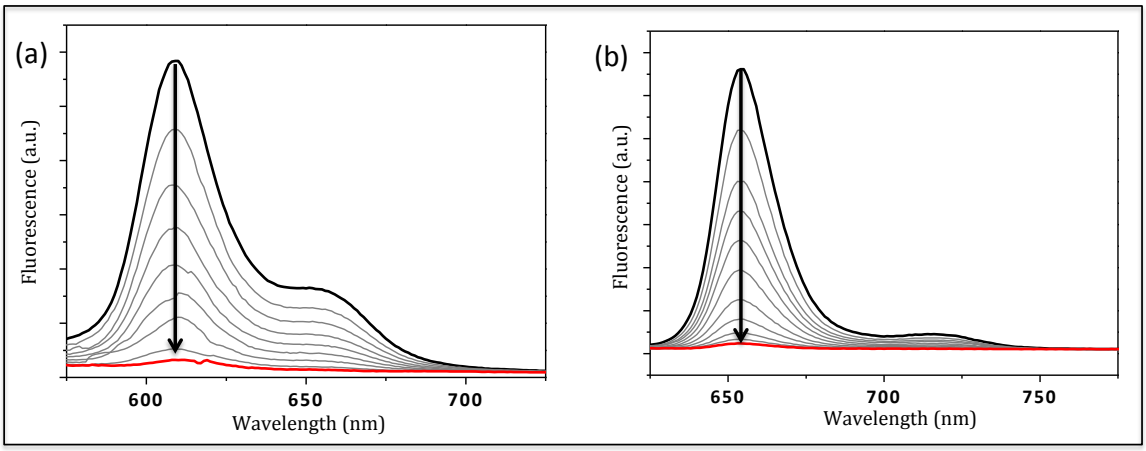

Figure 3.7. (a) Emission spectra demonstrating the fluorescence quenching of **ZnTPPS^{4-}** that occurs upon the addition of **ZnTTFP^{2+}** in PhCN at 298 K. (b) Emission spectra demonstrating the fluorescence quenching of **H_2TPPS^{4-}** seen upon the addition of **ZnTTFP^{2+}** in PhCN at 298 K. In both titrations the initial spectra are highlighted in black and the final spectra (after the addition of 2 molar equivalents of **ZnTTFP^{2+}**) are highlighted in red.

In an effort to evaluate the thermodynamic behavior associated with the proposed complexation process involving **ZnTTFP^{2+}** and **MTPPS^{4-}**, isothermal

titration calorimetry (ITC) was performed in PhCN (Figure 3.8). In these experiments, a concentrated solution of 4TBA•**ZnTPPS** or **H_2TPPS**•4TBA was titrated into **ZnTTF**•$2ClO_4$. Although the binding model is not perfectly clear, these studies provided evidence for strong binding interactions between the porphyrins. For example, in the titration of **ZnTTF**•$2ClO_4$ with 4TBA•**H_2TPPS**, two sigmoidal curve segments are seen in the integrated heat signal. Several binding models are available to describe the binding thermodynamics. In fact, careful selection of a pertinent model is essential to achieving good fits and meaningful results from ITC analyses. In this case study, two binding models are worthy of consideration: *one-site* (or *n*-number of identical sites) and *two-sites* (two independent sites). In the *one-site* model, multiple binding events can be modeled accurately modeled as long as all of the binding sites studied are identical, independent of one another, and exhibit the same binding thermodynamics. Assuming these requirements hold true for a system, the *one-site* expression models multiple binding events in a single sigmoidal heat signature. The stoichiometry of the binding event is determined by the inflection point, or "*n*-value", of the resultant sigmoidal heat signature. In the *two-sites* model, it is assumed that there are two distinct binding interactions with distinct thermodynamics and saturation points. Separate heat signals and isotherms are observed in this binding model. The *n*-value of each event is equivalent to the stoichiometry of *only* that event. For example, a *two-sites* model with $n = 1$ for the first event and $n = 2$ for the second, would bind one equivalent of ligand in the first event and two (thermodynamically identical) equivalents in the second event.

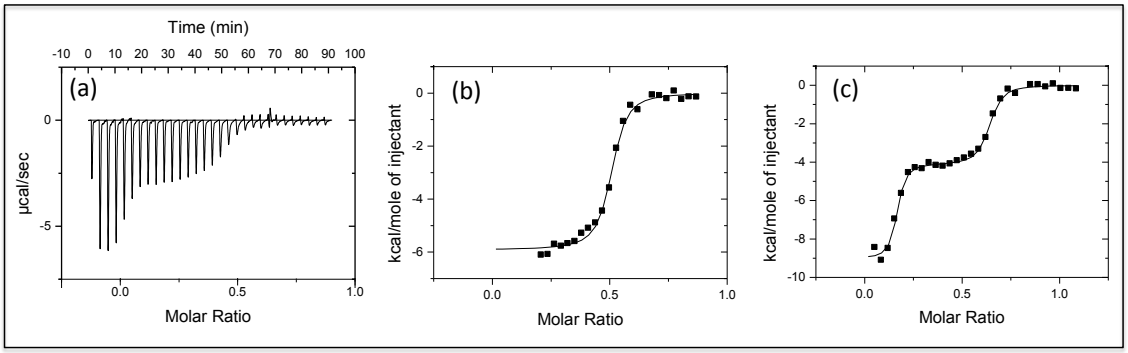

Figure 3.8. (a) The raw ITC calorimetry data for the titration of 4TBA•**H_2TPPS** into **ZnTTF**•$2ClO_4$. The data was recorded in PhCN at 298 K. The data obtained from the titration in (a) was fit to a *one-site* model (b) and a *two-sites* model (c).

The titration data from the addition of 4TBA•**H_2TPPS** into **ZnTTF**•$2ClO_4$ fits equally well to both binding models. A comparison of the binding models is shown in Figure 3.8. In the *ones-site* model, the calculated association constant is 1.28×10^6 M^{-2} with an *n*-value of 0.496. The *n*-value indicates that ca. 0.5 equivalents of 4TBA•**H_2TPPS** (referenced to **ZnTTF**•$2ClO_4$) are present in solution at the equivalence point. Put another way, the binding stoichiometry is 2:1, **H_2TPPS^{4-}** to **ZnTTF^{2+}**. Examination of the thermodynamics indicates that the binding equilibrium is favored on both enthalpic and entropic grounds. However, the contribution to binding from enthalpy (≈ -5,900 cal/mol) is over twice that of the entropy contribution (≈ -2,400 cal/mol). The favorable entropy seen upon porphyrin-porphyrin interaction may result from the increase in the overall molarity of the solution that occurs upon binding. Since, the binding process occurs in accord with the following equation:

4TBA•**H_2TPPS** + 2(**ZnTTF**•$2ClO_4$)➔**ZnTTFP_2•H_2TPPS** + 4($TBAClO_4$)

upon porphyrin-porphyrin interaction, two additional molar equivalents of salts are released into solution as $TBAClO_4$. This presumably leads to a decrease in the order

of the system *via* an increase in the number of discreet complexes in solution. It is thought that this increases the overall entropy and helps drive the binding process.

To obtain a good fit to the *one-site* equation, points from the first initial exothermic process (deemed to be "initialization" points)[28] were discarded. On the other hand, use of the *two*-sites equation allows the initialization points to also be fit with a binding isotherm (Figure 3.8c). In the latter model, the binding events are each fitted to separate thermodynamic data. The first (arbitrarily assigned) event has several thermodynamic parameters similar to those obtained with the *one*-site method. Specifically, an *n*-value near 0.5 (0.474) and a similar binding constant (1.27×10^6 M^{-2}) were observed. The contributions to binding from enthalpy and entropy were slightly different, however. In the *two-sites* equation more emphasis is put on the increase in entropy (ΔS = 14.2 cal/mol) and less on the favorable heat loss from enthalpy ($\Delta H \approx$ -4130 cal/mol) compared to the *one-site* equation.

The second binding event in the *two-sites* model fits the data for the "initialization" points that were removed from the *one-site* model. This fitting gives rise to a very strong binding profile (2.00×10^8 $M^{-6.5}$)[29], with large contributions from both enthalpy ($\Delta H \approx$ -4130 cal/mol) and entropy (ΔS = 7.73 cal/mol). The *n*-value is ca. 0.153. This leads us to suggest that if the heat signal in question results from binding between 4TBA•**H_2TPPS** and **ZnTTF**•$2ClO_4$ the stoichiometry at the equivalence point would be ≈ 6.5 to 1, **ZnTTF** to **H_2TPPS**. Presumably, a discreet complex with over 6 equivalents of **$ZnTTFP^{2+}$** surrounding one molecule of **H_2TPPS** is unlikely, based on steric considerations. Therefore, this exothermic process in thought to reflect non-specific interactions within the system, such as solvation

changes, changes in the conformation of the porphyrins, increasing ionic strength, and electrostatic effects.

Similar analyses were performed for the titration of 4TBA•**ZnTPPS** into **ZnTTF**•$2ClO_4$. The important thermodynamic parameters obtained from fitting the titration data to both the *one-site* and *two-sites* binding equations are summarized in Table 3.1. Similar conclusions to those drawn from the calorimetry experiments with 4TBA•**H_2TPPS** were arrived at in these latter trials. However, the binding constants were lower for this set of porphyrins.

Table 3.1. Thermodynamic data for the titration of 4TBA•**MTPPS**s (H_2 and Zn) into **ZnTTFP**•$2ClO_4$ in PhCN at 298 K. The units for ΔH, $T\Delta S$, and $\Delta\Gamma$ are all kilocalories per mole. The units for K_{a1} are M^{-2}. The units for K_{a2} are M^{-X}, where x is the number of stoichiometric equivalents of **ZnTTFP** to **MTTPS** at the equivalence point.

	Model	n_1	K_{a1} / 10^5	ΔH_1	$T\Delta S_1$	$\Delta\Gamma_1$	n_2	K_{a2} / 10^5	ΔH_2	$T\Delta S_2$	$\Delta\Gamma_2$
H_2TPPS	*one-site*	0.496	12.8 ± 2.2	− 5.91 ± 0.08	2.42	8.33	–	–	–	–	–
	two-sites	0.474	12.7 ± 3.5	− 4.13 ± 0.09	4.20	8.33	0.153	2000 ± 776	-9.03 ± 0.018	2.30	11.33
ZnTPPS	*one-site*	0.469	2.53 ± 0.55	− 5.37 ± 0.22	2.00	7.37	–	–	–	–	–
	two-sites	0.456	4.24 ± 0.94	− 2.93 ± 0.13	4.74	7.67	0.157	102 ± 20.7	− 13.3 ± 0.23	– 3.70	9.60

In summary, by three separate methods strong evidence for a supramolecular interaction between **MTPPS^{4-}** and **ZnTTFP^{2+}** has been presented. Based on the *n*-value in ITC analyses, and the method of continuous variations in absorption spectroscopy, a 2:1 **MTPPS^{4-}** to **ZnTTFP^{2+}** complex is expected in solution. The magnitude of the association constant is not well established due to a lack of sufficient information that can be extracted from the absorption and emission titration curves as well as the presence of an uncharacterized initialization

exotherm in the ITC that complicate the latter analyses. However, efforts to fit the data using various models point to a strong interaction (above 10^5 M^{-2}).

In the future, titrations ^{1}H NMR could help to shed light on the scale of the binding constant. ^{1}H NMR titrations were previously performed in DMSO-d_6. However, these experiments were unsuccessful, due to the broadening of the peaks assigned to **ZnTTFP^{2+}** upon the addition of even very small amounts of **MTPPS^{4-}**. Presumably, the observed broadening of peaks was a result of aggregation of the porphyrin complexes at the concentration required for NMR analyses. Using C_6D_5CN instead of DMSO-d_6 in NMR spectroscopic titrations could possibly circumvent the deleterious aggregation phenomenon observed in the latter solvent. However, C_6D_5CN is extremely expensive (> \$500 / g). Therefore, it was determined that the information that possibly would be gained from this study was not worth the cost of the experiment.

3.4 Crystal Structure of the ZnTPPS-(ZnTTFP)$_2$ Complex

Attempts to grow a single crystal of the **ZnTPPS-(ZnTTFP)$_2$** complex were met with difficulty. The mixture of the two porphyrins proved to be insoluble in every solvent investigated except dimethyl sulfoxide and PhCN. Due to the extremely low volatility of these solvents, neither is ideal for single crystal growth. Crystallization vials containing these solvents, unsurprisingly, never evolved single crystals. Solvent diffusion and layering methods also failed to produce crystalline solids with these non-volatile solvents.

After exhaustive testing of crystallization conditions and solvents, X-ray quality crystals were eventually obtained for the **ZnTPPS-(ZnTTFP)$_2$** complex. The

successful method relied on the slow *in situ* formation of **ZnTPPS-(ZnTTFP)$_2$**. From previous crystallization attempts it was discovered that the unmixed porphyrin salts, 4TBA•**ZnTPPS** and **ZnTTFP**•2ClO_4, were soluble in methanol (MeOH), tetrahydrofuran (THF), and slightly soluble in acetonitrile (MeCN). However, upon mixing solutions of the porphyrin salts (dissolved in any combination of these solvents), immediate precipitation was observed. Thus, due to solubility considerations, it was realized that precise control over the stoichiometry of the crystallization vial by premixing the porphyrins was not possible. Therefore, a careful layering technique was used. Specifically, **ZnTTFP**•2ClO_4 was dissolved in MeCN with 5% MeOH added to effect complete dissolution. This solution was used to partially fill a NMR tube. After this, around 1 cm of THF was carefully layered over the MeCN solution. Then, a solution of 4TBA•**ZnTPPS** in THF was carefully layered over the pristine THF layer. The tube was protected from light and stored upright to limit the surface area (and subsequently mixing) between the solvent layers. Over the next two weeks, dark green X-ray quality crystals grew as needles between the solvent layers.

The single crystals grown from this method were subjected to X-ray diffraction analyses, and the structure was solved by Dr. Vince Lynch at the University of Texas Dept. of Chemistry and Biochemistry X-ray facility. A 2:1 complex of **ZnTTFP^{2+}** to **ZnTPPS^{4-},** arranged in a slipped-sandwich configuration, was observed (Figure 3.9). Additionally, the crystal structure displays a marked absence of external counterions, as would be expected for an electronically neutral supramolecular complex. Electrostatic interactions between the sulfonate groups of **ZnTPPS** and

the dithiole rings in **ZnTTFP** are clearly evident. However, there seems to be little to no contribution to binding from either donor-acceptor interactions or sulfonate coordination to the zinc center of **ZnTTFP**.

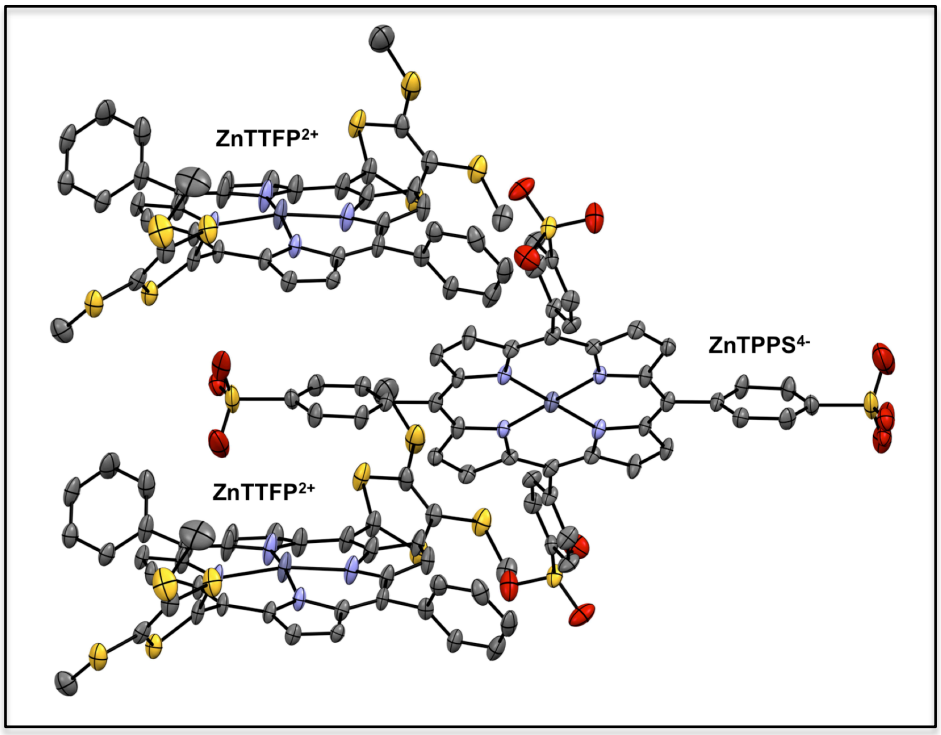

Figure 3.9. X-ray crystal structure of the 2:1 supramolecular complex formed between **ZnTTFP**$^{2+}$ and **ZnTPPS**$^{4-}$. Thermal ellipsoids are scaled to the 50% probability level. Hydrogen atoms and solvent molecules are omitted for clarity. This data for the structure was obtained and solved by Dr. Vince Lynch at the University of Texas Dept. of Chemistry and Biochemistry X-ray facility.

The absence of apparent donor-acceptor interactions is most likely the result of the electrostatic effects that dictate the binding behavior in the solid state. This conclusion was reached based on the packing structure of the **ZnTTFP$_2$-ZnTPPS** complex (Figure 3.10). In this structure, back to back dimers of **ZnTTFP** are observed with the dithole rings between the adjacent dications nearly orthogonal to one another. Interestingly, all molecules of **ZnTTFP** seen in the structure are oriented parallel to one another in the form of dimeric sheets. The **ZnTPPS** moiety

resides in another plane between dimers of **ZnTTFP**. The orientation of the **ZnTPPS** moeities allows for close contact between the anionic sulfonate groups and the cationic dithiole rings. Thus, we believe that non-parallel alignment facilitates close, stabilizing contacts between the locally charged species, eliminating close π-π contacts.

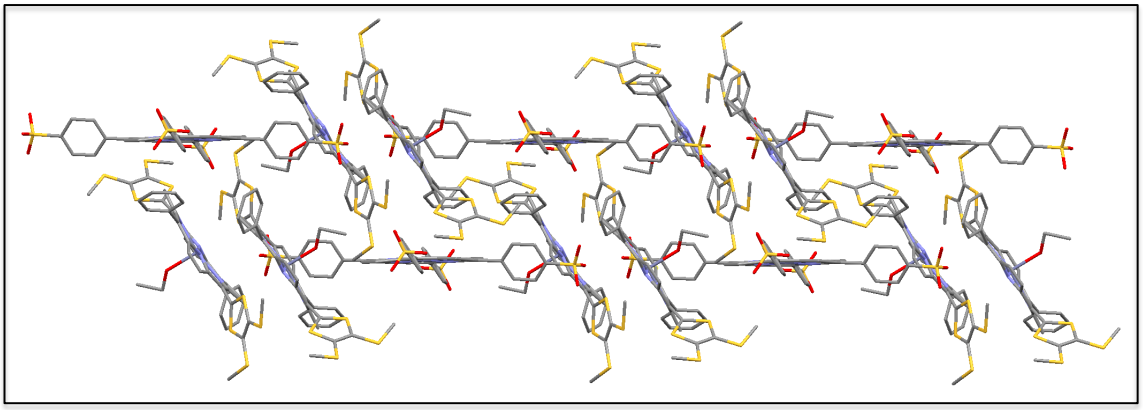

Figure 3.10. Crystal packing structure of the **ZnTPPS-(ZnTTFP)$_2$** complex. The data for the structure was obtained and solved by Dr. Vince Lynch.

3.5 Photoinduced Electron Transfer in Complexes

The fluorescence emission of **MTPPS^{4-}** undergoes bleaching upon the addition of **ZnTTFP^{2+}** (cf., Section 3.3). This was taken as initial evidence of electronic coupling between the two porphyrins. Specifically, electron transfer from the electron rich **MTPPS^{4-}** to the electron deficient **ZnTTFP^{2+}** was hypothesized. To probe this effect in greater depth, electrochemical and advanced photophysical studies were undertaken. This latter work was carried out by Prof. Shunichi Fukuzumi and Prof. Dongho Kim and their respective groups.

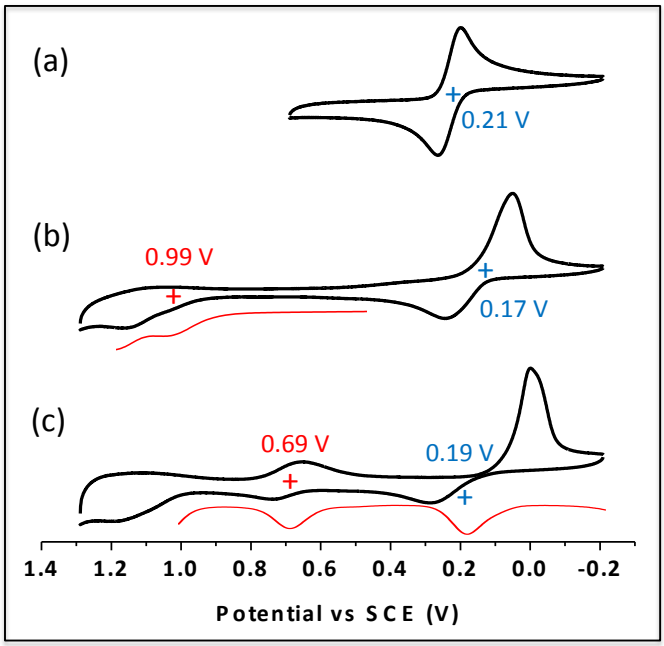

Figure 3.11. Stacked cyclic voltammetric (CV) and differential pulse voltammetric (DPV) curves derived from electrochemical studies of (a) a 2.0 mM solution of **ZnTTFP•**$2ClO_4$, (b) a mixture of a 2.0 mM solution of **ZnTTFP•**$2ClO_4$ and a 1.0 mM solution of 4TBA•**H_2TPPS** and (c) a mixture of a 2.0 mM solution of **ZnTTFP•**$2ClO_4$ and a 1.0 mM solution of 4TBA•**ZnTPPS**. CV analyses are traced in black and DPV analyses are traced in red. All spectra were performed in PhCN containing 100 mM $TBAPF_6$ as a supporting electrolyte.

Electrochemical studies using cyclic voltammetric (CV) and differential pulse voltammetric (DPV) methods were carried out in an effort to determine the redox potentials of the supramolecular complexes in PhCN (Figure 3.11). Based on these analyses, the two-electron reduction of **ZnTTFP•**$(ClO_4)_2$ occurs at 0.21 V vs SCE. This redox event occurs at an identical potential to that reported for the two-electron oxidation of **ZnTTFP** in PhCN (Chapter 2.5).[2.30] After the addition of 4TBA•**MTPPS** (forming a supramolecular complex), the two-electron reduction wave of **ZnTTFP•**$(ClO_4)_2$ becomes quasi-reversible. Additionally, a slight shift in the redox potentials is seen. Quantitatively, the **ZnTTFP•**$(ClO_4)_2$ reduction peaks are cathodically shifted from 0.21 V, before the addition of **$MTTFP^{4-}$**, to 0.17 V and

0.19 V after the addition of 4TBA•**H_2TPPS**$^{4-}$ and 4TBA•**ZnTPPS**$^{4-}$, respectively. The one electron oxidation peaks (attributed to **MTTFP**$^{4-}$) are also shifted in comparison with the previously reported values for pristine 4TBA•**H_2TPPS**$^{4-}$ and 4TBA•**ZnTPPS**$^{4-}$ (to 0.99 and 0.69 V, respectively).[2.31]

The photodynamics of the **MTPPS**-(**ZnTTFP**)$_2$ complexes were examined by femtosecond laser flash photolysis in the group of our collaborator Prof Fukuzumi. While not the work of the author, a brief synopsis is appropriate here. Upon photoexcitation at 390 nm, fast energy transfer from the S2 excited state of the **MTPPS**$^{4-}$ (M = H_2 and Zn) moiety to the S1 excited state of **ZnTTFP**$^{2+}$ is observed. The corresponding rate constant is 1.8×10^{10} s^{-1} (Figure 3.12a). This is followed by intersystem crossing to populate the triplet excited state, ^{3}[**ZnTTFP**$^{2+}$]*, with the rate constant of 3.1×10^8 s^{-1}.

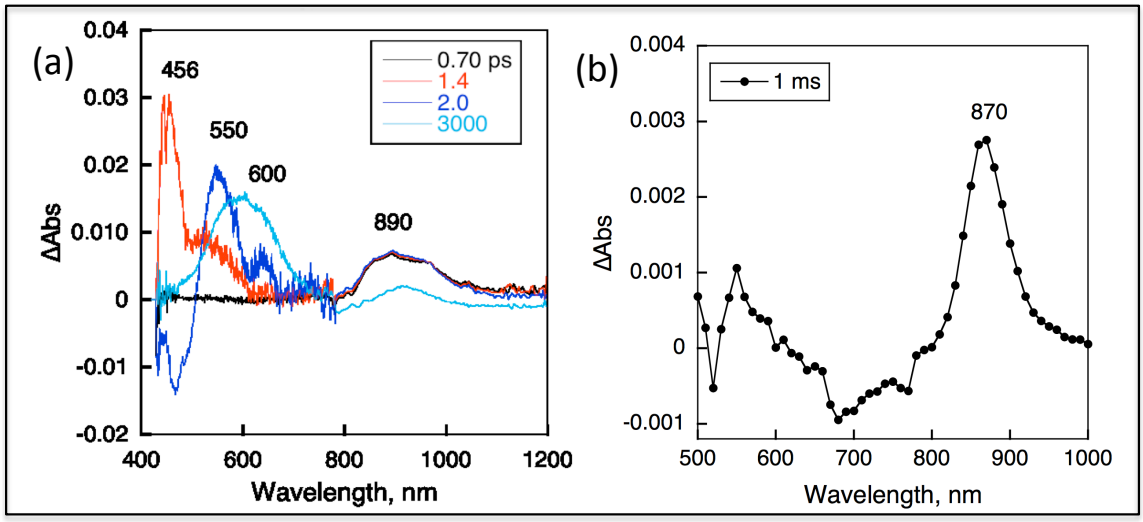

Figure 3.12. Transient absorption spectra of the **ZnTPPS**-(**ZnTTFP**)$_2$ complex generated *in situ* in deaerated PhCN at 298 K recorded after (a) femtosecond laser excitation and (b) nanosecond laser excitation at 390 nm. This work was performed in the group of Prof. Fukuzumi at Osaka University.

In contrast to what was seen under conditions of femtosecond laser flash photolysis, transient absorption spectra obtained by nanosecond laser flash photolysis reveal features consistent with photoinduced electron transfer from **H_2TPPS**$^{4-}$ to **ZnTTFP**$^{2+}$ (Figure 3.11b). The sharp absorption band at 870 nm is diagnostic of **ZnTTFP**$^{\bullet+}$. (Note: the absorption spectrum of this species is shown in Figure 2.21). The absorption due to **H_2TPPS**$^{\bullet3-}$ appears around 600 nm, and is overlapped with the absorption feature due to **ZnTTFP**$^{\bullet+}$. Electron transfer from **H_2TPPS**$^{4-}$ to ^{3}[**ZnTTFP**$^{2+}$]* may occur in the time region between 3 ns and 1 ms, because the CS state was not observed at 3 ns and the CS state was at maximal intensity by 1 ms. The transient absorption due to the CS state is surprisingly persistent. The decay of the CS state obeys first-order kinetics and the slope of the first-order plots are unchanged, irrespective of the laser intensity and therefore the concentration of the photoinduced CS state. This is consistent with charge recombination occurring within the supramolecular complex with no contribution from intermolecular charge recombination between the CS states of two separate supramolecular complexes. Intermolecular charge recombination, although not formally prohibited, may be reduced due to electrostatic repulsion. The positively charged porphyrins (**ZnTTFP**$^{2+}$ or **ZnTTFP**$^{\bullet+}$) surrounding the electron donor moiety (**H_2TPPS**$^{\bullet3-}$) presumably act to repel other supramolecular complexes, protecting the donor from intermolecular back electron transfer. The first-order decay rate constant calculated for the CS state, **H_2TPPS**$^{\bullet3-}$/(**ZnTTFP**$^{\bullet+}$)(**ZnTTFP**$^{2+}$), was determined to be 12 s^{-1}. This corresponds to an extremely long CS lifetime of 83

ms. Repeating the studies with **ZnTPPS**$^{4-}$ resulted in similar photophysics with a shortened (but still relatively long) CS lifetime of 43 ms.

At the writing of this dissertation the lifetimes of the complexes photoinduced CS states (discussed above) were still a matter of debate. Specifically, the extremely long-lived lifetimes obtained in Prof. Fukuzumi's research group have yet to be reproduced in Prof. Kim's group. Instead, lifetimes over an order of magnitude shorter were recorded. However, considerable differences in the respective experimental setups have been noted, including solvent purification strategies, excitation wavelengths, instrumentation, etc. Current research is directed at understanding the discrepancies between the two experimental methods. Obtaining an accurate and concordant value for the CS state lifetime understandably precludes the publication of this work and it is hoped that this matter is resolved soon.

3.6 Future Direction

As noted above, the first pending item concerning this project involves determining the CS lifetime for the self-associated ensemble. Only after this value is determined will potential applications become clear. Further ^{1}H NMR titrations are also needed and would give additional insight into the strength of the binding interaction between the ionic porphyrins.

The nanostructure of the composites should also be examined by microscopy techniques. At the microscopic level, fern-shaped "leafs" are observed upon slow mixing of the porphyrins. However, the nanostructure is unknown. The work of Shelnutt has established that the balance of charges between ionic porphyrins

determines the morphology of the nanostructures. Therefore, we expect modified nanoscale morphologies for **ZnTTFP/MTPPS** compared to what has previously been reported for other ionic porphyrin systems (e.g. tubes, rod, sheets, clovers). Realizing a new nanoform would expand the number of structures that can be produced from ionic porphyrin building blocks and possibly render the novel structures suitable for alternative applications.

In the same vein, the structure and binding of **ZnTTFP/MTPPS** complexes could be altered by external stimuli. For instance, **ZnTTFP^{2+}** is redox active. Thus, subjecting the porphyrin complex to electrolysis will reduce **ZnTTFP^{2+}** and lead to the alteration or destruction of the **ZnTTFP/MTPPS** nanostructure. Further, this process should be reversible. It is hypothesized that switching the potential oxidatively to a value above the oxidation half-wave potential of **ZnTTFP** would result in oxidation the oxidation of **ZnTTFP** to **ZnTTFP^{2+}**, restoring the nanostructure.

Other external stimuli could also affect the structure. For example, pH has been shown to have a drastically change the morphology of ionic porphyrin structures by manipulating the charge balance between the porphyrins. Similar experiments could be performed with **ZnTTFP/MTPPS** complexes. Additionally, axial coordination could have a pronounced effect on the morphology of nanostructures. For example, coordination of the central metal with halogens such as chloride, decrease the charge of a porphyrin complex by one. This, in turn, would alter the stoichiometry of any ionic porphyrin complexes produced and subsequently the

structure. Displacement of the halogen with a competing ligand could restore the original balance of charge and possibly reform the original nanostructure.

The conductivity of **ZnTTFP/MTPPS** complexes, and their applicability to serve as organic conductors is also of future interest. The dark and light conductivity of the crystalline and non-crystalline forms of **ZnTTFP/MTPPS** should be examined. In the crystal structure, segregated stacks of $\mathbf{ZnTTFP^{2+}}$ and $\mathbf{ZnTPPS^{4-}}$ were observed. Slipped stacks of $\mathbf{ZnTTFP^{2+}}$ were also observed within close contact of one another. However, the stacks of the porphyrins are not coplanar, which could diminish the conductivity of the complex. Irradiating the complex with light should lead to increased conductivity. Upon irradiation, the expected increase in the number of holes and electrons within the structure would serve to increase the charge mobility and subsequently the conductivity. For these reasons, conductivity measurements of the **ZnTTFP/MTPPS** complex are warranted. These studies could be accomplished using conductive AFM measurements.

Finally, manipulation of the central metal atoms within the porphyrins is expected to modify the properties and potential applications of the ensuing ionic porphyrin complexes. For example, although $\mathbf{ZnTTFP^{2+}}$ is an efficient electron acceptor, replacing the zinc(II) atom with tin(IV) is expected to enhance the electron affinity of the porphyrin. Consequently, the electronics of ionic complexes made from $\mathbf{SnTTFP^{2+}}$ will have altered electronics.

In conclusion, the chemistry and photophysics of ionic porphyrin complexes warrants further study. Strong association constants, induced by ionic bonding, allows for the facile syntheses of complex porphyrin dimers. Of particular interest

are porphyrin-donor/porphyrin-acceptor complexes. In this regard, fewer than 10 papers have been published—all using Sn(IV) porphyrins as the electron acceptor. The work in this Chapter introduces a new porphyrin analogue, **ZnTTFP^{2+}**, that may serve to expand the "toolbox" of available materials useful for creating self-assembled porphyrin structures. Based on the Job plot analyses detailed in this Chapter, **ZnTTFP^{2+}** forms 2:1 complexes with **MTPPS^{4-}** and displays intriguingly long-lived (albeit unconfirmed) excited state dynamics. The work with this molecule is still in its infancy. The development of additional charged redox active monomers in the years to come should help expand the chemistry of ionic porphyrin complexes.

3.7 Chapter 3 References

1. (a) Chen, Z. P.; Debije, M. G.; Debaerdemaeker, T.; Osswald, P.; Würthner, F. *ChemPhysChem* **2004**, 5, 137. (b) Jones, B. A.; Ahrens, M. J.; Yoon, M.-H.; Facchetti, A.; Marks, T. J.; Wasielewski, M. R. *Angew. Chem., Int. Ed.* **2004**, 43, 6363. (c) An, Z.; Yu, J.; Jones, S. C.; Barlow, S.; Yoo, S.; Domercq, B.; Prins, P.; Siebbeles, L. D. A.; Kippelen, B.; Marder, S. R. *Adv. Mater.* **2005**, 17, 2580. (d) Shin, W. S.; Jeong, H.-H.; Kim, M.-K.; Jin, S.-H.; Kim, M.-R.; Lee, J.-K.; Lee, J. W.; Gal, Y.-S. *J. Mater. Chem.* **2006**, 16, 384. (e) An, Z.; Odom, S. A.; Kelley, R. F.; Huang, C.; Zhang, X.; Barlow, S.; Padilha, L. A.; Fu, J.; Hagan, D. J.; Van Stryland, E. W.; Wasielewski, M. R.; Marder, S. R. *J. Phys. Chem. A* **2009**, 113, 5585. (f) Cui, S.; Liu, H.; Gan, L.; Li, Y.; Zhu, D. *Adv. Mater.* **2008**, 20, 2918. (g) Zhou, W. D.; Li, Y. L.; Zhu, D. B. *Chem. Asian J.* **2007**, 2, 222. (h) Gan, H.; Liu, H.; Li, Y.; Zhao, Q.; Li, Y.; Wang, S.; Jiu, T.; Wang, N.; He, X.; Yu, D.; Zhu, D. *J. Am. Chem. Soc.* **2005**, 127, 12452.
2. *The Porphyrin Handbook*. Vol 1-10. Kadish, K. M.; Smith, K. M.; Guilard, R. Eds. Academic Press, New Jersey, 1999. Waltham, Massachusetts.
3. (a) Pierson, B. K.; Castenholz, R. W. In *The Photosynthetic Bacteria*; Clayton, R. K., Sistrom, W. R., Eds.; Plenum Publishing Corp., 1978 NewYork. (b) Ganapathy, S.; Oostergetel, G. T.; Wawrzyniak, P. K.; Reus, M.; Chew, A. G. M.; Buda, F.; Boekema, E. J.; Bryant, D. A.; Holzwarth, A. R.; de Groot, H. J. M. *Proc. Natl. Acad. Sci. U.S.A.* **2009**, 106, 8525. (c) Cohen-Bazire, G.; Pfennig, N.; Kunisawa, R. *J. Cell Biol.* **1964**, 22, 207. (d) Holt, S. C.; Conti, S. F.; Fuller, R. C. *J. Bacteriol.* **1966**, 91, 311.
4. (a) D'Souza, F.; Ito, O. *Chem. Commun.* **2009**, 4913. (b) Boyd, P. D. W.; Reed, C. A. *Acc. Chem. Res.* **2005**, 38, 235.
5. (a) Wang, C.; Tang, W.; Zhong, H.; Zhang, X.; Shen, Y. *Chinese J. Chem.* **2007**, 27, 2020. (b) O'neil, M. P.; Niemezyk, M. P.; Svec, W. A.; Gosztola, D.; Gaines III, G. L.; Wasielewski, M. R. *Science* **1992**, 257, 63. (c) Debreczeny, M. P.; Svec, W. A.; Wasielewski, M. R. *Science* **1996**, 274, 584. (d) Scandola, F.; Chiorboli, C.; Prodi, A.; Iengo, E.; Alessio, E.; *Coord. Chem. Rev*. **2006**, 250, 1471.
6. (a) Kurreck, H.; Huber, M. *Ang. Chem. Int. Ed.* **1995**, 34, 849. (b) Buranda, T.; Soice, N.; Lin, S.; Larsen, R.; Ondrias, M. *J. Phys. Chem.* **1996**, 100, 18868
7. Wasielewski, M. R. *Chem. Rev.* **1992**, 92, 435
8. (a) Sessler, J. L.; Lawrence, C. M.; Jayawickramarajah, J. *Chem. Soc. Rev.* **2007**, 36, 314. (b) Sánchez, L.; Martín, N.; Guldi, D. M. *Ang. Chem. Int. Ed.* **2005**, 49, 5374.
9. (a) D'Souza, F.; Rath, N. P.; Deviprasad G. R.; Zandler, M. E. *Chem. Commun*., **2001**, 267. (b) Mateo-Alonso, A.; Ehli, C.; Guldi D. M.; Prato, M. *J. Am. Chem. Soc.*, **2008**, 130, 14938 (c) Dietel, E.; Hirsch, A.; Eichhorn, E.; Rieker, A.; Hachbarth S.; Roder, B. *Chem. Commun*., **1998**, 1835. (d) Schuster, D. I.; Cheng, P.; Jarowski, P. D.; Guldi, D. M.; Luo, C.; Echegoyen, L.; Pyo, S.; Holzwarth, A. R.; Braslavsky, S. E.; Williams R. M.; Klihm, G. *J. Am. Chem. Soc*., **2004**, 126, 7257.
10. (a) W, Z.-Q.; Shao, X.-B.; Li, C.; Hou, J.-L.; Wang, K.; Jiang, X.-K.; Li, Z.-T. *J. Am. Chem. Soc.* **2005**, 127, 12460. (b) Ciammaichella, A.; Dral, P. O.; Clark, T.;

Tagliatesta, P.; Sekita, M.; Guldi, D. M. *Chem.-Eur. J.* **2012**, 18, 14008.
11. MacMahon, S.; Fong, R.; Baran, P. S.; Safonov, I.; Wilson, S. R.; Schuster, D. I. *J. Org. Chem.* **2001**, 66, 5499
12. Faul, F. J. C.; Antonietti, M. *Adv. Mater.* **2003**, 15, 673.
13. (a) Ojadi, E.; Selzer, R.; Linschitz, H. *J. Am. Chem. Soc.* **1985**, 107, 7783. (b) van Willigen, H.; Das, U.; Ojadi, E.; Linschitz, H. *J. Am. Chem. Soc.* **1985**, 107, 7784.
14. (a) Fermín, D. J.; Duong, H. D.; Ding, Z.; Brevet, P. F.; Girault, H. H. *Electrochem. Commun.* **1999**, *1*, 29. (b) Eugster, N.; Fermín, D. J.; Girault, H. H. *J. Phys. Chem. B* **2002**, 3428.
15. (a) Yamamoto, K.; Nakazawa, S.; Matsufuji, A.; Taguchi, T. *J. Chem. Soc., Dalton Trans.* **2001**, 251. (b) Hikal, W. M.; Harmon, H. J. *Polyhedron*. **2009**, 28, 113.
16. D'Souza, F.; Hsieh, Y.-Y.; Deviprasad, G. *Chem. Commun.* **1998**, 1027.
17. (a) Fermín, D. J.; Duong, H. D.; Ding, Z.; Brevet, P. F.; Girault, H. H. *J. Am. Chem. Soc.* **1999**, *121*, 10203. (b) Eugster, N.; Fermín, D.; Girault, H. H. *J. Am. Chem. Soc.* **2003**, 125, 4862.
18. Vinodu, M. V.; Padmanabhan, M. *J. Porphyrins Phthalocyanines.* **2001**, 5, 763.
19. Yamada, Y.; Mihara, N.; Shibano, S.; Sugimoto, K.; Tanaka, K. *J. Am. Chem. Soc.* **2013**, 135, 11505.
20. Wang, Z.; Medforth, C. J.; Shelnutt, J. A. *J. Am. Chem. Soc.* **2004**, 126, 15954.
21. Wang, Z.; Medforth, C. J.; Shelnutt, J. A. *J Am. Chem. Soc.* **2004**, 126, 16720.
22. Martin, K. E.; Wang, Z.; Busani, T.; Garcia, R. M.; Chen, Z.; Jiang, Y.; Song, Y.; Jacobsen, J. L.; Vu, T. T. ; Schore, S. E.; Swartzentruber, B. S.; Medforth, C. J.; Shelnutt, J. A. *J. Am. Chem. Soc.* **2010**, 132, 8194.
23. Tian, Y.; Martin, K. E.; Shelnutt, J. Y.-T.; Evans, L.; Busani, T.; Miller, J. E.; Medforth, C. J.; Shelnutt, J. A. *Chem. Commun.* **2011**, 6069.
24. Tian, Y.; Busani, T.; Uyeda, G. H.; Martin, K. E.; van Swol. F.; Medforth, C. J.; Mantaño G. A.; Shelnutt, J. A. *Chem. Commun.* **2012**, 4863.
25. Tian, Y.; Beavers, C. M.; Busani, T.; Martin, K. E.; Jacobsen, J. L.; Mercado, B. Q.; Swartzentruber, B. S.; van Swol. F.; Medforth, C. J.; Shelnutt, J. A. *Nanoscale*, **2012**, 4, 1695.
26. Martin, K. E.; Tian, Y.; Busani, T.; Medforth, C. J.; Franco, R.; van Swol. F.; Shelnutt, J. A. *Chem. Mater.* **2013**, 441.
27. (a) Zakavi, Z.; Rahiminezhad, H.; Alizadeh, R. *Spectrochim. Acta Part A.* **2010**, 994. (b) Masayuki, E.; Mamoru, F.; Tetsuro, M. *Chem.-Eur. J.* **2007**, 13. 8660.
28. In ITC experiments, the first few integrated points in a titration, termed "initialization points", are generally discarded. These points often give erroneous data as a result of: bubbles in the tip of the syringe, extremely exo- or endothermic dilution processes, poor systemic initialization, etc. In the case of the titrations of **MTPPS**s^{4-} into **ZnTTFP**$^{2+}$, the points determined to be initialization points in the *one-site* model were more persistent than those normally observed. Thus, this data was fit with to the *two-sites* model for further analyses.
29. The unit of the binding event reflects the stoichiometric equivalents or *n*-value of the calculated equivalence point. At an *n*-value of ca. 0.15, over 6.5 equiv of guest are expected to bind to the host. Therefore, the units of the binding event were tentatively designated $M^{-6.5}$.

30. Bill, N. L.; Ishida, M.; Bahring, S.; Lim, J. M.; Lee, S. S.; Davis, C.; Lynch, V.; Nielsen, K.A.; Jeppesen, J.O.; Ohkubo, K.; Fukusumi, S.; Kim D.; Sessler, J. L.; *J. Am. Chem. Soc.* **2013**, 135, 10852-10862
31. Ohkubo, K.; Kawashima, Y.; Fukuzumi, S. *Chem. Commun.,* **2012**, 48, 4314.

Chapter 4

BODIPY ExTTF: A Redox Switchable Near-Infrared Emitting Fluorescent Probe

4.1 Introduction

Cancer is one of the deadliest known diseases. In 2007, it was estimated that 13% of human mortalities worldwide directly resulted from cancerous causes. Traditionally cancer has been treated with surgery, radiation therapy and chemotherapy. However, all of these treatments are non-ideal due to their serious side effects (chemotherapy, radiation therapy) or difficulty of implementation (surgery). Recently, photodynamic therapy (PDT) has arisen as a superior treatment method. The benefits of PDT over other treatment protocols include: 1) patients who are too weak to undergo surgery, chemotherapy, or radiation treatments can be treated with PDT; 2) the treatment does not effect areas unexposed to light, sparing healthy tissues from detrimental effects; 3) fewer side effects such as nausea, vomiting and immune disorders; 4) it can be applied in areas where surgery is impossible or impractical; 5) it is a non-invasive treatment; and 6) it can be used in adjunct with other treatment methods.

The effectiveness of PDT modalities is directly related to the properties of the dyes used as sensitizers. Specifically, dyes administered to a patient (either locally

or systemically) must be prone to activation by photoirradiation (with visible or near infrared light), and subsequently generate cytotoxic reactive oxygen species (e.g., singlet oxygen). Current technology utilizes porphyrinoids as sensitizors, with a handful of examples approved for clinical usage. However, porphyrinoids have intrinsic drawbacks. Namely, in general porphyrins lack absorption above 600 nm and have deleterious aggregation tendencies. Boron-dipyrromethenes (BODIPYs) on the other hand, can be tuned to absorb above 600 nm and lack aggregation effects. Thus, they are well suited to replace porphyrinoids as dyes for PDT applications. To this end, initial studies of BODIPY dyes used in PDT applications have been reported. Although the initial work is promising, there is still room for improvement. Specifically, further red-shifting of the absorption bands and optimization of the quantum yield of singlet oxygen generation are warranted.

In this chapter, we report our work with π-extended tetrathiafulvalene BODIPY (**ex-BODIPY**). To shift the absorption of BODIPY further into the red spectral region, we designed **ex-BODIPY** to include electron donating dithiole rings and extended the π-conjugation through vinyl linkages. Initial photosensitizing studies demonstrate **ex-BODIPY** is capable of generating reactive oxygen species upon exposure to light. In addition, **ex-BODIPY** was shown to act as an efficient fluorescent redox switch.

All work detailed in this chapter was performed at the University of Texas at Austin. Dr. Vincent Lynch collected the data and refined the preliminary crystal structure shown in Section 4.5. The author of this dissertation carried out the remainder of the work.

4.2 BODIPY PDT Dye Candidates

Boradiazaindacenes, commonly referred to as boron-dipyrromethenes (BODIPYs), are widely used as fluorescent dyes due to their outstanding photophysical properties.[4.1] Generally, BODIPYs exhibit large absorption extinction coefficients, high fluorescence quantum yields and excellent photostability. Understandably, such favorable characteristics have stimulated significant research utilizing BODIPYs as a photoactive component. Improvements in functional group incorporation and post-synthetic modification protocols have led to BODIPYs finding use in a diverse variety of applications including as chemosensors,[4.2] sensitizers for solar cells,[4.3] so-called energy-transfer cassettes,[4.4] light harvesters,[4.5] fluorescent organic devices,[4.6] and laser dyes.[4.7] Further, significant optimization of the band gaps normally seen for BODIPYs has been achieved, providing dyes that emit and absorb light throughout the visible spectrum. Recently, the attractive photophysical properties of BODIPYs have been extended to include dyes that emit in the near infrared (NIR) region of the electromagnetic spectrum. This research, in turn, has widened the scope or potential applications for this class of chromophores.

From a medical standpoint, dyes that absorb and/or emit light in the so-called "therapeutic window" (between 650 and 900 nm) are particularly attractive. In the therapeutic window, light absorption by cells, tissues and water, autofluorescence, and light scattering are substantially diminished compared to similar parameters at shorter wavelengths.[4.8] For example, the transmission of light through the dermis and other bodily tissues diminishes exponentially with the *in vivo* pathlength of transmission. Short wavelength light (blue and ultraviolet) is transmitted much

shorter distances than longer wavelength light (red and near infrared (NIR)). Specifically, blue light is only able to penetrate a few millimeters into the skin, whereas red light can penetrate up to 22 cm.[4.8] Thus, dyes that absorb and/or emit in this spectral region, allow the photochemical characteristics of the dye to be accessed at greater depths within bodily tissues, that dyes that absorb at shorter wavelengths.

One intriguing application of dye absorption in the therapeutic window is photodynamic therapy (PDT). PDT methods rely on the preferential localization of photoactive drugs within tumor cells, which upon exposure to light generate reactive oxygen species—irreparably damaging the diseased cells. To date, this treatment method has shown promise in the treatment of malignant tumors,[4.9] age-related macular degeneration,[4.10] actinic keratosis,[4.11] cardiovascular illnesses,[4.12] and multidrug-resistant tumors.[4.13]

A small number of functionalized porphyrins have been utilized for PDT applications. However, in this regard, porphyrins have significant disadvantages. One of the most prominent among these is that porphyrins generally do not absorb light in the therapeutic window. The lack of long wavelength absorption minimizes porphyrins utility as PDT dyes in all but the most superficial afflictions (i.e. conditions that are on the skin surface such as melanoma and basal-cell carcinoma). Alternatively, compounds that absorb at longer wavelengths such as phthalocyanines,[4.14] perlenediimides,[4.15] texaphyrins,[4.16] and others[4.17,] are attractive substitutes for porphyrins. BODIPY-based dyes also provide a viable alternative for

use as PDT sensitizers. Thus, efforts to realize red-NIR absorbing BODIPY dyes are a topic of current interest.

Photodynamic therapy relies on a drug being capable of fulfilling a variety of roles. First, the compound must selectively locate within the cells to be treated. Many poly-pyrrolic macrocycles satisfy this requirement intrinsically, prompting their use in PDT therapy. Second, the compound must efficiently absorb light at wavelengths capable of reaching the affected area. Third, the excited singlet state of the dye must undergo intersystem crossing to produce the corresponding triplet state. This triplet must be energetically and kinetically competent to transfer its energy to triplet oxygen, thereby generating singlet oxygen ($^1O_2$). This is known as a Type II process.[4.18] It has been well established that intersystem crossing is accelerated by the heavy atom effect and therefore halogens such as bromine and iodine are commonly incorporated into PDT sensitizer designs.[4.18b]

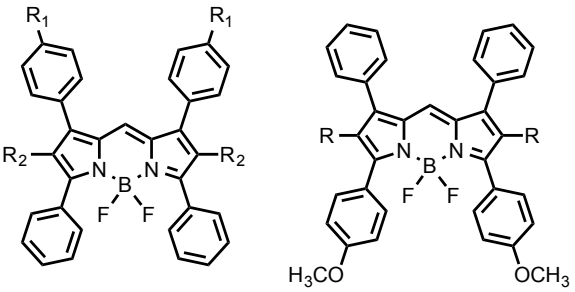

4.1a R_1 = H, R_2 = H
4.1b R_1 = Br, R_2 = H
4.1c R_1 = H, R_2 = Br

4.2a R = H
4.2b R = Br

A few examples have been reported detailing BODIPYs or aza-BODIPYs that absorb light in the therapeutic window and show promise as PTD drug candidates. A leading example from the O'Shea group utilizes derivatives of tetraphenyl aza-BODIPY compounds **4.1**.[4.18-4.21] In fundamental work, the investigators found the efficiency of singlet oxygen production was closely tied not only to the presence of heavy-atoms (bromine) but also to the regio-connectivity of the heavy-atoms.

Specifically, **4.1a** was found to not generate $^1O_2$. Conversely, **4.1b** had moderate activity due to intramolecular heavy atom effects, and **4.1c** was shown to be effective at generating $^1O_2$.

After **4.1** showed promising results for photoinduced $^1O_2$ generation, it and close congeners, such as the methoxy-derivative **4.2**, were subjected to cellular studies.[4.19] Although **4.2b** has been shown to intersystem cross to the triplet state efficiently, it fortunately retains adequate fluorescence quantum yield (Φ = 0.1) for the biodistribution and clearance of the drug to be monitored *via* fluorescence spectroscopy. When **4.2b** (as a formulation with Cremophor) was incubated with HeLa and MRC5-SV40 cell lines it was found to localize perinuclearly. Cytotoxicity studies demonstrated that compounds **4.1** and **4.2** have considerable phototoxicity. In general, both compounds display negligible dark toxicity in HeLa and MRC5-SV40 cell lines. However, after exposure to a long wavelength light source (600-750 nm, with an intensity of 8 J/cm^2), significant toxicity was observed. Quantitatively, compound **4.1a** was found to have an EC_{50} value of 3.1 x 10^{-6} M for MRC5-SV40 cells and 2.8 x 10^{-6} M for the HeLa [4.22] cell line. More promising was compound **4.2b**, of which EC_{50} values of 3.7 x 10^{-8} M and 6.3 x 10^{-8} M were found for MRC5-SV40 and HeLa cells, respectively. These studies also further highlighted the benefit of heavy atoms to enhance intersystem crossing and generate reactive oxygen species efficiently. For example, the heavy-atom free compound **4.2b** was found to be 1000-fold less active than **4.2a**. Predictably, increasing the light fluence rate led to enhanced cytotoxicity in all cases.

In vivo PDT murine studies were performed using **4.2b** as the photoactive drug.[4.20,4.21] Compound **4.2b** was found to be well tolerated *in vivo* and cleared from the body within 48 h of administration based on fluorescence measurements (Figure 4.1). Nude mice implanted with MDA-MB-231-GFP breast cancer xenografts (grown to 7-9 mm in diameter) were injected with **4.2b** and immediately exposed to 690 nm light in the area around the tumor. Following treatment, the tumors underwent necrotic damage, taking up to 30 days to heal. In contrast healthy tissue surrounding the tumor suffered from edema and redness. However, these side-affects subsided within two days. The treatment was found to be anti-vascular in nature, requiring immediate exposure to light after injection for best results. Optimal procedures resulted in a 71% cure rate[4.23] after six months.

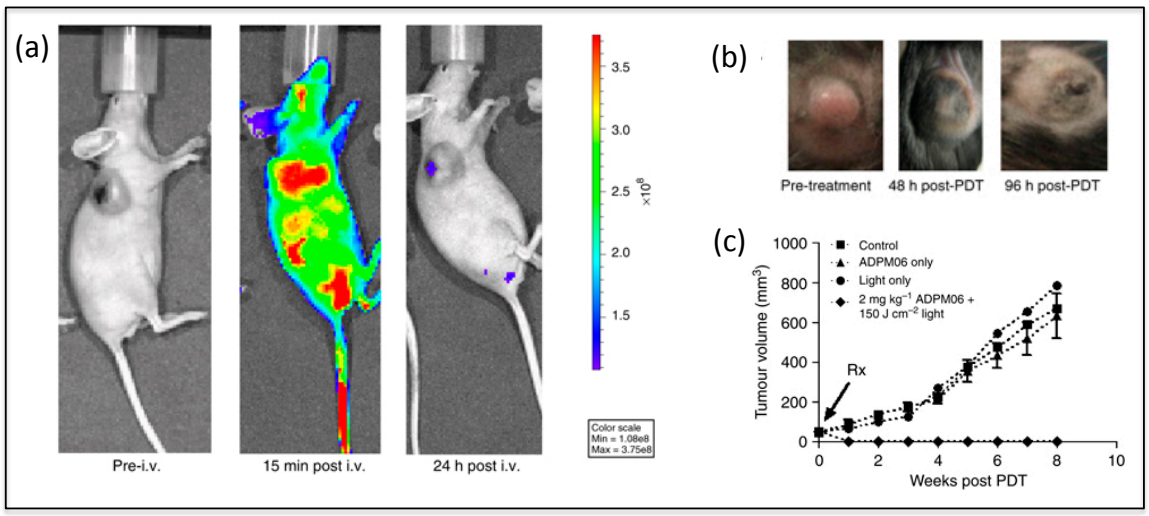

Figure 4.1. (a) Fluorescence images of a mouse injected intravenously with **4.2b** displaying the bioclearance of the drug. The left is the background fluorescence pre-treatment, the middle is 15 minutes post-treatment and the right is 24 h post-treatment. (b) Photographs demonstrating the tumor regression of a xenografted MDA-MB-231-GFP breast cancer tumor implanted into a nude mouse after PDT treatment with **4.2b**. Left is pre-treatment, middle is 48 h post-treatment and right is 96 h post-treatment. (c) Graph of tumor volume over time for PDT treatment with **4.2b** and controls. In this graph compound **4.2b** is referred to by its designation in the originally published manuscript: ADMO6. Figure adapted with permission from Macmillan Publishers Ltd. *Br. J. Cancer,* **2009**, 101, 1565.

A drawback of promising targets **4.1**, **4.2**, and molecules of similar ilk is their intrinsic lack of water solubility, requiring a formulating agent for administration. To address the aforementioned solubility issues and confer amphiphilic character, the Akkaya group introduced several triethylene glycol moieties around the periphery of red-absorbing BODIPY molecule **4.3**.[4.24] In buffered aqueous solutions, **4.3** showed no signs of aggregation (up to mM concentrations) and demonstrated strong absorbance at 660 nm (ε = 102,000 M^{-1} cm^{-1}). Initial studies with 1,3-diphenylisobenzofuran (DPBF) in 2-propanol revealed **4.3** to be an efficient generator of $^1O_2$. Cell studies demonstrated compound **4.3** has an EC_{50} value of 200 nM in K562 human erythroleukemia cells irradiated under 625 nm LED irradiation at 2.5 mW cm^{-2} fluence.

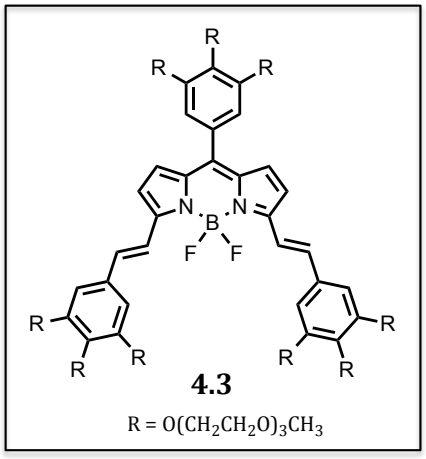

Other promising BODIPY-based PDT systems absorbing in the therapeutic window have been reported. To put the author's work in context, a few of these are reviewed briefly below. Asymmetrical distyryl-diiodo BODIPY compounds (**4.4**) were prepared by Ng and Lo and reported in 2011. These systems are attractive since they allow the solubility, functionality and absorption profiles of the compounds to be easily adjusted by successive Knoevenagel condensations.[4.25] Cationic species **4.4d** shows

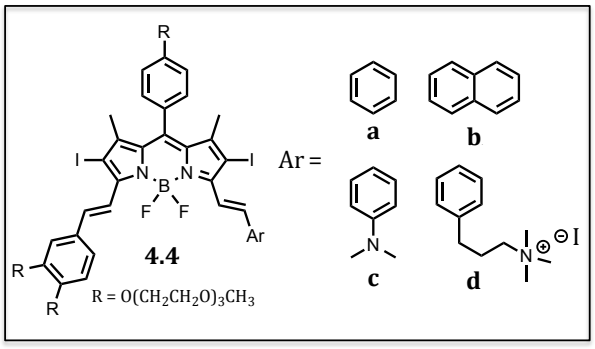

the highest phototoxicity, with an IC_{50} of 15 nM after irradiation above 610 nm. Diiodo-BODIPYs with tweezer-like pyrene arms (**4.5**) interact non-covalently with single-wall carbon nanotubes (SWNT).[4.26] This interaction is proposed to have the potential to serve as a delivery system. However, lower levels of singlet oxygen generation is observed for **4.5** bound to SWNT than with just **4.5** alone in DPBF degradation studies.

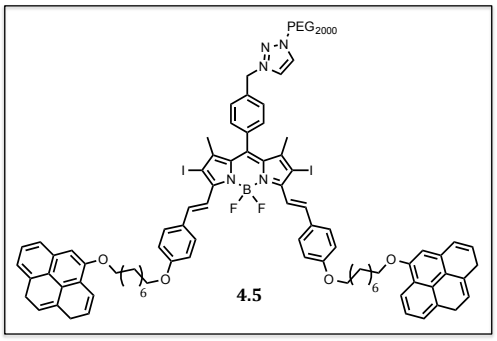

Heterocyclic rings have also been appended to BODIPY cores through both vinyl and *meso* linkages.[4.27] *Meso*-linked heterocycles with iodine substituents, such as **4.6**, were reported generate $^1O_2$ based on phosphorescence measurements at 1270 nm after irradiation at 532 nm. It is clear, based on qualitative analyses, that compound **4.6a** (with an pendant furan moiety) produces more $^1O_2$ than the analogous compounds **4.6b** and **4.6c**. However, no quantitative measurements of singlet oxygen quantum yield have been reported. Finally, a BODIPY core directly annulated to bithiophene moieties (**4.7**) shows promise as a PDT drug candidate.[4.28] Compound **4.7** was found to efficiently generate $^1O_2$ when irradiated with 635 nm laser light (by both DPBF and $^1O_2$ phosphorescence experiments). The quantum yield of singlet oxygen was found to be $\Phi_\Delta = 0.61$, calculated from the slope of the DPBF photodegradation study. In

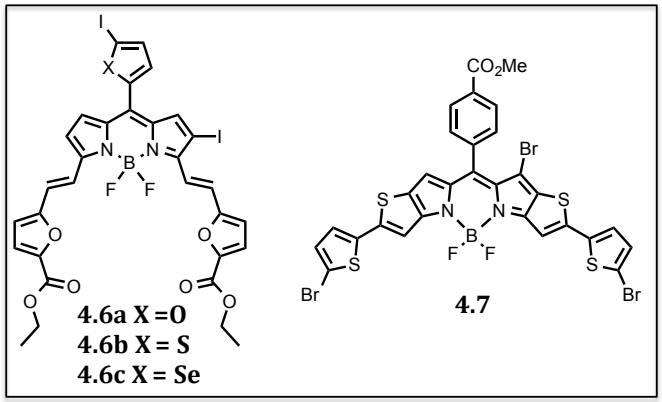

cellular studies with the HeLa cell line, negligible dark toxicity was observed for **4.7**. Conversely, irradiation of HeLa cells treated with **4.7** at 635 nm, led to significant cytotoxicity (IC_{50} = 7.12 μM). In summary, BODIPY based dyes absorbing at wavelengths above 600 nm and capable of intersystem crossing show promise as PDT drug candidates. However, only a few examples have been reported to date.

A large number of far-red to NIR absorbing and/or emitting BODIPY dyes have been reported for applications outside of PDT. Unmodified BODIPYs generally absorb around 500 nm. However, the basic core can be subjected to a variety of structural modifications to induce bathochromic shifts to the absorbing and emitting wavelengths. For example, red-shifted BODIPYs can be achieved by 1) replacement of the *meso* carbon with a nitrogen atom, forming aza-BODIPYs,[4.19,4.29] 2) extension of the conjugated skeleton,[4.30] 3) substitution of the central core with electron-donating groups,[4.31] 4) annulation of the pyrrole rings,[4.32] and 5) rigidification of the BODIPY skeleton.[4.33] A combination of one or more of the aforementioned structural modifications allows the absorption and emission of BODIPYs to be shifted over 200 nm, extending well into the NIR.

Taken collectively, the literature dictates that the design of a new potential PDT-active BODIPY should include a number of traits for optimal performance. First, one or more of the features known to induce bathochromic shifts in the absorption and emission wavelengths should be incorporated into the BODIPY framework to bring the photophysical properties of the target compound into the "therapeutic window". Second, a mechanism facilitating intersystem crossing and subsequent generation of singlet oxygen is necessary. Third, if possible, hydrophilic moieties to improve the

solubility characteristics of the BODIPY targets should be considered. With these design parameters in mind, we targeted π-extended TTF compound **ex-BODIPY** as a potential PDT agent (Figure 4.2). We hypothesized that extension of the conjugated framework with an electron-rich dithiole ring would induce a bathochromic shift in the absorption and emission wavelengths. Further, the proposed structure has several sulfur atoms to help facilitate intersystem crossing through the heavy-atom effect. Lastly, the proposed configuration is expected to allow for further synthetic modifications that might permit the solubility and/or photophysical parameters to be fine-tuned for a specific application. For example, in principle, the *meso*-aryl group could be replaced by a triethylene glycol-substituted phenyl ring so as to engender water solubility, as was done in the case of compound **4.3**, reported previously. This chapter details our work with **ex-BODIPY** and attempts to highlight future potential applications of this novel molecule.

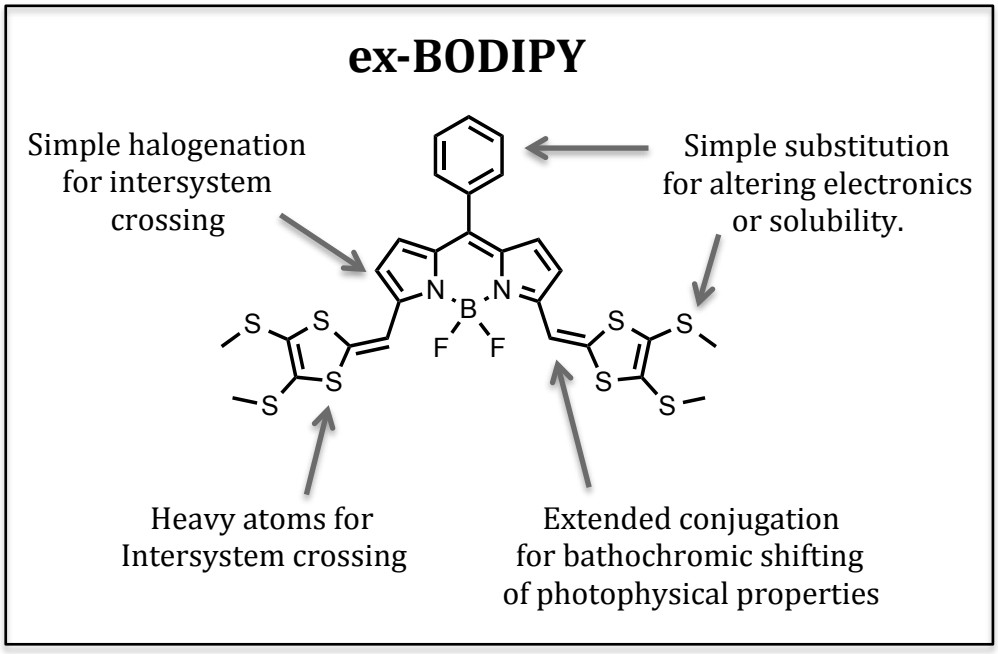

Figure 4.2. Proposed structure of **ex-BODIPY** highlighting the favorable design characteristics and sites amenable to further modification.

4.3 Synthesis of ex-BODIPY

The synthesis of **ex-BODIPY** originates from the condensation of pyrrole with benzaldehyde in the presence of acid, generating *meso*-phenyl dipyrromethane **4.8** (Scheme 4.1). Subjecting **4.8** to Vilsmeier formylation conditions resulted in 1,9-diformyl-5-phenyl-dipyrromethane **4.9**. Once in hand, compound **4.9** was transformed into diformyl BODIPY **4.10** by modifying a procedure used to prepare diformyl *meso*-toluyl BODIPY.[4.34] Specifically, **4.9** was exposed to 2,3-dichloro-4,5-dicyanoquinone (DDQ), generating the oxidized dipyrromethene *in situ*. Subsequently, addition of excess triethylamine (TEA) followed quickly by careful addition of excess $BF_3{\bullet}(OEt)_2$ to the dipyrromethene species afforded diformyl-BODIPY **4.10**. Addition of the $BF_3{\bullet}(OEt)_2$ to the deprotonated dipyrromethene was carried out as rapidly as possible, while simultaneously avoiding exotherms. This strategy proved essential to achieving the highest possible (albeit still relatively low) reaction yields. Compound **4.10** was isolated by column chromatography as a brightly fluorescent yellow-orange solid.

Scheme 4.1. Synthesis of diformyl BODIPY **4.10**.

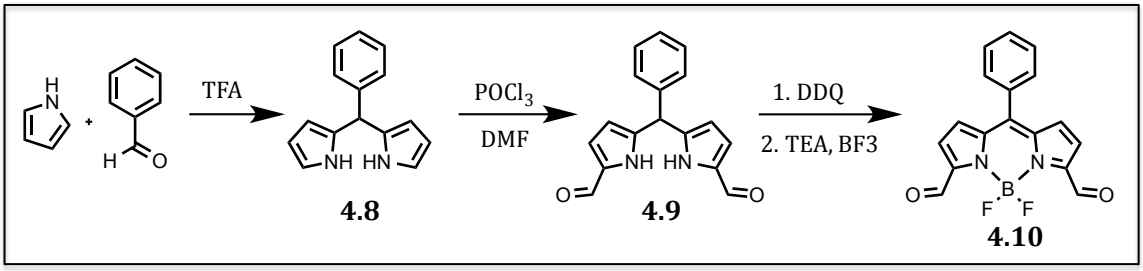

Initial attempts to generate **ex-BODIPY** by coupling thione **2.24** to **4.10** through a triethylphosphite promoted coupling protocol resulted in no observed product and degradation of the starting material (Scheme 4.2). However, the coupling of

dithiolidene rings to **4.10** was achieved through the utilization of a Horner-Wadsworth-Emmons (HWE) type procedure. Dithiole-phosphonate ester **4.14** has previously been reported in the literature,[4.35] and synthesis of this compound follows three preparative steps from **2.24**. First, the methylated salt of **2.24** is prepared by exposure of this compound to a methylating agent, such as dimethylsulfate. Subsequent, addition of $NaBH_4$ results in compound **4.12**. Exposure of **4.12** to hydrofluoroboric acid and acetic anhydride in diethyl ether leads to the elimination of the thiomethyl moiety, precipitating salt **4.13** from solution. Finally, cation **4.13** is reacted with triethyl phosphite to afford the HWE coupling partner, **4.14**, in 72 % overall yield. After column chromatography, **4.14** is isolated as a red oil. If sufficiently pure, **4.14** will crystallize in the freezer overnight as a red crystalline solid.

Scheme 4.2. Synthesis of **ex-BODIPY** from the HWE coupling of diformyl BODIPY **4.10** to phosphonate ester **4.14**.

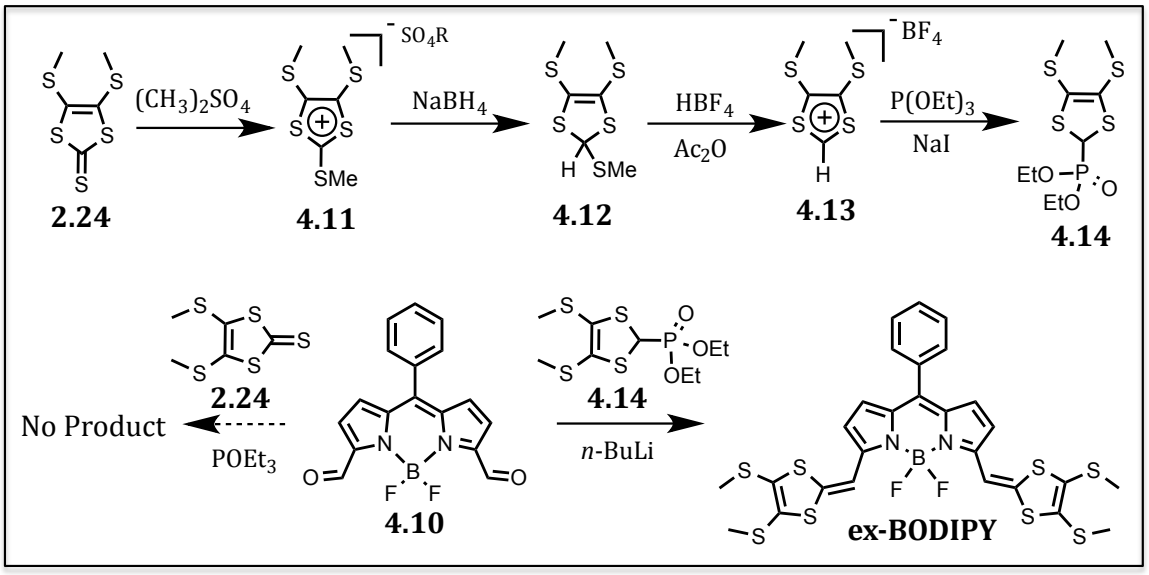

Deprotonation of **4.14** with *n*-BuLi,[4.36] followed by addition of **4.10** resulted in the formation of **ex-BODIPY** in 85% yield. Flash column chromatography of **ex-**

BODIPY over silica gel provided compound sufficiently pure to allow for characterization and further studies. However, leaving the **ex-BODIPY** compound on the column for prolonged periods of time led to degradation of the target compound and the formation of a dark green, intensely colored spots with slower retention times. However, isolation of **ex-BODIPY** followed by thorough drying gave a bench-stable crystalline compound. The ^{1}H NMR spectrum and mass spectrum are fully consistent with the proposed structure of **ex-BODIPY**.

4.4 Redox Properties

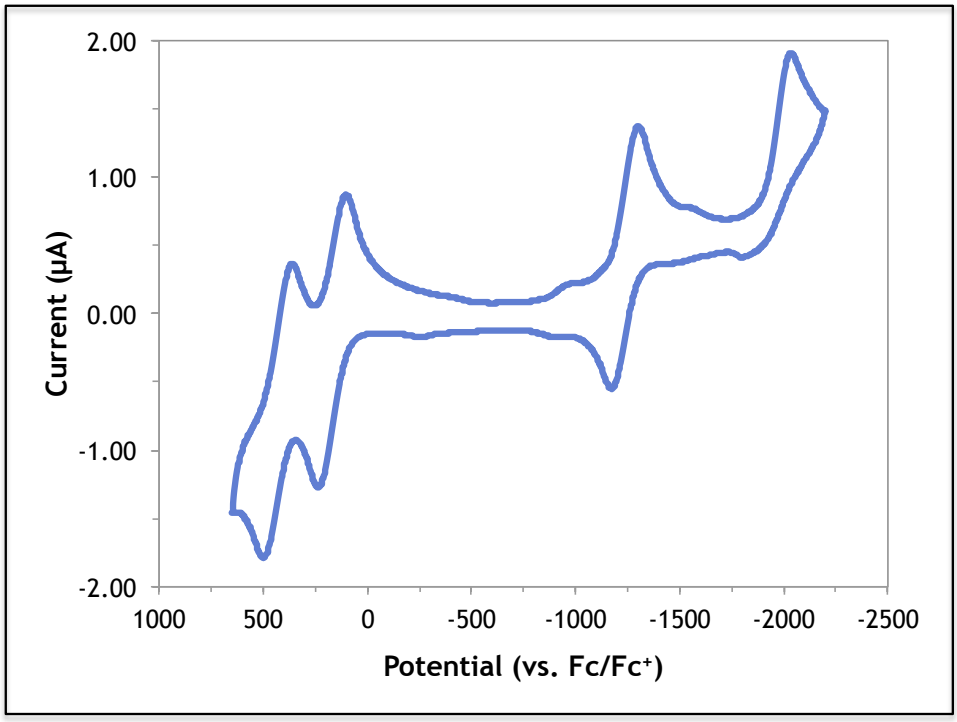

Figure 4.3. CV of a 1 mM dichloromethane solution of **ex-BODIPY** at 298 K in the presence of $TBAPF_6$ (100 mM) as the supporting electrolyte. Glassy carbon working electrode, Pt wire auxillary electrode and Ag/AgCl reference electrode. Values reported are referenced to an internal Fc/Fc^+ standard.

The redox character of **ex-BODIPY** was studied by cyclic voltammetry (CV) in dichloromethane, scanning in both the positive and negative directions (Figure 4.3). Unlike **MTTFP**s (Chapter 2), two reversible oxidation waves are observed at mild

potentials for **ex-BODIPY**. Specifically, the half-wave potential of the first one-electron oxidation (E_{1ox}) is centered at c.a. 169 mV (vs. Fc/Fc^+) while the second one-electron process (E_{2ox}) occurs at c.a. 433 mV. The significant splitting (> 250 mV) between E_{1ox} and E_{2ox} is an indication that the radical cation state is easily accessible and relatively stable in solution under these experimental conditions.

Although the dithiole rings are separated by the same number of bonds in both **MTTFP** and **ex-BODIPY**, the former is marked by a single two-electron oxidation peak whereas the latter has a pair of one-electron oxidation peaks split by 0.26 V. We take this as a direct indication that in **ex-BODIPY** the geometry of the pyrrolic core is most likely planar, allowing for significant electronic communication between the dithiole rings. This stands in direct contrast to what is observed for the saddle-shaped **MTTFP**s. The effects of Columbic repulsion between the positive charges localized on the oxidized dithole rings have frequently been invoked to justify the splitting of the first and second oxidation potentials of exTTFs (Chapter 1.1). In the case of pristine TTF, the difference between the half-wave potentials (E_2 - E_1) is equal to 0.44 V,[4.37] whereas in **ex-BODIPY** the difference is 0.26 V. Although a large decrease in E_2 - E_1 is observed in **ex-BODIPY** compared to TTF, the observed oxidative splitting of **ex-BODIPY** is larger than other π-extended TTFs separated by just a single double bond. Alkene bridged exTTF Systems with similar levels of conjugation to **ex-BODIPY** have no splitting between the first and second oxidation waves. Instead, these alkenyl-bridged exTTFs appear to oxidize *via* a single two-electron process. Most likely the discrepancy in the oxidation behavior between **ex-BODIPY** and multi-olefinic systems results from the latter compounds being twisted

or distorted from planarity in the neutral state (similar to **MTTFP**s). Upon oxidation, these compounds undergo a structural change, which "inverts" the potentials for the second oxidation process. The rigidity of the BODIPY core most likely locks the molecule in a planar stereochemical orientation. This prohibits distortion from planarity and leads to the observed oxidative splitting. Regardless, the splitting is of an unexpectedly large magnitude to result solely from Columbic repulsion. Therefore, it is our opinion that factors other than dithiole electrostatic interactions most likely contribute.

The reduction chemistry of **ex-BODIPY** was also investigated by cyclic voltammetry. A CV scan of **ex-BODIPY** towards negative potentials displayed two reduction waves, assigned to reduction processes of the BODIPY core. The first process (arising at -1.24 V vs. Fc/Fc^+) is reversible whereas the second (c.a. -2.0 V vs. Fc/Fc^+) results in an irreversible wave.[4.38] For comparison, previously reported tolyl-substituted compounds **4.15** and **4.16** are used as relevant models. The CVs of compounds **4.15** and **4.16** are displayed in Figure 4.4.[4.34] The CVs of **ex-BODIPY** and **4.15** are rather similar to one another. The first reductions (E_{1red}) of both compounds happen at nearly identical potentials (-0.79 V[4.39] for **ex-BODIPY** and -0.80 V for **4.15** vs. SCE). Further, the second reduction potentials (E_{2red}) are both irreversible, although E_{2red} of **4.15** is considerably cathodically shifted (-1.82 V) compared to what is seen for the same process in the case of **ex-BODIPY** (-1.59 V). Diformyl compound **4.16**, the *meso*-toluene substituted analogue of **4.10**, has gives rise to reduction peaks that are anodically shifted compared to **ex-BODIPY** and **4.15**. This result is ascribed to the electron-withdrawing effect of the appended

formyl groups, which should facilitate reduction. Although the diformyl compound is easily reduced, no oxidative peaks were observed in the case of **4.16** within the electrochemical window of dichloromethane. Further, the first oxidation wave for **4.15** occurs at 1.68 V vs. SCE, nearly 0.8 V higher than the corresponding value for **ex-BODIPY**. In summary, the **ex-BODIPY** target retains the reductive properties of the BODIPY core, while enhancing the oxidative prowess of the molecule. The effect of modifying one redox property and not another is to shorten the band gap relative to **4.15** and **4.16** and provide more facile access to multiple reversible redox states.

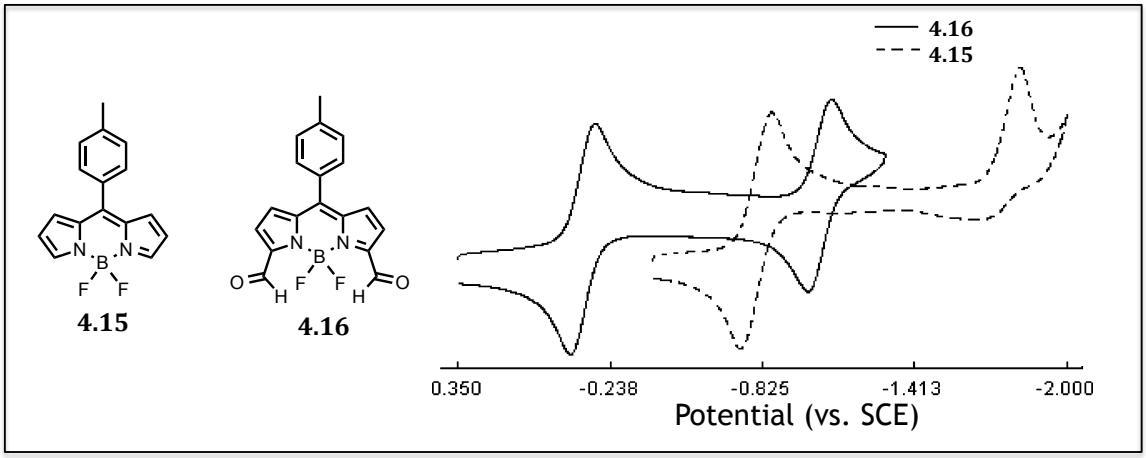

Figure 4.4. Chemical structures and CVs of BODIPY reference compounds **4.15** and **4.16**.

4.5 Photophysical Studies and Oxidation of ex-BODIPY

BODIPY-based molecules are appreciated for exhibiting well-defined and sharp absorption bands that can be tuned to absorb light throughout the visible spectrum. The ultraviolet/visible/near infrared absorption spectrum of **ex-BODIPY** was recorded in dichloromethane and is shown in Figure 4.5. **Ex-BODIPY** is characterized by an absorption maximum in the NIR portion of the spectrum (λ_{max} = 754 nm) with less intense bands being observed throughout the visible region. The

molar absorptivity at 754 nm is relatively high (ε = 96,000 M^{-1} cm^{-1}), thus providing conformation that in a dichloromethane solution **ex-BODIPY** efficiently absorbs NIR radiation. The estimated optical band gap from the absorption spectrum is 1.64 EV. On the other hand, the calculated band gap from the CV is only 1.41 EV. It is unclear what causes the optical band-gap to be significantly higher than the electrical gap.

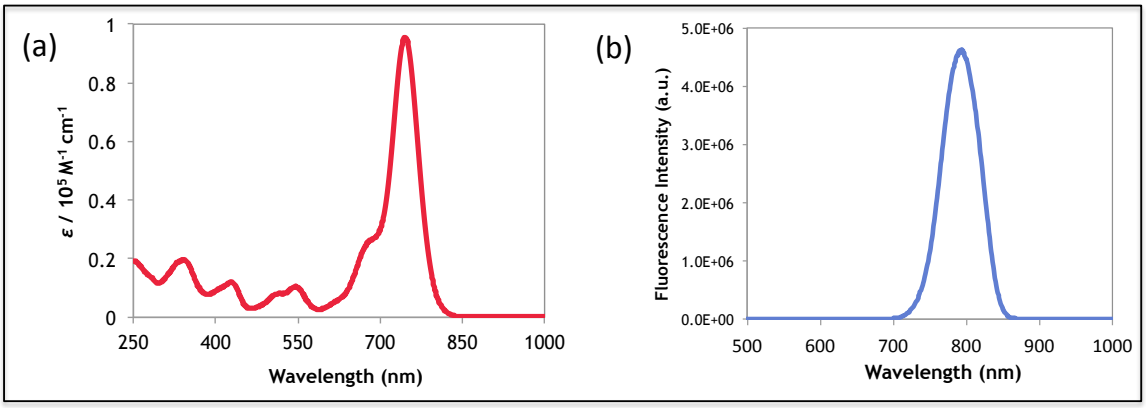

Figure 4.5. (a) UV/vis/NIR absorption spectra of **ex-BODIPY** recorded in CH_2Cl_2 at 298 K. (b) The emission spectra of **ex-BODIPY** recorded upon excitation at 754 nm in CH_2Cl_2 at 298 K.

The steady-state emission spectrum of **ex-BODIPY** was measured by exciting the sample at the absorption maximum (754 nm) in CH_2Cl_2 at 298 K (Figure 4.5). A sharp fluorescence emission signal was seen under these conditions with λ_{max} = 803 nm. This value is noteworthy as it is among the highest ever reported for BODIPY derivative seen to date. Independent of precedent, it means that light emission takes place entirely within the infrared region of the electromagnetic spectrum.

The fluorescence quantum yield of **ex-BODIPY** was calculated using indocyanine green (ICG) as a fluorescent standard. In dimethyl sulfoxide (DMSO), the quantum yield of fluorescence for ICG is reported to be Φ_F = 0.106.[4.40] The fluorescence quantum yield of an unknown sample can be estimated from a known standard using the equation:

$$\Phi_{\mathrm{f}}^{s} = \frac{F^{s}\mathrm{A_r}n_{s}^{2}}{F^{r}\mathrm{A}_{s}n_{r}^{2}}\ \Phi_{\mathrm{f}}^{r}$$

where Φ_{f}^{s} and Φ_{f}^{r} are the fluorescence quantum yields of the sample and the reference, respectively; F^{s} and F^{r} are the integrated fluorescence intensities (areas) of the sample and reference spectra, respectively; A_{s} and A_{r} are the absorbance of the sample and reference at the excitation wavelength, respectively; the refractive indices of the sample and reference are n_{s}^{2} and n_{r}^{2}, respectively.

To calculate the fluorescence quantum yield of **ex-BODIPY**, a DMSO solution of ICG and a separate DMSO solution of **ex-BODIPY** were prepared. Using the same solvent for the fluorescence measurements of both the sample and reference compounds eliminates the refractive index considerations from the quantum yield calculations. Additionally, the concentrations of the solutions were adjusted[4.41] to ensure that the dyes had identical absorbances as 750 nm (the excitation wavelength), removing light absorption considerations from the quantum yield calculation. Using this method, **ex-BODIPY** was found to have a low fluorescence quantum of Φ_{f} = 0.019 for **ex-BODIPY**. The low fluorescence quantum yield could possibly be the result of the four sulfur atoms of the dithiolidine ring facilitating intersystem crossing to the triplet state through the heavy atom effect.

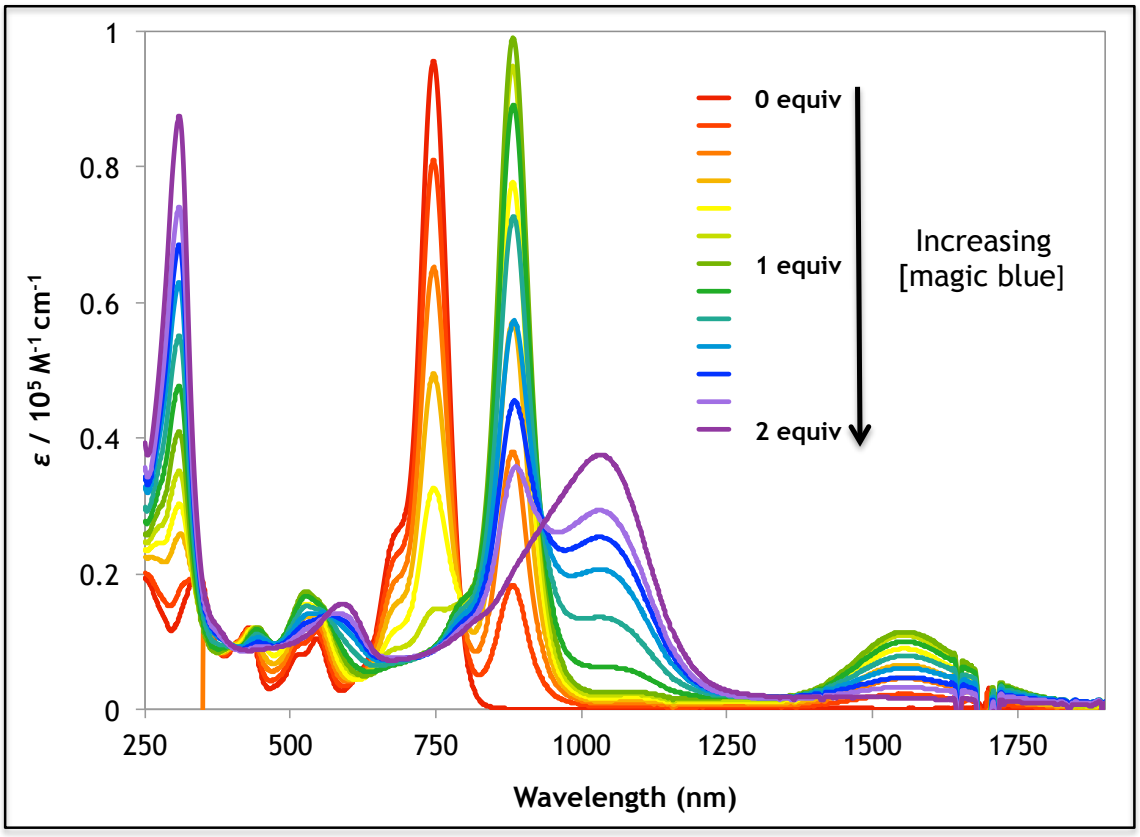

Figure 4.6. Chemical oxidation of **ex-BODIPY** with tris(4-bromophenyl)aminium hexachloroantimonate ("magic blue") in dichloromethane. Of particular note are the spectra of pristine **ex-BODIPY** (red), and the ones recorded after one molar equivalent of magic blue has been added (yielding **ex-BODIPY$^{\bullet+}$,** yellow-green), and two molar equivalents of magic blue have been added (giving **ex-BODIPY^{2+},** violet).

Oxidative titrations of **ex-BODIPY** with tris(4-bromophenyl)aminium hexachloroantimonate (magic blue) were carried out to define the species produced upon oxidation. These changes were followed by absorption spectroscopy (Figure 4.6). Upon treatment of **ex-BODIPY** with increasing amounts of magic blue, the band at λ_{max} = 754 nm was attenuated. Concurrently, an increase in a sharp, intense band at λ_{max} = 886 nm and a broad less-intense band at λ_{max} = 1572 nm were seen.[4.42] These changes in optical signature continued until one molar equivalent of magic blue had been added, at which point complete disappearance of the original peak at 754 nm was noted. Additionally, the newly formed peaks reached a

maximal intensity at this point. Broad absorption bands above 1000 nm are diagnostic of TTF radical-cations. Thus, the spectra obtained after addition of one equivalent of magic blue is assigned to the one-electron oxidized species **ex-BODIPY$^{\bullet+}$**. Further addition of oxidant resulted in a decrease in the intensity of the peaks assigned to **ex-BODIPY$^{\bullet+}$** and an increase in a broad band with λ_{max} = 1032 nm. This band is assigned to the two-electron oxidized dication **ex-BODIPY^{2+}**. After two molar equivalents of oxidant had been added, the peak attributed to **ex-BODIPY^{2+}** reached maximal intensity. Further addition of oxidant resulted in no additional spectral changes to the **ex-BODIPY^{2+}** species. However, a peak attributed to unreacted magic blue was observed (λ_{max} = 700 nm). This band grows without saturation upon addition of further aliquots (not pictured). The emission spectra of **ex-BODIPY$^{\bullet+}$** and **ex-BODIPY^{2+}** could not be studied with the equipment in the Sessler lab. Both species are expected to produce fluorescence signals outside the range of the detector in our fluorimeter (> 1000 nm).

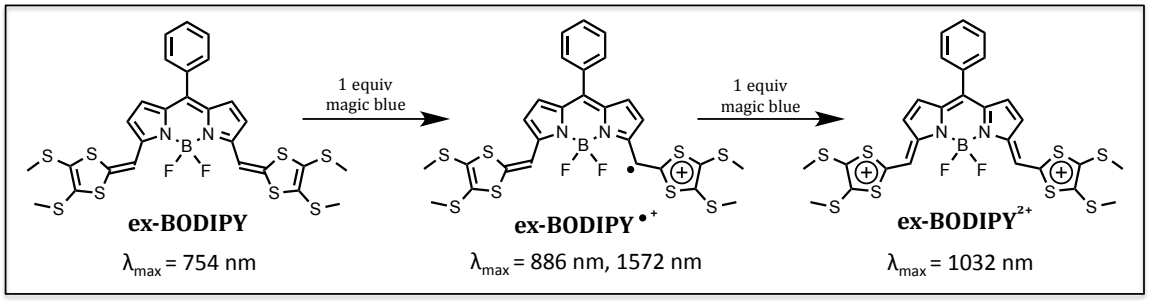

To correlate the absorption spectroscopy oxidation data with the electrochemistry data we turned to spectroelectrochemistry. Using a specialized 1 mm pathlength cuvette, with a semi-transparent platinum mesh working electrode, we were able to observe the solution-state absorption spectral changes

induced by electrochemical oxidation (Figure 4.7). In these studies, the **ex-BODIPY** sample was bulk electrolyzed at -50 mV (vs. Fc/Fc^+) for two minutes. After bulk electrolysis, the current was discontinued and the UV/vis/NIR absorption spectrum was taken without disturbing the sample. Following the absorption reading, the potential was ramped 100 mV anodically, resubjected to bulk electrolysis for two minutes, and the absorption spectrum was then recorded. This process was repeated eight times, until the potential used for bulk electrolysis was equal to 750 mV. The traces obtained by this method are not as well defined as the traces acquired by chemical oxidation. However, when the spectroelectrochemistry data is considered in concjuction with the chemical oxidation data, direct correlations between the electrochemistry and absorption profiles can be made.

Examination of Figure 4.7 shows that at -50 mV, the absorption spectra closely mimics that of **ex-BODIPY**. Namely, the spectrum is defined by an intense peak with $\lambda_{max} \approx 750$ nm, and less-intense bands throughout the visible region. At this potential only the neutral form is present is solution, as inferred from the CV analysis. Upon ramping the voltage to potentials more positive than the first oxidation of **ex-BODIPY**, an increase in the intensity of the peaks with $\lambda_{max} \approx 890$ nm and 1570 nm is seen. These changes closely mimic those present after addition of one equivalent of chemical oxidant. At 350 mV (between the first and second oxidation waves of **ex-BODIPY**), both transient peaks reach a maximum. Further, the peak centered at 750 nm is no longer visible. Thus, similar to the chemical oxidation titration, this spectrum is thought to reflect the presence of the radical cation **ex-BODIPY**$^{\bullet+}$. Ramping the potential to higher voltages results in attenuation

of the peaks assigned to **ex-BODIPY**$^{\bullet+}$ and an increase in those assigned to **ex-BODIPY**$^{2+}$ (broad peak at $\lambda_{max} \approx 1030$ nm). At 750 mV this peak reaches a maximum. Additional ramping of the voltage results in a lack of spectral changes, as is expected from the previously reported CV data.

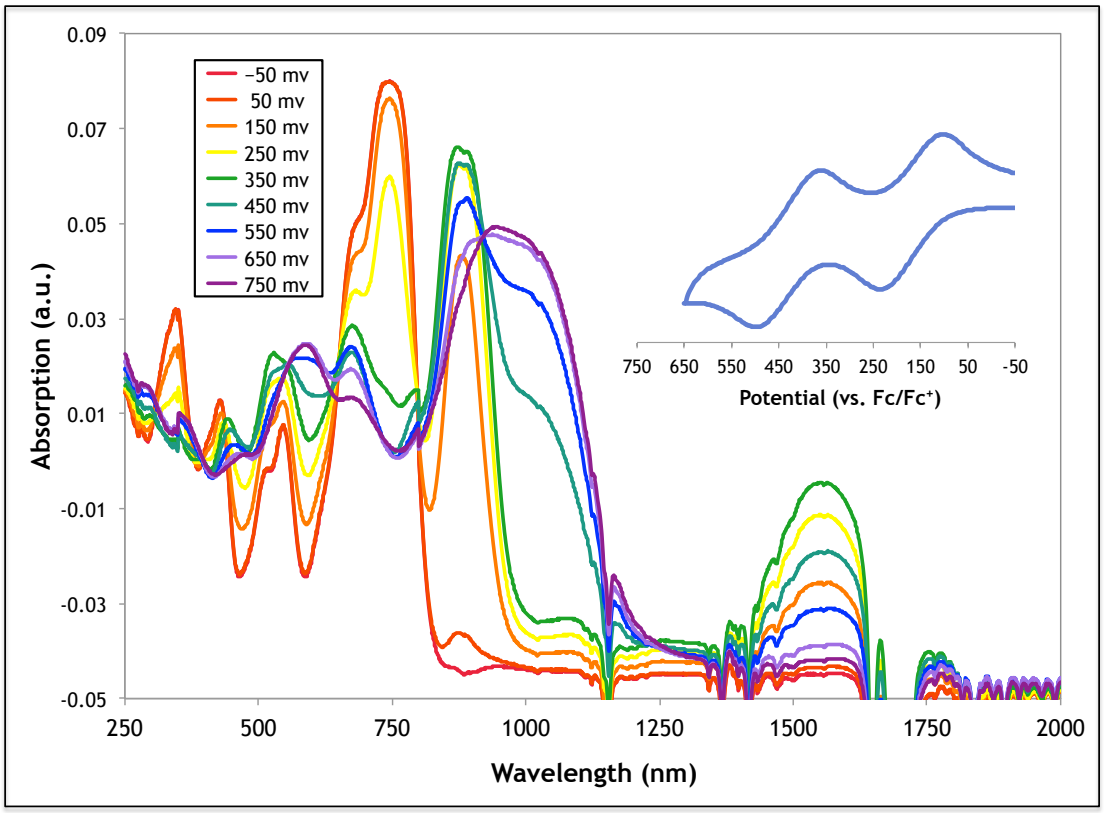

Figure 4.7. Spectroelectrochemical oxidation of **ex-BODIPY** from -50 mV (red) to 750 mV (violet) in CH_2Cl_2 at 298 K. The sample was bulk electrolyzed for two minutes before taking an absorption reading and then subjecting the sample to further oxidation. The potentials were ramped in 100 mV intervals. The values reported are referenced to Fc/Fc^+.

4.6 Crystal Structure of Radical Cation Dimer Ex-BODIPY$_2$

Initial attempts to grow a crystal structure of **ex-BODIPY** suitable for X-ray diffraction analyses were met with difficulty. Upon letting a dichloromethane solution of **ex-BODIPY** stand overnight exposed to light, the solution containing the compound changed from a maroon color to an intense blue color. In contrast, a

solution kept in the freezer or carefully protected from light did not change color over the course of several days.[4.43] UV/vis absorption spectroscopy of the blue colored solution showed that a large amount of **ex-BODIPY** remained. However, superimposed with the spectrum of **ex-BODIPY** was a new, not-yet-seen band at λ_{max} = 525 nm. Excitation of the solution at 525 nm led to an emission band with bright yellow fluorescence with λ_{max} = 561 nm. Further, a ^{1}H NMR spectrum of the blue solution shows two sets of pyrrolic peaks—inidcating the compound is no longer symmetric. With this information in hand, we hypothesized that a light induced dimerization could lead to the observed properties of the unknown blue compound.

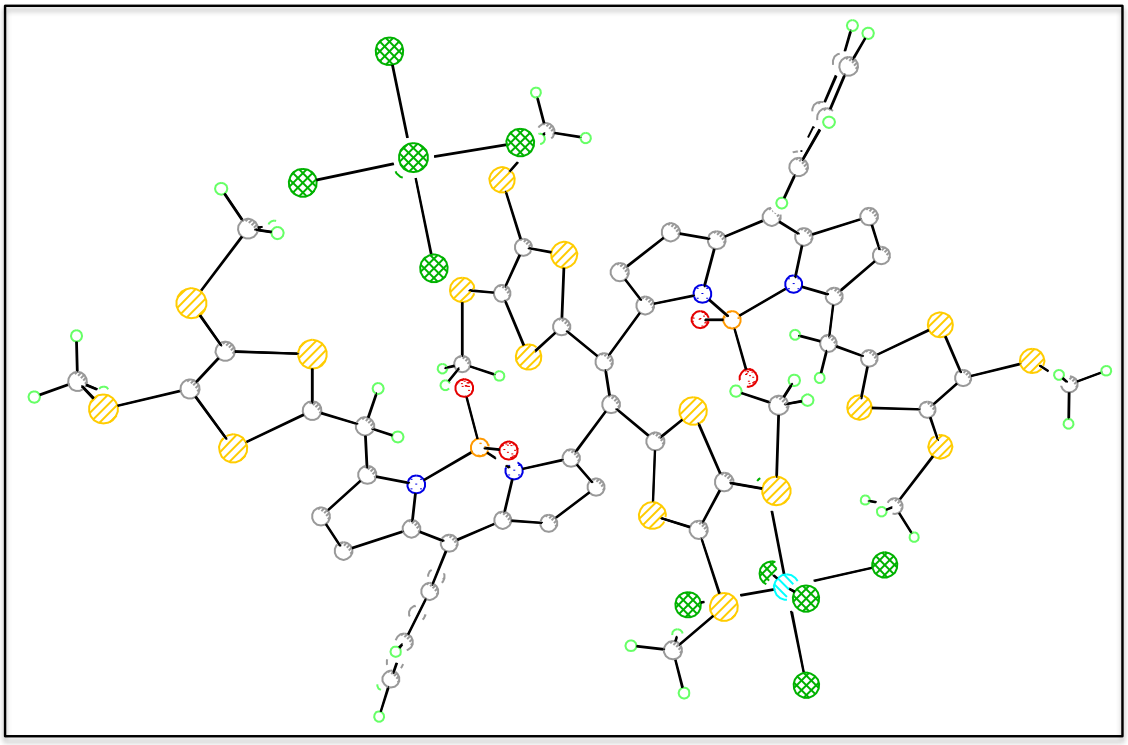

Figure 4.8. Crystal structure of the dimer of (**ex-BODIPY**)$_2^{2+}$•2 $SbCl_6^{2-}$. Ellipsoids are scaled to the 50% probability level.

To test our hypothesis, we subjected **ex-BODIPY** to one molar equivalent of magic blue in dichloromethane (to presumably give **ex-BODIPY**$^{\bullet+}$) and let the resulting solution slowly evaporate. Over several days, dark blue crystals grew. These crystals were subjected to X-ray diffraction analysis by Dr. Vincent Lynch. As predicted, the resulting structure revealed that, at least in in the solid state, the chemical species obtained in this way a dimer made up of partially oxidized **ex-BODIPY** molecules (Figure 4.8). Within the dimeric structure, the BODIPY cores are found to be coplanar, with the appended non-oxidized dithiole ring slightly tilted from the BODIPY plane. The oxidized dithiole rings on the other hand, are more-or-less orthogonal to the plane of the BODIPY core, extending above and below the plane of the rest of the dimer. Unfortunately, this structure had a large solvent void (ca. 22%) and further conclusions are limited. However, the preliminary analysis lends support for the structure of the unknown blue solution.

4.7 Generation of Singlet Oxygen

As a first step towards testing the potential utility of **ex-BODIPY** as a PDT photosensitizer, we carried out studies designed to measure its ability to photo-catalyze the production of singlet oxygen. In these studies, the photoinduced degradation of DPBF in the presence and absence of **ex-BODIPY** was monitored as an indicator of singlet oxygen generation. DPBF is an efficient $^1O_2$ trap that changes color upon exposure to singlet oxygen. As a consequence, quantifying the disappearance of the DPBF absorption as a function of putative photosensitizer concentration provides a means to quantify $^1O_2$ generation. To facilitate comparisons with other species studied as $^1O_2$ sensitizers, we set the **ex-BODIPY**

and starting DPBF concentrations to 9.0 nm and 50 μM, respectively, and performed the studies in 2-propanol. In the dark, no degradation of the oxygen trap was observed over five minutes for both the solution containing **ex-BODIPY** dye the control solution with only DPBF (Figure 4.9). Following this initial 5 minute period, both solutions were exposed to 625 nm laser light from a commercial laser pointer (max power < 5 mW). The degradation of DPBF, presumed to reflect the formation of singlet oxygen, was monitored as a function of the absorptivity at 411 nm (λ_{max} of DPBF). Although the control study demonstrated some degradation of the trap under identical experimental conditions, the solution containing the photosensitizer led to 42.1% greater degradation after 30 minutes of exposure to laser light. Specifically, the control study retained 72.7% of the original absorption intensity, whereas, the solution doped with **ex-BODIPY** retained 61.2% of the absorption observed at the onset of the experiment. We take this as initial evidence that irradiation of **ex-BODIPY** at suitable wavelengths will generate singlet oxygen.

Although the laser light used was powerful enough to degrade the trap without an additional photosensitizer, the wavelength of excitation was well below (over 125 nm) the λ_{max} of **ex-BODIPY**. Further studies using less intense light but at an excitation wavelength closer to 754 nm are warranted before more substantive conclusions concerning the efficacy of **ex-BODIPY** as a potential PDT drug can be made. Utilizing an LED light array, instead of a laser, is one possible solution to both of these problems. Additionally, a positive control could shed light on the efficiency of singlet oxygen generation. Promising results would pave the way for future cell-based studies.

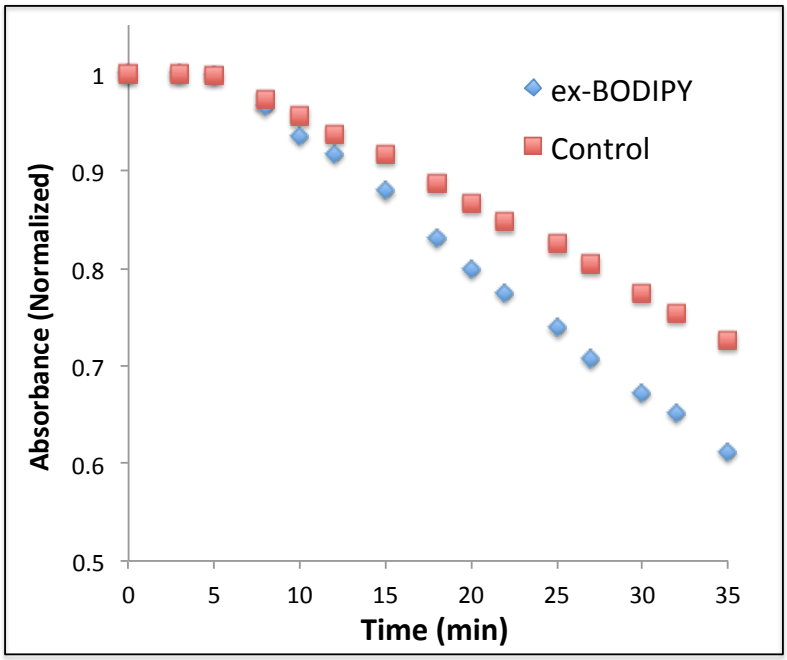

Figure 4.9. Bleaching of 1,3-diphenylisobenzofuran (50 μM) in the presence of **ex-BODIPY** (9 nM, blue diamonds) and without dye (red squares). For the first five minutes the solutions were kept in the dark, at the fifth minute the solutions were exposed to 625 nm laser irradiation. Absorption values were recorded at 410 nm and plotted as the difference based on the absorption at the commencement of the study.

4.8 Future Direction

As discussed, a current topic of interest for **ex-BODIPY**s is photodynamic therapy applications. However, the work done on the compound in this regard is still at the preliminary stages. Thus, initial future directions will focus on expanding the PDT work to include cell studies, followed by the optimization of the structure to better

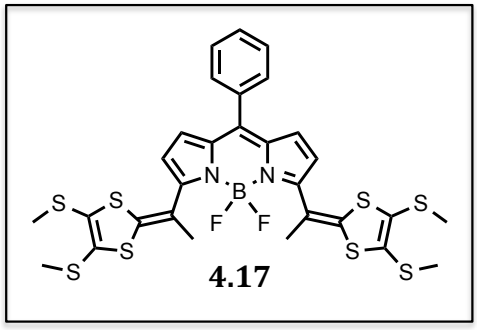

4.17

fulfill the parameters requisite for a viable PDT sensitizer. For instance, the photophysical stability of **ex-BODIPY** is subpar due to the photo-induced dimerization discussed in section 4.5 of this chapter. Adding steric bulk

to the point of dimerization should prevent the requisite close contact needed to dimerize **ex-BODIPY**. Thus, incorporation of an acyl group, instead of the formyl group in **4.10** is proposed. This will eventually lead to compound **4.17** after HWE coupling with **4.14**. The extra methyl group should provide enough steric bulk to eliminate dimerization, increasing photostability.

Further, the solubility profile of **ex-BODIPY** can be tuned, to confer water solubility. In analogy to the work with BOIDPY **4.3**, decorating the *meso*-phenyl group with polyethylene glycol substituents should increase the lipophilicity of **ex-BODIPY**. The thiomethyl substitutents of the dithiolidene rings can also be exchanged with lipophilic groups. Specifically, the bis(cyanoethyl) protected thione **4.18** is know. Upon exposure to basic condition, the bis(cyanoethyl) groups are cleaved, affording dithiolates. The dithiolate anions can then be reacted with lipophilic electrophiles in a S_N2 type mechanism. Polyethylene glycol moieties could easily be incorporated with this method, as several halogenated precursors are known (Scheme 4.3). Manipulating the lipophilicity of the BODIPYs has the potential to alter the bioavailability, ease of use, and the tissue localization of the dyes. Thus, assuming light induced cytotoxicty, these studies are warranted to evaluate the *in vivo* efficacy of the dye.

Scheme 4.3. Proposed incorporation of polyethylene glycol moieties through deprotection of bis(cyanoethyl)thiols, followed by reaction with halogenated polyethylene glycols.

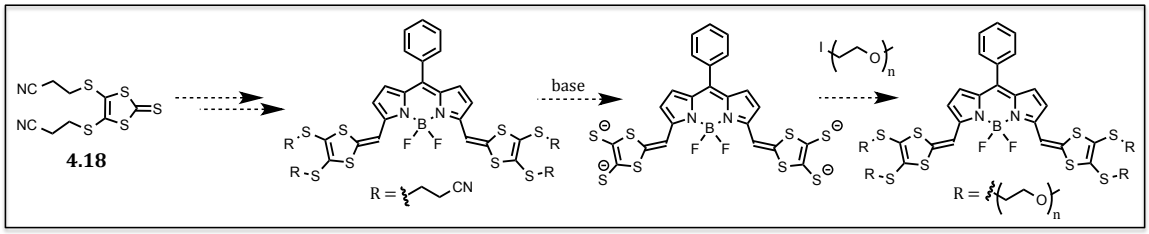

Another parameter that can be optimized in **ex-BODIPY** is the quantum yield of intersystem crossing. It is well established that intersystem crossing is a prerequisite for singlet oxygen generation. However, **ex-BODIPY** displays steady state fluorescence, an indication that incomplete intersystem crossing is taking place. Previous BODIPY work, as briefly reviewed in Section 4.1 of this Chapter, utilizes halogenated BODIPYs for efficient intersystem crossing. Generally, the halogens are appended to the β-positions of the pyrrole rings. Fortunately, in **ex-BODIPY** the β-positions are free and could thus be substituted with halogens to enhance (presumably) intersystem crossing.

We also envision **ex-BODIPY**s finding use outside of PDT applications. For instance, key optical communication wavelengths are at 850-950, 1310, and 1550 nm. As shown by the spectroelectrochemistry in Figure 4.7, **ex-BODIPY** displays strong electrochromic behavior. Further, the radical cation state shows strong absorbance in the 850-950 range and less-intense absorbance in the 1550 nm communications window. Thus, **ex-BODIPY**$^{\bullet+}$ could serve to attenuate light at key communications wavelengths without having an effect on the 1310 nm wavelength. The elcectrochromic behavior of **ex-BODIPY** could lead to it being used as an electrochromic switch.

In summary we have synthesized a π-extended tetrathiafulvalene-BODIPY chimera. This compound displays absorption and emission features that are significantly bathochromic shifted compared to other BODIPYs. In fact, it displays some of the longest wavelength absorption and emission bands known for this class of molecule. Upon oxidation, two thermodynamically stable states (the radical

cation **ex-BODIPY**$^{\bullet+}$ and the dication **ex-BODIPY**$^{2+}$) are observed. Both of these compounds show even further red-shifted absorption bands. Initial studies with the singlet oxygen trap DPBF provide support for the notion that **ex-BODIPY** can generate singlet oxygen. Thus, we believe that **ex-BODIPY** has the potential to serve as a dye for PDT applications. Further studies of **ex-BODIPY** as a PDT drug candidate, including cell studies, will be needed to substantiate this prediction.

4.9 Chapter 4 References

1. (a) Loudet, A.; Burgess, K. *Chem. Rev.* **2007**, 107, 4891. (b) Ulrich, G.; Ziessel, R.; Harriman, A. *Angew. Chem.* **2008**, 120, 1202. (c) Ziessel, R.; Ulrich, A.; Harriman, A. *New. J. Chem.* **2007**, 31, 496.
2. (a) Bozdemir, O.A.; Guliyev, R,; Buyukcakir, O.; Selcuk, S; Kolemen, S.; Gulseren, G.; Nalbantoglu, T.; Boyaci, H.; Akaya, E.U., *J. Am. Chem. Soc.* **2010**, 132, 8029. (b) Sunahara, H.; Urano, Y.; Kojima, H.; Nagano, T. *J. Am. Chem. Soc.* **2007**, 129, 5597. (c) Zeng, L.; Miller, E.W.; Pralle, A.; Isacoff, E.Y.; Change, C.J.;*J J. Am. Chem. Soc.* **2006**, 128, 10. (d) Yamada, K.; Nomura, Y.; Citerio, D.; Iwasawa, N.; Suzuki, K. *J. Am. Chem. Soc.* **2005**, 127, 6956. (e) Cheng, T.; Xu, Y.; Zhang, S.; Zhu, W.; Qian, J.; Duan, L. *J. Am. Chem. Soc.* **2008**, 130, 16160. (f) Peng, X.; Du, J.; Fan, J.; Wang, J.; Wu, Y.; Zhao. J.; Sun, S.; Zu, T. *J. Am. Chem. Soc.* **2007**, 129, 1500. (g) Jiao, L.; Li, J.; Zhang. S.; Wei, C.; Hao, E.; Vicente, M.G.H., *New. J. Chem.* **2009**, 33, 1888.
3. (a) Ertan-Ela, S.; Yilmaz, M.D.; Icli, B.; Dede, Y.; Icli, S.; Akkaya, E.U., *Org. Lett.* **2008**, 10, 3299. (b) Rousseau, T.; Cravino, A.; Bura, T.; Ulrich, G.; Ziessel, R.; Roncali, J. *Chem. Commun.* **2009**, 1673. (c) Collado, D.; Casado, J.; Gonzalez, J.T.L.; Perez-Inestrosa, E.; Pappenfus, T.M.; Raposo, M.M.M. *Chem. Eur. J.* **2011**, 17, 498.
4. (a) Harriman, A.; Ziessel, R. *Chem. Commun.* **2011**, 47, 611. (b) Gu, Z.; Guo, D.; Sun, M.; Liu, Y. *J. Org. Chem.* **2010**, 75, 3600. (c) Benniston, A.C.; Copley, G.; Harriman, A.; Howgego, D.; Harrington, R.W.; Clegg. W. *J. Org. Chem.* **2010**, 75, 2018. (d) Shin, J.Y.; Tanaka, T.; Osuka. A.; Miao, Q.; Dolphin, D. *Chem. Eur. J.* **2009**, 15, 12955.
5. (a) Yilmaz, M.D.; Bozdemir, O.A.; Akkaya, E.U. *Org. Lett.* **2006**, 8, 2871. (b) Yuan, M.; Yin, X.; Zheng, H.; Ouyang, C.; Zuo. Z.; Liu, H.; Li, Y.; *Chem. Asian J.* **2009**, 4, 707. (c) Zrig, S.; Remy, P.; Andrioletti, B.; Rose, E.; Asselberghs, I.; Clays, K. *J. Org. Chem.* **2008**, 73, 1563. (d) Pochorovski, I.; Breiten, B.; Schweizer, W.B.; Diederich, F. *Chem. Eur. J.* **2010**, 16, 12590.
6. Ulrich, G.; Goeze, C.; Guardigli, M.; Roda, A.; Ziessel, R. *Angew. Chem. Int. Ed.* **2005**, 44, 3694
7. (a) Banuelos-Prietol, J.; Agarrabeitia, A.R.; Garcia-Moreno, I.; Lopez-Arbeloal, I.; Costela, A.; Infantes, L.; Perez-Ojeda, M.E.; Palacios-Cuesta, M.; Ortiz, M.J. *Chem. Eur. J.* **2010**, 16, 14094. (b) Mula, S.; Ray, A.K.; Banerjee, M.; Chaudhuri, T.; Dasgupta, K.; Chattopadhyay, S. *J. Org. Chem.* **2008**, 73, 2146.
8. Weissleder, R. *Nat. Biotechnol.* **2001**, 19, 316
9. (a) Bonnet, R. *Chemical Aspects of Photodynamic Therapy.* Gordon and Breach Science. Amsterdam, 2000. (b) Dogherty, T.J.; Gomer, C.J.; Henderson, B.W.; Jori, G.; Kessel, D.; Korbelik, M.; Moan, J.; Peng, Q. *J. Natl. Cancer Inst.* **1998**, 90, 889.
10. Bonnet, R.; Martinez, G. *Tetrahedron,* **2001**, 57, 9513
11. Ericson, M.B.; Wennber, A.M.; Larko, O. *Ther. Clin. Risk Manag.* **2008**, 4, 1.
12. Kossodo, S.; LaMuraglia, G.M. *Am. J. Cardiovasc. Drugs*, **2001**, 1, 15
13. (a) Capella, M.A.M.; Capella, L.S.J. *J. Biomed. Sci.* **2003**, 10, 361. (b) Feuerstein, T.; Berkovitch-Luria, G.; Nudelman, A.; Rephaeli, A.; Malik, Z. *Photochem.*

Photobiol. Sci. **2011**, 12, 1926. (c) Li, W.; Zhang, W.J.; Ohnishi, K.; Yamada, I.; Ohno, R.; Hashimoto, K. *J. Photochem. Photobiol. B.* **2001**, 60, 79.
14. Rodriquez, M.E.; Moran, F.; Bonansea, A.; Monetti, M.; Fernandez, D.A.; Strassert, C.A.; Rivarola, V.; Awruch, J. Dicelio, L.E. *Photochem. Photobiol. Sci.* **2003**, 2, 998.
15. Yukruk, F.; Dogan, A.:.; Canpinar, H.; Guc, D.; Akkaya, E.U. *Org. Lett.* **2005**, 7, 2885.
16. (a) Sessler, J.L.; Miller, R.A. *Biochem. Pharmacol.* **2000**, 59, 733. (b) Mody, T.D.; Sessler, J.L. *J. Porphyrins Phthalocyanines,* **2001**, 5, 134. (c) Magda, D.J.; Wang, Z.; Gerasimchuk, N.; Wei, W.; Anzenbacher, P.; Sessler, J.L. *Pure Appl. Chem.* **2004**, 76, 365.
17. (a) Ramaiah, D.; Eckert, I.; Arun, K.T.; Weidenfeller, L.; Epe, B. *Photchem. Photobiol.,* **2002**, 76, 672. (b) Ramaiah, D.; Eckert, I.; Arun, K.T.; Weidenfeller, L.; Epe, B. *Photchem. Photobiol.,* **2004**, 79, 99. (c) Detty, M.R.; Gibson, S.L.; Wagner, S.J. *J. Med. Chem.*, **2004**, 47, 3897.
18. (a)Plaetzer, K,; Krammer, B.; Berlanda, J.; Berr, F.; Kiesslich, T. *Lasers Med. Sci.* **2009**, 24, 259. (b) Killoran, J.; Allen, L.; Gallagher, J.F.; Gallagher, W.M.; O'Shea, D.F. *Chem. Commun.* **2002**, 1862.
19. Gorman, A.; Killoran, J.; O'Shea, C.; Kenna, T.; Gallagher, W.M.; O'Shea, D.F. *J. Am. Chem. Soc.* **2004**, 126, 10619.
20. Byrne, A.T.; O'Connor, A.E.; Hall, M.; Murtagh, J.; O'Neill, K.; Curran, K.M.; Mongrain, K.; Rousseau, J.A.; Lecomte, R.; McGee, J.J.; O'Shea, D.F.; Gallagher, W.M. *Br. J. Cancer.* **2009**, 101, 1565
21. Gallagher, W.M.; Allen, L.T.; Kenna, T.; Hall, M.; Gorman, A.; Killoran, J.; O'Shea, D.F. *Br. J. Cancer.* **2005**, 92, 1702.
22. Considerable dark toxicity was seen for this compound in HeLa cells, EC_{50} = 2.7×10^{-5}.
23. Animals were considered "cured" after completel tumor regression, defined as the absence of a palpable tumor.
24. Atilgan, S.; Ekmekci, Z.; Dogan, A.L.; Guc, D.; Akkaya, E.U. *Chem. Commun.* **2006**, 4398
25. He, H.; Lo, P.C.; Yeung, S.L.; Fong, W.P.; Ng, D.K.P. *Chem. Commun.* **2011**, 47, 4748.
26. Erbas, S.; Gorgulu, A.; Kocakusakogullari, M; Akkaya, E.U. *Chem Commun.* **2009**, 4956.
27. Kim. S.; Ohulchanskyy, T.Y.; Baev, A.; Prasad, P.N., *J. Mater. Chem.* **2009**, 19, 3181.
28. Yang, Y.; Guo, Q.; Chen, H.; Zhou, Z.; Guo, Z.; Shen, Z. *Chem. Commun.* **2013**, 3940.
29. (a) Bellier, Q.; Dalier, F.; Jeanneau, E.; Maury, O.; Andraud. C. *New. J. Chem.* **2012**, 768. (b) Zhao, W.; Carreira, E.M.; *Angew. Chem. Int. Ed.* **2005**, 44, 1677.
30. (a) Rohand, T.; Baruah, M.; Qin, W.; Boëns, N.; Dehaen, W. *Chem. Commun.* **2006**, 266 (b) Rohand, T.; Qin, W.; Boëns, N.; Dehaen, W. *Eur. J. Org. Chem.* **2006**, 4658 (c) Leen, V.; Braeken, E.; Luckermans, K.; Jackers, C.; Auweraer, M.; Boëns, N.; Dehaen, W. *Chem. Commun.* **2009**, 4515 (d) Li, L. ; Nguyen, B.; Burgess, K. *Bioorg. Med. Chem. Lett.* **2008**, *18*, 3112 (e) Zhang, D. ; Wen, Y.;

Xiao, Y.; Yu, G.; Liu, Y.; Qian, X. *Chem. Commun.* **2008**, 4777. (f) Rurack, K.; Kollmannsberger, M.; Daub, J. *Angew. Chem. Int. Ed.* **2001**, *40*, 385; (g) Baruah, M.; Qin, W.; Flors, C.; Hofkens, J.; Vallée, R. A. L.; Beljonne, D.; van der Auweraer, M.; Borggra- eve, W. M. D.; Boëns, N. *J. Phys. Chem. A* **2006**, *110*, 5998.

31. (a) Yu, Y.H.; Descalzo, A.B.; Shen, Z.; Rohr, H.; Liu, Q.; Wang, Y.W.; Spieles, M.; Li, Y.Z.; Rurack, K.; Your, X.Z. *Chem. Asian J.,* **2006**, 1, 176. (b) Buyukcakir, O.; Bozdemir, O. A.; Kolemen, S.; Erbas, S.; Akkaya, E. U. *Org. Lett.* **2009**, *11*, 4644 (c) Bellier, Q.; Pegaz, S.; Aronica, C.; Le Guennic, B.; Andraud, C.; Maury, O. *Org. Lett.* **2011**, 13, 22. (d) Zhang, D.; Martin, V.; Garcia-Moreno, I.; Costela, A.; Perez-Ojeda, M.E.; Xiao, Y. *Phys. Chem. Chem. Phys.* **2011**, 13, 13026.
32. (a) Shen, Z.; Rohr, H.; Rurack, K; Uno, H.; Spieles, M.; Shulz, B.; Reck. G.; Ono, N. *Chem. Eur. J.* **2004**, 10, 4853. (b) Umezawa, K.; Nakamura, Y.; Makino, H.; Citterio, D.; Suzuki, K. *J. Am. Chem. Soc.* **2008**, 130, 1550. (c) Goeb, S.; Ziessel, R. *Org. Lett.* **2007**, 9, 737. (d) Umezawa, K.; Matsui, A.; Nakamura, Y.; Citterio, D.; Suzuki, K. *Chem. Eur. J.* **2009**, 15, 1096.
33. (a) Zhao, W.; Carreira, E.M.; *Chem. Eur. J.* **2006**, 12, 7254. (b) Loudet, A.; Bandichhor, R.; Burgess, K.; Palma, A.; McDonell, S.O.; Hall, M.J.; O'Shea, D.F. *Org. Lett.* **2008**, 10, 4771. (c) Wang, Y.W.; Descalzo, A.B.; Shen, Z.; You, X.Z.; Rurack, K. *Chem. Eur. J.* **2010**, 16, 2887. (d) Descalzo, A.B.; Xu, H.J.; Xue, Z.L.; Hoffmann, K.; Shen, Z,; Weller, M.G.; You, X.Z.; Rurack, K. *Org. Lett.* **2008**, 10, 1581. (e) Shen, Z.; Rohr, H.; Rurack, K.; Uno, H.; Spieles, M.; Schulz, B.; Reck, G,; Ono, N. *Chem. Eur. J.* **2004**, 10, 4853. (f) Chen, J.; Burghart, A.; Derecskei-Kovacs, A.; Burgess, K. *J. Org. Chem.* **2000**, 65, 2900. (g) Jiao, L.; Yu, C.; Li, J.; Wang, Z.; Wu, M.; Hao, E. *J. Org. Chem.* **2010**, 75, 6053.
34. Madhu, S.; Rao, M.R.; Shaikh, M.S.; Ravikanth, M. *Inorg. Chem.* **2011**, 50, 4392.
35. Moore, A.J.; Bryce, M.R. *J. Org. Chem.* **1994**, 59, 6847.
36. Deprotonation with lithium diisopropyl amine and addition of **4.10** resulted in no detectable formation of product.
37. *TTF Chemistry: Fundamentals and Applications of Tetrathiafulvalene*. Yamada, J.; Sugimoto, T. eds.; Springer, Berlin, 2004.
38. The irreversibility of the second reduction wave is most likely a result of decomposition of the electron rich small molecule.
39. This value was calculated by adding 0.45 V to the value determined relative to Fc/Fc^+, thus in principle referencing the potential to SCE.
40. (a) Brouwer, A. M. *Pure Appl. Chem.* **2011**, 83, 2213. (b) Reindl, S.; Penzkofer, A.; Gong, S. H.; Landthaler, M.; Szeimies, R. M.; Abel, C.; Baumler, W. *J. Photochem. Photobio., A* **1997**, 105, 65.
41. The absorbances of the solutions were kept under 0.05 AU to ensure self-quenching of the fluorescence intensities was minimized.
42. The peak at 311 nm that grows throughout the entirety of the titration is assigned to the reduced end product of magic blue, *tris*-4-bromophenyl amine.
43. Attempts to grow crystals of **ex-BODIPY** in the dark were met with disappointment.

Chapter 5

Experimental Procedures and X-Ray Data

5.1 General Procedures

All chemical were obtained from a chemical supply company (Acros, Aldrich, TCI America, Strem, etc.) in reagent-grade purity and used without further purification unless otherwise noted. All solvents were of ACS grade quality. When necessary, solvents were dried using various techniques: tetrahydrofuran (THF) was dried by passage through two columns of activated alumina; acetronitrile, methanol, and dimethylformamide were dried by passage through two columns of molecular sieves; toluene was distilled over sodium; benzonitrile (PhCN) was distilled over P_2O_5 immediately before use, collecting only the middle 50% of the distillate; dichloromethane (CH_2Cl_2) was freshly distilled from CaH_2; triethylamine was distilled over barium oxide.

Column chromatography was performed using Silicycle Silia Flash® P60 grade silica gel (40-63 μM) and alumina purchased from Sorbent Technologies (neutral, standard activity I, 50-200 μM). Thin layer chromatography (TLC) analyses were performed on silica gel (glass backed, 250 μM) or neutral alumina TLC plates (polyester backed, 200 μM) both obtained from Sorbent Technologies.

Electrochemical Measurements: All electrochemical measurements were carried out using a CV-50 electrochemical analyzer in either CH_2Cl_2 or PhCN at 298 K in the

presence of 0.1 M TBAPF6 as the supporting electrolyte. A glassy carbon working electrode was used, as well as a platinum wire counter electrode and an Ag/AgCl reference electrode. All samples were internally referenced to the ferrocene (Fc)/ ferrocinium (Fc^+) redox couple. The working electrode was routinely polished using standard polishing procedures. Standard scan rates were 50 mV/s unless otherwise noted.

Nuclear Magnetic Resonance (NMR) Spectroscopy: All NMR solvents were purchased from Cambridge Isotope Laboratories and used without further purification. ^{1}Hydrogen (400 MHz) and ^{13}Carbon (100 MHz) NMR spectra were measured using a Varian 400/54/ASW instrument. Chemical shifts (δ-scale) are reported in ppm relative to residual solvent and internal standard signals (DMSO-d_6: 2.50 ppm, CD_3Cl: 7.26 ppm and acetone-d_6: 2.05 ppm for ^{1}H, and CD_3Cl: 77.2 ppm, and CD_3CN: 1.3 ppm for ^{13}C).

Electron Paramagnetic Resonance Spectroscopy: The EPR spectra were recorded on a JEOL X-band spectrometer (JES-RE1XE) under non-saturating microwave power conditions (1.0 mW) operating at 9.2 GHz. The magnitude of the modulation was chosen to optimize the resolution and the signal to noise ratio (S/N) of the observed spectrum (modulation width, 20 G; modulation frequency, 100 kHz). The g values were calibrated using an Mn2+ marker.

Mass Spectroscopy: High and low-resolution mass spectra were obtained by the Mass Spectrometry Facility of the Department of Chemistry and Biochemistry at The University of Texas and recorded on an Agilent 6530 Accurate Mass QTOF/LC-MS (ESI) and a Ionospec 9.4 FT-ICR (MALDI).

Femtosecond Transient Absorption: The femtosecond time-resolved transient absorption (TA) spectrometer consisted of NIR optical parametric amplifier (OPA) system (Quantronix, Pallitra) pumped by a Ti:sapphire regenerative amplifier system (Quantronix, Integra-C) operating at 1 kHz repetition rate and an optical detection system. The generated OPA output signals had a pulse width of ~ 100 fs in the range of 480-700 nm which were used as pump pulses. White light continuum (WLC) probe pulses were generated using a sapphire window (3 mm of thickness) by focusing of small portion of the fundamental 800 nm pulses. The time delay between pump and probe beams was carefully controlled by making the pump beam travel along a variable optical delay (Newport, ILS250). Intensities of the spectrally dispersed WLC probe pulses are monitored by two miniature spectro-graphs (OceanOptics USB2000+). To obtain the time-resolved transient absorption difference signal (ΔA) at a specific time, the pump pulses were chopped at 25 Hz and absorption spectra intensities were saved alternately with or without the pump pulse. Typically, 6000 pulses were used to excite the samples to obtain the TA spectra at a particular delay time. The polarization angle between pump and probe beam was set at the magic angle (54.7°) in order to prevent polarization-dependent signals. Cross-correlation fwhm in pump-probe experiments was less than 200 fs and chirp of WLC probe pulses was measured to be 800 fs in the 400-1200 nm region. To minimize chirp, all reflection optics were used in the probe beam path and a 2 mm path length quartz cell was employed. After the TA experiments, the absorption spectra of all compounds were carefully checked so as to avoid artifacts arising from, e.g., photo-degradation or photo-oxidation of the samples in question.

Absorption and Emission Experiments: UV-Vis-NIR spectra were recorded on a Varian Cary 5000 UV-Visible spectrophotometer at 298 K using a 1 cm path length quartz cuvette. Fluorescence spectra were recorded on a Horiba Jobin Yvon Nanolog at 298 K using a 1 cm path length cuvette.

Two-Photon Absorption Experiments: Two-photon absorption (TPA) spectra were measured in the NIR region using the open-aperture Z-scan method with 130 fs pulses from an optical parametric amplifier (Light Conversion, TOPAS) operating at a repetition rate of 2 kHz generated from a Ti:sapphire regenerative amplifier system (Spectra-Physics, Hurricane-X). The NIR beam was divided into two parts. One was monitored by a Ge-PIN photodiode (New Focus) as an intensity reference, and the other was used for the transmittance measurement. After passing through a 10 cm focal length lens, the laser beam was focused and passed through a 1 mm quartz cell. Since the position of the sample cell could be controlled along the laser beam direction (z axis) using the motor-controlled delay stage, the local power density within the sample cell could be simply controlled under constant laser intensity. The transmitted laser beam from the sample cell was then detected by the same photodiode as used for reference monitoring. The on-axis peak intensity of the incident pulses at the focal point, I0, ranged from 40 to 60 GW cm-2. For a Gaussian beam profile, the nonlinear absorption coefficient can be obtained by curve fitting of the observed open-aperture traces T(z) with the following equation:

$$T(z) = 1 - \frac{\beta I_0 (1 - e^{-\alpha_0 l})}{2\sqrt{2}\alpha_0 [1 + (z/z_0)^2]}$$

where α0 is the linear absorption coefficient, l the sample length, and z0 the diffraction length of the incident beam. After the non-linear absorption coefficient has been obtained, the TPA cross section σ(2) of one solute molecule (in units of GM, where 1 GM = 10-50 cm4 s photon-1 molecule-1) can be determined by using the following relationship:

$$\beta = \frac{10^{-3}\sigma^{(2)}N_A d}{h\nu}$$

where NA is the Avogadro constant, d is the concentration of the compound in solution, h is the Planck constant, and ν is the frequency of the incident laser beam.

Density Functional Theory (DFT) Calculations: Theoretical calculations were performed with the Gaussian09 program suite using a supercomputer (KISTI, IBM).[5.1] All optimized structures were obtained using the density functional theory (DFT) calculations with Becke's three-parameter hybrid exchange functionals and the Lee-Yang-Parr correlation functional (B3LYP) employing the 6-31G(d) basis set for all atoms.[5.2] The global ring centers for the NICS(0) values were designated at the non-weighted mean centers of the macrocycles. The NICS(0) value was obtained with gauge independent atomic orbital (GIAO) method based on the optimized geometries. To simulate the ground-state absorption spectra, the time-dependent (TD) DFT calculation was employed with (U)B3LYP/6-31G(d) level. In the specific case of dication, **H_2TTFP**$^{2+}$, the Handy and co-workers' of long-range corrected TD-CAMB3LYP/6-31G(d) level calculations[5.3] that gives rise to the consistent transitions for charged derivatives were carried out.

High Pressure Liquid Chromotagraphy (HPLC): HPLC spectra were taken on a Shimadzu High Performance Liquid Chromatograph (Fraction Collector Module FRC-10A, Auto Sampler SIL-20A, System Controller CBM-20A, UV-Vis Photodiode Array Detector SPD-M20A, Prominence).

5.2 Synthetic Procedures and Characterization Data

5.2.1 Synthesis of 5,15-dioxo-10,20-diphenylporpho- dimethene (**2.26**)

5,15-Diphenylporphyrin (**2.25**) was prepared by following the previously reported synthetic procedure.[5.4] Following **2.25** (0.77 g, 1.66 mmol) was dissolved in a mixture of chloroform (100 mL) and acetic acid (20 Ml). A solution of PbO_2 (4.0 g, 16.7 mmol) was added and the reaction mixture was stirred for 5 h open to air, where after the mixture was slowly poured into a saturated aqueous sodium bicarbonate solution (300 mL) to quench the acetic acid and the organic and aqueous phase were separated. The organic phase was passed through a short plug of celite to remove residual lead salts. The aqueous layer was extracted twice with dichloromethane (2 x 100 mL) and the two organic fractions were also passed through the celite. The celite was washed thoroughly with dichloromethane until the filtrate was colorless. The combined organic filtrates were evaporated and the residue purified by column chromatography over silica gel using 30% hexanes/dichloromethane as the eluent. The dark yellow band was collected affording .46g (56% yield) of **2.26** as a black solid. The black crystalline solid could be further purified by recrystallizing from hot toluene. The ^{1}H NMR spectral data matched that reported previously[5.5] ($CDCl_3$, 298 K) δ 6.2-2.6 (br s, 4H, β-H), 7.17 (d, J = 4.4Hz, 4H, β-H), 7.35-7.45 (m, 10H, Ph-H), 13.85 (br s, 2H, N-H) ppm.

5.2.2 Synthesis of H_2TTFP

To a mixture of 5,15-dioxo-10,20-diphenylporphodimethene (**2.26**) 100 mg, 0.203 mmol) and 4,5-bis(methylthio)-1,3-dithiole-2-thione (**2.24**)[5.6] (100 mg, 0.444 mmol) in a dried 100 mL round bottom flask was added freshly distilled triethylphosphite (3 ml) and the reaction mixture was heated slowly to 90 °C under a nitrogen atmosphere. After stirring the reaction mixture for 1 h at 90 °C, another 100 mg (0.444 mmol) aliquot of **2.24** was added to the reaction mixture. The mixture was stirred for additional 1 h affording a dark green solution. After cooling to room temperature, the reaction mixture was filtrated using a fine fritted glass filter to give a dark green solid as a "first crop". The remaining filtrate was poured into cold methanol (100 mL) and the resulting precipitate was collected by filtration to yield a "second crop". The first crop obtained in this way proved sufficiently pure to be used in further reactions. The second crop was purified by column chromatography over silica gel (to remove the product of the homocoupling of **2.24**) using 30% hexanes/dichloromethane as the eluent; this provided analytically pure **H_2TTFP** (total yield, 102 mg, 27%). R_f = 0.3. ^{1}H NMR: (acetone-d_6, 298 K) δ 2.48 (s, 12H, S-CH_3), 6.61 (d, J = 4.3 Hz, 4H, β-H), 6.90 (d, J = 4.3 Hz, 4H, β-H), 7.55 (m, 10H Ph-H) 12.59 (s, 2H, NH); ^{13}C NMR ($CDCl_3$, 298 K): δ 19.1, 114.1, 117.9, 127.4, 127.9, 128.5, 129.6, 130.9, 138.0, 140.0, 141.7, 152.3. HRMS-Positive-ESI: m/z 849.04578. Calcd.: 849.04654. MP > 300 °C.

5.2.3 Procedure for the Oxidation of H_2TTFP to H_2TTFP^{2+}

Freebase **H_2TTFP** (20 mg, 0.024 mmol) was dissolved in a minimal amount of dichloromethane (2 mL). Crystalline $NOPF_6$ (≈ 45 mg, 0.257 mmol) was quickly weighed and added in excess and the reaction was stirred for 15 min. A precipitate was immediately noticeable. After 15 min, the residual solvent proved to be nearly colorless, and at this time the solvent and precipitate were decanted from the leftover solid $NOPF_6$. The solution was filtered and the solids washed with water and dichloromethane until the filtrate was colorless. The solid material was dried under vacuum at RT to give pure **H_2TTFP^{2+}•2PF_6**. ^{1}H NMR (DMSO-d_6, 298 K): δ -2.75 (s, 2H, NH), 3.11 (s, 12H, S-CH_3), 7.92 (m, 6H, Ph-H), 8.24 (dd, J = 1.45, 7.75), 8.99 (br s, 4H, β-H), 9.68 (br s, 4H, β-H). ^{13}C NMR ($CDCl_3$, 125 MHz, 298 K): δ 19.4, 125.9, 127.0, 128.4, 131.3, 134.3, 134.5, 141.4, 148.9, 152.0, 155.5 HRMS-Positive-ESI: z = 1, m/z 849.04693, calcd.: 849.04654. z =2, m/z 425.02727. Calcd.: 425.02691 MP > 300 °C.

5.2.4 General Metalation Procedure for H_2TTFP

Compound **H_2TTFP** (20 mg, 0.024 mmol) was dissolved in dichloromethane (50 ml) and excess metal acetate, $M(OAc)_2$ (100 mg) dissolved in MeOH (1 mL) was added. The solution was stirred for 1 h or until all of **H_2TTFP** was consumed, as judged by TLC analysis. After removal of the solvent, the residue was purified by column chromatography over silica gel to give the target complexes,:

ZnTTFP: Eluent dichloromethane; R_f = 0.8, (87% yield) ^{1}H NMR (DMSO-d_6, 400 MHz, 298 K): δ 2.43 (s, 12H, S-CH_3), 6.40 (d, J = 4.2 Hz, 4H, β-H), 6.85 (d, J = 4.2 Hz, 4H, β-H), 7.47 (m, Ph-H). ^{13}C NMR ($CDCl_3$, 125 MHz, 298 K): δ 19.0 116.3, 117.8, 127.1,

127.5, 128.0, 130.7, 131.6, 139.5, 141.7, 155.7. HRMS-Positive-MALDI: m/z 909.9524, Calcd.: 909.9522. This compound was further analyzed by a single crystal X-ray diffraction analysis. MP > 300 °C.

CuTTFP: Eluent 30% hexanes/dichloromethane; R_f = 0.9, (73% yield). As noted in the main text, the EPR spectrum of this complex is consistent with the proposed structure. A clean HPLC chromatogram of this paramagnetic species was also obtained. HRMS-Positive-MALDI: m/z 908.9516. Calcd.: 908.9527. This compound was further analyzed by a single crystal X-ray diffraction analysis. MP > 300 °C.

NiTTFP: Eluent dichloromethane; R_f = 0.9, (82% yield). ^{1}H NMR (DMSO-d_6, 400 MHz 298K): δ 2.46 (s, 12H, S-CH_3), 6.65 (d, J = 4.5 Hz, 4H, β-H), 6.89 (d, J = 4.5 Hz, 4H, β-H), 7.52 (m, 10H, Ph-H). ^{13}C NMR could not be taken due to precipitation from DMSO-d_6 upon standing over several hours. HRMS-Positive-MALDI: m/z 903.9587. Calcd.: 903.9584. MP > 300 °C.

5.2.5 Preparation of ZnTTFP•TBACl

For absorption and CV studies, **ZnTTFP•**TBACl was prepared *in situ* by the addition of 1.2 molar equivalents of tetrabutylammonium chloride to **ZnTTFP** in PhCN. **ZnTTFP•**TBACl can be isolated as its crystalline salt by the addition of 3 molar equivalents of tetrabutylammonium chloride to **ZnTTFP** in dichlormethane followed by slow diffusion of hexanes at 277 K for several days.

5.2.6 Oxidation of ZnTTFP to $ZnTTFP^{2+}$

ZnTTFP (50 mg, 0.055 mmoles) was dissolved in 25 ml dichloromethane. $Cu(OTf)_2$ (100mg, 0.27 mmoles) was dissolved in 1 ml of MeOH. The MeOH solution was added to the dichloromethane solution. Stirring for 15 minutes led to precipitation of **ZnTTFP**•OTf_2. **ZnTTFP**•OTf_2 was filtered from solution and washed with water and dichloromethane. Following, the compound was thoroughly dried to give **ZnTTFP**•OTf_2.

5.2.7 Synthesis of 1,9-Diformyl-5-Phenyl BODIPY (4.10)

1,9-diformyl-5-phenyl dipyrromethane (**4.9**) was prepared following similar synthetic protocols to those previously reported.[5.7] Following, 500 mg (1.80 mmole) of **4.9** was dissolved in 30 mL of toluene and the mixture was heated to 90°C until the compound was completely dissolved. Following, at the same temperature, 600 mg (2.64 mmole) of 2,3-dichloro-5,6-dicyano-1,4-benzoquinone (DDQ) was added and the solution was stirred for 1 h upon. At this point, TLC analyses in 1:3 ethyl acetate:hexanes showed nearly all of the original starting material had been consumed. The reaction flask was removed from the heating source and allowed to cool for 10 minutes. Then 2.20 mL (15.8 mmol) of triethylamine, followed in rapid succession by 2.0 mL (16.2 mmol) of BF_3•Et_2O were added to the solution. Immediately, a fluorescent product was observed. The solution was stirred for a further 30 min and then evaporated to dryness. The residue was columned over silica using 1:3 ethyl acetate:hexanes (R_f = 0.4) as an eluent. The product, compound **4.10**, was isolated as a bright yellow-orange solid.

^{1}H NMR ($CDCl_3$, 400 MHz, 298 K): δ 7.14 (d, J = 4.3 Hz, 2H, β-H), 7.23 (d, J = 4.3 Hz, 2H, β-H), 7.40-7.55 (m, 5, Ph-H), 10.51 (br s, 2H, CHO). ^{13}C NMR (100 MHz, $CDCl_3$, 298 K): δ 120.4, 129.7, 130.5, 131.5, 132.8, 138.0, 144.1, 149.9, 153.8, 184.3. HRMS-Positive-MALDI: m/z 278.1052. Calcd.: 278.1055.

5.2.8 Synthesis of ex-BODIPY

In dry THF, under a nitrogen atmosphere, 215 mg (0.65 mmol) of phosphonate ester **4.14**,[5.8] was dissolved. The solution was then cooled to -78°C in a dry ice/acetone bath. At this time, 0.3 mL (0.75 mmol) of a 2.5 M solution of *n*-butyllithium in hexanes was slowly added to the reaction *via* a syringe. Following, the solution was stirred for 30 min. Then, 100 mg of **4.10** (0.31 mmol) was added, the cooling bath was removed, and the reaction was allowed to warm to room temperature. After stirring at room temperature for 30 min, the THF was evaporated. The residue was dissolved in dichloromethane and extracted twice with water and an additional time with brine. The dichloromethane was removed and the residue was flash columned (30% hexanes in ethyl acetate) over silica. The second spot was collected and was the desired product. Note: It is essential that the column purification be done as quickly as possible. Letting the compound stand on silica led to the formation of an uncharacterized decomposition product, which was intense green in color. ^{1}H NMR ($CDCl_3$, 400 MHz, 298 K): δ 6.68 (d, J = 4.2 Hz, 2H, β-H), 6.77 (d, J = 4.2 Hz, 2H, β-H), 7.20 (s, 2H, vinyl-H), 7.45-7.55 (m, 5H, Ph-H). ^{19}F NMR ($CDCl_3$, 400 MHz, 298 K): δ -141.9 (q) ^{13}C NMR δ 19.3, 113.8, 117.8, 124.7, 125.3, 128.0, 131.1, 133.2, 139.5, 148.4, 153.9.

5.3 Crystallographic Data and Methods

5.3.1 General X-Ray Experimental

X-ray quality crystals were grown by the author of this manuscript. Specific conditions to obtain the crystals are given on a crystal-by-crystal basis. Dr. Vincent Lynch from the University of Texas Chemistry and Biochemistry Department performed all of the data collection and solved all of the structures presented in this dissertation. Following is a brief outline of the methods he used:

Unless otherwise stated, the data was collected on a Rigaku ACF-12 with a Saturn 724+ CCD and a Rigaku SCX-Mini diffractometer with a Mercury 2 CCD using a graphite monochromator with MoKa radiation (λ = 0.71075 Å). The data was collected at 100 K using a Rigaku XStream low temperature device. In all cases, the data reduction was performed using Rigaku Americas Corporation's Crystal Clear version 1.40.[5.9] Each structure was solved by direct methods using SIR97[5.10] and refined by full-matrix least-squares on F^2 with anisotropic displacement parameters for the non-H atoms using SHELXL-97.[5.11] The contributions to the scattering factors due to the solvent molecules were removed by use of the utility SQUEEZE[5.12] in PLATON98.[5.13] Structure analysis was aided by use of the programs PLATON98 as incorporated into WinGX.[5.14] The hydrogen atoms on carbon were calculated in ideal positions with isotropic displacement parameters set to 1.2xUeq of the attached atom (1.5xUeq for methyl hydrogen atoms). Details of crystal data, data collection and structure refinement for each analyzed sample are listed in the sections below. Definitions used for calculating R(F), $R_w(F^2)$ and the goodness of fit, S, are :

$R_w(F^2) = \{\Sigma_w(|F_o|^2 - |F_c|^2)^2/\Sigma_w(|F_o|)^4\}^{1/2}$ where w is the weight given each reflection.

$R(F) = \Sigma(|F_o| - |F_c|)/\Sigma|F_o|\}$ for reflections with $F_o > 4(\sigma(Fo))$.

$S = [\Sigma_w(|F_o|^2 - |F_c|^2)^2/(n - p)]^{1/2}$, where n is the number of reflections and p is the number of refined parameters.

The data was checked for secondary extinction effects but no correction was necessary. Neutral atom scattering factors and values used to calculate the linear absorption coefficient are from the International Tables for X-ray Crystallography (1992).[5.15] All figures were generated using SHELXTL/PC[5.16] or Mercury/Mac.

5.3.2 X-Ray Crystal Structure of H_2TTFP

Crystals grew as dark, violet prisms by slow evaporation from a 1:1 mixture of CH_2Cl_2 and CH_3CN at 277 K. The data crystal was cut from a larger crystal and had approximate dimensions; 0.38 x 0.12 x 0.08 mm. A total of 1368 frames of data were collected using w-scans with a scan range of 0.5° and a counting time of 30 seconds per frame. The function, $\Sigma w(|F_O|^2 - |F_C|^2)^2$, was minimized, where $w = 1/[(s(F_O))^2 + (0.087*P)^2 + (0.109*P)]$ and $P = (|F_o|^2 + 2|F_c|^2)/3$. $R_w(F^2)$ refined to 0.170, with R(F) equal to 0.0632 and a goodness of fit, S, = 1.11. Further details of this structure and its refinement may be obtained from the Cambridge Crystallographic Data Centre by referencing CCDC 931728.

Table 5.1. X-ray crystal data and structure refinement for **H_2TTFP.**

Empirical formula	C43 H35 N4 S8	
Formula weight	864.23	
Temperature	100(2) K	
Wavelength	0.71073 Å	
Crystal system	Triclinic	
Space group	P-1	
Unit cell dimensions	a = 11.7903(9) Å	a= 112.244(2)°.
	b = 12.3315(10) Å	b= 93.709(3)°.
	c = 15.2801(12) Å	g = 90.497(2)°.
Volume	2050.6(3) $Å^3$	
Z	2	
Density (calculated)	1.400 Mg/m^3	
Absorption coefficient	0.473 mm^{-1}	
F(000)	898	
Crystal size	0.38 x 0.12 x 0.08 mm	
Theta range for data collection	3.11 to 27.48°.	
Index ranges	-15<=h<=15, -16<=k<=14, 0<=l<=19	
Reflections collected	9340	
Independent reflections	9340	
Completeness to theta = 27.48°	99.3 %	
Absorption correction	Semi-empirical from equivalents	
Max. and min. transmission	1.00 and 0.530	
Refinement method	Full-matrix least-squares on F^2	
Data / restraints / parameters	9340 / 0 / 493	
Goodness-of-fit on F^2	1.111	
Final R indices [I>2sigma(I)]	R1 = 0.0632, wR2 = 0.1628	
R indices (all data)	R1 = 0.0739, wR2 = 0.1701	
Largest diff. peak and hole	0.956 and -0.811 $e.Å^{-3}$	

5.3.3 X-Ray Crystal Structure of CuTTFP

Crystals grew as long, violet needles by slow evaporation from dicloromethane. The data crystal was cut from a larger crystal and had approximate dimensions; 0.50 x 0.10 x 0.08 mm. A total of 1080 frames of data were collected using w-scans with a scan range of 0.5° and a counting time of 22 seconds per frame. The function, $\Sigma w(|F_O|^2 - |F_C|^2)^2$, was minimized, where $w = 1/[(\sigma(F_O))^2 + (0.0513*P)^2 + (0.5119*P)]$ and $P = (|F_O|^2 + 2|F_C|^2)/3$. $R_W(F^2)$ refined to 0.128, with R(F) equal to 0.0482 and a goodness of fit, S, = 1.19. Further details of this structure and its refinement may be obtained from the Cambridge Crystallographic Data Centre by quoting CCDC 931726.

Table 5.2. X-ray crystal data and structure refinement for **CuTTFP.**

Empirical formula	C42 H30 Cu N4 S8	
Formula weight	910.72	
Temperature	153(2) K	
Wavelength	0.71075 Å	
Crystal system	Triclinic	
Space group	P-1	
Unit cell dimensions	a = 11.954(2) Å	a = 11.954(2)
	b = 12.065(2) Å	b = 12.065(2)
	c = 14.235(3) Å	g = 90.783(5)°.
Volume	1963.7(6) $Å^3$	
Z	2	
Density (calculated)	1.540 Mg/m^3	
Absorption coefficient	1.020 mm^{-1}	
F(000)	934	
Crystal size	0.50 x 0.10 x 0.08 mm	
Theta range for data collection	3.01 to 27.48°.	
Index ranges	-15<=h<=15, -15<=k<=15, -18<=l<=18	
Reflections collected	20796	

Table 5.2 cont'd.

Independent reflections	8958 [R(int) = 0.0541]
Completeness to theta = 27.48°	99.4 %
Absorption correction	Semi-empirical from equivalents
Max. and min. transmission	1.00 and 0.683
Refinement method	Full-matrix least-squares on F^2
Data / restraints / parameters	8958 / 0 / 500
Goodness-of-fit on F^2	1.191
Final R indices [I>2sigma(I)]	R1 = 0.0482, wR2 = 0.1187
R indices (all data)	R1 = 0.0645, wR2 = 0.1281
Largest diff. peak and hole	0.988 and -0.669 e.$Å^{-3}$

5.3.4 X-Ray Crystal Structure of CuTTFP•CF_3SO_3

Crystals grew as green laths by careful layering of a THF containing $Cu(CF_3SO_3)_2$ onto a toluene solution of **CuTTFP** and allowing the solution to stand for 2 days. The data crystal had approximate dimensions; 0.29 x 0.07 x 0.04 mm. A total of 720 frames of data were collected using w-scans with a scan range of 0.5° and a counting time of 50 seconds per frame. A molecule of toluene was disordered about a crystallographic inversion center at 0, ½, ½. Attempts to model the disorder were unsatisfactory. The contributions to the scattering factors due to these solvent molecules were removed by use of the utility SQUEEZES in PLATON98. The function, $\Sigma w(|F_O|^2 - |F_C|^2)^2$, was minimized, where $w = 1/[(\sigma(F_O))^2 + (0.1772*P)^2 + (1.916*P)]$ and $P = (|F_O|^2 + 2|F_C|^2)/3$. $R_W(F^2)$ refined to 0.337, with R(F) equal to 0.118 and a goodness of fit, S, = 1.07. Further details of this structure and its refinement may be obtained from the Cambridge Crystallographic Data Centre by quoting CCDC number 931727.

Table 5.3. X-ray crystal data and structure refinement for **Cu TTFP•2 CF_3SO_3.**

Empirical formula	C51 H44 Cu F6 N4 O6 S10	
Formula weight	1307.04	
Temperature	153(2) K	
Wavelength	0.71075 Å	
Crystal system	Monoclinic	
Space group	P21/n	
Unit cell dimensions	a = 6.813(2) Å	a = 6.
	b = 14.693(5) Å	b = 14.693(5)
	c = 27.160(10) Å	g = 90°.
Volume	2718.3(17) $Å^3$	
Z	2	
Density (calculated)	1.597 Mg/m^3	
Absorption coefficient	0.861 mm^{-1}	
F(000)	1338	
Crystal size	0.29 x 0.07 x 0.04 mm	
Theta range for data collection	3.00 to 25.00°.	
Index ranges	-8<=h<=8, 0<=k<=17, 0<=l<=32	
Reflections collected	4713	
Independent reflections	4713	
Completeness to theta = 25.00°	98.6 %	
Absorption correction	Semi-empirical from equivalents	
Max. and min. transmission	1.00 and 0.214	
Refinement method	Full-matrix least-squares on F^2	
Data / restraints / parameters	4713 / 0 / 325	
Goodness-of-fit on F^2	1.074	
Final R indices [I>2sigma(I)]	R1 = 0.1178, wR2 = 0.3102	
R indices (all data)	R1 = 0.1759, wR2 = 0.3374	
Largest diff. peak and hole	1.213 and -1.338 $e.Å^{-3}$	

5.3.5 X-Ray Crystal Structure of ZnTTFP

Crystals grew as violet prisms by slow evaporation from a 1:1 DCM/THF solution. The data crystal was cut from a larger crystal and had approximate dimensions; 0.48 x 0.20 x 0.08 mm. A total of 1844 frames of data were collected using w-scans with a scan range of 0.5° and a counting time of 30 seconds per frame. A molecule of what appeared to be tetrahydrofuran was disordered near ½, 1, 0. Attempts to model the disorder were unsatisfactory. The contributions to the scattering factors due to this solvent molecule were removed by use of the utility SQUEEZE in PLATON98. The hydrogen atoms on the water molecule were located in a ΔF map. However, these hydrogen atoms did not refine adequately. As a result, the O-H bond lengths were set to 0.80 Å and their positional parameters were tied to that of O1W in the final refinement model. The function, $\Sigma w(|F_O|^2 - |F_C|^2)^2$, was minimized, where $w = 1/[(\sigma(F_O))^2 + (0.128*P)^2]$ and $P = (|F_O|^2 + 2|F_C|^2)/3$. $R_W(F^2)$ refined to 0.218, with R(F) equal to 0.0747 and a goodness of fit, S, = 0.993. Further details of this structure and its refinement may be obtained from the Cambridge Crystallographic Data Centre by quoting CCDC 931725.

Table 5.4. X-ray crystal data and structure refinement for **ZnTTFP.**

Empirical formula	C52 H52 N4 O5 S8 Zn	
Formula weight	1134.83	
Temperature	100(2) K	
Wavelength	0.71075 Å	
Crystal system	Triclinic	
Space group	P-1	
Unit cell dimensions	a = 12.755(2) Å	a = 12.755(2)
	b = 13.918(2) Å	b = 13.918(2)

Table 5.4 cont'd.

	c = 16.006(3) Å g = 93.010(3)°.
Volume	2583.5(7) $Å^3$
Z	2
Density (calculated)	1.459 Mg/m^3
Absorption coefficient	0.851 mm^{-1}
F(000)	1180
Crystal size	0.48 x 0.20 x 0.08 mm^3
Theta range for data collection	1.60 to 25.00°.
Index ranges	-15<=h<=14, -16<=k<=15, 0<=l<=19
Reflections collected	8784
Independent reflections	8784
Completeness to theta = 25.00°	96.6 %
Absorption correction	Semi-empirical from equivalents
Max. and min. transmission	1.00 and 0.639
Refinement method	Full-matrix least-squares on F^2
Data / restraints / parameters	8784 / 0 / 585
Goodness-of-fit on F^2	0.993
Final R indices [I>2sigma(I)]	R1 = 0.0747, wR2 = 0.1954
R indices (all data)	R1 = 0.0940, wR2 = 0.2182
Largest diff. peak and hole	1.149 and -1.023 $e.Å^{-3}$

5.3.6 X-Ray Crystal Structure of ZnTTFP(TBACl)

Crystals grew as dark green laths by diffusion of hexanes into dichloromethane. The data crystal was cut from a larger crystal and had approximate dimensions; 0.60 x 0.31 x 0.20 mm. The data were collected at -120 °C on a Nonius Kappa CCD diffractometer using a Bruker AXS Apex II detector and a graphite monochromator with MoKa radiation (l = 0.71075Å). Reduced temperatures were maintained by use of an Oxford Cryosystems 600 low-temperature device. A total of 1300 frames of data were collected using w-scans with a scan range of 1.2° and a counting time of

30 seconds per frame. Data reduction was performed using SAINT V8.27B. The function, $\Sigma w(|F_o|^2 - |F_c|^2)^2$, was minimized, where $w = 1/[(\sigma(F_o))^2 + (0.1496*P)^2 + (487.17*P)]$ and $P = (|F_o|^2 + 2|F_c|^2)/3$. $R_w(F^2)$ refined to 0.542, with R(F) equal to 0.210 and a goodness of fit, S, = 1.25. Further details of this structure and its refinement may be obtained from the Cambridge Crystallographic Data Centre by quoting CCDC 0001834.

Table 5.5. X-ray crystal data and structure refinement for **ZnTTFP-TBACl.**

Empirical formula	C59 H68 Cl3 N5 S8 Zn	
Formula weight	1275.38	
Temperature	153(2) K	
Wavelength	0.71073 Å	
Crystal system	Monoclinic	
Space group	P21/n	
Unit cell dimensions	a = 15.5587(13) Å	a= 90°.
	b = 17.4010(15) Å	b= 102.706(5)°.
	c = 24.074(2) Å	g = 90°.
Volume	6358.2(9) $Å^3$	
Z	4	
Density (calculated)	1.332 Mg/m^3	
Absorption coefficient	0.816 mm^{-1}	
F(000)	2664	
Crystal size	0.60 x 0.31 x 0.20 mm	
Theta range for data collection	1.43 to 25.00°.	
Index ranges	-18<=h<=18, -20<=k<=20, -28<=l<=28	
Reflections collected	140754	
Independent reflections	11203 [R(int) = 0.0990]	
Completeness to theta = 25.00°	99.8 %	
Absorption correction	Semi-empirical from equivalents	
Max. and min. transmission	1.00 and 0.855	
Refinement method	Full-matrix least-squares on F^2	
Data / restraints / parameters	11203 / 456 / 693	

Table 5.5 cont'd.

Goodness-of-fit on F^2	1.249
Final R indices [I>2sigma(I)]	R1 = 0.2099, wR2 = 0.5358
R indices (all data)	R1 = 0.2200, wR2 = 0.5424
Largest diff. peak and hole	1.763 and -1.651 e.$Å^{-3}$

5.3.7 X-Ray Crystal Structure of ZnTTFP•2C_{60}

X-ray Experimental for $(C_{42}H_{30}N_4S_8)Zn - 2C_{60} - 3/2\ CH_2Cl_2$: Crystals grew as plates by slow evaporation from dichloromethane. The data crystal was cut from a larger crystal and had approximate dimensions; 0.36 x 0.20 x 0.04 mm. The data were collected on a Rigaku SCX-Mini with a Mecury 2 CCD using a graphite monochromator with MoKα radiation (λ = 0.71075Å). A total of 1080 frames of data were collected using w-scans with a scan range of 0.5° and a counting time of 35 seconds per frame. The data were collected at 153 K using an Oxford Cryostream low temperature device. The function, $\Sigma w(|F_O|^2 - |F_C|^2)^2$, was minimized, where $w = 1/[(\sigma(F_O))^2 + (0.1*P)^2]$ and $P = (|F_O|^2 + 2|F_C|^2)/3$. $R_W(F^2)$ refined to 0.331, with R(F) equal to 0.171 and a goodness of fit, S, = 1.63.

The structure of the porphyrin complex contains two equivalents of C_{60}. One molecule of C_{60} was encapsulated within **ZnTTFP**. This molecule was disordered. The disorder molecule was modeled by fitting an idealized C60 molecule to the complex. Two idealized C60 molecules were fitted. A second C60 molecule was found outside the complex. This molecule was well defined. The geometry of the C60 molecules was restrained to have approximately equivalent geometries throughout the refinement process. One molecule of DCM was disordered about a general position and one molecule of DCM was disordered about a crystallographic inversion center. The geometry of the DCM molecules was also restrained to be equivalent. No H atoms on the DCM molecules were included in the final refinement

model. Disorder was also found for two of the CH3-S moieties on the TTF porphyrin complex.

Table 5.6. X-ray crystal data and structure refinement for **ZnTTFP•2C_{60}.**

Empirical formula	C163.50 H33 Cl3 N4 S8 Zn	
Formula weight	2481.14	
Temperature	100(2) K	
Wavelength	0.71075 Å	
Crystal system	Triclinic	
Space group	P-1	
Unit cell dimensions	a = 13.712(4) Å	a= 75.245(9)°.
	b = 17.971(5) Å	b= 72.237(8)°.
	c = 21.550(5) Å	g = 86.377(10)°.
Volume	4889.3(2) $Å^3$	
Z	2	
Density (calculated)	1.685 Mg/m^3	
Absorption coefficient	0.578 mm^{-1}	
F(000)	2502	
Crystal size	0.36 x 0.20 x 0.04 mm	
Theta range for data collection	3.00 to 27.44°.	
Index ranges	-17<=h<=17, -23<=k<=23, -27<=l<=27	
Reflections collected	51799	
Independent reflections	22187 [R(int) = 0.1128]	
Completeness to theta = 27.44°	99.4 %	
Absorption correction	Semi-empirical from equivalents	
Max. and min. transmission	1.00 and 0.773	
Refinement method	Full-matrix-block least-squares on F^2	
Data / restraints / parameters	22187 / 35138 / 2232	
Goodness-of-fit on F^2	1.607	
Final R indices [I>2sigma(I)]	R1 = 0.1194, wR2 = 0.3041	
R indices (all data)	R1 = 0.1711, wR2 = 0.3312	
Largest diff. peak and hole	1.496 and -0.803 $e.Å^{-3}$	

5.4 Chapter 5 References

1. Gaussian 09, Revision A.1, Frisch, M. J.; Trucks, G. W.; Schlegel, H. B.; Scuseria, G. E.; Robb, M. A.; Cheeseman, J. R.; Scalmani, G.; Barone, V.; Mennucci, B.; Peterson, G. A.; Nakatsuji, H.; Caricato, M.; Li, X.; Hratchian, H. P.; Izmaylov, A. F.; Bloino, J.; Zheng, G.; Sonnenberg, J. L.; Hada, M.; Ehara, M.; Toyota, K.; Fukuda, R.; Hasegawa, J.; Ishida, M.; Nakajima, T.; Honda, Y.; Kitao, O.; Nakai, H.; Vreven, T.; Montgomery, Jr., J. A.; Peralta, J. E.; Ogliaro, F.; Bearpark, M.; Heyd, J. J.; Brothers, E.; Kudin, K. N.; Staroverov, V. N.; Kobayashi, R.; Normand, J.; Raghavachari, K.; Rendell, A.; Burant, J. C.; Iyengar, S. S.; Tomasi, J.; Cossi, M.; Rega, N.; Millam, N. J.; Klene, M.; Knox, J. E.; Cross, J. B.; Bakken, V.; Adamo, C.; Jaramillo, J.; Gomperts, R.; Stratmann, R. E.; Yazyev, O.; Austin, A. J.; Cammi, R.; Pomelli, C.; Ochterski, J. W.; Martin, R. L.; Morokuma, K.; Zakrzewski, V. G.; Voth, G. A.; Salvador, P.; Dannenberg, J. J.; Dapprich, S.; Daniels, A. D.; Farkas, Ö.; Foresman, J. B.; Ortiz, J. V.; Cioslowski, J.; Fox, D. J. Gaussian, Inc., Wallingford CT, **2009**.
2. (a) Becke, A. D. *Phys. Rev. A* **1988**, 38, 3098. (b) Lee, C.; Yang, W.; Parr, R. G. *Phys. Rev. B* **1988**, *37*, 785.
3. Yanai, T.; Tew, D.; Handy, N. *Chem. Phys. Lett*. **2004**, *393*, 51.
4. (a) Brückner, C.; Posakony, J. J.; Johnson, C. K.; Boyle, R. W.; James, B. R.; Dolphin, D. *J. Porphyrins Phthalocyanines* **1998**, 2, 455. (b) Boyle, R. W.; Brückner, C.; Posakony, J. J.; James, B. R.; Dolphin, D. *Org. Synth.* **1999**, 76, 287 and *Org. Synth.* **2004**, *Coll. Vol. 10*, 10, 370.
5. Lahaye, D.; Muthukumaran, K.; Hung, C-H.; Gryko, D; Reboucas, J. S.; Spasojevic, I.; Batinic-Haberle, I.; Lindsey, J. S. *Bioorg. Med. Chem*. **2007**, *15*, 7066.
6. Compound **2.24** was made by Steffen Bähring using procedures previously reported. Steimecke, G.; Sieler, H. J.; Kirmse, R.; Hoyer, E. *Phosphorus Sulfur* **1979**, *7*, 49. (b) Simonsen, K. B.; Svenstrup, N.; Lau, J.; Simonsen, O.; Mork, P.; Kristensen, G. J.; Becher, J. *Synthesis* **1996**, 407.
7. Pereira, N.; Serra, A.C.; Pineiro, M.; Gonsalves, A.M d'A. Rocha; Abrantes, M.; Laranjo, M.; Botelho, F. *J. Porpyrins Phthalocyanines,* **2010**, 14, 438.
8. Moore, A.J.; Bryce, M.R. *J. Org. Chem.* **1994**, 59, 6847.
9. Crystal Clear 1.40 (2008). Rigaku Americas Corporation, The Woodlands, TX.
10. SIR97. A program for crystal structure solution. Altomare, A., Burla, M. C., Camalli, M., Cascarano, G. L., Giacovazzo, C., Guagliardi, A., Moliterni, A. G. G., Polidori, G. and Spagna, R. *J. Appl. Cryst*. **1999**, 32, 115.
11. Sheldrick, G. M. SHELXL97. Program for the Refinement of Crystal Structures. *Acta Cryst*. **2008**, *A64*, 112.
12. Sluis, P. v. d.; Spek, A. L. SQUEEZE. *Acta Cryst*. **1990**, *A46*, 194-201.
13. Spek, A. L (1998). PLATON, A Multipurpose Crystallographic Tool. Utrecht University, The Netherlands.
14. WinGX 1.64. An Integrated System of Windows Programs for the Solution, Refinement and Analysis of Single Crystal X-ray Diffraction Data. Farrugia, L. J. *J. Appl. Cryst*. **1999**, *32*. 837-838.

15. International Tables for X-ray Crystallography (1992). Vol. C, Tables 4.2.6.8 and 6.1.1.4, A. J. C. Wilson, editor, Boston: Kluwer Academic Press.
16. Sheldrick, G. M. (1994). SHELXTL/PC (Version 5.03). Siemens Analytical X-ray Instruments, Inc., Madison, Wisconsin, USA.